



# DISSERTATION

Titel der Dissertation

High index difference polymer waveguide Mach-Zehnder interferometer  
biosensor, compatible with injection molding and spin-coating

angestrebter akademischer Grad

Doktor der Naturwissenschaften (Dr. rer.nat.)

Verfasserin / Verfasser:	Mag. Roman Bruck
Matrikel-Nummer:	9902906
Dissertationsgebiet (lt. Studienblatt):	Physik
Betreuerin / Betreuer:	Univ.-Prof. Dr. Martin Neumann

Wien, im Dezember 2010





## Imagine...

Like phoenix from the ashes, the human society rose after world war II to a society with wealth, health and a degree of personal liberty so far unmatched in human history.

Especially in the "rich countries", the societies face far-reaching changes and challenges. People are getting older and older and the anticipated average life span is steadily increasing from decade to decade. This generation is the first that can freely choose what it wants to eat. And how much.

These, in fact, positive developments also have some downsides. So far, it was simply not necessary for the human body to be operational for one hundred years. So far, it was simply not necessary for the human mind to develop methods against overweight due to excess food availability. The world might be changing fast, but this is not the case for the human body, or the human mind. Additionally, the world, as we know it today, is changing, due to environmental pollution and overexploitation of natural resources.

In a new world, new diseases are arising. For other, already known, diseases new diagnostic tests and therapies are being developed. In our society, the need for medical care is constantly on the rise. Sometimes, a correct diagnosis and the corresponding medical treatment is time-critical. Often, they are expensive. Too often, they are too expensive.

And now, imagine a new diagnostic device, so cheap that every doctor can afford buying one. Imagine sensor chips, produced at nearly no cost at all that are able to analyze literally hundreds of different molecules from a droplet of your blood. So fast that you can wait at the doctor's office for your results. Imagine this diagnostic device to be portable. Imagine its applications in developing countries. Imagine the price of a fast and correct diagnosis to reduce by an order of magnitude. Imagine the device to be, where it really matters.

This is what this work is all about. Hidden behind and buried under mathematical equations, scientific phrases, diagrams, tables, pictures, descriptions and data analysis, this thesis is about people and their needs.





## Personal note and acknowledgements

After five years of work as a PhD student at the Austrian Institute of Technology (AIT) and the University of Vienna, my PhD thesis is now finished. Five years of learning and of doing research, of being supervised and supervising others. Five years of writing publications, proposals and reports. Five years of hard work, of frustration and of success.

What I liked most at my work at the AIT was that my job integrated nearly every aspect in the development of our biosensor device. Starting with the material selection, the simulations, the design and the layout of the sensor, the fabrication of the devices in the cleanroom and ending with the characterization and the measurements performed on these samples. All these tasks were done by my hands. For me, having control on every aspect of the device development is a great thing. Sure, it is a lot of work, but you are mostly independent (and you are the one responsible when something goes wrong...). And it is a great opportunity to acquire skills in multiple fields.

When you are doing research, you are never alone. There is always interaction with your supervisor, colleagues in your group, colleagues in your department or people from other groups that are doing research in a related field. However, there is also your family, your friends and some life outside the lab. So, it is time to make some acknowledgements:

I want to thank my parents Michael and Brigitte for their (not only financial) support and their presence. Without their support, I would not have been able to finish neither my master nor my PhD degree. I want to thank them for continue smiling when I start to talk science and they do not understand a single word of what I am saying. It is true when I say that I have one of the best parents in the world.

My girlfriend Bettina Seeland for being with me. She was always the first to share my setbacks and my success. I love you, babe! In good as in bad times...

To my supervisor at the AIT, Rainer Hainberger, for guiding me, helping me and giving me time and opportunity to develop my skills. His advice turns out to be true at a frustrating high rate.

To my colleagues at the AIT and in our photonics group. There was so much interaction and mutual assistance in so many ways that it is impossible to name all of it. Thank you guys! Especially, I want to thank Paul Müllner, who has not only be a colleague, but a good friend in my whole time as PhD student. I share many, many things with him and we are a damn good team. I want to thank Eva Melnik, who developed the surface modification protocol of the sensor surface. She made the chemical part of the sensor working and facilitated all the biosensing experiments.

I want to thank my supervisor at the University of Vienna, Martin Neumann, who accompanied me during my diploma and my PhD thesis.

I want to thank Nadja Imhof for her artwork "At the doctor's office", on page I



# Contents

<b>Imagine...</b>	<b>I</b>
<b>Personal note and acknowledgements</b>	<b>III</b>
<b>Table of content</b>	<b>VI</b>
<b>1 Introduction</b>	<b>1</b>
1.1 Aim of this work . . . . .	3
1.2 Outline . . . . .	4
1.3 General remarks . . . . .	5
<b>2 Optical waveguides</b>	<b>7</b>
2.1 Optical basics and definitions . . . . .	7
2.2 Principles of planar waveguides . . . . .	9
2.2.1 Three layer slab waveguide . . . . .	9
2.2.2 Rib- and wire-type waveguides . . . . .	12
2.3 Coupling methods for thin film waveguides . . . . .	15
2.3.1 End face coupling . . . . .	16
2.3.2 Taper structures . . . . .	17
2.3.3 Prism coupling . . . . .	19
2.3.4 Grating couplers . . . . .	21
<b>3 Evanescent wave sensor principles for biosensing</b>	<b>25</b>
3.1 Evanescent waveguide sensors . . . . .	25
3.1.1 Sensitivity parameters for evanescent waveguides . . . . .	26
3.1.2 Young interferometers . . . . .	28
3.1.3 Mach-Zehnder interferometers (MZIs) . . . . .	30
3.1.4 Ring resonators . . . . .	33
3.2 Grating sensors . . . . .	35
3.3 Surface plasmon resonance sensors . . . . .	38
3.4 Comparison of presented sensor concepts . . . . .	40
<b>4 Design of the MZI sensor</b>	<b>43</b>
4.1 Material selection . . . . .	43
4.1.1 Introduction to polymers . . . . .	44
4.1.2 Comparison between polymers and inorganic materials . . . . .	45
4.1.3 Overview of transparent polymers . . . . .	46
4.1.4 Requirements for polymers used . . . . .	47
4.1.5 Selected polymers and properties . . . . .	49

---

4.2	Simulations and MZI layout . . . . .	50
4.2.1	Waveguide optimization . . . . .	51
4.2.2	Y-branches for the MZI . . . . .	52
4.2.3	Lateral tapers . . . . .	56
4.2.4	Grating couplers . . . . .	58
4.2.5	High index coating for grating couplers . . . . .	73
4.2.6	Summary of grating coupler simulations . . . . .	83
4.2.7	Further enhancement possibilities for grating couplers . . . . .	83
<b>5</b>	<b>Experiments and results</b>	<b>85</b>
5.1	Sample fabrication . . . . .	85
5.2	Analysis of waveguide cross section . . . . .	88
5.3	Grating couplers with high index coating . . . . .	89
5.4	First measurements with end face coupled MZIs . . . . .	93
5.5	MZI online measurements of biotin-streptavidin binding . . . . .	96
5.5.1	Modification of the polyimide (PI) surface . . . . .	96
5.5.2	Reproducibility of binding experiments and blocking of the modified PI surface . . . . .	98
5.5.3	Concentration dependent measurements . . . . .	103
5.6	Verification on MZIs with grating couplers . . . . .	105
<b>6</b>	<b>Summary and conclusion</b>	<b>109</b>
<b>7</b>	<b>Outlook</b>	<b>111</b>
7.1	Injection molding results . . . . .	111
7.2	Online measurements of DNA binding . . . . .	116
	<b>Bibliography</b>	<b>119</b>
	<b>Appendix</b>	<b>128</b>
	Abstract in english . . . . .	128
	Abstract in german . . . . .	129
	List of publications and presentations . . . . .	130
	Curriculum vitae . . . . .	131

# 1 Introduction

Medicine can be defined as the task of improving humans health, wellbeing and life span. It has been an important part of each human society. In modern medicine, tools for diagnosis and therapy are in a state of a continuing revolution. A correct diagnosis is always a prerequisite for a successful therapy.

The need for diagnostic tests is ever-growing in our society. Peoples life span is increasing. Terminal illnesses become curable if correctly diagnosed early enough. New diseases are found. New diseases come into existence due to changes in humans life or the environment we are living in. All this generates an increasing demand for existing diagnostic test, but also for new diagnostic tools and principles.

Currently, most clinical diagnostic tests are laborious, require sophisticated equipment operated by specially trained staff, and are, therefore, expensive. These tests often involve time consuming labeling techniques that attach fluorescent or radioactive markers on the analytes to be measured. In order to overcome these disadvantages new sensor schemes were investigated and integrated photonic biosensors, in particular those based on the evanescent wave principle, in combination with microfluidic systems were found to represent a promising way for the development of a new generation of diagnostic tools and affordable point of care diagnostic systems. Such sensors promise:

- Label free analyte detection employing selective molecular binding processes of the target analyte on the sensor surface.
- Fast sensor response, which is mainly limited by the kinetics of the analyte in the fluidic system. The optical sensor itself reacts instantaneously.
- Real time measurements of the analyte binding processes providing additional information on dynamic properties of the analyte, such as the binding affinity.
- High level of integration and small device footprints enable arrays of sensors that can be combined in a single fluidic package, allowing for multi-parameter analysis while keeping the sample volume consumption low.
- High electromagnetic compatibility and no interference effects with electric devices.

Possible applications for photonic biosensors are *e.g.* the specific detection of proteins and DNA/RNA as well as pollutant detection. Proteins play an important role in the human body. They are not only involved to all activities within human cells, they are also indispensable for the function of the human body as a whole. The detection of specific proteins is essential for medical diagnosis, but can also be of relevance in online monitoring applications, *e.g.* in pharmaceutical or food industry. In medical applications, the detection of specific DNA/RNA sequences is necessary for the diagnosis of genetic diseases. Genetic diseases can often be triggered from different defects in DNA/RNA sequences. Information which particular defect in the DNA/RNA sequence is the cause of a disease helps to decide which therapy is best for a certain patient. One example in the broad range of potential applications in the diagnostic industry for evanescent biosensors are diagnostic tests for autoimmune diseases. It is accepted in the field of autoimmune diagnostics that the affinity of the antibodies is a crucial parameter,

which is not measurable with state-of-the-art routine diagnostic systems. All conventional diagnostic methods represent end point measurements that do not allow the calculation of antibody affinity by real time monitoring.

Because of hygienic standards and to prevent cross contaminations, sensors including the fluidic systems have to be designed as single use systems for most medical applications. Therefore, fabrication costs are another critical parameter that has to be taken into account for the development of new sensor systems. The implementation of a cheap, reliable and sensitive real time bio-affinity measurement will be welcomed by the diagnostic industry for many fields of applications. Photonic biosensors in the field of pollutant detection can be applied for example as tool for quality management in industrial processes or monitoring of pollutants in the environment, if the pollutant can be specifically bound to the sensor surface.

Knowing the importance of these possible applications and motivated by the promised advantages, scientists spent a lot of time and effort in the development of evanescent wave photonic biosensors. Evanescent sensing devices for biosensing have been proposed and demonstrated in various configurations, *e.g.* as grating sensors in titanium dioxide[1], as Mach-Zehnder interferometers (MZIs) in silicon oxynitride[2], as MZIs made from silicon nitride (SiN) waveguides on patterned polymer substrates[3] or as ring resonators in silicon on insulator (SOI)[4, 5]. So far, such devices have always been realized in inorganic materials systems[6, 7], where the waveguides structures were fabricated using standard semiconductor technology.

The ultimate goal of the research activities that act as a framework for this work, is the realization of disposable all-polymer optical sensor chips for the label-free detection of bio-molecules[8], employing evanescent waveguides in an integrated MZI configuration[9, 10, 11]. These all-polymer sensor chips should comprise a low index polymer substrate that is fabricated by injection molding and carries all necessary optical structures for the sensor as well as a high index core layer and a low index cladding layer applied by spin coating. This approach takes full advantage of the mature technology platform that is available for polymer processing. The use of transparent polymers as optical waveguide materials has attracted great attention for a wide range of applications[12]. Polymers provide tunable properties, and therefore, allow large flexibility on the design of optical elements. The processing of polymers is based on powerful technologies such as injection molding, hot embossing and spin coating, which are suited for cost-effective mass production. Polymers in optics and photonics have become an important factor and a wide variety of applications has been demonstrated. Examples are polymer waveguide grating couplers[13], polymer arrayed waveguide gratings[14], and polymer waveguide amplifiers[15].

The proposed sensor design is based on the highly sensitive MZI. An additional advantage of the MZI concept is the simple read out system, which can be composed of a single mode laser diode with a fixed wavelength and a simple photodiode. This sensor concept, realized with inorganic materials, has successfully been used for the detection of small concentrations of biomolecules. MZI biosensors have been realized for example with SiN rib waveguides[16, 17, 18] or with SOI wire waveguides[19]. Polymer based integrated optical MZIs have been applied to bulk sensing, *e.g.* [8, 20] and have been proposed for biosensing[21, 22]. However, biosensing using spin coated high index contrast thin film polymer waveguides has so far not been reported.

## 1.1 Aim of this work

The focus of this work is the development and demonstration of polymer waveguide based sensors, employing a MZI configuration of evanescent waveguides for the detection of biomolecules in medical applications. The sensor has to be designed in a way that allows the transfer of the sensor layout on a patterned injection molded polymer substrate, where the high index polymer waveguide core layer and the low index polymer cladding can be applied by spin coating steps.

The given task necessitates several innovative approaches. The sensitivity of evanescent optical sensors for biosensing applications strongly depends on the refractive index contrast of the material system used. Comparing with inorganic material systems, such as SOI or SiN/SiO<sub>2</sub>, the maximum refractive index contrast in polymer material systems is rather small. In most polymer material systems, refractive index differences between core and cladding layers are in the range of a few tenths or a few hundredths, which leads to dimensions for single mode waveguide cross sections of several micrometers, *e.g.* [12, 23, 24].

For this application, a polymer material system has to be found that provides a sufficient refractive index contrast, allows the fabrication of the sensor device in the above mentioned way and is chemically stable in biosensing experiments. A higher refractive index contrast necessitates much smaller waveguide dimensions for single mode operation, which is a prerequisite for the MZI, and puts greater demands on the technology platform used.

A solution has to be found for efficiently coupling light into and out of the sensor chip on the injection molded substrate. For this purpose, grating couplers offer several advantages. They can be placed freely on the device, they do not require a high quality sample end facet and they are compatible with planar waveguide technology. In most cases, grating couplers can be patterned in the same fabrication steps as the waveguides, and therefore, add no additional complexity to the fabrication process. Unfortunately, small grating couplers that allow the coupling of light into narrow single mode waveguides show only very little coupling efficiency when realized in low-index contrast materials systems such as polymers.

A surface modification protocol for the chosen waveguide core polymer has to be developed. This protocol must not thin nor attack the core layer. In addition, the distance of the molecular binding sites for the target molecules to the polymer surface has to be kept low in order to expose the target molecules to the maximum intensity of the evanescent tail of the guided mode, and therefore, achieve maximum sensitivity.

There are also some practical aspects that have to be considered in the definition of the aims in this work. The only single mode waveguide geometry compatible with injection molding and spin coating is the inverted rib waveguide, where a waveguide trench, patterned into the injection molded substrate, is filled up with the high index polymer in the spin coating step of the core layer. Therefore, the sensor has to be designed to work with transversal electrical (TE) polarization. Although the transversal magnetic (TM) waveguide mode in thin film waveguides has a higher surface sensitivity[25], TE polarization is favored in this sensor design due to the fact that rib waveguides suffer from lateral leakage for TM polarization[26, 27].

In this work, the sensor design has to be optimized for two important wavelengths, 633 nm and 1.31  $\mu\text{m}$ . 633 nm is a typical sensing wavelength due to the widespread use of HeNe laser sources for sensing applications. Driven by telecommunication applications, there are compact and high quality components available at a reasonable price for the second wavelength of 1.31  $\mu\text{m}$ . The maximum achievable

sensitivity is higher for the wavelength of 633 nm than for 1.31  $\mu\text{m}$ . Nevertheless, due to the fact that optical structures scale their dimensions with the wavelength, the fabrication of the optical structures for 1.31  $\mu\text{m}$  is relaxed compared to 633 nm.

Finally, the biosensing ability of the sensor device is to be demonstrated in the biotin-streptavidin system. The interaction between biotin and streptavidin is commonly used to validate the sensitivity of biosensors[28, 29] because of the high mass of the protein streptavidin (60 kDa) that serves as analyte and the strong affinity between biotin and streptavidin (binding constant  $K_a \approx 10^{14}$ ). Furthermore, surface bound streptavidin provides free binding sites for biotin and can be utilized for immobilization of biotinylated ligands such as biotin-tagged DNA strands. Thus, the biotin-streptavidin biorecognition system can serve as flexible platform for advanced biosensing experiments[30].

## 1.2 Outline

At the beginning, chapter 2 derives the properties of optical waveguides and gives an introduction on the theoretical background of optical waveguide theory as well as an overview of coupling methods for thin film waveguides. The choice of grating couplers as coupling elements is motivated in this chapter.

An overview of principles of evanescent wave biosensors and references to commercially available optical sensor products are given in chapter 3. This chapter also defines the sensitivity parameters and explains the MZI as a highly sensitive device that allows for simple and cheap read-out systems.

In chapter 4, the selected materials for the sensor device are presented. It also contains the results of all simulations performed in the context of the design of the sensor based on the selected materials and provides necessary information on the simulation methods that have been used in order to optimize the sensor device. Apart from simulations on the elements of the MZI, such as simulations of waveguide modes and the behavior of Y-branches, a considerable part of the chapter deals with simulations on grating couplers. Background information is given to the above mentioned fact that grating couplers for small beam diameters, which are needed to couple light into narrow single mode waveguides, show only a poor efficiency in low index contrast material systems. To overcome this limitation and to increase the coupling efficiency of such grating couplers, the deposition of a thin high index layer on top of the gratings is proposed and rigorously simulated.

The experimental part of this work is reviewed in chapter 5. The fabrication of the samples is described and the waveguide cross section of the realized inverted rib polymer waveguides is analyzed. Then, the positive effect of the high index layer on the efficiency of grating couplers, predicted in the simulations in chapter 4, is experimentally verified. An optimized surface modification protocol for the polymer surface is presented and the binding capacity of streptavidin on the sensor surface is quantified. The measurement setup for experiments with MZI sensors is described and finally, the polymer waveguide based biosensor is demonstrated. Biotin-streptavidin binding experiments are shown and the dynamic range of the sensor as well as the reproducibility of the experiments are investigated.

Chapter 6 summarizes this work and the most important results.

An outlook on the development of the fabrication process of the injection molded substrates and preliminary results on experiments of DNA detection are given in chapter 7.



## 1.3 General remarks

If not otherwise stated, the following assumptions are valid throughout this work:

1. Light is always propagating in the  $z$ -direction also called the longitudinal direction. The second horizontal coordinate is referred as  $x$ -direction or as lateral direction. The vertical direction is termed  $y$ -direction.
2. All media are assumed to be homogeneous, isotropic and lossless, *i.e.* no absorption takes place.
3. Within the Maxwell's equations, the relative permeability  $\mu_r$  is set to unity and the relative permittivity  $\epsilon_r$  does not depend on time. Moreover, it is assumed that the free charge density  $\rho_f$  and the free current density  $j_f$  are zero for the whole volume.
4. Laser sources are always assumed to be monochromatic. For both wavelengths, laser sources with a very narrow spectral widths are available, so that effects stemming from the non-monochromatic behavior of the laser source can be neglected for all applications within this work.
5. Light is always TE polarized, *i.e.* the main field component is the lateral electric field  $E_x$ . Therefore, all waveguide modes are TE or TE-like modes.



## 2 Optical waveguides

This chapter gives a basic introduction on the principles of optical waveguides and provides an overview of common waveguide geometries in integrated optics. At the end of this chapter, concepts for coupling light into and out of integrated optical waveguides are discussed. The information given here is the theoretical background that is necessary for the following chapters.

### 2.1 Optical basics and definitions

All optical theory is based on Maxwell's equations and all optical phenomena must satisfy these equations. In a complete form the Maxwell equations are[31]:

$$\nabla(\epsilon\vec{E}) = \rho_f \quad (2.1)$$

$$\nabla(\mu\vec{H}) = 0 \quad (2.2)$$

$$\nabla \times \vec{E} = -\mu \frac{\partial \vec{H}}{\partial t} \quad (2.3)$$

$$\nabla \times \vec{H} = j_f + \epsilon \frac{\partial \vec{E}}{\partial t} \quad (2.4)$$

In these equations,  $\vec{E}$  is the electric field,  $\vec{H}$  is the magnetic field,  $\rho_f$  is the free charge density and  $j_f$  is the free current density. The dielectric permittivity  $\epsilon$  is defined as  $\epsilon = \epsilon_0 \cdot \epsilon_r$ , where  $\epsilon_0$  is the permittivity of free space and  $\epsilon_r$  is the relative permittivity of the medium. The magnetic permeability  $\mu$  is defined in a similar way as  $\mu = \mu_0 \cdot \mu_r$ , where  $\mu_0 = 1/(\epsilon_0 c_0^2)$  is the permeability of free space and  $\mu_r$  depends on the medium. The time is labeled as  $t$ . The symbols used in this section are summarized in Table 2.1. Using assumptions from section 1.3, namely  $\rho_f = 0$  and  $j_f = 0$ , Maxwell's equations can be written as

$$\nabla(\epsilon\vec{E}) = 0 \quad (2.5)$$

$$\nabla(\mu\vec{H}) = 0 \quad (2.6)$$

$$\nabla \times \vec{E} = -\mu \frac{\partial \vec{H}}{\partial t} \quad (2.7)$$

$$\nabla \times \vec{H} = \epsilon \frac{\partial \vec{E}}{\partial t} \quad (2.8)$$

The variables of the electric field  $\vec{E}$  and the magnetic field  $\vec{H}$  are linked to the electric displacement field  $\vec{D}$  and to the magnetic induction  $\vec{B}$  in the following way:

$$\vec{D} = \epsilon\vec{E} \quad (2.9)$$

$$\vec{B} = \mu\vec{H} \quad (2.10)$$

**Table 2.1:** Summary of the basic electromagnetic symbols.

symbol	name	value	unit
$\vec{E}$	electric field		V/m
$\vec{H}$	magnetic field		A/m
$\vec{D}$	displacement field		As/m <sup>2</sup> = C/m <sup>2</sup>
$\vec{B}$	magnetic induction		Vs/m <sup>2</sup> = T
$\rho_f$	free charge density		C/m <sup>3</sup>
$j_f$	free current density		A/m <sup>2</sup>
$\epsilon$	dielectric permittivity		As/(Vm)
$\epsilon_0 = 1/(\mu_0 c_0^2)$	permittivity of free space	$8.854188 \cdot 10^{-12}$	As/(Vm)
$\mu$	magnetic permeability		N/A <sup>2</sup>
$\mu_0$	permeability of free space	$4\pi \cdot 10^{-7}$	Vs/(Am)
$\omega$	angular frequency		1/s
$\vec{k}$	wave vector		1/m
$\vec{k}_0$	free space wave vector		1/m
$n$	refractive index		1
$\lambda$	wavelength		m
$\lambda_0$	free space wavelength		m
$t$	time		s
$c_0$	speed of light in vacuum	299792458	m/s

By taking the curl of equation (2.7) and using the vector identity  $\nabla \times \nabla \times \vec{E} = \nabla(\nabla \cdot \vec{E}) - \nabla^2 \vec{E}$  as well as equations (2.5) and (2.8), the wave equation for the electric field can be found:

$$\nabla^2 \vec{E} = \left( \frac{\partial^2}{\partial x^2} + \frac{\partial^2}{\partial y^2} + \frac{\partial^2}{\partial z^2} \right) \vec{E} = \epsilon \mu \frac{\partial^2 \vec{E}}{\partial t^2} \quad (2.11)$$

This equation describes the propagation of electromagnetic waves. It admits solutions of the form of monochromatic plane waves[32], which have a common multiplicative term  $e^{i(\vec{k} \cdot \vec{x} - \omega t)}$ , where  $\omega$  is the angular frequency and  $\vec{k}$  is the wave vector of the propagating wave. For this kind of solutions, there are some important basic definitions:

$$n = \sqrt{\epsilon_r \mu_r} = \sqrt{\frac{\epsilon \mu}{\epsilon_0 \mu_0}} \quad (2.12)$$

$$\vec{k}_0 = \frac{\vec{k}}{n} \quad (2.13)$$

$$\lambda = \frac{2\pi c_0}{\omega n} = \frac{2\pi}{|\vec{k}|} \quad (2.14)$$

$$\lambda_0 = n\lambda \quad (2.15)$$

Here,  $n$  is the refractive index and  $\vec{k}_0$  is the so called free space wave vector. The wavelength is labeled as  $\lambda$  and  $\lambda_0$  is the free space wavelength. By choosing an appropriate geometric structure for the propagation of a plane wave, a plane wave can be confined in one or more directions. This allows to guide electromagnetic waves along predefined paths. Such wave guiding structures are the basis of integrated optics. The next section gives an introduction to planar concepts of wave guiding structures.

## 2.2 Principles of planar waveguides

### 2.2.1 Three layer slab waveguide

The easiest system for one dimensional (1D) wave guiding is a three layer step index slab system. A high index core layer with a constant refractive index is surrounded by low index materials whose refractive indices are not necessarily equal, but constant within each medium, as depicted in Fig. 2.1a). If it is assumed that the solution of Maxwell's equation is in the form of a propagating plane wave in the  $z$ -direction

$$\vec{E} = \vec{E}(x, y)e^{i(\omega t - \beta z)} \quad (2.16)$$

$$\vec{H} = \vec{H}(x, y)e^{i(\omega t - \beta z)} \quad (2.17)$$

where  $\beta$  is the propagation constant of the plane wave, then Maxwell's equations (2.7) and (2.8) can be rewritten in the following form[33]:

$$\frac{\partial E_z}{\partial y} + i\beta E_y = -i\omega\mu_0 H_x \quad (2.18) \quad \frac{\partial H_z}{\partial y} + i\beta H_y = i\omega\epsilon E_x \quad (2.21)$$

$$-i\beta E_x - \frac{\partial E_z}{\partial x} = -i\omega\mu_0 H_y \quad (2.19) \quad -i\beta H_x - \frac{\partial H_z}{\partial x} = i\omega\epsilon E_y \quad (2.22)$$

$$\frac{\partial E_y}{\partial x} - \frac{\partial E_x}{\partial y} = -i\omega\mu_0 H_z \quad (2.20) \quad \frac{\partial H_y}{\partial x} - \frac{\partial H_x}{\partial y} = i\omega\epsilon E_z \quad (2.23)$$

where  $E_x$  is the  $x$ -component of the electrical field  $\vec{E}(x, y)$ , defined as  $E_x = \vec{E}(x, y) \cdot \hat{x}$  if  $\hat{x}$  is a vector pointing in the positive  $x$ -direction with a length of  $|\hat{x}| = 1$ . All other field components of  $\vec{E}$  and  $\vec{H}$  are defined in an analogous way. For a slab waveguide, it can be assumed that there is no  $x$ -axis dependence on the electromagnetic fields  $\vec{E}$  and  $\vec{H}$ . Thus, the derivations  $\partial\vec{E}/\partial x$  and  $\partial\vec{H}/\partial x$  can be set equal to zero, which leads to a further simplification of the equations (2.18) to (2.23):

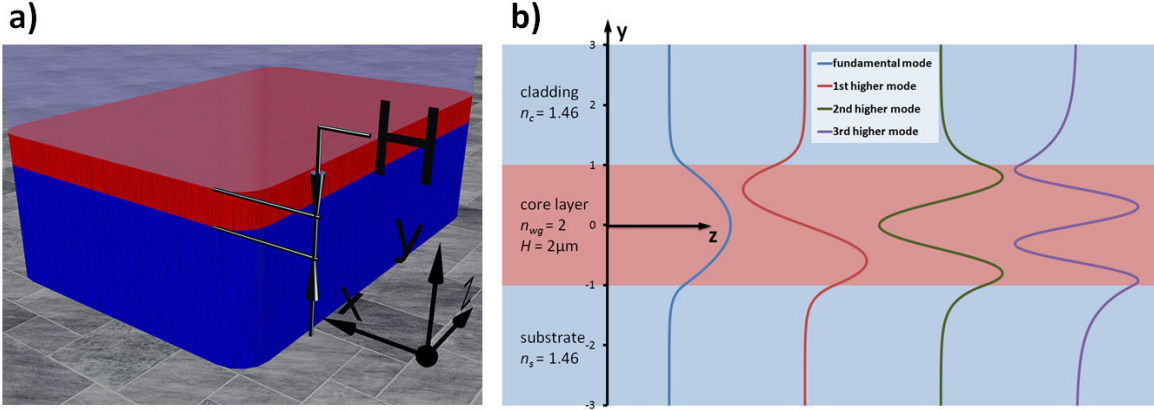


**Figure 2.1:** **a)** Sketch of a slab waveguide with thickness  $H$ . The high index layer (red) is surrounded by low index layers (blue). **b)** Profiles of the TE main field component  $E_x$  of lowest order guided modes of a  $2\ \mu\text{m}$  thick slab waveguide with a refractive index of 2, surrounded by layers with a refractive index of 1.46.

$$\frac{\partial E_z}{\partial y} + i\beta E_y = -i\omega\mu_0 H_x \quad (2.24)$$

$$\beta E_x = \omega\mu_0 H_y \quad (2.25)$$

$$\frac{\partial E_x}{\partial y} = i\omega\mu_0 H_z \quad (2.26)$$

$$\frac{\partial H_z}{\partial y} + i\beta H_y = i\omega\epsilon E_x \quad (2.27)$$

$$-\beta H_x = \omega\epsilon E_y \quad (2.28)$$

$$-\frac{\partial H_x}{\partial y} = i\omega\epsilon E_z \quad (2.29)$$

By inserting (2.28) and (2.29) into (2.24) as well as (2.25) and (2.26) into (2.27), this system of six equations decouples into two systems of three equations, which can be written in the following form by additionally replacing  $\epsilon$  with  $\epsilon = \epsilon_0 n^2$  [34]:

$$\frac{\partial^2 H_x}{\partial y^2} + (\omega^2 \mu_0 \epsilon_0 n^2 - \beta^2) H_x = 0 \quad (2.30)$$

$$E_y = -\frac{\beta}{\omega\epsilon_0 n^2} H_x \quad (2.31)$$

$$E_z = \frac{i}{\omega\epsilon_0 n^2} \frac{\partial H_x}{\partial y} \quad (2.32)$$

$$\frac{\partial^2 E_x}{\partial y^2} + (\omega^2 \mu_0 \epsilon_0 n^2 - \beta^2) E_x = 0 \quad (2.33)$$

$$H_y = \frac{\beta}{\omega\mu_0} E_x \quad (2.34)$$

$$H_z = -\frac{i}{\omega\mu_0} \frac{\partial E_x}{\partial y} \quad (2.35)$$

Equations (2.30) and (2.33) are wave equations for two different types of modes. The field components  $H_x, E_y, E_z$  compose the transversal magnetic mode (TM mode), which has to satisfy equations (2.30) to (2.32). The three field components left,  $E_x, H_y, H_z$ , compose the transversal electric mode (TE mode), which has to satisfy equations (2.33) to (2.35). These two modes are orthogonal to each other, so they are completely separated and cannot interfere. As a result, both modes can be treated separately for a three layer slab waveguide. In a slab waveguide, where the high index material is present in the region  $0 < y < H$ , the main field for TE modes  $E_x$  can be written in the form[34]

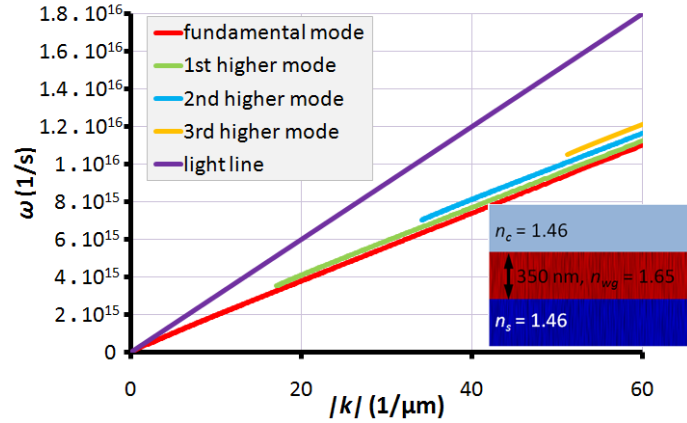


**Figure 2.2:** Dispersion relation of the first TE modes of a 350 nm thick slab waveguide ( $n_{wg} = 1.65$ ) surrounded by low index layers ( $n_s = n_c = 1.46$ ). Due to the symmetric waveguide structure, at least one guided mode exists for arbitrary low frequencies.

$$E_x = E_0 \cos(\Phi) e^{\gamma_s y} \quad \text{for } y < 0 \quad (2.36)$$

$$E_x = E_0 \cos(k_y y + \Phi) \quad \text{for } 0 < y < H \quad (2.37)$$

$$E_x = E_0 \cos(k_y H + \Phi) e^{-\gamma_c (y-H)} \quad \text{for } y > H \quad (2.38)$$

with a cosine shape in the core layer and exponentially decaying fields into the substrate and the cladding. The parameters  $k_y$ ,  $\Phi$ ,  $\gamma_c$  and  $\gamma_s$  define the profile of the waveguide mode and are to be determined. After some mathematical steps, details of which can be found in references [33] and [34], it can be shown that  $k_y$  satisfies an eigenvalue equation of the form

$$2ak_y = (m+1)\pi - \tan^{-1} \frac{k_y}{\gamma_s} - \tan^{-1} \frac{k_y}{\gamma_c} \quad (2.39)$$

The optical structure supports a discrete set of modes identified by the corresponding mode number  $m$ . For each guided mode, there exists a solution  $k_{y,m}$  for this eigenvalue equation. By using[34]

$$k_{y,m} = k_0 \sqrt{n_{wg}^2 - n_{eff,m}^2} \quad (2.40)$$

$$\gamma_{c,m} = k_0 \sqrt{n_{eff,m}^2 - n_c^2} \quad (2.41)$$

$$\gamma_{s,m} = k_0 \sqrt{n_{eff,m}^2 - n_s^2} \quad (2.42)$$

each solution  $k_{y,m}$  can be translated into an corresponding effective index  $n_{eff,m}$  for the specific waveguide mode. This effective index is always lower than the index of the core layer  $n_{wg}$  because part of the mode penetrates into the surrounding layer with a lower index. Furthermore, the effective index of the mode has to be higher than the refractive indices of the substrate and of the cladding, to ensure that the mode is guided and shows no radiative losses into the cladding or the substrate. All modes with a lower effective index are radiative modes, which are not guided by the waveguide structure. Therefore, for guided modes the following equation holds

$$\max(n_s, n_c) < n_{eff,m} < n_{wg} \quad (2.43)$$

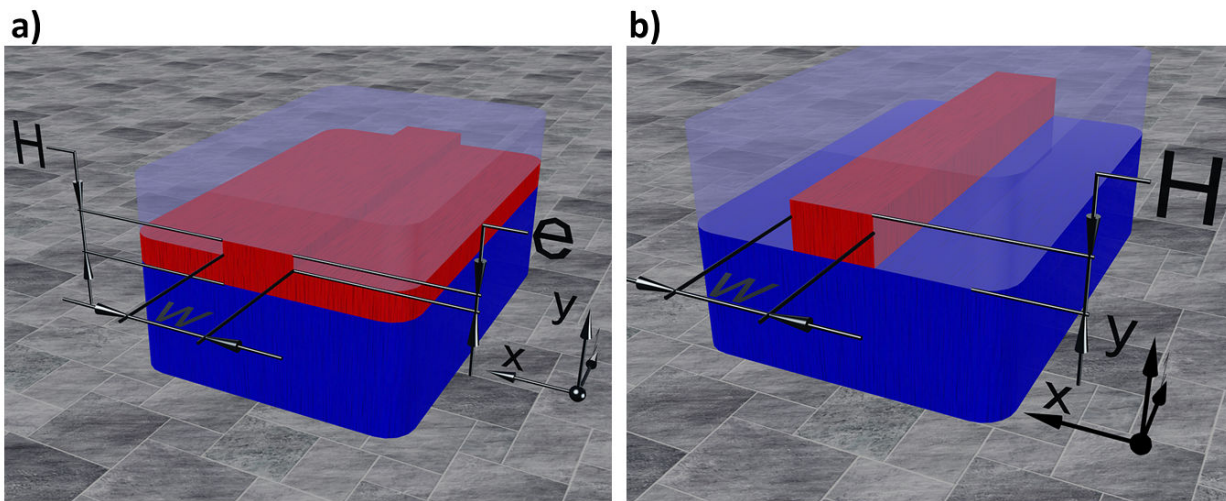


**Figure 2.3:** a) Sketch of a rib-type waveguide. The rib of the waveguide has a width  $w$ , a total height  $H$  and an etch depth  $e$ . b) Sketch of a wire-type waveguide of width  $w$  and height  $H$ .

Each three layer slab system with a high index core layer supports a number of guided modes. For a nonsymmetrical system, where  $n_s \neq n_c$ , the number of guided modes can become zero. The thinner the core layer becomes, the larger is the fraction of the field that penetrates into the surrounding layers, but the fewer guided modes are supported. In a symmetric system at least one guided TE and one guided TM mode are supported by the structure. Waveguides that do not support guided higher order modes are called single mode waveguides. In each waveguide, there is an infinite number of modes available, but only a finite number of these modes are guided. All other modes are radiating modes. All modes, guided and radiating, are orthogonal to each other. They form a basis system for the electromagnetic field. The eigenvalue equation (2.39) for  $k_y$  cannot be solved analytically due to the fact that this equation is transcendental. Approximations are needed or the eigenmode equation has to be solved numerically for each mode.

### 2.2.2 Rib- and wire-type waveguides

The three layer slab waveguide in the previous section was used as an example to show the mechanism of wave guiding. For most applications, a 1D light confinement in vertical direction is not sufficient. In addition to vertical confinement, lateral confinement is necessary to enable the realization of complex integrated optical waveguide devices, where waveguides and even arrays of waveguides can be built on a single chip. Such waveguides allow for waveguide bends, Y-branches, couplers, interferometers and a lot of more complex devices with a simple planar fabrication process. Several types of waveguides facilitate two dimensional (2D) light confinement. Figure 2.3 shows two examples of such waveguides. A wire-type waveguide has a high index core with a certain width  $w$  and height  $H$ , which is surrounded by materials with lower refractive indices. The principle of wave guiding used in this case is analogous to the three layer slab system, but is valid in the vertical and the lateral direction. Based on the effective index method (EIM)[33, 35], the lateral confinement of the rib-type waveguides can be explained as follows. If the inner region II and the outer regions I and III of the rib waveguide (see Fig. 2.4) are treated as separated and independent horizontal slab waveguide systems, an optical mode propagating in the inner region II has a higher effective index than in the two outer regions. By replacing the



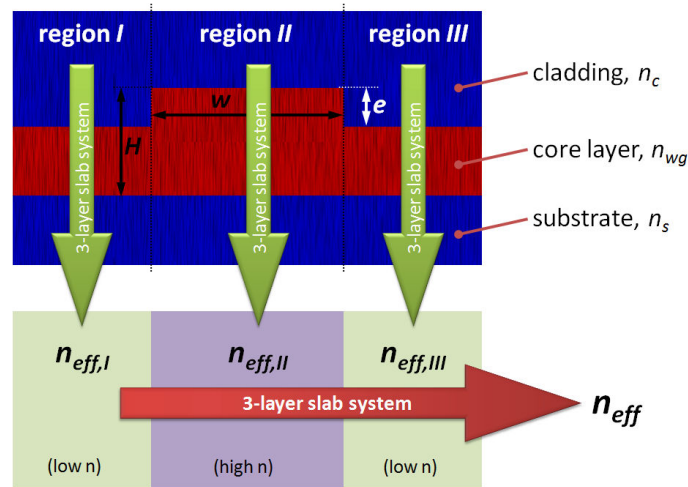


**Figure 2.4:** Sketch of the working principle of the effective index method for a rib-type waveguide. The waveguide is divided into three different regions I - III, treated as independent horizontal three layer slab systems. For each region, a horizontal effective index  $n_{eff,I-III}$  can be calculated. After this step, the three regions are considered to form a vertical three layer slab system, which can be solved in the same manner. The final value  $n_{eff}$  is an approximation to the effective index of a guided mode in the rib-type waveguide.

three regions of the rib waveguide with homogeneous media with refractive indices equivalent to the corresponding horizontal slab waveguides, a vertical slab waveguide is formed (see Fig. 2.4), which leads to lateral confinement.

The calculation of the fields in these wire- and rib-type waveguides is not as easy as in the case of a slab waveguide due to the fact that the decoupling of Maxwell's equations into two independent equation systems is not possible. In these geometries, there are no pure TE- or TM-modes. All modes are still orthogonal to each other and form a basis system for the electromagnetic fields, but every mode contains all six field components. Nevertheless, in many cases, *e.g.* for thin but wide rib or wire waveguides, the modes in these waveguides carry most of their optical power in the TE or the TM field components. In such cases, these modes are called TE-like or TM-like, with TE or TM major field components and TM or TE minor field components, respectively. In many publications, the reference to these types of modes is simplified from TE-like modes or TM-like modes to only TE modes or TM modes, but the reader has to be aware of the fact that this is only a simplification and these modes are not pure TE or TM.

The calculation of the fields and the effective index of the modes in rib- or wire-type waveguides is complex. One approach to this problem is the use of approximation methods such as Marcantili's method[36] or the effective index method [33, 35] (see Fig. 2.4). Both methods work well for a certain range of parameters but do not provide good approximations for all waveguide cross sections. A precise method for all waveguide cross sections is the calculation of the fields using numerical methods, *e.g.* finite element methods (FEMs). FEMs[38] can implement different methods for finding optical waveguide modes. The common point for all FEMs is a discretization of the waveguide cross section into a number of very small elements. Then, a set of mathematical basis functions is applied at the boundaries or the vertices of all these elements. The condition that the mathematical functions have to be continuous at the boundaries of adjacent elements creates a huge set of equations, which can be solved by a software package. Figure 2.5 shows examples of fundamental TE modes for a rib- and a wire-type waveguide calculated by using a FEM.

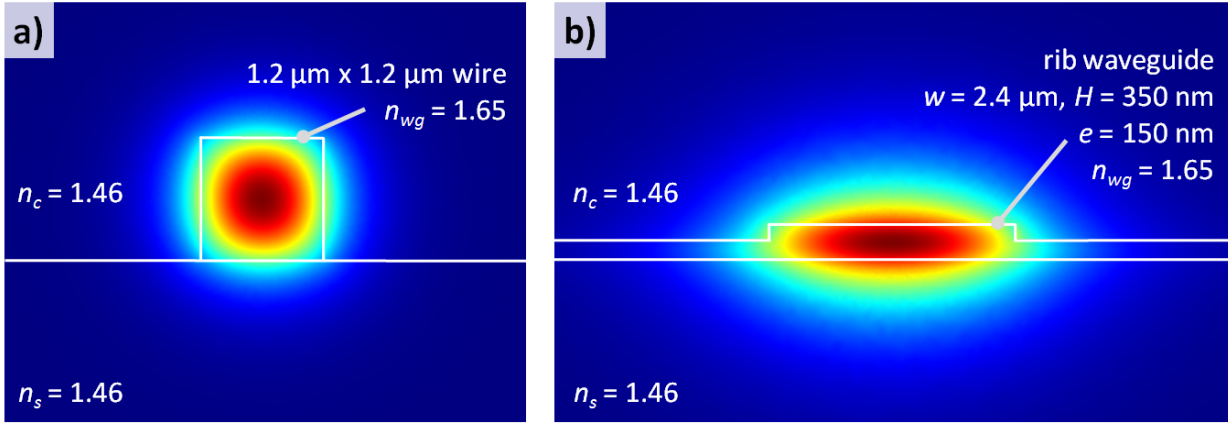


**Figure 2.5:** Finite element method (FEM) simulations of the  $E$ -field distribution performed with a commercial FEM simulation package[37] of a **a)** wire-type waveguide and **b)** rib-type waveguide. The substrate and the cladding have a refractive index of  $n_s = n_c = 1.46$  and the core layer has a refractive index of  $n_{wg} = 1.65$ .

Even if the calculation of the mode fields in a rib-type waveguide is complex, there exist simple criteria to determine whether the waveguide shows single mode behavior. There are several approaches to formulate single mode criteria for rib waveguides and some of them are summarized here to give a short overview. All single mode criteria describe basically the limit when the first higher mode is becoming radiant. If the first higher mode becomes radiant, only the fundamental mode remains guided. Based on the mode-matching method presented by Petermann[39], Soref et al. presented an analytical approximation of a single mode criterion for rib waveguides[40]:

$$s < 0.3 + \frac{r}{\sqrt{1-r^2}} \quad (2.44)$$

In this equation,  $r$  and  $s$  are defined by  $r = \frac{H-e}{H}$  and  $s = \frac{w}{H}$ . For a given thickness of the core layer and a given etch depth, the maximum width of the rib waveguide for single mode operation can be obtained using this criterion. A second analytical approximation is based on the EIM. The so called Pogossian criterion[41, 42]

$$s < \frac{r}{\sqrt{1-r^2}} \quad (2.45)$$

looks very similar to the Soref criterion, but it is based on a different approximation. Both criteria show good agreement for large waveguide cross sections, while the single mode criterion used in this work achieves better accuracy for waveguides with small cross sections. The criterion used here is a modification of Soref's criterion that uses exact values for the effective indices of the three layer slab modes. Furthermore, a fit parameter based on comprehensive numerical work is introduced that also takes into account the differences between TE-like and TM-like modes. This semi-analytical single mode criterion for rib-type waveguides with small cross section was published in 2006[43]:

$$s < \alpha_{SMC} + \frac{\pi}{k_0 H \sqrt{n_{eff,II}^2 - n_{eff,I}^2}} \quad (2.46)$$

The factors  $n_{eff,I}$  and  $n_{eff,II}$  are the effective indices for the three layer slab system in the outer and the inner region respectively and are obtained by solving equation (2.39) for the fundamental mode. The fit parameter  $\alpha_{SMC}$  is polarization dependent. For TE-like modes it can be taken as a constant  $\alpha_{SMC,TE} = 0.31 \pm 0.02$ . For TM polarization  $\alpha_{SMC,TM}$  is a function of the core layer thickness,  $\alpha_{SMC,TM} = 0.28(1 - e^{H/360}) \pm 0.03$ .

## 2.3 Coupling methods for thin film waveguides

Coupling into thin film waveguides is still a very challenging task. Since the beginning of integrated optics, this topic has attracted a lot of interest. In the "outer" or macroscopic world, light propagation happens via freely propagating beams directly from a laser source for short distances or via low loss optical fibers for distances up to hundreds of kilometers. In integrated optics, efficient optical elements and low loss waveguides exist, but the key factor for a highly efficient device is a good coupling element between the micro and the macro world. There is still no ultimate solution to this challenge.

One approach in integrated optics is the integration of laser sources and the photodetectors on the device, so that all optical elements are integrated on a single chip and electrical contacts are the only connections to the world outside the chip. However, for many devices this approach is neither feasible nor practical. Especially in the case of disposable devices, fabrication costs are critical, which prohibits an integration of active optical elements.

Coupling into thin film waveguides is usually done from freely propagating beams or directly from optical fibers. Freely propagating beams can be delivered directly from laser sources or from optical fibers that are attached to a collimating or focusing optic. In most cases, it can be assumed that freely propagating beams have a Gaussian shape. Typical beam diameters are in the range of 0.5 mm to 2 mm if the beam is delivered directly from a laser source. If a collimating optic is used, beam diameters are usually 0.5 mm or larger, whereas with focusing optics, beam diameters down to the micrometer scale are possible in the focal plane.

The other case is coupling from an optical fiber where the core diameter of optical fibers determines the diameter of the out-coming beam, which can vary from a few microns up to several hundreds of microns. Single mode fibers are used for high performance telecommunication links or for the transportation of light to sensor devices, where coherent light is needed. The core diameter of these fibers is dependent on the used wavelength and is approximately 4  $\mu\text{m}$  for a wavelength of 633 nm and nearly 9  $\mu\text{m}$  for a wavelength of 1.55  $\mu\text{m}$ . The beam shape of single mode fibers can also be assumed to be Gaussian.

In comparison to these dimensions, the dimensions of integrated optical waveguides are very small. The core layer thickness of thin film waveguides can go down to a few tens of nanometers for high index difference waveguide systems, while the width of the waveguides is typically less than a micron for such systems. For efficient coupling, this mismatch in the mode shapes has to be overcome. The following sections give a short overview of popular coupling methods for thin film waveguides and emphasize their suitability for high index difference polymer single mode waveguides.

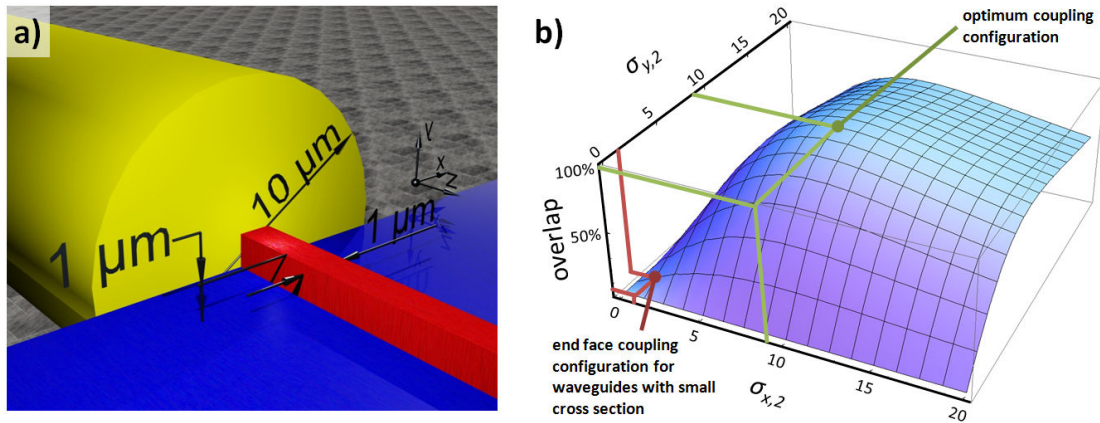


**Figure 2.6:** **a)** Typical dimensions for waveguides with small cross sections when using end face coupling. In the near infrared, single mode fibers have core diameters in the range of 10  $\mu\text{m}$  and dimensions of waveguides with small cross sections are often smaller than 1  $\mu\text{m}$  x 1  $\mu\text{m}$ . **b)** Calculated geometrical overlap of a Gaussian fiber mode with  $\sigma_{x,1} = 9 \mu\text{m}$  and  $\sigma_{y,1} = 9 \mu\text{m}$  and a Gaussian beam with variable  $\sigma_{x,2}$  and  $\sigma_{y,2}$  (see equations (2.47) and (2.48)). For waveguides with small cross sections, end face coupling efficiencies are only a few percent.

### 2.3.1 End face coupling

End face coupling is one of the easiest possibilities to couple light into a thin film waveguide. A cleaved fiber is brought in proximity or even in contact with the end facet of the waveguide (see Fig. 2.6a)). This coupling method is often used for low index difference waveguide systems, where the dimension of waveguides are similar to the diameter of optical fibers, *e.g.* for low index contrast polymer waveguides or optical waveguides made from glass. The theoretical coupling efficiency  $\eta$  of end face coupling, which is defined as the ratio between the incoming optical power and the power that is coupled into the waveguide is determined from an overlap integral. Assuming that a propagating mode is converted into another propagating mode with a different mode profile, the conversion efficiency between these two modes is given by[35]

$$\eta = \frac{4\beta_1\beta_2}{(\beta_1 + \beta_2)^2} \frac{\left[ \int E_1(x, y) \cdot E_2^*(x, y) dx dy \right]^2}{\int E_1(x, y) \cdot E_1^*(x, y) dx dy \cdot \int E_2(x, y) \cdot E_2^*(x, y) dx dy} \quad (2.47)$$

where  $E_1(x, y)$  and  $E_2(x, y)$  are the amplitude profiles and  $\beta_1$  and  $\beta_2$  are the propagation constants of these two modes. The first term in this equation takes the impedance mismatch between these two modes into account. It handles the difference in the propagation constants and integrates phenomena such as reflection due to different refractive indices, while the second term is the geometric overlap of these two modes. Equation (2.47) is valid for all cases of mode conversion where the propagation direction is not changed, which is usually the case if the mode conversion takes place at an interface orthogonal to the propagation direction. As an example, for two Gaussian modes with

$$E_{1/2}(x, y) = \frac{1}{\pi\sigma_{x,1/2}\sigma_{y,1/2}} e^{-\frac{x-x_{0,1/2}}{\sigma_{x,1/2}}^2} e^{-\frac{y-y_{0,1/2}}{\sigma_{y,1/2}}^2} \quad (2.48)$$

a maximum conversion is obviously achieved if both beams are identical. As shown in Fig. 2.6b), the efficiency of the mode conversion drops rapidly if the mode diameters are not matched, even neglecting the mismatch in the propagation constants. End face coupling only provides good coupling efficiency for waveguides having the similar dimensions as optical fibers. This is usually valid in waveguide systems with very low index contrasts only. For waveguides with small cross sections such as waveguides made of high index material systems or waveguides optimized for surface sensing, the efficiency of end face coupling is usually low. For near infrared wavelengths, the core diameter of optical fibers is around 9  $\mu\text{m}$ . Polymer rib waveguides optimized for surface sensing, as used in this work, have a core layer thickness of less than 400 nm and a waveguide width of 2.4  $\mu\text{m}$  for this wavelength. A simple calculation to give an estimation of the coupling efficiency, assuming that the mode profile within the waveguide is Gaussian as well as the mode profile of the optical fiber, leads to a theoretical coupling efficiency of 4.4% or -13.5dB for  $\sigma_{x,1} = 9 \mu\text{m}$ ,  $\sigma_{x,2} = 2.4 \mu\text{m}$ ,  $\sigma_{y,1} = 9 \mu\text{m}$ ,  $\sigma_{y,2} = 0.4 \mu\text{m}$ ,  $x_{0,1} = x_{0,2} = 0$ , and  $y_{0,1} = y_{0,2} = 0$ . Moreover, end face coupling needs direct access to the end facet of the waveguide, which cannot be guaranteed on an injection molded substrate with spin coated layers on top. Additionally, for achieving high coupling efficiency, the quality of the waveguide end facet is critical. On inorganic substrates a high quality end facet can be realized by polishing and/or wafer cleaving. This kind of treatment is not possible on polymer substrates.

Equation (2.47) is only valid for the calculation of the coupling efficiency for end face coupling if there is no gap between the optical fiber and the waveguide, which is usually not the case. If there is a gap, equation (2.47) has to be applied twice. Firstly, equation (2.47) has to be applied to the interface at the end of the fiber. The change of the mode profile as a result of the propagation of the mode through the gap can be neglected in many cases. Secondly, equation (2.47) has to be applied to the interface between air and the waveguide. The air gap between the optical fiber and the waveguide forms a cavity, where multiple reflections lead to interferences, which affect the overall coupling efficiency and introduce a wavelength dependent behavior. This effect is neglected in the treatment above, but has to be taken into account for a rigorous analysis of end face coupling. Often tilted end facets are used to avoid multiple reflections between the fiber and the facet of the sample. The tilt angle is typically 8°.

### 2.3.2 Taper structures

In order to optimize the mode overlap at the coupling plane tapers, which are also called spot size converters, can be used. Tapers are used to slowly change the cross section of a waveguide in the direction of propagation. Tapers can be implemented in many different shapes. Simple lateral tapers change only the width of waveguides, while three dimensional (3D) tapers also change the waveguide height (see Fig. 2.7). For a waveguide with a constant cross section, all waveguide modes are orthogonal and independent. Therefore, coupling between these modes is not possible and the energy in each mode is preserved.

In a taper structure, coupling between waveguide modes is introduced. If only the fundamental mode is excited at the beginning of a taper, energy from this mode couples, at different rates, into all other waveguide modes. As these higher modes gain energy during propagation through the taper, the energy in these modes couples again into all other modes. If it is additionally taken into account that energy is as well coupled to radiating modes, which leak energy out from the taper structure and that the number of guided modes can change during propagation through the taper, an analytical description of the energy distribution of waveguide modes in a taper is complex.

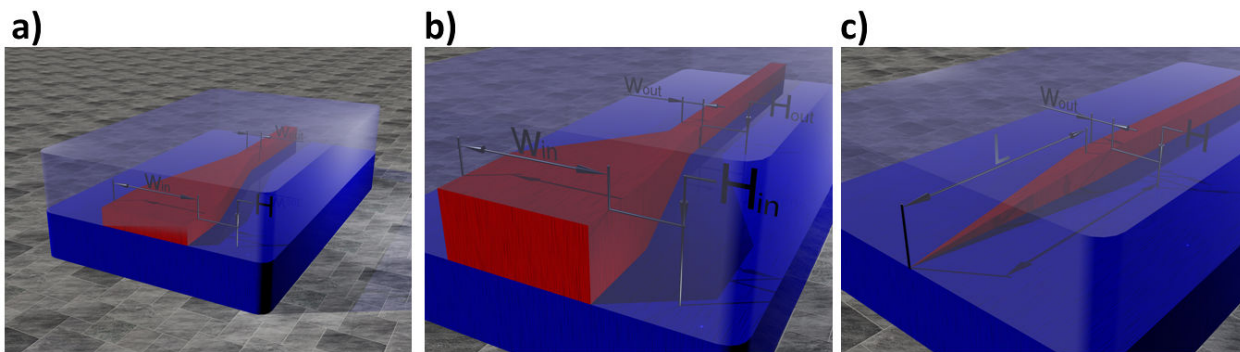


**Figure 2.7:** Sketch of a **a)** lateral taper, **b)** three-dimensional (3D) taper and **c)** a inverse taper.

This problem is especially critical for tapers into single mode waveguides, where all energy in higher order modes radiates away at the end of the taper. One way to overcome this problem is the use of adiabatic tapers, *e.g.* [44, 45]. This kind of tapers varies the cross section of the waveguide very slowly, so that coupling between modes can be neglected. Adiabatic tapers are capable of nearly lossless conversion of mode profiles, but have the geometric disadvantage of being very long. To reduce the necessary length of tapers the shape of the tapers can be adjusted in such a way that the overall mode coupling is minimized. As presented in reference [46], the strength of the mode coupling depends, among other factors, on the difference of the propagation constants of the different modes. The higher the difference between the propagations constants, the lower the coupling of these modes is. In consequence, the waveguide cross sections of adiabatic tapers can be varied faster where mode coupling is weak due to high difference in the propagation constants and vary slower where strong mode coupling occurs.

### Lateral tapers

Lateral tapers are easy to produce and compatible with planar waveguide technology. They can be used to adjust the width of the waveguide to the diameter of the single mode fiber to increase the coupling efficiency of end face coupling. By setting  $\sigma_{x,1} = \sigma_{x,2} = 9 \mu\text{m}$  in the example from section 2.3.1, the coupling efficiency increases to 8.87% or -10.5dB, which is a relative increase of 3dB. Nevertheless, the main problem, the mode mismatch in the vertical direction, still remains unresolved. Therefore, lateral tapers are not the best solution to increase the coupling efficiency for end face coupling, but they play an important role in the coupling via grating couplers (see section 2.3.4 and 4.2.4), where they are used to reduce the waveguide width behind the gratings to the desired width.

### 3D tapers

3D tapers have the capability to adjust the lateral as well as the vertical mode size to the diameter of the fiber. The only remaining mismatches are the non-Gaussian shape of the mode in the waveguide and the difference of the propagation constants between the mode in the fiber and the waveguide. 3D tapers offer good coupling efficiency at the cost of very complicated fabrication. In general, they are not compatible with planar waveguide processing. Many 3D tapers are separated into vertical tapers, which reduce the waveguide height and a lateral taper. In many cases, the fabrication of 3D tapers necessitates complicated fabrication procedures, involving multiple etching steps or polishing

and bonding steps, e.g. [47, 48]. Due to the complicated fabrication process and the fact that end face coupling cannot be used for an injection molded substrate, 3D tapers are not a practical solution for the coupling into injection molded disposable sensor chips.

### Inverse taper

An interesting and comparatively new coupling concept is the use of inverse tapers [49, 50, 51]. This kind of tapers has a very narrow tip made from the core material at the end facet, which slowly becomes larger until the final waveguide cross section is reached (see Fig. 2.7c)). For large waveguide cross sections, the waveguide mode is strongly confined within the core layer. The mode profile is approximately as large as the core layer. By reducing the cross section of the core layer, the mode profile becomes smaller, but in exchange, the confinement of the mode in the core material is reduced. For very small core layers, the confinement is reduced strongly and the mode profile becomes larger again. This effect is exploited at the tip of an inverse taper.

Compared to 3D tapers, the effective index of a mode at the end facet is lower for inverse tapers due to the fact that there is hardly any high index material present at the beginning of the inverse taper. Thus, this coupling method is of particular interest for high index material systems, where strong reflections at the end facet due to the high effective index of the guided modes can be reduced by use of an inverse taper. This kind of taper is mostly used in silicon photonics, where 3D taper structures can be produced by grey-scale e-beam lithography followed by an etch step. Etching of silicon is an extremely well-known and stable process. The main disadvantages for this kind of taper are the expensive fabrication and the difficult positioning of the tip of the taper directly at the sample end facet. The quality and the size of the tip is critical for the performance of these tapers. For all these reasons, the realization of an inverse taper seems to be practical for inorganic materials only.

### 2.3.3 Prism coupling

For this coupling method, a prism with a refractive index higher than the guided mode is put on top of a waveguide, as shown in Fig. 2.8. If an incident light beam hits the prism under the appropriate angle, light can be coupled into the waveguide. Without the underlying waveguide, the light would be reflected at the bottom of the prism. However, reflected light comes with an evanescent tail that slightly penetrates into the low index material below. Therefore, mode coupling can occur between the evanescent tail of the reflected light in the prism and the guided mode [52]. The strength of the mode coupling is determined by an overlap integral between these two evanescent tails [53]. This coupling method can be used for in-coupling and out-coupling. The basic equations are the same for both cases.

For efficient coupling, the incident or outgoing beams have to satisfy a phase matching condition with the propagating waveguide mode. The phase matching condition is  $k_{z,inc} = k_0 n_{eff}$ , where  $k_{z,inc}$  is the  $z$ -component of the wave vector of the incident or outgoing beam in the prism and  $k_0 n_{eff}$  is the wave vector of the guided mode. Written in the following form, this defines the angle of optimized coupling[54].

$$n_P k_0 \sin \Theta_P = k_0 n_{eff} \quad (2.49)$$



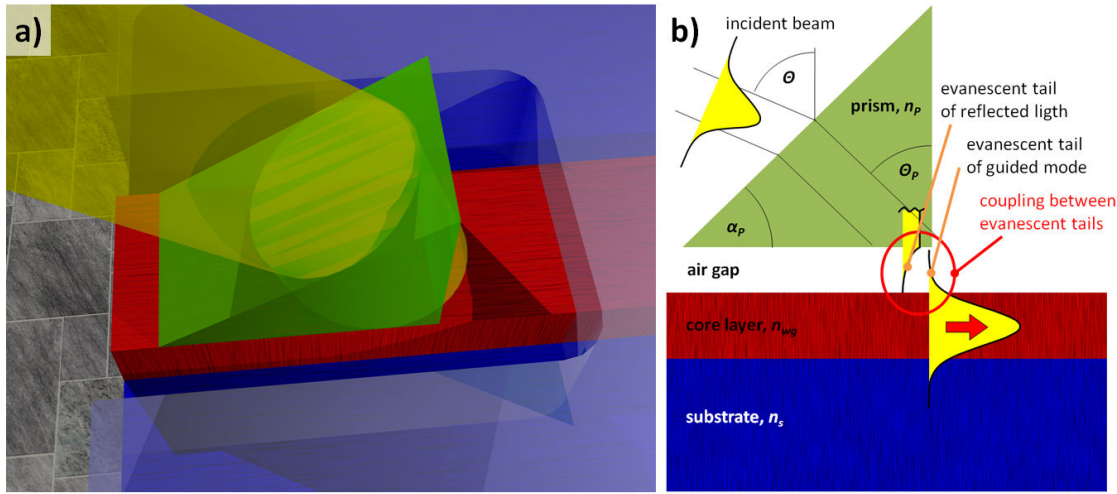


**Figure 2.8:** a) Sketch of a prism coupler for thin film waveguides and b) depiction of the mode coupler scheme. If the phase matching condition between the incident beam and the guided mode is satisfied, coupling occurs due to the overlap of the mode profiles.

The prism has a refractive index of  $n_p$ , while the incoming or outgoing beam is propagating under the angle  $\Theta_p$  in the prism. The angle  $\Theta$  of the propagating beam outside of the prism can be calculated using Snell's law as

$$\sin(\Theta_p - \alpha_p) = n_p \sin(\Theta - \alpha_p) \quad (2.50)$$

by assuming that the medium outside of the prism is air. The necessary wave vector  $k_0 n_{eff}$  is always larger than  $k_0$ , so it cannot be reached by a beam propagating in air. Therefore, a prism with  $n_p > n_{eff}$  and with a non-horizontal interface is required. Prisms are often used as wave vector converters if components of wave vectors larger than  $k_0$  are needed. For optimized coupling, not only the coupling angle  $\Theta_p$ , but also the size and the shape of the beam as well as the exact position of the beam have to be adjusted to the coupling strength of the mode coupling. The coupling strength, calculated by an overlap integral as mentioned above, can be strongly influenced by the gap between the prism and the waveguide, which leads to certain disadvantages for this coupling method. First of all, the prism needs direct access to the waveguide core layer. Therefore, no cladding layer is possible in the coupling region, which would in other cases also act as a protection to the core layer. The second point is the strong dependence of the coupling strength on the gap between the prism and the waveguide. A single dust particle can change the size of the gap, and therefore, the coupling strength. While it might be possible to adjust the position and the angle of the beam during a measurement to counterbalance a change in the coupling strength, it is nearly impossible to change the beam shape and size, which would be additionally necessary for optimized coupling.

In the case of prism coupling for optical sensor chips, the prism can be directly mounted during the processing of the sensor chips in a cleanroom or the prism is part of the readout system and is pressed on the sensor chip during measurements. The first possibility should give more reproducible results but complicates the fabrication process and increases costs because of the fact that two high quality prisms are needed for each sensor. The latter possibility needs no change in the fabrication process except the opening of the cladding in the coupling region. However, reproducibility of the coupling conditions cannot be guaranteed between different chips because of the reasons mentioned above.



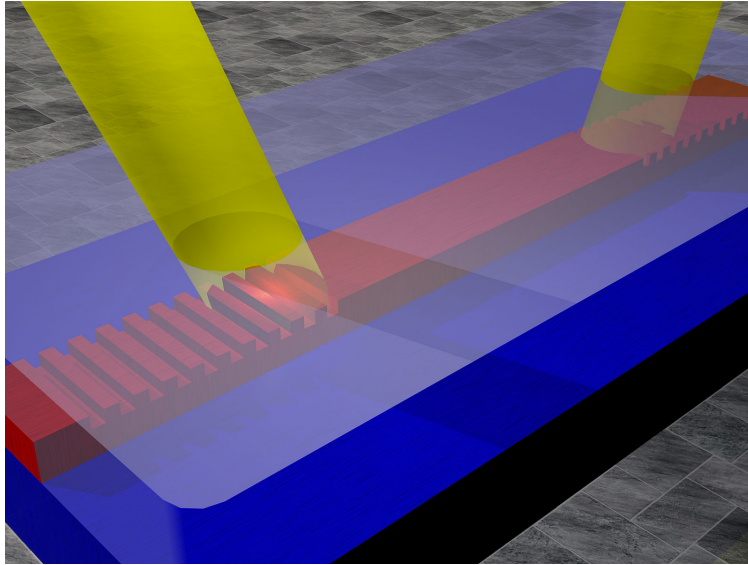


**Figure 2.9:** Grating couplers as in- and out-coupler for a thin film waveguide.

### 2.3.4 Grating couplers

Grating couplers are planar coupling elements. Their periodic structure leads to a change in the propagation direction of a certain amount of reflected or transmitted light by adding multiples of so called grating vectors to the wave vector of the propagating light. In general, periodic structures are possible in up to three (not necessarily rectangular) dimensions. In optical applications, 2D or 3D periodic structures are called photonic crystals. Photonic crystals can have a lot of interesting properties and attracted a lot of attention for different applications from ultra compact waveguides (e.g. [55, 56]) to sensing (e.g. [57, 58]) but are, with a few exceptions (e.g. [59, 60]), not used for coupling into thin film waveguides. 1D periodic structures are referred as diffraction gratings, or in a simple way just as gratings. Gratings are wavelength selective devices and are used in a variety of applications in many fields of optics, ranging from telecommunication up to sensing (e.g fiber bragg gratings[61, 62, 63]). The focus of this section are grating couplers, *i.e.* gratings that are used to couple light into a thin film waveguide or out of a thin film waveguide (see Fig. 2.9).

Grating couplers are resonant diffraction devices. Based on the Huygens' principle, every period acts as a point source. Due to the periodic structure of gratings, the sum of the waves from all the point sources interfere constructively for specific directions only. These directions are spaced by grating vectors  $\Delta k = |\Delta \vec{k}|$ . The grating vector lies in the direction of the periodicity and has the length[64]

$$\Delta k = |\Delta \vec{k}| = \frac{2\pi}{\Lambda} \quad (2.51)$$

where  $\Lambda$  is the period of the grating. If a propagating wave with a wave vector  $\vec{k}$  is incident on a grating, part of the light is reflected and part of the light is transmitted. In addition, the transmitted as well as the reflected beam is diffracted into several diffraction orders, each with a different wave vector, as shown in Fig. 2.10a). Each diffraction order propagates in a different direction away from the grating. The number of diffraction orders depends on the grating period and the refractive index of the surrounding media. The length of the wave vector of the diffraction order is determined by the medium in which the

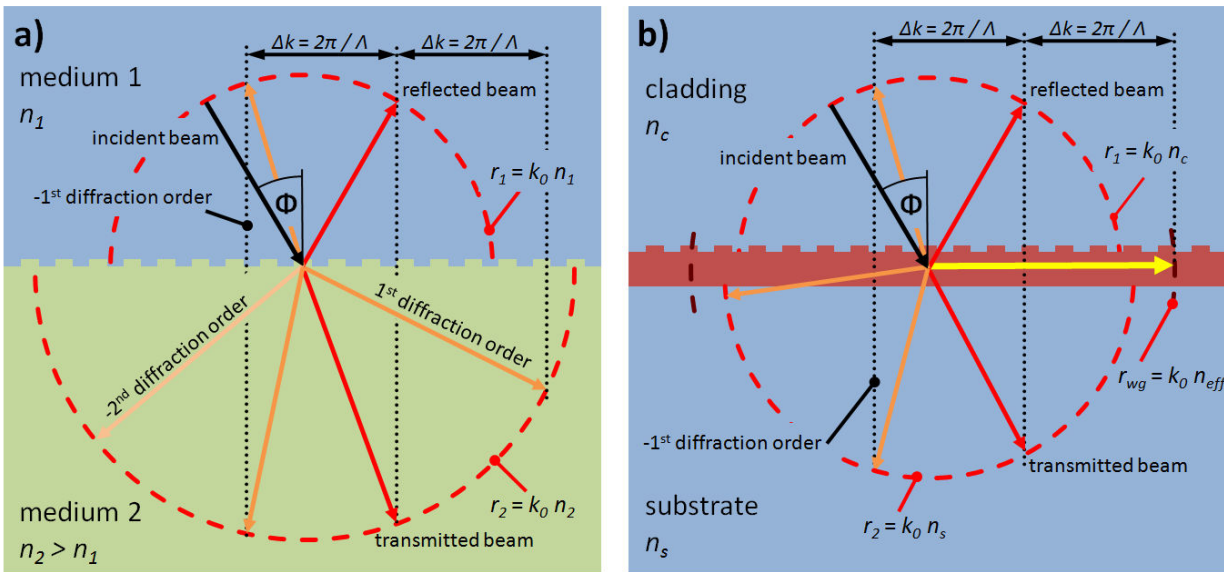


**Figure 2.10:** **a)** Wave vector diagram of a grating at an interface of dielectric materials. The lengths of the wave vectors are defined by the refractive indices of the materials and the used wavelength. Due to the presence of a grating, several diffraction orders are introduced in addition to the reflected and transmitted beam. Compared to the reflected and the transmitted beam, the  $z$ -components of the diffraction orders are changed by multiples of the grating vector  $\Delta k$ . **b)** If a grating is present at a waveguide, additional possible wave vectors are introduced. For each mode that is supported by the waveguide structure, two wave vectors, one in the positive and one in the negative  $z$ -direction, are added. The length of these wave vectors is defined by the effective indices of the guided modes in the waveguide. If the coupling condition (2.52) is satisfied, coupling from the incident beam to the guided mode is possible.

wave propagates. In isotropic media the norm of the wave vector is independent from the propagation direction, thus all possible wave vectors lie on a circle with the radius  $r_j = k_0 n_j$  for the medium with the number  $j$ , as sketched in Fig. 2.10. Assuming that the grating is periodic in the  $z$ -direction, the grating is able to change the  $z$ -components of the wave vector of the reflected and the transmitted wave by adding multiples of the grating vector. If a waveguide is present in the grating area, as sketched in Fig. 2.10b), additional possible wave vectors arise for the modes in the waveguides. These wave vectors point in the  $z$ -direction and scale with the effective index of the waveguide modes. To enable efficient coupling from an incident beam to a waveguide mode or from a waveguide mode to an outgoing beam, the difference between the  $z$ -component of the wave vector of the beam and the wave vector of the mode has to be a multiple of the grating vector, which leads to the well known coupling condition for grating couplers (e.g. [65, 66])

$$|k_{inc}^{\vec{z}}| \sin \Phi + m \Delta k = k_0 n_{eff} \quad (2.52)$$

with the integer  $m$  as the order of diffraction. This equation defines the basic correlation between the coupling angle, the period of the grating and the effective index of the waveguide mode. As denoted in equation (2.51), the grating vector depends only on the period of the grating and not on the shape of the grating or on the refractive indices. The shape and the refractive indices have no influence on the basic coupling condition, but one has to keep in mind that the coupling condition is a simple correlation between wave vectors and makes no statements about the efficiency of the coupling between

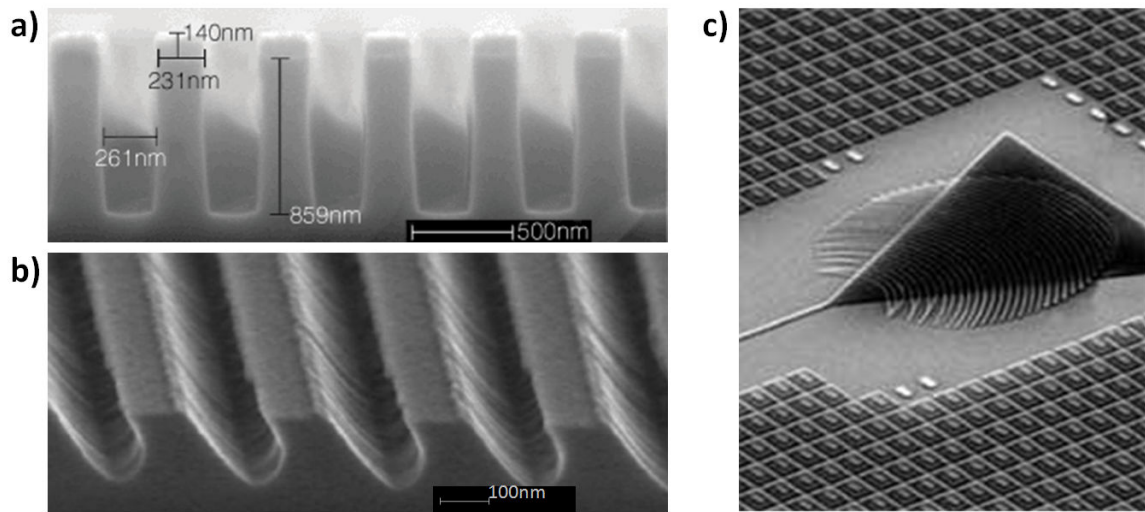


**Figure 2.11:** Examples of grating couplers: **a)** Binary grating coupler fabricated in doped  $\text{SiO}_2$  by deep UV photolithography[67]. **b)** Slanted grating coupler fabricated in InGaAs/AlGaAs with chemically assisted ion beam etching[68]. **c)** Focusing grating coupler[69] fabricated in silicon by Luxtera[70].

the radiating beams and the diffraction orders. The coupling condition is a necessary, but not a sufficient condition for efficient coupling. This is where the shape and the materials of the grating and the waveguide come into play. The issue of efficient coupling and the prerequisites to achieve it, as well as the implications will be examined in more detail in section 4.2.4.

Many implementations of grating couplers are used for different fields of applications. General advantages of grating couplers are their compatibility to a planar fabrication processes as well as free positioning of the gratings over the complete area of the sample. There is no need for cleaving the edges of the devices. Moreover, grating couplers can offer relaxed alignment tolerances compared to end face coupling due to larger beam diameters used. The most common example for grating couplers are binary line gratings, *e.g.* in polymers[13], silicon nitride[71] or silicon[72]. These grating have rectangular cross sections of alternating materials with different refractive indices (see Fig. 2.11a)). The main advantage of this kind of gratings is their compatibility with standard fabrication processes. In most cases, these gratings can be patterned in the same fabrication step as the waveguides, and therefore, add no additional complexity to the fabrication process. Even if perfect vertical sidewalls cannot be achieved easily, binary line gratings are often used as a model to describe experimentally realized grating structures. A disadvantage of binary line gratings is the limited coupling efficiency, especially for in-coupling purposes. If used for out-coupling, due to symmetry, binary line gratings couple light from a waveguide to both the substrate and the cladding at more or less at the same rates. As will be shown in section 4.2.4, this behavior limits the maximum coupling efficiency for in-coupling to approximately 40%.

One possibility to overcome this limitation are slanted or blazed grating couplers, *e.g.* [68, 73] (see Fig. 2.11b)). They break the symmetry of the binary gratings and favor diffraction into the cladding or into the substrate, which is desirable for in-coupling too. However, the fabrication of slanted grating couplers poses a challenge to standard process technology and are not compatible with injection molding. Another interesting example of grating couplers are focusing gratings (see Fig. 2.11c)), *e.g.* [74, 75, 76, 77]. For instance, these gratings are able to transform an incoming plane wave into a focus-

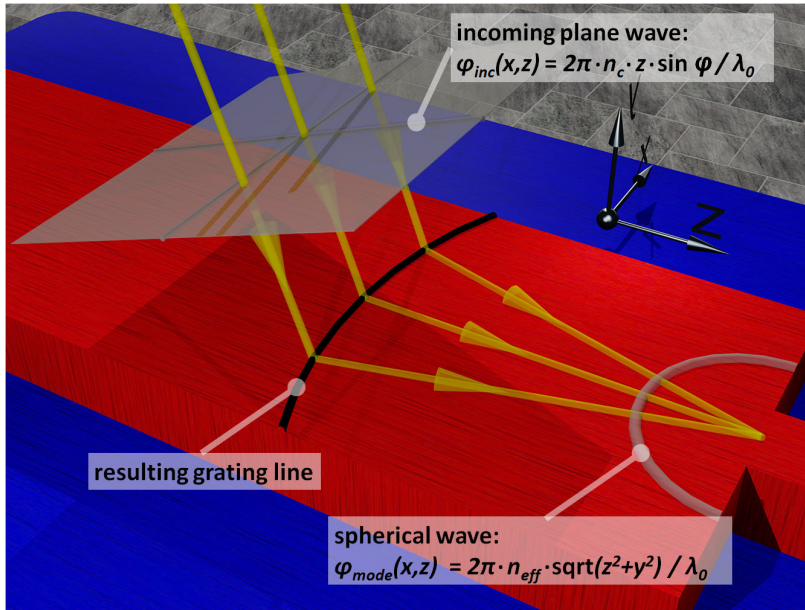


**Figure 2.12:** Example of a focusing grating that translates an incoming plane wave with an angle of incidence  $\varphi$  into a spherical wave that has its focal point at the beginning of the waveguide. The three depicted light rays have the same optical length and they indicate how the grating line can be obtained using equation (2.53).

ing wave in the thin film waveguide. At the focal point of the grating, the focused wave can be coupled into a narrow waveguide. The grating lines are determined by a correlation between the phase of the incoming beam at the grating interface  $\phi_{inc}(x, z)$  and the phase of the propagating mode  $\phi_{mode}(x, z)$  in the following way (see also Fig. 2.12)[78]:

$$\phi_{inc}(x, z) + \phi_{mode}(x, z) = 2\pi m \quad (2.53)$$

This equation states that for each point of the  $m$ -th grating line the wave travels the same optical length to the focal point, so that all parts of the wave can interfere constructively at the focal point. If  $\phi_{inc}$  and  $\phi_{mode}$  are known as a function of the coordinates  $x$  and  $z$  at the grating interface, reversion of equation (2.53) gives a formula for coordinates of a grating line for each integer  $m$ .

The design of focusing gratings requires very good knowledge of the material parameters and the geometrical parameters of the fabricated gratings since all these parameters influence the effective index of the waveguide mode in the grating region, and therefore,  $\phi_{mode}(x, z)$ . Especially for polymers, the exact optical parameters are often unknown, which complicates the use of focusing grating couplers for polymer waveguides. Equation (2.53) is valid for line gratings as well, which are just a special case of focusing gratings, where a plane wave is transformed into another plane wave. In the case of line gratings, changes in the effective index of the waveguide mode can be compensated with a change in the angle of incidence, which is in general not possible for focusing gratings.

Because of the compatibility with the fabrication process, binary line grating couplers were chosen as coupling elements for the polymer biosensor chip. They allow for an easy readout system owing to relaxed alignment tolerances and reproducible coupling efficiency of grating couplers as well as the fact that a large distance between the grating and the optics that tailors the incident beam is possible, which makes a possible readout system more robust.

## 3 Evanescent wave sensor principles for biosensing

The common characteristic of the following examples of evanescent wave sensors is that the propagation of light is altered by a change of the refractive index in one of the neighboring layers. As explained in section 2.2, the effective index of a guided mode is dependent on the refractive indices of these low index layers due to the fact that an evanescent tail of the waveguide mode penetrates into the surrounding layers. Therefore, the propagation of the guided mode can be affected by refractive index changes in one or more of these layers. This fact is exploited by sensors described in this chapter.

There are two main applications for evanescent wave sensors. Firstly, if a complete neighboring layer changes its refractive index, which can be the case if an analyte that is rinsed over a waveguide is exchanged. This case is referred as homogeneous sensing. The second case is surface sensing, where only a very thin layer at the interface of the waveguide core to a neighboring layer changes its thickness or its refractive index. For homogeneous sensing applications, a completely symmetric system is best, where the refractive indices of the substrate and the cladding are equal, thus allowing the waveguide core layer to be made arbitrarily thin. Then, nearly all of the optical energy of the mode is propagating in the cladding and the substrate layer. Therefore, a change in the refractive index of one of these layers has a strong influence on the effective index of the guided mode for very thin waveguides. In the case of surface sensing, the layer that can affect the effective index of the guided mode is very thin, which makes this effect considerably smaller. As a consequence, the energy in this thin sensing layer has to be maximized to maximize the sensor sensitivity, which will be discussed in section 3.1.1. Major applications for surface sensing are medical, biological or biochemical applications, where in many cases a monolayer of receptors is attached to the surface of the core layer[79]. Biomolecules can be captured by these receptors and change the optical properties of the sensing layer.

Evanescent wave sensors can be implemented in many different configurations. The following examples of biosensors provide a short overview about typical sensors and the sensing techniques they are based on. This chapter will also motivate the choice of an integrated Mach-Zehnder-interferometer for the polymer biosensor, which is in the focus of this thesis.

### 3.1 Evanescent waveguide sensors

Sensors based on evanescent waveguides directly measure changes of the effective index of a waveguide mode. Evanescent waveguide need to show single mode behavior, hence different modes are affected in a different way by a change in optical properties of a neighboring layer because of their different evanescent fields. To avoid unpredictable interferences between different guided modes, single mode behavior has to be ensured for the waveguides used.



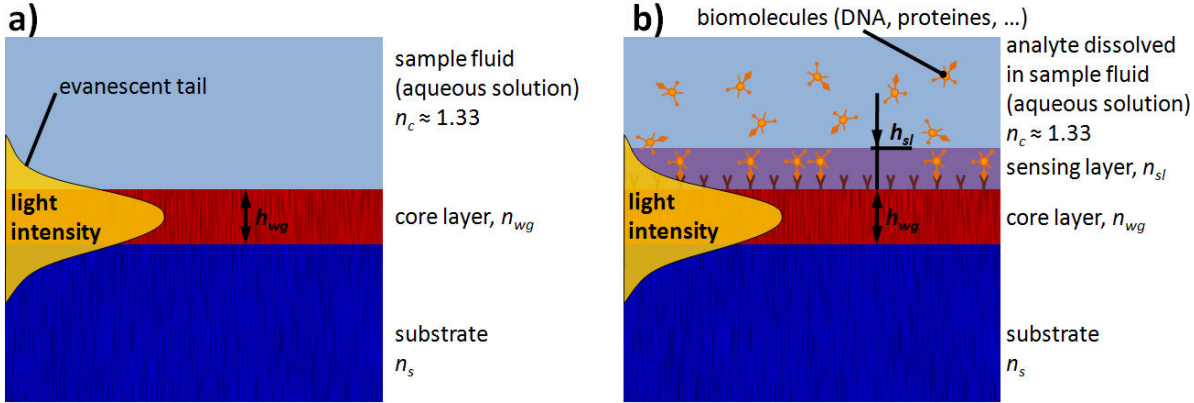


**Figure 3.1:** Principle of **a)** homogeneous and **b)** surface sensing. In a) the refractive index of the sample fluid changes during a measurement, whereas in b) the thickness and/or the refractive index of the sensing layer changes through binding of biomolecules on a biosensitive layer.

### 3.1.1 Sensitivity parameters for evanescent waveguides

In order to maximize the sensor sensitivity, evanescent waveguides have to be designed properly. The quantity to be measured is the change in the effective index of the fundamental waveguide mode. Therefore, the change in the fundamental mode should be maximized for a given change of either the refractive index of a homogeneous sample fluid or a change of the optical thickness (i.e. a change of the thickness and/or the refractive index) of a thin sensing layer at the interface of the waveguide in the case of surface sensing.

For homogeneous sensing (see Fig. 3.1a)), the optimization of the waveguide is straight forward. If it is ensured that the sample fluid, which represents the cladding layer in this case, is thick enough, the waveguide thickness has to be reduced as far as possible, such that as much energy as possible is present in the sample fluid. For surface sensing applications, two corresponding figures of merit for the sensitivity were proposed. Parriaux et al.[79] introduced the surface sensitivity parameter

$$S_P = \frac{\partial n_{eff}}{\partial \eta_P} \quad (3.1)$$

as the change of the effective index of the fundamental mode  $n_{eff}$  relative to the change of the dielectric load term  $\eta_P$  of the sensing layer defined as

$$\eta_P = k_0 h_{sl} (n_{sl}^2 - n_c^2) \quad (3.2)$$

where  $h_{sl}$  is the thickness (see Fig. 3.1b)) and  $n_{sl}$  is the refractive index of the sensing layer. Any change of the thickness or of the refractive index of the sensing layer leads to a change of the dielectric load term. On the other hand, the surface sensitivity parameter defined by Tiefenthaler et al.[1]

$$S_T = \left( \frac{\partial n_{eff}}{\partial h_{sl}} \right)_{n_{sl}=const} \quad (3.3)$$

is defined as the change of  $n_{eff}$  with respect to the change of the thickness of the sensing layer  $h_{sl}$ , whereas the refractive index  $n_{sl}$  is assumed to be constant.

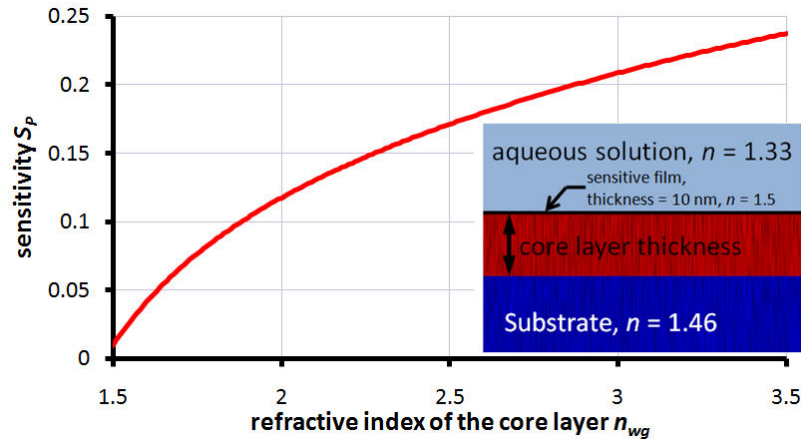


**Figure 3.2:** Sensitivity parameter  $S_P$  of an optimized slab system as a function of the refractive index of the core layer, calculated for the three-layer slab system shown in the inset. The core layer thickness is optimized for a given refractive index value (see Fig. 3.3a)).

The sensitivity parameter  $S_P$  is wavelength independent due to the fact that  $\eta_P$  includes the product  $k_0 h_{sl}$ , which is equivalent to the optical thickness of the sensing layer. If the thickness of the sensing layer is held constant and the wavelength is reduced, the optical thickness of the sensing layer is increased and more power can be confined within the sensing layer, resulting in a higher sensitivity. This wavelength dependence is already taken into account in the definition for  $S_P$ , which allows for an easier comparison of waveguide structures. In return,  $S_T$  gives an absolute number for the sensitivity based on the wavelength and materials used as well as on the waveguide cross section. Since it is not fully clear how binding events on a biosensitive layer change the optical properties of this layer, it cannot be stated which of these two models is the more correct one. Nevertheless, both sensitivity parameters give very similar results if compared for the same wavelength. For further considerations,  $S_P$  will be taken as the default sensitivity parameter because it is based on a more general model that incorporates all changes of the sensing layer, which can occur due to immobilization of additional molecules at the surface. The optimum waveguide cross section is the one with the largest sensitivity parameter. For the three layer slab system, this optimization can be done analytically. More complicated waveguide cross sections have to be numerically optimized or approximated by an analytical model. The surface sensitivity parameter  $S_P$  only depends on the waveguide cross section and the refractive index of the materials used, whereas the sensitivity of the sensor is proportional to the surface sensitivity parameter, but also depends on the type of sensor used, the length of the waveguide with the sensing layer on top and the wavelength.

Figure 3.2 shows the maximum achievable sensitivity parameter  $S_P$  of a three layer slab system as function of the refractive index of the waveguide core layer for a substrate with a refractive index of 1.46. The biosensitive layer was assumed to be 10 nm thick with a refractive index of 1.5[10] and the sample fluid had a refractive index of 1.33. The thickness of the core layer was optimized for each refractive index value. The calculation confirms a strong dependence on the optimized sensitivity parameter on the refractive index of the core material. The achievable sensitivity increases with the index of the core layer. Thus, high index difference material systems such as SOI are preferable for surface sensing. Although  $S_P$  is not the only parameter that influences the overall sensor sensitivity, an optimization of the waveguide geometry with respect to the surface sensitivity is absolutely necessary in order to design an effective sensor system. Together with the length of the waveguide that is exposed

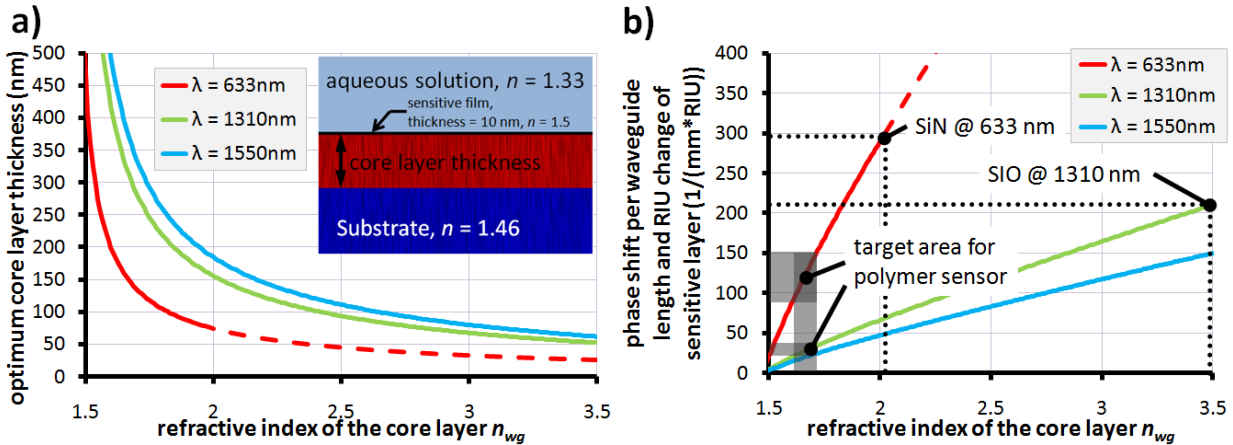


**Figure 3.3:** **a)** Optimum core layer thickness  $h_{wg}$  for the three-layer slab system shown in the inset as function of the refractive index of the core layer. **b)** Phase shift  $\Delta\Phi$  (see equation (3.6)) per millimeter length of the waveguide and refractive index unit (RIU) change of the sensitive layer for an optimized system, given for three different wavelength. The achievable phase shift increases with one over the square of the wavelength. As indicated in the graph, silicon nitride at a wavelength of 633 nm is the best currently available sensor platform for surface sensing, because no suitable materials with a higher refractive that are transparent for visible light are known. So far, wavelengths below 633 nm are not used for sensing applications because suitable laser sources are not available at a reasonable price.

to the sample fluid and the wavelength,  $S_P$  has a direct impact on the phase shift that occurs during a measurement (see equation (3.9) in section 3.1.3). This phase shift is the desired parameter for the interferometric devices discussed below. Figure 3.3b) gives the phase shift that can be expected for a 1 mm long waveguide, if the sensing layer changes its refractive index by 1 refractive index unit (RIU).

One way to increase the sensitivity of biosensors is to increase the interaction between the evanescent tail of the propagating mode and the analyte. For instance, this can be achieved by the use of hydrogel films on the sensor surface. Hydrogel films are 3D polymer networks that can be functionalized with binding sites for biomolecules to act as 3D binding matrices for biomolecules[80]. They can be attached as thin films on the sensor surface[81, 82]. Due to the increased number of binding sites and the increased interaction volume between the analyte and the evanescent tail of the propagating mode, the effective index of the mode can be stronger influenced during the measurement than in the case of pure surface sensing. Hydrogel enhanced sensors are not in the focus of this work, but have been already shown, for instance on SOI ring resonators[81] or on surface plasmon resonance sensors[80, 83].

### 3.1.2 Young interferometers

In a Young interferometer[84, 85, 86], an interference pattern between two different coherent light beams is used to obtain information about the relative phase between these two beams. In integrated optics, a Young interferometer is composed of two single mode waveguides that guide the two beams. An integrated Young interferometer, as shown in Fig. 3.4, also includes the beam splitter on the sensor chip, which can be realized as Y-branch or 3dB-coupler. The two arms of the interferometer are named as reference arm, which is protected by the cladding, and the sensor arm, where a measurement window is opened in the cladding, so that the analyte can interact directly with the sensor surface and consequently with the evanescent part of the guided mode in the sensing arm and influence their



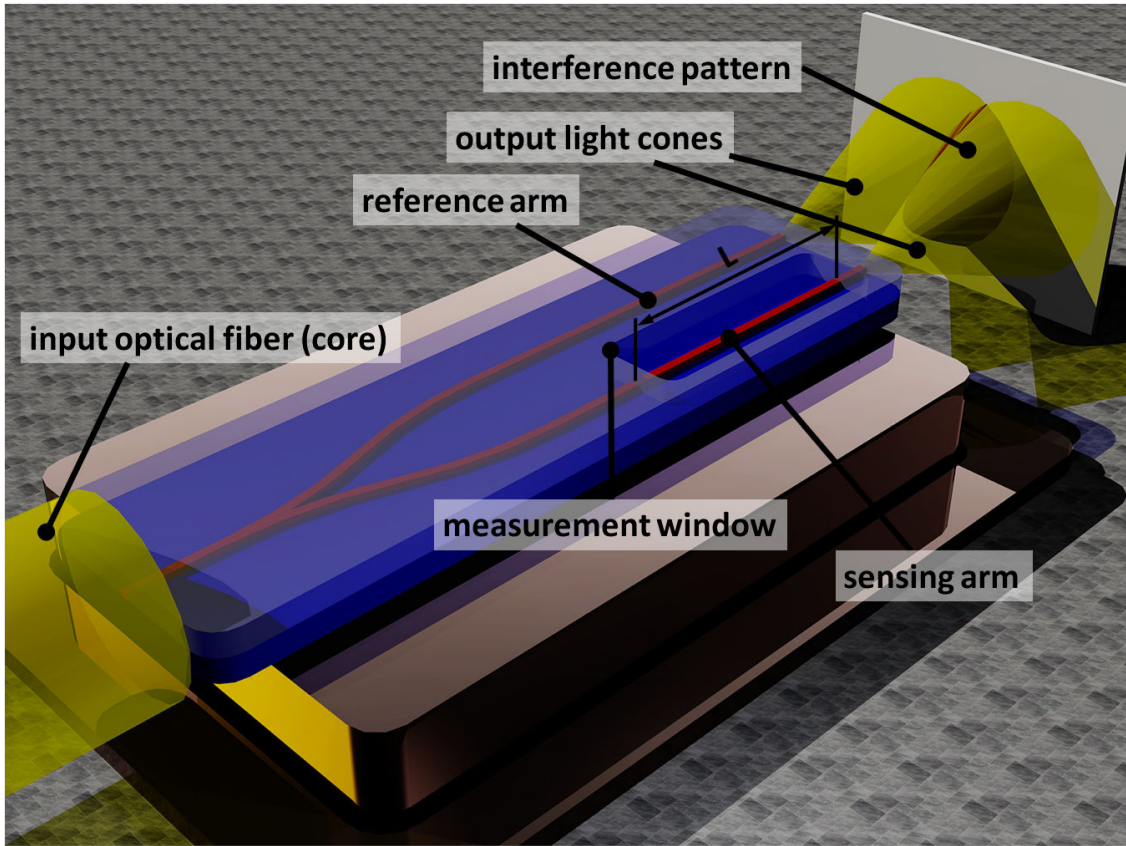


**Figure 3.4:** Working principle of a Young interferometer in integrated optics: the in-coupled light is split into the reference and the sensing waveguide; at the end of the waveguides, the light propagates in free space and the interference pattern of the two light cones can be monitored to obtain information about the phase shift in the measurement window.

propagation. At the end of the sample, the waveguides end and the guided modes are converted into freely propagating beams that can interfere at a distant screen. On the screen, the intensity signal is captured by a CCD line array. After the beam splitter, the guided modes, which propagate through the two arms of the interferometer, accumulate a certain phase. In the regions that are covered with the cladding they accumulate the same amount of phase. The only region, where the propagation of the two guided modes can be different, is the region of the measurement window, where the analyte can interact with one of these guided modes. The phase that is accumulated in these light path is  $\Phi_s = n_{eff,s}L$  and  $\Phi_r = n_{eff,r}L$  for the sensing and the reference arm, respectively, where  $L$  is the length of the measurement window. The phase difference at the end of the measurement window is given by

$$\Delta\Phi_{s-r} = \frac{2\pi}{\lambda_0} (n_{eff,s} - n_{eff,r}) L \quad (3.4)$$

The phase difference of the two interfering beams at the screen is given by[87]:

$$\Delta\Phi_{YI}(x) = \frac{2\pi}{\lambda_0} \left( \frac{xw_{YI}}{d} - (n_{eff,s} - n_{eff,r})L \right) \quad (3.5)$$

where  $w_{YI}$  is the distance between the two arms of the interferometer,  $x$  is the lateral position on the screen and  $d$  is the distance of the end of the sample to the screen. If  $\Delta\Phi_{YI}(x)$  is an even multiple of  $\pi$ , the two beams interfere constructively and the intensity has a maximum, whereas if  $\Delta\Phi_{YI}(x)$  is an odd multiple of  $\pi$ , the two beams interfere destructively and the intensity has a minimum. The intensity signal, therefore, has a sine modulation with a period of  $\Lambda_{YI} = \lambda_0 d / w_{YI}$ . In most cases,  $\Phi_r$  can be set constant during a measurement because of the protection by the cladding layer. Even if  $\Phi_r$  changes due to external influences such as a temperature change or applied pressure, in a first order approximation  $\Phi_s$  should change in the same way, which is one asset of devices with integrated referencing. Therefore, the phase difference is only affected by a change of the refractive index of a sample fluid or the optical properties of the sensing layer in the measurement window. During a measurement,  $n_{eff,s}$  changes by an amount of  $\Delta n_{eff}$ . As a consequence, also  $\Phi_s$  changes and the phase shift  $\Delta\Phi$  is added to the phase difference at the beginning of the measurement  $\Delta\Phi_{s-r,0}$ . The phase shift  $\Delta\Phi$  is defined as

$$\Delta\Phi = \frac{2\pi}{\lambda_0} \Delta n_{eff} L \quad (3.6)$$

This phase shift  $\Delta\Phi$  leads to a left or a right shift of the sine modulation of the intensity signal, which can be detected by the CCD array.

The Young interferometer needs a CCD detector array for analyzing the output signal. The data from the CCD array has to be analyzed by some kind of logic or software to detect and trace the lateral shifts of the intensity distribution. The propagation length of the radiating beams  $d$  needs to be long enough to achieve the desired resolution. The biochip holder as well as the CCD array need to be mounted on a stiff support to avoid influences from mechanical vibrations, which can have a significant effect due to the large propagation length  $d$  of the free radiating beams. For all these reasons, a Young interferometer needs a large, complicated, and therefore, expensive readout system.

As any other interferometer too, the Young Interferometer is only capable of detecting changes of the phase difference between the sensor and the reference arm, and therefore, changes in the effective index of the guided mode in the sensing arm. By using  $\Phi_s = 2\pi n_{eff,s} L / \lambda_0$  and  $\Phi_r = 2\pi n_{eff,r} L / \lambda_0$ , it is theoretical possible to calculate the accumulated phase of each guided mode in the reference and in the sensing arm of the interferometer, and therefore, also an absolute value for  $\Delta\Phi_{s-r}$ . However, it has to be mentioned that smallest deviations in the fabrication process or of the material parameters strongly affect  $\Phi_{s,r}$ , which prevents a precise calculation of an absolute value of  $\Delta\Phi_{s-r}$ . Therefore, in practical applications, it is not possible to calculate an absolute value of  $\Delta\Phi_{s-r}$ . However, this behavior poses no principal limitation for the applicability of interferometers for biosensing.

Biosensors based on the Young interferometer are already commercially available, *e.g.* ReliaSense from nGimat[88] or implemented in a silicon oxynitride material system by Farfield Group Ltd[89].

### 3.1.3 Mach-Zehnder interferometers (MZIs)

The Mach-Zehnder interferometer[10, 11, 9] (MZI) functions similar to the Young interferometer, with the difference that it additionally incorporates a beam combining component at the end of the MZI. In integrated optics this is done by an additional Y-branch or a 3dB-coupler, as shown in Fig. 3.5. In comparison to a Young interferometer, the device length increases because additional space for the beam combining component is needed, but in return, there is no more need for an extra space for

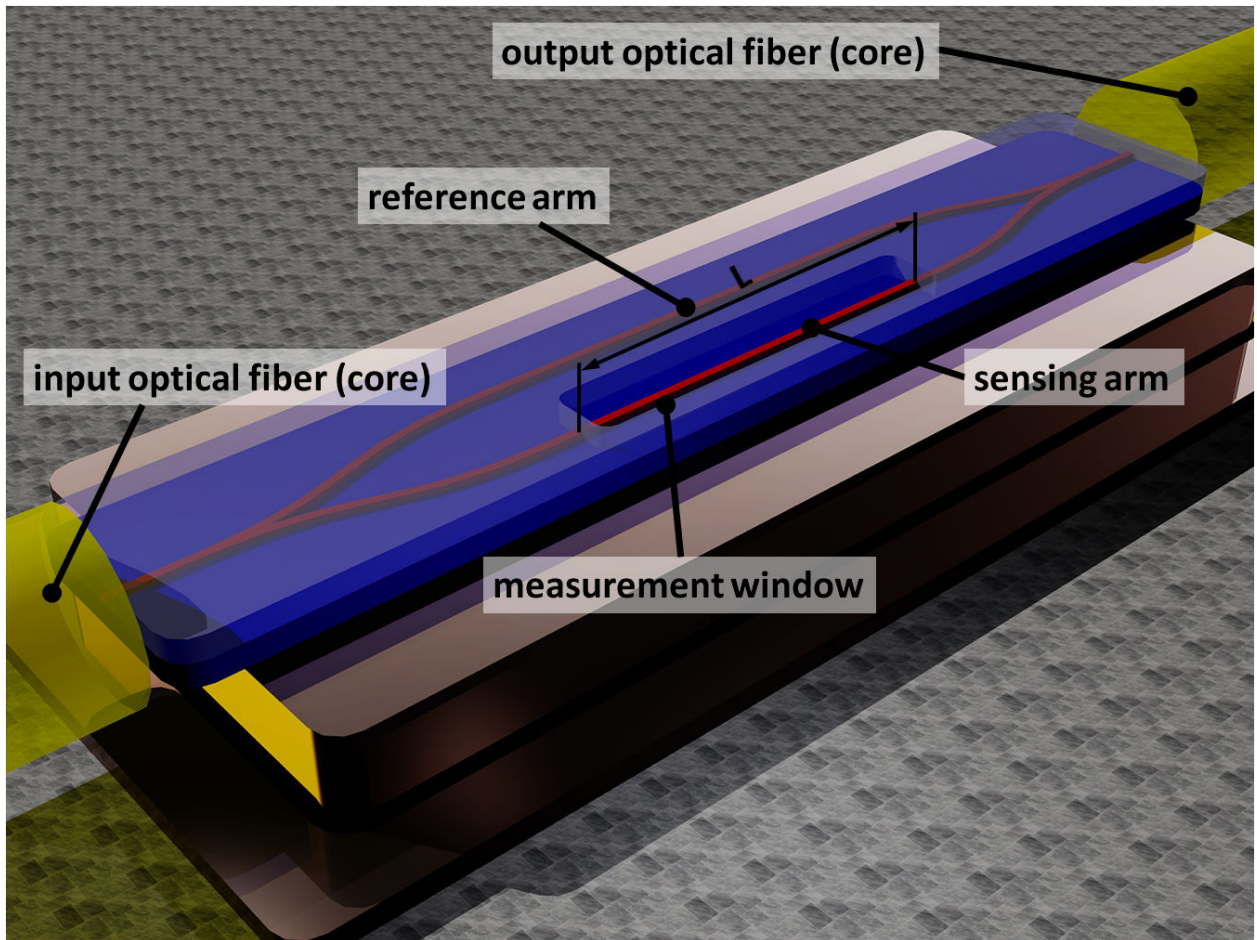


**Figure 3.5:** Schematic of a Mach-Zehnder interferometer: in comparison to the Young interferometer, the light of the sensing and of the reference arm is recombined and transferred to an output optical fiber or directly to a photodiode.

freely propagating beams. The propagating modes within a MZI behave in the same way as in a Young interferometer, *i.e.* equation (3.5) for the phase difference as well as the equation for the phase shift (3.6) are still valid. In contrast to the Young interferometer, the two guided modes are recombined at the end of the interferometer. The efficiency of the recombination at the end of the MZI is dependent on the phase difference of the two propagating modes in the beam combining element. In the case that a Y-branched is used as beam combining component, this behavior can be explained as follows: if the phase difference is an even multiple of  $\pi$ , the modes from the two arms can interfere constructively, whereas if the phase difference is an odd multiple of  $\pi$ , the two modes will excite higher order modes at the output waveguide, which will be radiated away due to the single mode behavior of the output waveguide[87]. Therefore, the measurement signal of a MZI is the transmitted optical power at the end of the output waveguide. Under the assumption that at the beginning of the beam combining element the optical power is the same in both arms and equal to  $P_{in}/2$ , the transmitted power  $P_{out}$  of the MZI shows a sinusoidal behavior that can be written as[90]:

$$P_{out} = P_{in} \frac{1 + \sin \Delta\Phi_{s-r}}{2} \quad (3.7)$$

A MZI is a highly sensitive detector for phase differences. The fact that a MZI translates a phase difference, which is usually hard to measure, into a modulation of optical power, which can be measured easily, makes this sensor concept attractive. During a measurement, the phase shift  $\Delta\Phi$  leads to a variation of the transmitted power  $\Delta P_{out}$  in the following way:

$$\Delta P_{out} = P_{in} \frac{\sin(\Delta\Phi_{s-r,0} + \Delta\Phi) - \sin \Delta\Phi_{s-r,0}}{2} \quad (3.8)$$

The phase shift  $\Delta\Phi$  can be expressed as  $\Delta\Phi = 2\pi\Delta n_{eff}L/\lambda_0$ , or in the case of surface sensing by the use of equation (3.3) for the sensitivity parameter as

$$\Delta\Phi = \frac{2\pi}{\lambda_0} S_P \Delta\eta_p L \quad (3.9)$$

The phase shift for a given change in the thickness of the sensing layer is determined by three independent factors. The first factor is the surface sensitivity parameter, which is dependent on the materials used and the waveguide cross section. It has to be optimized for a maximum phase shift. The second factor is the length of the measurement window. The maximum length of the measurement window is restricted by the desired overall size of the sensor chip, by propagation losses in the waveguides, which restrict the maximum length of the waveguides, and by the fluidic system, which is needed to control the flux of sample fluids over the sensor. Finally, a reduction of the wavelength can also be used to increase the phase shift.

An MZI combines a highly sensitive interferometric measurement principle with the possibility to use a very simple readout system since it only needs a laser source with a constant wavelength and a photodiode to measure the output signal. These are the reasons, why the MZI concept was found to be the best option for the polymer waveguide based biosensor. The main drawback of a MZI is the sinusoidal characteristic of the output signal, which has several consequences. Firstly,  $\Delta P_{out}$  as a function of  $\Delta\Phi$  is not unique, hence  $\Delta P_{out}$  remains unchanged by adding multiples of  $2\pi$  to  $\Delta\Phi$ . As a result,  $\Delta\Phi$  cannot be determined correctly by simply comparing  $P_{out}$  before and after the measurement, because all information on  $2\pi$ 's in the phase shift will be lost. The output signal needs to be tracked during the measurement and each pass of the output signal through a minimum and a maximum has to be recorded. Each pass from a maximum to a minimum or vice versa corresponds to a phase shift of  $\pi$ . Only then can the full phase shift be calculated from the collected  $\pi$ 's from the tracking and  $\Delta P_{out}$ , which is unique within the interval  $j\pi \leq \Delta\Phi_{s-r} \leq (j+1)\pi$ , where  $j$  is an integer. The second consequence of the sinusoidal characteristic is that the sensor response  $R_{MZI}$ , defined as

$$R_{MZI} = \frac{\partial P_{out}}{\partial \eta_p} \quad (3.10)$$

is not constant, but strongly depends on  $\Delta\Phi_{s-r,0}$ . There are even points where  $R_{MZI}$  is equal to zero, which is the case if  $\Delta\Phi_{s-r,0} = j\pi$ . The maximum sensor response is gained if  $\Delta\Phi_{s-r,0} = (j+1/2)\pi$ , which are also points of maximum phase shift before reaching an extremum. These points of maximum sensitivity are called quadrature points.

Most of the listed drawbacks of a MZI do not apply to finalized readout systems. Nowadays, any sensing platform needs an integrated computer or at least a computer interface for an easy user interface and data recording. The tracking of the output signal and the calculation of the phase shift, which is the desired parameter, can therefore, easily be done by software. The last point, which cannot be

corrected by software, is the low sensitivity at the extrema of the output signal. There exist several ideas for external tuning of MZIs in a way such that the phase difference  $\Delta\Phi_{s-r}$  can be adjusted to the next quadrature point. These ideas, mostly used for MZI-based modulators, incorporate the tuning of the effective index of the guided mode in one arm employing *e.g.* the electrooptic[91, 92] or thermooptic[93, 94] effects. Another option is changing the wavelength of the laser source. However, tuning of a MZI is not in the task of this work. Nevertheless, the sensor should be designed in a way that the phase shift during the measurement is large enough to ensure accurate and reproducible results. For a phase shift of at least  $\pi/2$ , the change in the output power will be large enough for a conclusive measurement, even if the sensor is near an extremum of the output power at the beginning of the measurement.

To overcome the drawback of low sensitivity of MZI sensors at the extrema of the output signal, Luff et al. proposed an alternative design for MZI sensors[95]. This alternative design incorporates the use of a three-waveguide coupler at the output of the MZI. If the three-waveguide coupler is properly designed, the interference pattern of the three output waveguides are shifted by  $2\pi/3$  with respect of each other, which guarantees that at least one of the output signals is in a sensitive region of the sinusoidal characteristic. An additional advantage of this design is that the sum of the output powers of the three waveguides remains constant, which allows compensating for fluctuations and drifts in the in-coupled power to the MZI input waveguide. One disadvantage of this MZI design is a more complicated readout system, which needs three photodiodes that can be analyzed simultaneously. Another disadvantage is the more complicated output coupler that depends stronger on material parameters and poses higher demands to the fabrication process due to reduced fabrication tolerances compared to a Y-branch output waveguide coupler.

### 3.1.4 Ring resonators

Ring resonators are mostly realized in high index difference material systems. They consist of a straight single mode waveguide and a single mode ring waveguide in close proximity, as shown in Fig. 3.6. A certain fraction of the power of the guided mode propagating through the straight waveguide couples into the ring waveguide, where it propagates further on. The power transfer between the straight waveguide and the ring resonator depends not only on the power ratio of these modes in proximity, but also on the phase correlation between them. The in-coupled power in the ring waveguide can influence the coupling after a complete round trip through the ring waveguide, depending on the accumulated phase in this round trip. If, in a simple model, the propagation in the ring waveguide is assumed to be lossless, the steady state solution for a ring resonator is the following: if the accumulated phase during a round trip is an even multiple of  $\pi$ , all the power from the straight waveguide will be coupled into the ring waveguide, whereas if the phase between the straight and the ring waveguide is not matched, no power will be coupled into the ring waveguide.

As the accumulated phase during a round trip depends on the wavelength used, ring resonators strongly show wavelength sensitive behavior. This fact can be exploited for sensing applications (*e.g.* [81, 96, 97]). If the output power of the straight waveguide is plotted as function of the wavelength, it exhibits multiple absorption peaks, one for each time the accumulated phase for one round trip is a multiple of  $2\pi$ . These resonant wavelengths, measured in free space, are given by [31]

$$\lambda_m = \frac{2\pi R n_{eff}}{m} \quad (3.11)$$



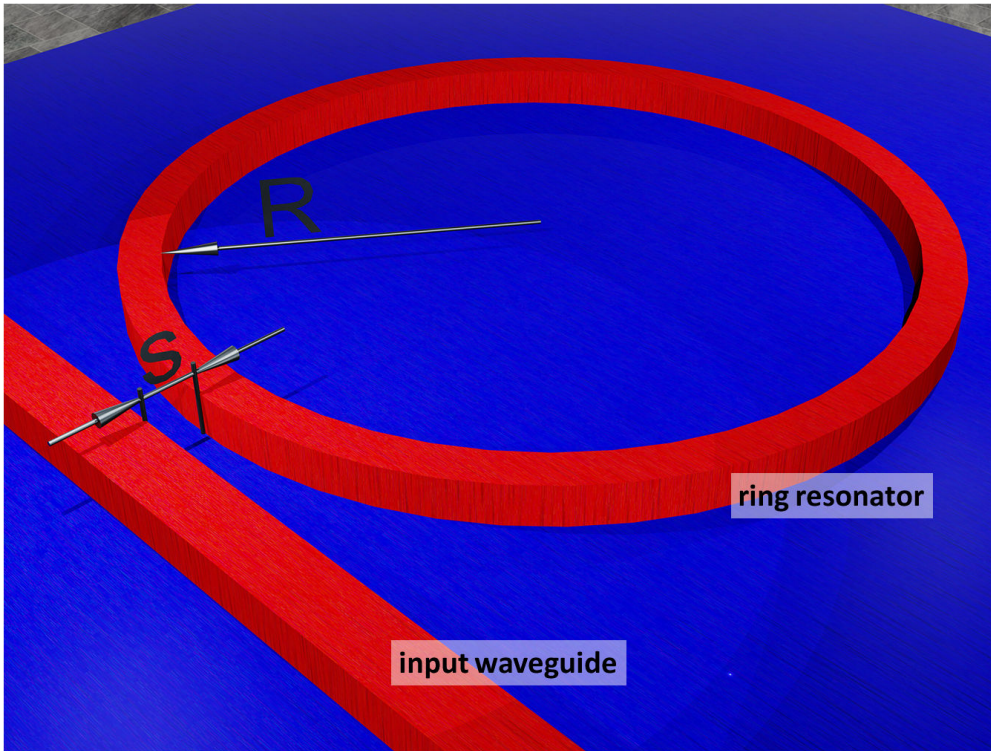


**Figure 3.6:** Sketch of a ring resonator with the radius  $R$  and the separation  $s$  from the input waveguide, as depicted within the picture.

where  $R$  is the radius of the ring waveguide,  $n_{eff}$  is the effective index of the guided mode in the ring waveguide, which is also a function of the wavelength and  $m$  is an integer. If the effective index of the guided mode is changed during a measurement, the resonant wavelengths shift by an amount of

$$\Delta\lambda_m = \frac{2\pi R \Delta n_{eff}}{m} \quad (3.12)$$

which can be measured. The absorption peaks are separated by the so called free spectral range  $\Delta\lambda$  defined by[31]

$$\Delta\lambda = \frac{\lambda_m^2}{2\pi R n_g} \quad (3.13)$$

where  $n_g$  is the group index of refraction and  $\lambda_m$  is the nearest resonant wavelength. For practical implementations of ring resonators, two additional parameters need to be taken into account. The quality factor  $Q$  is defined as[98]

$$Q = \frac{\lambda_0}{\Delta\lambda_{3dB}} \quad (3.14)$$

where  $\Delta\lambda_{3dB}$  is the difference between the two wavelengths at which the output power of the straight waveguide is half of the maximum output power. High  $Q$ -factors are desirable because the minima in the transmission spectrum become narrower, thus reducing the detectable wavelength shift.

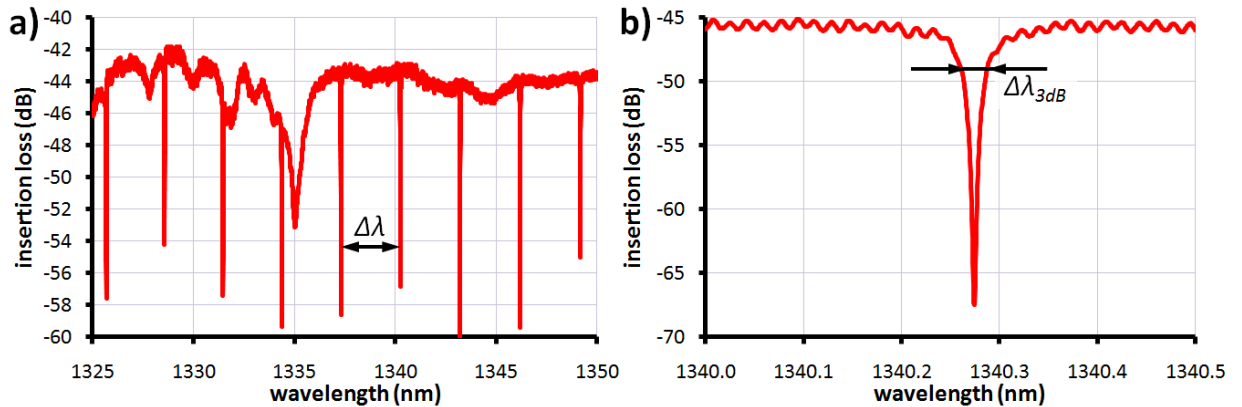


**Figure 3.7:** Measured transmission of a straight waveguide with an adjacent ring resonator in a 220 nm thick SOI material system. The ring resonator has a radius of 20  $\mu\text{m}$ , which results in a free spectral range  $\Delta\lambda$  of nearly 3 nm in this configuration. Measured by Paul Muellner and published with his permission. **a)** gives the transmission in the wavelength range from 1325 nm to 1350 nm and **b)** shows a detailed transmission curve for the resonance around 1340 nm. The measured  $Q$ -factor for this resonance is larger than 50000.

The second parameter is the extinction ratio, which is defined as the ratio between the maximum output power of the straight waveguide if no power is coupled into the ring waveguide and the minimum output power if the maximum amount of power is coupled into the ring waveguide. The higher this ratio, the easier shifts of the resonant wavelengths can be followed. These two parameters are related to the coupling coefficient between the straight waveguide and the ring waveguide as well as to the propagation losses in the ring waveguide, whether they arise from absorption losses, scattering losses or from bending losses.

Ring resonators are often realized in high index difference material systems such as SOI where bending radii can be reduced to several tens of microns without introducing too much radiation losses in the bended waveguides. In low index difference material systems, larger bending radii must be used in order to reduce bending losses. This not only increases the required space for a sensor but also reduces  $\Delta\lambda$ , which complicates the measurement of the shifts of the resonant wavelength. Nevertheless, polymer ring resonators for surface sensing applications were successfully reported, *e.g.* by Chao et al. in 2006[99].

## 3.2 Grating sensors

Grating sensors are composed of a corrugated waveguide that acts as a grating input coupler and a single mode waveguide that transports the in-coupled light to a photodiode. As can be seen from equation (2.52) in section 2.3.4,

$$|k_{inc}^{\rightarrow}| \sin \Phi + m\Delta k = k_0 n_{eff} \quad (3.15)$$

the angle for optimized in-coupling depends on the effective index of the fundamental waveguide mode  $n_{eff}$  in the grating region. In this equation  $|k_{inc}^{\rightarrow}|$  is the wave vector of the incident wave in the medium the wave propagates,  $\Phi$  is the angle of incidence,  $k_0$  the free space wave vector,  $m$  the order of diffraction and  $\Delta k = 2\pi/\Lambda$  the grating vector, where  $\Lambda$  is the period of the grating. By scanning the

angle of incidence to find the angle of maximum in-coupled power, the effective index of the waveguide mode can be calculated using equation (3.15). Since the corrugated waveguide is not covered with a cladding, a sample fluid can get directly into contact. Any change in the optical properties of the sample fluid influences the propagation of the mode in the grating region and influence, in consequence, the optimum angle, which is then measured.

The full width of half maximum (FWHM)  $\delta\bar{k}$  of the coupling efficiency into the corrugated waveguide is a function of the detuning variable  $\bar{k}$ , which is defined as[100]

$$\bar{k} = k_0 n_{eff} - |k_{inc}| \sin \Phi + m\Delta k \quad (3.16)$$

and gives the detuning from the optimum in-coupling configuration. The FWHM of the coupling efficiency is defined by the optical uncertainty principle[1]

$$L\delta\bar{k} \cong 2\pi \quad (3.17)$$

where  $L$  is the length of the grating sensor. The longer the grating sensor, the narrower the peak in the in-coupled power as function of the coupling angle. Therefore, long gratings, which exhibit very narrow peaks in the in-coupled power, are necessary for sensitive grating sensors. Long gratings allow for a precise measurement of the optimum coupling angle and make the detection of small shifts possible. In most configurations, grating sensors work with a fixed light source while a sensor chip containing the grating, the waveguide, the photodiode and a fluidic system, as sketched in Fig. 3.8[101, 71], is rotated to change the angle of incidence. The sensitivity of grating couplers can be maximized by optimizing the geometric parameters of the corrugated waveguide.

A sensitivity parameter similar to the sensitivity parameters for evanescent waveguides can be defined. This parameter gives the change of the effective index of the guided mode in the grating region if the refractive index of the sample fluid, in the case of homogeneous sensing, or the optical parameters of a thin sensing layer, in the case of surface sensing, changes. Due to the corrugated structure of the grating, the optimization is more complex than in the case of homogeneous waveguides and is done by means of numerical methods in most cases.

A main advantage of grating sensors is that the optimum coupling angle can be translated directly into an effective index of the waveguide mode in the grating area. Knowing the geometry of the grating and the optical properties of the materials used for the corrugated waveguide, the absolute value of the refractive index of the sample fluid in the case of homogeneous sensing or the absolute value of the thickness/refractive index of the thin layer in the case of surface sensing can be extracted from the effective index. A disadvantage for this type of sensors is the need for a sophisticated setup, comprising a very precise mechanical construction that allows for an automated rotation and a precise angle measurement as well as a lot of bulk optics for beam preparation.

Biosensors based on grating sensors with a rotating measurement setup are already commercially available, e.g. OWLS sensors from MicroVacuum[102].

As an alternative to a rotated measurement setup, fixed grating sensors can be used in combination with tunable laser sources or broadband light sources. In this case, the wavelength of optimum in-coupling in the corrugated waveguide changes. In such systems, there is no need for a precise mechanical setup



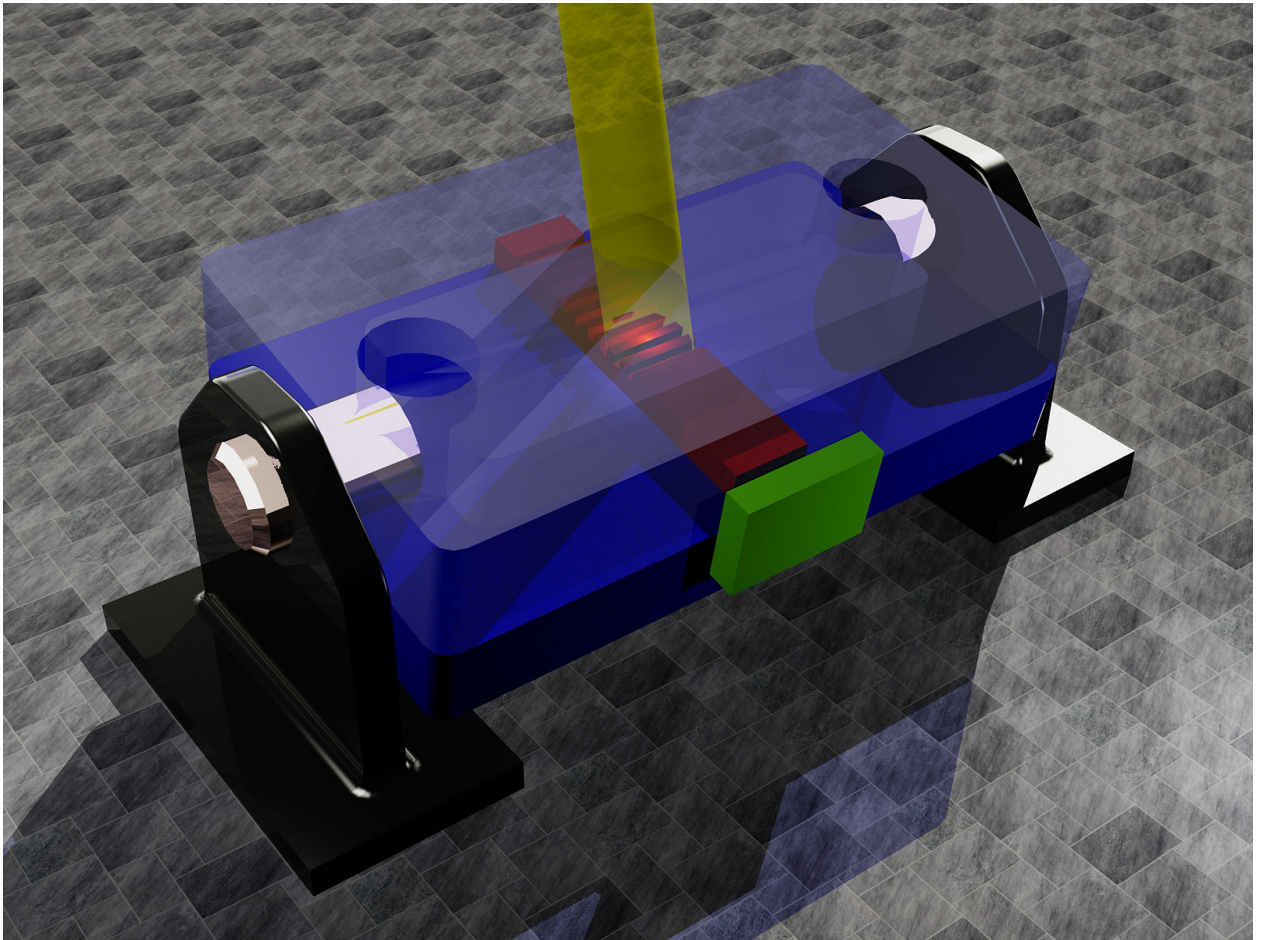


**Figure 3.8:** Measurement configuration of a grating sensor: a fixed laser light source illuminates a grating on a turnable chip. The in-coupled power is transferred to a photodiode (green). The sample fluid is rinsed through the flow chamber on top of the waveguide. Changes in the effective index in the grating region shift the optimum angle of incidence, which can be measured by a precise rotation control.

for angle measurements, but in return, a tunable light source or an optical spectrometer is needed. Grating sensors based on this measurement principle are commercially available from Dynetix Biosystems AG[103], which utilizes tunable vertical-cavity surface-emitting lasers (VCSEL's) as tunable laser sources[104] or from Corning Incorporated[105], whose Epic system utilizes a broad band light source and measures the wavelength of the reflected light of the grating sensors.

Another sensor principle based on gratings was proposed by Cunningham et al.[106]. A resonant guided mode phenomenon in grating structures is used to reflect a single wavelength at a high efficiency under normal incidence. If illuminated with a broadband light source, an optical spectrometer can analyze the precise wavelength of the reflected light, and therefore, detect changes of this wavelength during a measurement.

Such sensors are commercially available from SRU Biosensors[107] with an illumination from a broadband LED light source. A simple measurement setup and a cheap light source are advantages of this sensor system. A drawback is the need of a fast and precise spectrometer for the measurement of the reflected wavelength, which increases the cost of the readout system.

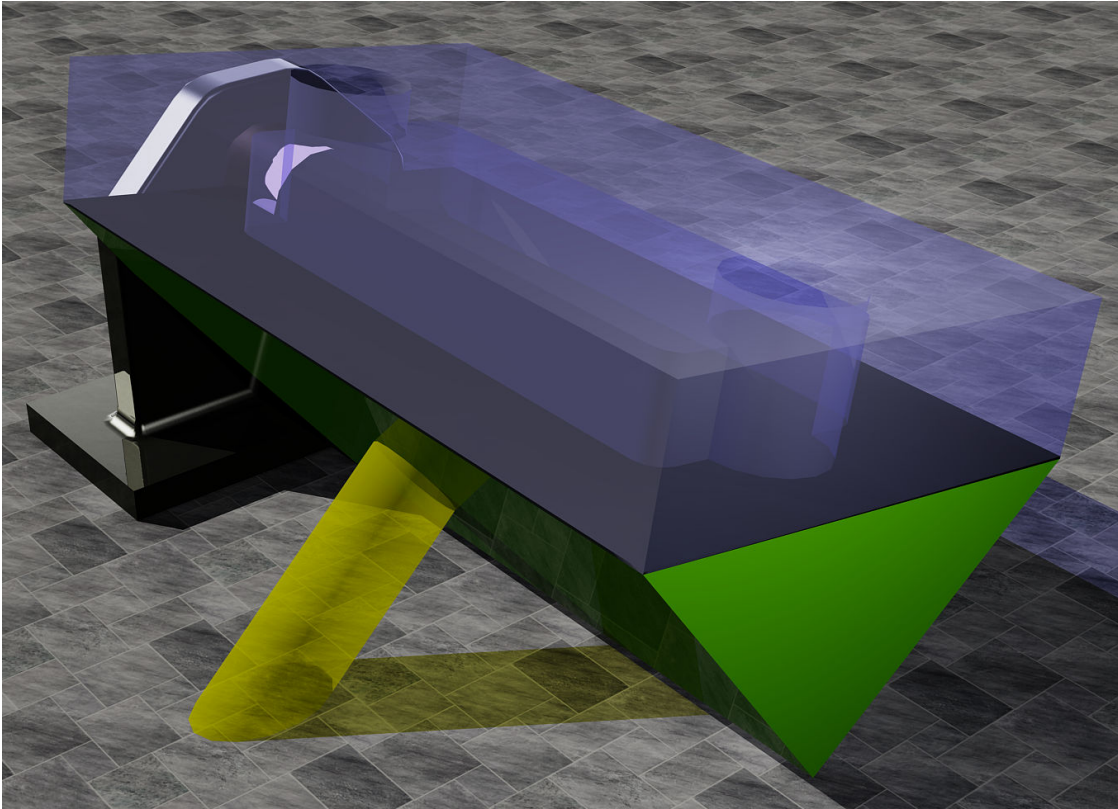


**Figure 3.9:** A surface plasmon resonance (SPR) sensor in typical Kretschmann-configuration. A laser beam enters the sensor through a prism at the backside. The prism is coated with a thin metal layer on top. At a specific angle, surface plasmons are excited, which show very strong absorbance and the reflected beam has a minimum in its intensity. Any change of the sample fluid or the sensing layer leads to a shift in the angle of maximum absorbance, which can be measured with a precise mechanical setup.

### 3.3 Surface plasmon resonance sensors

Surface plasmons (SPs) are light waves that are coupled to oscillations of free electrons in a metal or a conducting dielectric material, and propagate along the conducting material-dielectric interface[108]. In most cases, thin metal layers made from gold or silver are used as conducting material. The surface plasmon wave has a maximum at the interface between the metal and the dielectric and decays exponentially into both media[109]. Therefore, surface plasmons are sensitive to changes in the surrounding media. Surface plasmons can be excited by laser beams if the wave vector of the laser beam matches the wave vector of the surface plasmon  $k_{sp}$ , which is given by[110]:

$$k_{sp} = k_0 \sqrt{\frac{\epsilon_m \epsilon_d}{\epsilon_m + \epsilon_d}} \quad (3.18)$$

where  $k_0$  is the free space wave vector and  $\epsilon_m$  and  $\epsilon_d$  are the complex dielectric constants of the conducting material and the dielectric, respectively. Since the wave vector of surface plasmons is larger than  $k_0$ , a direct excitation of surface plasmons by a laser beam propagating in air is not possible. As a consequence, the wave vector of the laser beam has to be enlarged, *e.g.* by means of a prism or a grating.

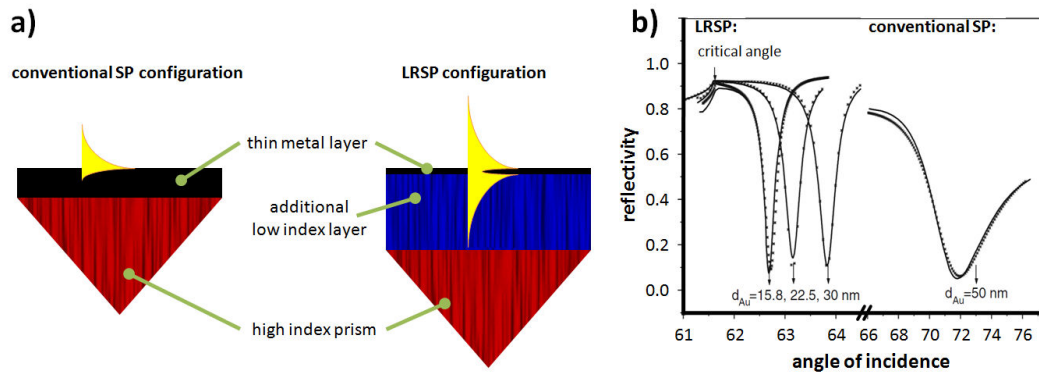


**Figure 3.10:** **a)** Comparison between configurations for conventional SP and LRSP sensors. The LRSP sensor has an additional low index layer between the high index prism and the metal layer. **b)** Reflectivity curves for conventional SP and LRSP sensors. The dips in the reflectivity for the LRSP are narrower compared to the conventional SP and become narrower the thinner the metal layer is. Reprinted with permission from reference[113].

Surface plasmons suffer from strong damping due to high absorbance if a metal layer is used as conducting material. The most common sensing configuration of surface plasmon resonance (SPR) sensors, the Kretschmann-configuration (see Fig. 3.9)[111, 112], uses attenuated total reflection at the bottom of a prism to excite surface plasmons on the interface between a thin metal film and the sample fluid. In a Kretschmann sensor, the laser beam enters a prism whose top side is covered with a thin metal layer. If, for a specific angle of incidence of the laser beam, the phase matching condition between the surface plasmons and the laser beam is satisfied, the power of the laser beam is transferred into the surface plasmons and subsequently absorbed in the metal layer and the power of the reflected laser beam exhibits a minimum. Any change in the sample fluid of the sensor, which acts as the dielectric layer for the surface plasmons, changes the wave vector of the surface plasmon, and therefore, the angle of incidence for which the phase matching condition is satisfied.

An additional concept for SPR sensors is the use of long range surface plasmons (LRSPs). If a very thin metal layer is surrounded by two dielectric layers with similar refractive indices, two surface plasmons at the opposite metal/dielectric interfaces can couple and form two new modes, the so called short range surface plasmons and the LRSP[114]. The LRSPs are of particular interest because they exhibit much lower damping compared to conventional surface plasmons[113] and penetrate deeper into the surrounding media. LRSP can be excited in a modified Kretschmann configuration, with an additional low index layer between the high index prism and the metal layer (see Fig. 3.10a)). The dip in the reflected power as function of the angle of incidence of LRSP is much narrower and shifted towards smaller angles compared to conventional surface plasmons[115]. The narrower dip in the reflected power allows for a more precise measurement of the angle of minimum reflection. The larger penetration depth of LRSP is an additional advantage for homogeneous measurement, because more power is present in the analyte, but is a disadvantage for surface sensing applications due to reduced field intensity at the layer interfaces.

The mode profile of surface plasmons is advantageous for surface sensing because the maximum intensity of the surface plasmon wave is located directly at the layer interface, where the sensing layer is present. While this fact promotes the eligibility of surface plasmon sensors for biosensing applications, the high intrinsic propagation loss of surface plasmons prevents the use of classical waveguide concepts.

**Table 3.1:** Comparison of published results of biosensors based on different sensor principles. The limit of detection is given in dimensions of refractive index unit (RIU) changes of bulk solutions.

Sensing principle	Limit of detection (RIU)	reference
SPR	$10^{-5}$ to $10^{-8}$	[122, 123, 124, 125, 126, 127]
LRSP	$10^{-7}$ to $10^{-8}$	[128, 114]
Young interferometer	$8.5 \times 10^{-8}$	[129]
Mach-Zehnder interferometer	$10^{-7}$	[90]
ring resonators	$10^{-4}$ to $10^{-7}$	[130, 131, 132, 133, 134]

SPR is the commercially most mature sensor concept for label-free biosensing and several companies offer products based on this technique, *e.g.* Biacore from GE Healthcare[116], ProteOn from Bio-Rad Laboratories [117], Plasmon Imager from Graffinity Pharmaceuticals[118], AP-3000 from Fujifilm[119], SensiQ from ICx Technologies[120] or SR 7000 from Reichert Analytical Instruments[121].

### 3.4 Comparison of presented sensor concepts

This section compares the presented sensor concepts with respect to their applicability to an integrated polymer-based sensor concept for biosensing. The principle of grating sensors is known for many years and this type of biosensor is already commercially available. As mentioned in section 3.2, the necessity for a stiff and precise mechanical measurement setup set limits to the miniaturization of these bulky devices. Interferometric devices such as the Young- and the Mach-Zehnder interferometer offer a highly sensitive measurement principle with the additional benefit of an internal reference, which cancels out most errors from parasitic effects such as thermal expansion and thermo-optic effects. Compared to the Young interferometer, the Mach-Zehnder interferometer brings the additional advantage of a very simple read-out system and reduced device footprint. Ring resonators are not feasible as rib waveguides in a polymer material system because of the low refractive index difference, which leads to very large waveguide bending radii. This not only increases the necessary footprint of the device, but also makes high Q-factors difficult to achieve due to large propagation losses in long waveguides. Surface plasmon resonance is a promising sensing concept and highly sensitive devices have been shown and are already commercially available from different vendors. The mode profile of surface plasmons is a strong advantage for surface sensing since the maximum light intensity is at the interface between the metal and the dielectric. Unfortunately, due to high propagation losses, surface plasmons cannot propagate over long distances. This prevents the use of interferometric waveguide concepts such as a Mach-Zehnder configuration.

Comparisons of different optical sensor principles for biosensing have been performed, for instance by Passaro et al. in 2007[135] and Fan et al. in 2008[6]. Table 3.1 shows an extract of these comparisons for the sensor types presented in this chapter. Passaro et al. concluded in their paper that interferometer configurations are most sensitive, but require comparatively long structures (tens of millimeters) compared to sensors based on micro cavities *e.g.* ring resonators.



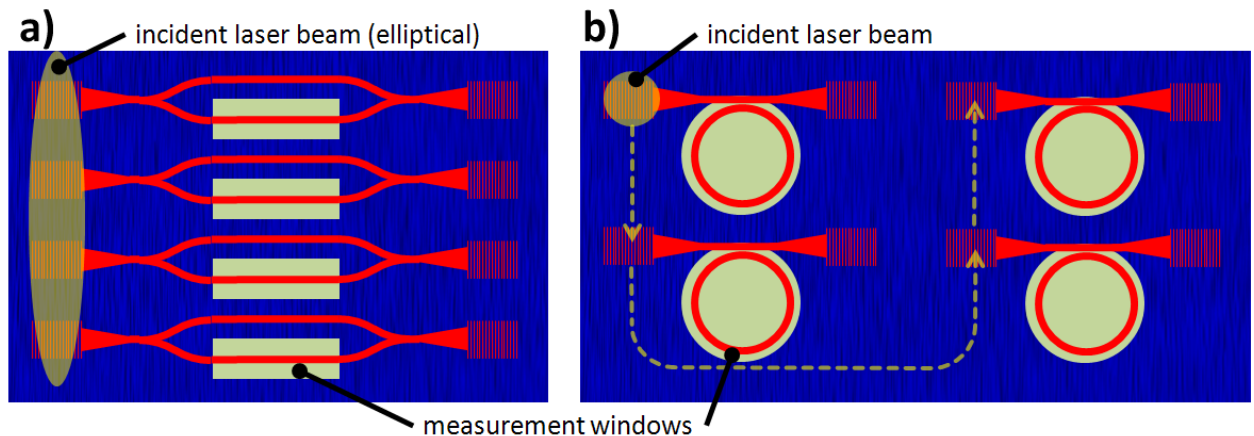


**Figure 3.11:** a) 1D array of MZI sensors with an elliptical laser beam that illuminates all input grating couplers simultaneously. b) 2D array of ring resonator sensors with grating couplers for the straight waveguides. In this example, the sensor elements are sequentially addressed by a moving laser beam.

### Multi-parameter analysis

An additional requirement for a (commercially) successful sensor platform is the ability to detect several analytes in a single run. The presented interferometric concepts, the Young and the Mach-Zehnder interferometer are longish structures that can be arranged in a 1D array. If the in-coupling is done by grating couplers, either a laser with a elliptical beam is incident on all grating simultaneously (see Fig. 3.11a) or a moving laser beam addresses the interferometers sequentially. In the first case, all interferometers can be measured simultaneously, but a laser with a comparatively high power is needed, because only a little amount of the laser power is coupled into the waveguides. In the latter case, a mechanical/optical setup that moves the beam from one grating to another has to be included in the read-out system and the interferometers can only be read-out sequentially, which complicates real-time measurements.

If end face coupling is used, the 1D array of interferometers can be illuminated by fiber arrays, which are commercially available. For an array of MZIs, the minimum spacing between the interferometers is given by the necessary spacing between the waveguides to prevent crosstalk and from the spacing required from the setup for the biofunctionalization of the sensor surface to allow for different biofunctionalization layers on sensing arms of neighboring MZIs. For an array of Young interferometers, an additional requirement for the minimum spacing between the interferometers is that the free propagating beams at the end of each Young interferometer do not interfere with the free propagating beams of the neighboring Young interferometers.

Due to their compactness, ring resonators can be arranged in a 2D array if the in- and out-coupling is done by grating couplers (see Fig. 3.11b)). Bailey et al.[136] demonstrated a multi-parameter sensor platform based on silicon ring resonators that are addressed sequentially by a moving laser beam. The incident laser beam stops at a input grating, performs a wavelength sweep and proceeds to the next grating. The transmitted light of the waveguide near the ring resonator is coupled out by means of a second grating and is then wavelength resolved detected. Due to the very large wavelength tolerance of grating couplers in SOI material systems, the wavelength dependent behavior of the grating couplers can be neglected for this application.

Grating sensors can be arrayed in a 1D array like MZIs or Young interferometers[137]. If additional gratings are used for out-coupling of the light that is in-coupled by the grating sensor, also 2D arrays of grating sensors are feasible. Such 2D arrays of sensor can be either sequentially addressed by a moving laser beam or simultaneously illuminated by a laser beam with a large diameter, where the out-coupled light is detected by a CCD-camera.

Arrays of SPR sensors are possible in one or two dimensions. Jakub Dostalek et al. demonstrated two dimensional arrays SPR sensors on a common metal sensor layer[127, 138]. 2D arrays of gratings are used to excite surface plasmons and each spot act as an independent sensor element. The reflected light from the sensor elements is then analyzed by a CCD array.

### **The choice of the Mach-Zehnder interferometer**

Ring resonators are not feasible on an injection molded substrate without an additional lithography step. On an injection molded substrate, only rib waveguides can be used for wave guiding, if the high index layer is applied by simple spin coating. The very large bending radii of polymer rib waveguides prevent the use of the ring resonator concept.

As a result of the special challenges when using an all polymer material system, such as high thermal expansion and large thermo-optic coefficients of polymers as well as the, compared to silicon wafers or glass substrates, flexible polymer substrate, an interferometric measurement principle with its integrated referencing is the best choice for the realization of an integrated polymer biosensor. Due to their longish structure, interferometers have a larger device footprint than *e.g.* grating sensors, which is, in this case, not a direct disadvantage hence the fabrication costs of the injection molded substrate do not depend directly on the size of the sensor chip, as is the case for semiconductor based technologies. The presented interferometric sensor concepts can be very easily arranged in 1D arrays to allow for multi-parameter analysis. Since the integration of a second Y-branch adds no additional complexity to the fabrication process and due to the much simpler read-out system, the Mach-Zehnder interferometer outperforms the Young interferometer for this application.

## 4 Design of the MZI sensor

This chapter deals with the design of the polymer biosensor. Based on the considerations in chapters 2 and 3, together with the final goal of a disposable polymer biosensor chip, which can be fabricated utilizing injection molding and spin coating, the following fundamental decisions about the sensor design were made:

- The substrate has to carry all wave guiding and coupling structures. The waveguide core layer and the upper cladding are applied by spin coating. The compatibility of the design with injection molding of the substrate necessitates a planar sensor layout that can be patterned in a single-step process.
- The sensor is to be based on a MZI. Its interferometric measurement principle not only provides a highly sensitive measurement platform for label-free detection of biomolecules, it also reduces errors from parasitic effects such as thermal expansion, which is of great benefit when using polymers.
- The MZI utilizes Y-branches instead of 3dB-couplers for splitting the incoming beam into the two arms of the interferometer and for recombining the two beams from the interferometer. Y-branches are inherently symmetric and wavelength independent, provided that the waveguides are single mode. They allow for larger fabrication tolerances and are not sensitive to small deviations of the refractive indices of the materials used.
- Grating couplers are selected for coupling the light in and out of the sensor. They are compatible with the planar fabrication process and can be patterned in the same step as the waveguide structures. End-fiber coupling and taper structures for coupling are not possible, given that the injection molded substrate is not cleavable and that homogeneous layer thicknesses of the waveguide core layer at the edges cannot be achieved by spin-coating. Furthermore, grating couplers allow for reduced alignment requirements, which is an important aspect for disposable sensor chips read out by an external device.

This chapter presents the materials selected for the polymer biosensor chip and simulations of all optical elements involved in the sensor layout. The results from these simulations lead to the final sensor layout.

### 4.1 Material selection

Polymers are an attractive material system for the realization of planar integrated optical waveguide devices in a wide range of applications[12]. Their fast and easy processing allows for cost-effective mass production, while their tunable properties provide high flexibility in design. The first necessary step for the sensor layout is the choice of suitable polymers that can be used as substrate, waveguide core layer, and cladding. The material selection is critical for successful realization of the sensor chips, but very time consuming. The enormous number of polymers comes with problems as well as possibilities.

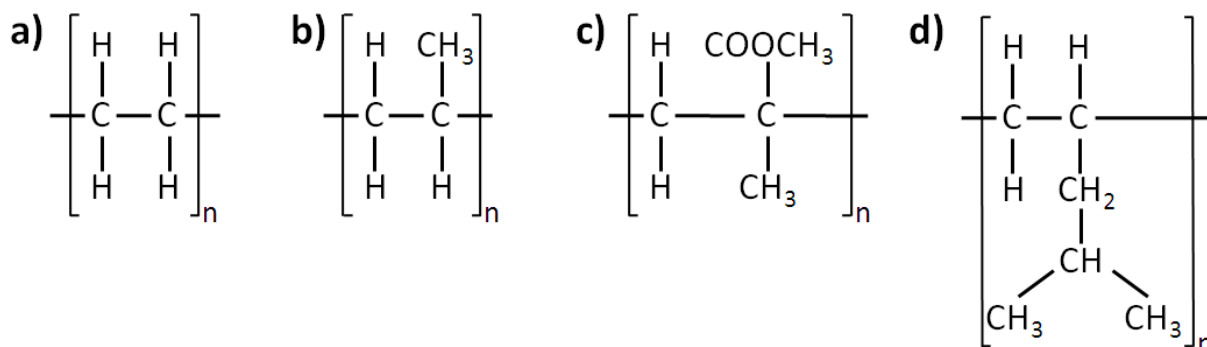


**Figure 4.1:** Chemical structure of simple technical polymers. **a)** Polyethylene (PE), **b)** polypropylene (PP), **c)** polymethylmethacrylate (PMMA), and **d)** polymethylpentene (PMP)

To further complicate matters, optical properties of polymers are often not well known. Datasheets of polymers contain, if at all, only the refractive index for one wavelength, but in most cases without specifying this wavelength. Data about absorption losses or the wavelength dependence of the refractive index is nearly impossible to get for most polymers.

#### 4.1.1 Introduction to polymers

The term polymer refers to the fact that these kind of molecules are chain molecules composed of a large number of repeating units, the so called monomers. In nature, only two types of atoms show the ability to build such chain molecules: carbon and silicon. Carbon based chain molecules play a very important role in nature. All life as we know it is based on carbon chain molecules.

The technical utilization of polymers started several decades ago. Technical polymers can roughly be divided into three groups. Thermoplastics are polymers that turn to a liquid state when heated above a certain temperature and freeze again to a solid state, when cooled sufficiently. Most thermoplastics are polymers whose chains associate through weak Van der Waals forces. Elastomers are highly elastic polymers and thermosetting resins, the third group, are rigid after being shaped during a curing process. The commercial success of polymers was mainly driven by thermoplastics and a growing technology platform that allows for the fast fabrication of large numbers of pieces at an extremely low cost. Injection molding and extruding are the two most prominent fabrication methods for polymers.

The backbone of most technical polymers predominantly consists of carbon, but can also contain small amounts of other atoms, *e.g.* nitrogen or oxygen. A carbon atom can bind to up to four neighboring atoms. In a chain molecule, at least two bonds of backbone atoms are required to build the chain. Therefore, each carbon atom in the backbone can donate two additional bonds to atoms or chemical groups on the side of the backbone that define the chemical behavior of the polymer. In simple polymers, most of these bonds are saturated with hydrogen. Figure 4.1 shows examples of chemical structures of simple technical polymers.



### 4.1.2 Comparison between polymers and inorganic materials

Organic and inorganic material systems for optical applications show very different behavior and properties. Silicon based materials are a commonly used inorganic material system for optical applications. Silicon dioxide ( $\text{SiO}_2$ ), silicon nitride ( $\text{SiN}$ ), silicon carbide ( $\text{SiC}$ ) and, in the end, silicon itself count to the family of silicon based materials. Silicon dioxide, with a refractive index of 1.46, is transparent for light from the UV region down to near infrared. It is an essential material for optics and *e.g.* lenses and optical fibers are made from  $\text{SiO}_2$ . In integrated optics,  $\text{SiO}_2$  is used for low index layers, *e.g.* for substrate or cladding layers. Silicon nitride is transparent for visible light and in the near infrared, where its refractive index is about 2[139]. Silicon nitride shows very low loss[140] and, together with  $\text{SiO}_2$ , it is an established material platform since about 1970[141].

Silicon oxynitride ( $\text{SiO}_x\text{N}_{1-x}$ ) is another silicon based material, which can be deposited with variable parts of oxygen and nitrogen. This allows tuning of the refractive index from the refractive index of silicon dioxide up to the refractive index of silicon nitride. By the use of this material system any refractive index difference up to 0.54 can be realized. For higher index differences silicon carbide or silicon can be used. Silicon carbide with a refractive index of between 2.4 and 3[142, 143], depending on the wavelength, is transparent for wavelength from 500 nm[143] to 2  $\mu\text{m}$  [144]. It has applications in integrated optics especially in high-temperature and high-energy physics because of its excellent mechanical properties and its heat conductivity[142].  $\text{SiC}$  can be also an attractive material for sensor applications due to its resistivity in harsh environments[143]. Nowadays, the focus of actual research is mostly on silicon. Silicon has a very high refractive index of about 3.48 and is transparent in the near infrared[139]. Therefore, it is compatible with common telecommunication wavelengths around 1.31  $\mu\text{m}$  and 1.55  $\mu\text{m}$ , which is why silicon is a great white hope for the realization of ultra-compact photonic devices.

Other important material systems are gallium arsenide ( $\text{GaAs}$ ) based materials, indium phosphate ( $\text{InP}$ ) and lithium niobate ( $\text{LiNbO}_3$ ). In the near infrared,  $\text{GaAs}$  has a refractive index of about 3.43, which can be increased to about 3.55 by alloying with indium, or decreased below 3 by allowing with aluminum. This easy adjustment of the refractive index value gives high flexibility in design of optical elements.  $\text{InP}$  has a refractive index of 3.1 in the near infrared region.  $\text{GaAs}$  and  $\text{InP}$  are comparatively expensive materials, which are of particular interest for the realization of active photonic devices. Their direct bandgap allows for easy excitation of photon emission.

$\text{LiNbO}_3$ , with a refractive index of 2.2 in the near infrared, attracted great attention due to its high nonlinear and electro-optic coefficients. It is, therefore, often used for nonlinear application scenarios, such as second harmonic generation and wavelength mixing, or the realization of modulators. Silicon based materials cover a very wide range of refractive index. Inorganic materials are usually very stiff and brittle.

Polymers, on the other, hand show very different behavior. Compared to their inorganic counterparts, most polymers are comparatively flexible and tensile. While most polymers are not attacked by acids and bases, organic solvents play an important role in their chemistry. Organic solvents can attack, degenerate or solve polymers. As discussed in more detail in section 4.1.3, the refractive index of transparent polymers is roughly in the range from 1.3 to 1.7. Even if there are some attempts to develop polymers with higher refractive indices, for example by incorporation of metal oxide nanoparticles[145, 146], this range is true for the majority of transparent polymers.

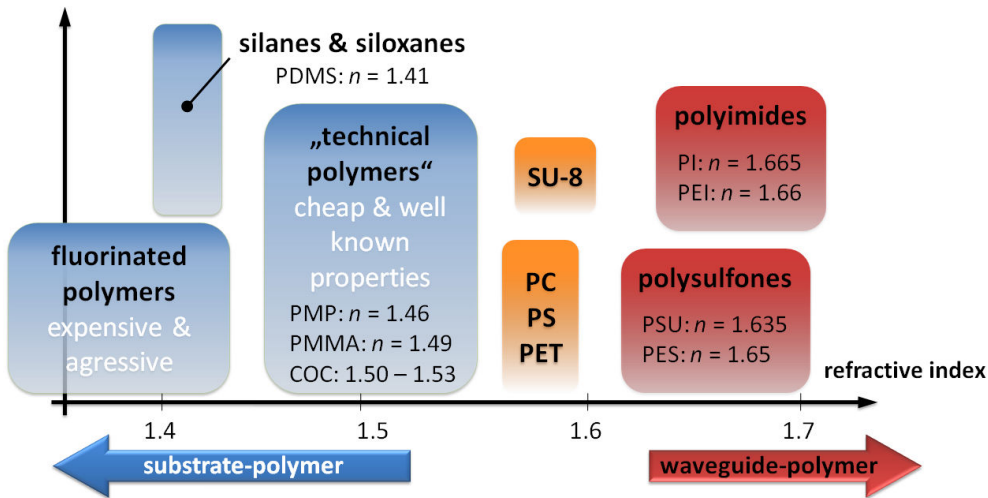


Figure 4.2: Overview chart of some transparent polymer families.

### 4.1.3 Overview of transparent polymers

Only a small fraction of polymers is transparent in the visible or near infrared range. Nevertheless, even this small fraction contains a large number of polymers and polymer families, which is why a comprehensive study of transparent polymer is not possible within this work. However, the chart in Fig. 4.2 gives a short overview of common transparent polymer families and the range of refractive indices these polymers have.

At the lower end of the refractive index scale are fluorinated polymers. Their refractive index can be as small as 1.31[147]. Fluorinated polymers are usually chemically inert and stable, but expensive in production and processing. They are chemically aggressive during the injection molding step and require special injection molding equipment. Silanes and siloxanes are polymers with a silicon based backbone. They are mainly elastomers, which prevents them to be used with injection molding. A famous siloxane is polydimethylsiloxane (PDMS), which already found a variety of applications in integrated optics and microfluidics. Many technical transparent polymers have refractive indices around 1.5. Among them are polymethylmethacrylate (PMMA) with a refractive index of 1.49 in the visible range, cyclic olefin copolymer (COC) with  $n = 1.50 - 1.53$  and polymethylpentene (PMP) with  $n = 1.46$ . Other technical polymers have slightly higher refractive indices such as polycarbonate (PC,  $n = 1.58$ ), polystyrene (PS,  $n = 1.57$ ) or polyethyleneterephthalate (PET,  $n = 1.58 - 1.62$ ).

For polymer waveguides, photoresists are commonly used. They are in most cases transparent to visible light and their refractive indices are known to optimize lithography. As an example, SU-8 from Microchem Corp. is presented. This negative-tone photoresist can be used for e-beam as well as conventional UV-lithography and has a refractive index of about 1.58[148]. Polymer families with a high refractive index are polysulfones and polyimides. The polymer family of polysulfones are used for high temperature applications. Polysulfone (PSU,  $n = 1.635$ ) and polyethersulfone (PES,  $n = 1.65$ ) are the most common representatives of this group. Polyimides are usually expensive high performance polymers with high temperature and chemical stability. The refractive index depends on the composition of the polyimide, but can go up to 1.665.

Absorption losses of polymers in the near infrared mainly come from overtones of fundamental molecular vibrations[149]. Especially the overtones of stretching vibrations in C-H and O-H bonds, which can be found in great quantities in polymers, are highly absorptive in the telecommunications windows. By replacing hydrogen with deuterium or fluorine in the molecular structure of polymers, the absorption can be reduced and shifted towards longer wavelengths[150]. Fortunately, the overtone absorption of C-C and C-O bonds, which build the backbone of most polymers, can be neglected because of very low overtone intensity for absorption wavelengths in the near infrared[151].

#### 4.1.4 Requirements for polymers used

As shown in Fig. 3.2, the maximum achievable surface sensitivity parameter strongly depends on the refractive index difference between the substrate and the waveguide core layer. The maximum index difference, and therefore, the maximum surface sensitivity parameter that can be reached in an all-polymer material system is in any case much smaller compared to the silicon-on-insulator platform. To achieve sufficient sensor sensitivity, it is important to maximize the refractive index difference between the substrate and the waveguide core layer. The requirement profiles for the three necessary polymers start with the requirement profile for the cladding, which is applied as the last polymer, and therefore, has the fewest requirements. For the other polymers, additional aspects have to be taken into account. They need to withstand the processing of the subsequent polymers, which should not to be underestimated since processing of polymers often includes thermal curing steps and organic solvents, which can attack the underlying polymers. Good optical properties such as high transparency, low absorption and low light scattering are demanded for all three polymers.

This is the requirement profile for the **cladding polymer**:

- The cladding polymer has to be spin-coatable in thicknesses of several micrometers.
- It has to be directly UV-patternable for the definition of measurement windows or microfluidic channels. Since etching of polymers is not possible as for silicon based materials, the measurement windows or microfluidic channels have to be patterned directly during the application of the cladding polymer.
- Chemical stability during the functionalization procedure of the sensor surface is required. Although only the core layer surface needs to be functionalized, it is very likely that also the cladding comes in contact with the liquids involved.
- The polymer for the cladding layer needs to be stable in the chemical environment of biosensing experiments.

This is the requirement profile for the **waveguide core polymer**:

- The refractive index of the waveguide core polymer has to be high.
- It has to be spin-coatable in thicknesses of several hundreds of nanometers.
- Chemical resistivity against any solvent, acid or base used during the application and the development of the cladding layer and the functionalization procedure of the sensor surface is required.
- If necessary, the waveguide core polymer needs to withstand a thermal curing step of the cladding layer.

- Good adhesion of the cladding polymer on the core layer is necessary to enable spin coating of homogeneous cladding layers. Surface pretreatments to increase the adhesion on the polymer surface such as corona pretreatment or exposure to oxygen plasma may be possible.
- The polymer for the core layer needs to be stable in the chemical environment of biosensing experiments.

This is the requirement profile for the **substrate polymer**:

- The refractive index of the substrate polymer has to be low.
- It has to be a thermoplastic polymer with good injection molding properties to ensure precise replication of optical sub- $\mu\text{m}$  structures from the injection molding stamp.
- Chemical resistivity against any solvent, acid or base used during the application the waveguide core layer as well as during the application and development of the cladding layer is essential. During the functionalization procedure of the waveguide core layer surface and the MZI measurements, the core layer covers the whole substrate and should protect it from any damage.
- If necessary, thermal stability during a thermal cure step of the waveguide core and cladding layer is required. This can be a critical point due to the fact that thermoplastic polymers are sensitive to high temperatures.
- Good adhesion of the waveguide core polymer on the substrate layer to enable spin coating of thin homogeneous core layers is necessary. Pretreatments to increase the surface adhesion may be possible.
- The substrate polymer should be cheap in order to keep the cost per sensor chip at a low level. The cost of the other polymers are not of such a high importance since only a very little amount of the other polymers is needed.

The refractive index of the cladding polymer is not of high importance, because no cladding is present in the measurement window and the surface sensitivity only depends on the refractive indices of the substrate and the waveguide core layer. An ideal choice for the refractive index of the cladding polymer would be the refractive index of the sample fluid, which would prevent radiation losses at the beginning and the end of the measurement window. However, these radiation losses have only minor influence on the sensor performance. Between the substrate and the waveguide core layer an index difference of about 0.2 seems feasible, without restricting the choices of the polymers too much.

The requirement profiles presented in this section provide a starting point for the material selection process. Unfortunately, some of these requirements are dependent on the properties of the neighboring polymers. Thus, the choice of a polymer for a specific layer can change the requirements for the other layers. For instance, the functionalization procedure depends on the waveguide core polymer, but also defines the requirements for the chemical stability of the cladding layer. The surface adhesion between two layers depends on the properties of both layers as well. In such a context, it is necessary to find a complete set of suitable polymers simultaneously, rather than finding one polymer after the other. Moreover, for most polymers, not all necessary data is available in advance.

#### 4.1.5 Selected polymers and properties

Following the guidelines given in the previous section, several polymers were selected as potential candidates. The data given in the lists below is mainly based on the datasheets provided by the manufacturers. For the substrate, the following two polymers were selected:

- **Polymethylpentene (PMP)** from Mitsui[152] has a refractive index of  $n = 1.46$ . It has excellent injection molding properties as well as good optical properties. For a thermoplastic polymer it has a very high thermal stability of 173°C (Vicat softening point) and is resistant against most organic solvents. It is completely non-toxic and meets the safety standards for food packaging. The main drawback of PMP is its very low surface tension, which leads to poor surface adhesion and makes surface pretreatments necessary before applying any additional layer. In addition, PMP has a high thermal expansion coefficient of 0.017 %/°C and shows shrinkage of more than 2% after the injection molding process.
- As an alternative to PMP, Zeonex, a **cyclo olefin polymer (COP)** from Zeon Chemicals[153] was identified. As PMP, it has excellent injection molding and superb optical properties. The refractive index of Zeonex ranges from 1.509 to 1.531. The chemical resistivity of Zeonex is not as good as that of PMP, but seems sufficient for the application as a substrate polymer. The thermal stability of Zeonex is guaranteed for temperatures up to 123°C, which is much lower than that of PMP and may cause problems during curing steps of the core layer or cladding polymers. In return, it has only very little thermal expansion of 0.007 %/°C and a higher surface tension than PMP.

Both substrate polymers are already used for the fabrication of optical components such as lenses. Therefore, the optical properties of these two polymers can be assumed to be good enough to allow propagation of a waveguide mode over the range of several centimeters without introducing too much optical loss. Due to the lower refractive index, the higher thermal stability and the better chemical resistivity, PMP is the first choice as substrate polymer if the problem of the poor adhesion on PMP surfaces can be solved. As candidates for the waveguide core polymer the following two polymers are shortlisted:

- PI2771 from HD Microsystems[154] is a **polyimide (PI)** that comes in a liquid state. After exposure to UV light and a thermal cure step, this PI forms a tough polymer layer. After curing, PI2771 is resistant against most common solvents and has a thermal stability of more than 400°C. The refractive index is about 1.65. PI2771 is designed to give film thicknesses of several microns after cure, but can be diluted with *n*-methyl-2-pyrrolidone (NMP) to reach thinner film thicknesses. The liquid, non-cured PI2771 solution has a reddish color, which indicates absorption losses for wavelengths shorter than red light.
- The second polymer for the waveguide core polymer is Ultrason E2020P, which is a **polyether-sulfone (PES)** from BASF[155]. It is a thermoplastic polymer that is commonly used for several technical applications. It has a high thermal stability of more than 180°C and a refractive index of about 1.65. In most cases, it is used for injection molding, but can be solved in organic solvents such as NMP, *n,n*-dimethylformamide (DMF) and *n,n*-dimethylacetamide (DMAA) to apply PES for spin coating. PES has a yellowish or brownish color but is, in principle, transparent for many wavelengths.

To the authors knowledge none of these two polymers have ever been used for optical applications such as wave guiding. Therefore, optical parameters of these materials are mostly unknown. Preliminary test of both polymers showed that they are sufficiently transparent for wavelengths of 633 nm and 1.31 μm

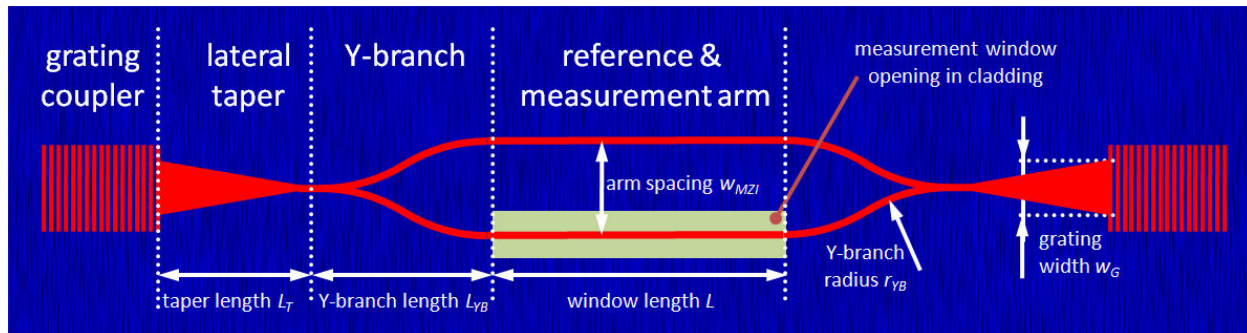


**Figure 4.3:** Sketch of the basic sensor layout.

to guide light without much loss over a distance of 2 cm. Spin coating test showed that if PI2771 is diluted with NMP, it can be spin coated down to film thicknesses of less than 200 nm. For PES, these tests showed that in a first attempt film thicknesses as small as 1  $\mu\text{m}$  can be reached by spin coating. Thinner film thicknesses cannot be reached because no homogeneous layer is formed during the spin coating step. This limitation may be overcome by adapting the spin coating procedure or by changing the organic solvent. Since the polyimide showed good performance in these first tests, it is used as default waveguide core layer polymer. For the cladding one polymer was found:

- **Ormoclad** from the Ormocer family, produced by micro resist technology[156] is a UV-patternable inorganic-organic hybrid polymer. It is designed as cladding for optical wave guiding applications, and therefore, has excellent optical properties. It has a refractive index of 1.52 and exhibit very low loss in the near infrared and visible range. It is to be applied by spin coating and can be diluted with Ormothin to adjust the film thickness. After spin coating and curing, employing UV light and a thermal cure step, it can be developed for the definition of the measurement windows.

Since Ormoclad is direct UV patternable and designed as cladding material for optical waveguides, it seems to be the optimum choice as a cladding material. To summarize this section, PMP is selected as substrate polymer, PI2771 as waveguide core layer polymer and Ormoclad as cladding. This gives a refractive index profile of 1.46 for the substrate, 1.65 for the core layer and 1.52 for the cladding. This material system is used for the simulations in the next section.

## 4.2 Simulations and MZI layout

The basic sensor layout is depicted in Fig. 4.3. The MZI is composed of single mode waveguides that are realized as inverted rib waveguides (see section 4.2.1 and Fig. 4.5 for details). Y-branches split the incoming light into the two arms of the interferometer and recombine it at the end of the interferometer. The in- and out-coupling is done by binary line grating couplers and lateral tapers reduce the width of the waveguides after the gratings to the width of the single mode waveguides. As required, the whole sensor has a planar layout and can be patterned in a single step process into an injection molded substrate. Several critical design parameters are shown in Fig. 4.3, e.g. the length of the Y-branches  $L_{YB}$ , which is defined by the spacing between the two arms of the interferometer and the bending radii  $r_{YB}$  of the waveguides in the Y-branches, the taper length  $L$  and the width of the gratings  $w_G$ , which is derived from the diameter of the incident beam on the grating. This section deals with all necessary design parameters.

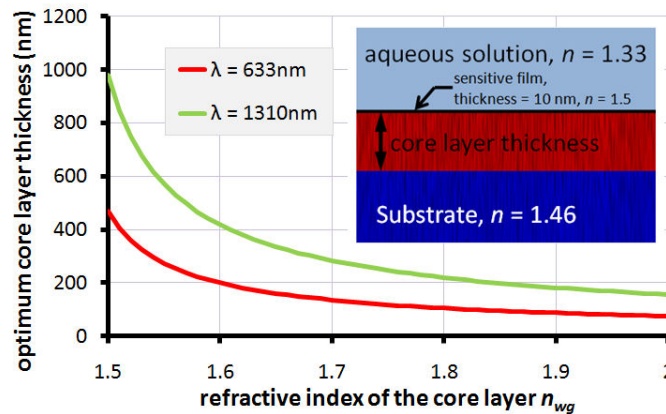


**Figure 4.4:** Optimum waveguide core layer thickness for surface sensing as function of the waveguide core layer refractive index. The inset shows the slab waveguide system used for these calculations.

Due to the small refractive index difference of polymer material systems, the surface sensitivity of this sensor cannot compete with surface sensitivities of high index difference material systems, such as SOI. However, in contrast to SOI, transparent polymers are not only transparent in the near infrared region, but also in the visible range. This allows for the use of smaller wavelengths to partly compensate for the lower surface sensitivity. Therefore, the sensor is designed for two different wavelengths. The first wavelength is 633 nm, which is a typical wavelength for sensing applications due to the widespread use of the HeNe laser, and the second wavelength is 1.31  $\mu\text{m}$ , which is a typical telecom wavelength. The sensitivity of the overall sensor is reduced when using the telecom wavelength compared to 633 nm, but in return, it allows for the use of compact, well established and high quality components. In addition, the requirements on the fabrication process are lower for the telecom wavelength due to a larger feature size of the optical structures. For all simulations PMP is assumed as substrate material and Ormoclad as cladding. Further on, the refractive indices of the polymers are assumed to be wavelength independent because no data about the wavelength dependence is available. In order to compensate for this uncertainty, a large safety margin is applied to all simulation results.

#### 4.2.1 Waveguide optimization

An inverted rib waveguide structure was chosen due to its compatibility with the injection molding and spin coating processes. The rib of the waveguides is realized as trench, patterned into the injection molded substrate. During the spin coating step with the waveguide core polymer, this trench is filled up with the high index polymer. The first step for the definition of the optimized waveguide cross section was the calculation of the optimum thickness of the waveguide core layer for surface sensing applications. This was done by an analytical calculation of the fields of the fundamental mode in a four layer slab waveguide using a Mathematica script. By variation of the thickness of the core layer, the optimum thickness was found for each refractive index. Figure 4.4 shows the results of this calculations for a PMP substrate and a sample fluid with a refractive index of 1.33. The biosensitive layer was assumed to be 10 nm thick, with a refractive index of 1.5[10].

The optimum total height of the rib waveguides is  $H = 366$  nm for a wavelength of 1310 nm and  $H = 160$  nm for a wavelength of 633 nm. The etch depth  $e$  is chosen to be 150 nm for 1310 nm wavelength and 40 nm for 633 nm wavelength. The maximum allowable rib widths of the waveguides to



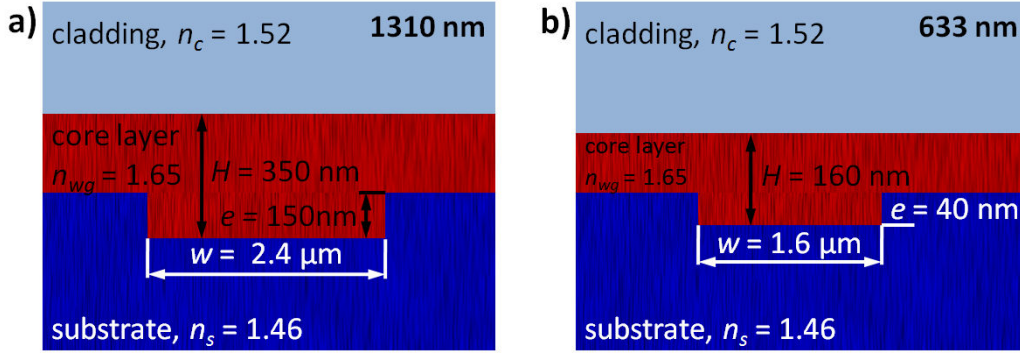


**Figure 4.5:** Waveguide cross sections for inverted single mode rib waveguides, optimized for surface sensing. For wavelengths of **a)** 1.31  $\mu\text{m}$  and **b)** 633 nm.

guarantee single mode operation were determined with a semi-analytical method[43] (see section 3.1.1) and amounted to 3.1  $\mu\text{m}$  and 1.9  $\mu\text{m}$  for the wavelengths of 1310 nm and 633 nm, respectively. Taking into account tolerances in the fabrication and uncertainties of the refractive indices, rib widths of  $w = 2.4 \mu\text{m}$  for  $\lambda = 1310 \text{ nm}$  and  $w = 1.6 \mu\text{m}$  for  $\lambda = 633 \text{ nm}$  were chosen. The final waveguide cross sections for both wavelengths are presented in Fig. 4.5.

#### 4.2.2 Y-branches for the MZI

The simulations for the design of the Y-branches in this section as well as the tapers in the following section were performed using a commercial simulation tool[157] based on the beam propagation method (BPM).

##### The beam propagation method (BPM)

The BPM is a comparatively fast simulation technique that allows the simulation of propagating waves over large distances, up to centimeters. It is a first order approximation to the Helmholtz equation for the propagation of monochromatic waves. The basic approach of the BPM, as outlined here, is based on a paper from R. Scamozzino et al.[158], which reviews several simulation methods for photonic devices. The wave equation (2.11) for the electric field is given by

$$\left( \frac{\partial^2}{\partial x^2} + \frac{\partial^2}{\partial y^2} + \frac{\partial^2}{\partial z^2} \right) \vec{E} = \epsilon\mu \frac{\partial^2 \vec{E}}{\partial t^2} \quad (4.1)$$

If a scalar electric field in the form  $\vec{E} = E(x, y, z)e^{-i\omega t}$  is assumed, the wave equation for such a field can be written in the form of the Helmholtz equation for monochromatic:

$$\left( \frac{\partial^2}{\partial x^2} + \frac{\partial^2}{\partial y^2} + \frac{\partial^2}{\partial z^2} + k(x, y, z)^2 \right) E(x, y, z) = 0 \quad (4.2)$$

In this equation,  $\epsilon\mu\omega^2$  is replaced by  $k(x, y, z)^2 = k_0^2 n(x, y, z)^2 = k_0^2 \epsilon(x, y, z)$ , where  $k(x, y, z)$  is the spatially dependent wavenumber with  $k_0 = 2\pi/\lambda_0$ . The geometry of the problem is given by the



refractive index distribution  $n(x, y, z)$ . In [158] it is argued that for typical guided wave problems, the most rapid variation in the field  $E$  is the phase variation due to propagation along the guiding axis and that this rapid variation in the field can be factored out of the problem by introducing the so called slowly varying field ansatz

$$E(x, y, z) = u(x, y, z)e^{i\bar{k}z} \quad (4.3)$$

In this ansatz, it is assumed that the field  $E$  is propagating into the  $z$ -direction and  $\bar{k}$  is a constant number to be chosen to represent the average phase variation of the field  $E$ . This first assumption leads to the paraxiality condition for the simple BPM that limit the BPM to waves propagating in a narrow angle around the  $z$ -axis. By replacing  $E$  by the slowly varying field  $u$  in the Helmholtz equation (4.2) yields the following equation:

$$\frac{\partial^2 u(x, y, z)}{\partial z^2} + 2i\bar{k}\frac{\partial u(x, y, z)}{\partial z} + \frac{\partial^2 u(x, y, z)}{\partial x^2} + \frac{\partial^2 u(x, y, z)}{\partial y^2} + (k(x, y, z) - \bar{k})^2 u(x, y, z) = 0 \quad (4.4)$$

The second assumption is that  $u$  varies sufficiently slow with  $z$ , so that the second derivative  $\frac{\partial^2 u}{\partial z^2}$  can be neglected with respect to  $2i\bar{k}\frac{\partial u}{\partial z}$  in the equation above. With this so called slowly varying envelope approximation and a slight rearrangement, equation (4.4) becomes

$$\frac{\partial u(x, y, z)}{\partial z} = \frac{i}{2\bar{k}(x, y, z)} \left[ \frac{\partial^2 u(x, y, z)}{\partial x^2} + \frac{\partial^2 u(x, y, z)}{\partial y^2} + (k(x, y, z) - \bar{k})^2 u(x, y, z) \right] \quad (4.5)$$

This is the basic equation for the BPM. For a given input field  $u(x, y, z = 0)$ , equation (4.5) gives the evolution of the field for  $z > 0$ . With this equation, the field  $u$  for  $z > 0$  can be integrated for a given input field with any suitable numerical scheme. The slowly varying envelope approximation reduces the physical problem from a second order boundary value problem to a first order initial value problem, which can be numerically integrated in a very efficient way. The price for this is a restriction of the propagating angle of the fields and the index contrast. In addition, neglecting the second order derivation eliminates backward traveling solutions. Therefore, effects such as reflection cannot be taken into account.

The most prominent numerical integration scheme for equation (4.5) is a finite difference method based on a Crank-Nicholson like approach that substitutes the field derivations by differences of the fields on a discrete grid in the following way[159]:

$$\frac{\partial u(x, y, z)}{\partial z} = \frac{u(a, b, c + 1) - u(a, b, c)}{\Delta z} \quad (4.6)$$

$$\frac{\partial^2 u(x, y, z)}{\partial x^2} = \frac{1}{2} \left[ \frac{u(a - 1, b, c) - 2u(a, b, c) + u(a + 1, b, c)}{\Delta x} + \frac{u(a - 1, b, c + 1) - 2u(a, b, c + 1) + u(a + 1, b, c + 1)}{\Delta x} \right] \quad (4.7)$$

$$u(x, y, z) = \frac{1}{2} [u(a, b, c) + u(a, b, c + 1)] \quad (4.8)$$

In these equations,  $u(a, b, c)$  is the field at the grid point with the coordinates  $x = a \cdot \Delta x$ ,  $y = b \cdot \Delta y$ ,  $z = c \cdot \Delta z$  if the grid points are  $\Delta x$  spaced in the  $x$  direction and so on. The Crank-Nicholson scheme

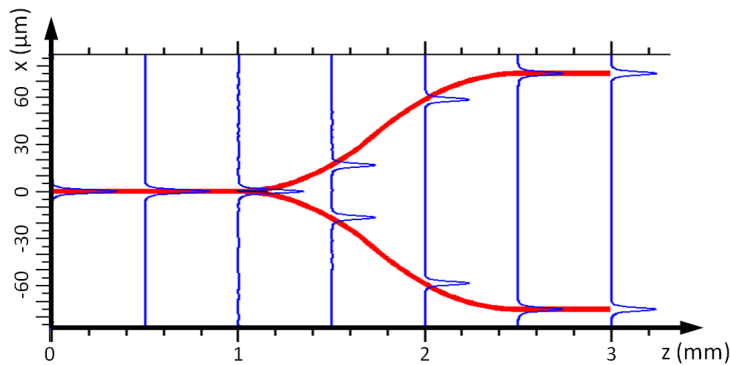


**Figure 4.6:** Screenshot of a 2D BPM simulation of a 1.5 mm long Y-branch made from 2.4  $\mu\text{m}$  wide waveguides. The cross section of the waveguide is given in Fig. 4.5b). The wavelength in this simulation is 1.31  $\mu\text{m}$ .

is an implicit numerical method that estimates the finite differences for the calculation of the fields in the next  $z$ -step as an average of the finite differences in the current  $z$ -step and the next  $z$ -step. Implicit numerical integration schemes tend to be more stable than their explicit counterparts. Given an input field  $u(a, b, 0)$ , step by step  $u(a, b, c)$  can be calculated for  $c = 1, 2, 3, \dots$ . Most BPM software packages rely on transparent boundary conditions[160] that allow radiational fields to radiate away from the simulation domain with negligible reflections on the domain boundaries. During the computation, only the fields of the current  $z$ -step (which is only a 2D array of data) must be stored for the calculation of the next  $z$ -step, which allows also for 3D BPM simulations on standard computers. This is a main advantage compared to the FDTD method as described in section 4.2.4. Depending on the geometry,  $\Delta z$  can in many cases be much larger than the wavelength, which allows for long propagation distances without the need for increased computational power.

A lot of extensions have been proposed for the BPM to overcome its limitations. To take polarization effects into account, semi-vector and full-vector BPMs[161, 162] have been introduced that allow for the simulation of all kinds of polarization effects at the price of higher memory requirements and longer simulation times. Another example is the so called wide-angle BPM [163] that eases the paraxiality condition of the basic BPM and enables the simulation of fields propagating in a larger angle to the  $z$ -axis. The modeling of reflections was successfully shown by introducing a bidirectional BPM[164].

## Simulation results

The Y-branches are important elements of the MZI and a proper design is necessary for good performance of the MZI. The Y-branch at the beginning of the MZI acts as a beam splitter. Due to its symmetrical design, it splits the incoming light to same parts into both outgoing waveguides. See Fig. 4.6 for a 2D BPM simulation of such a Y-branch. At the output of the MZI, the Y-branch is a combining element that is sensitive to the relative phase of the two incident modes. If two modes with the same phase, the same wavelength and the same amplitude are launched into the output Y-branch, the power of the two modes is combined at the end of the Y-branch. This is the reciprocal case of the Y-branch as beam splitter. If two modes with a phase difference of  $\pi$  are injected to the Y-branch, they excite higher order modes, which will then radiate away when the waveguide becomes narrower and shows single mode behavior again[31]. These two cases are depicted in Fig. 4.7. Any other case with a different phase difference can be seen as a superposition of these two fundamental examples.

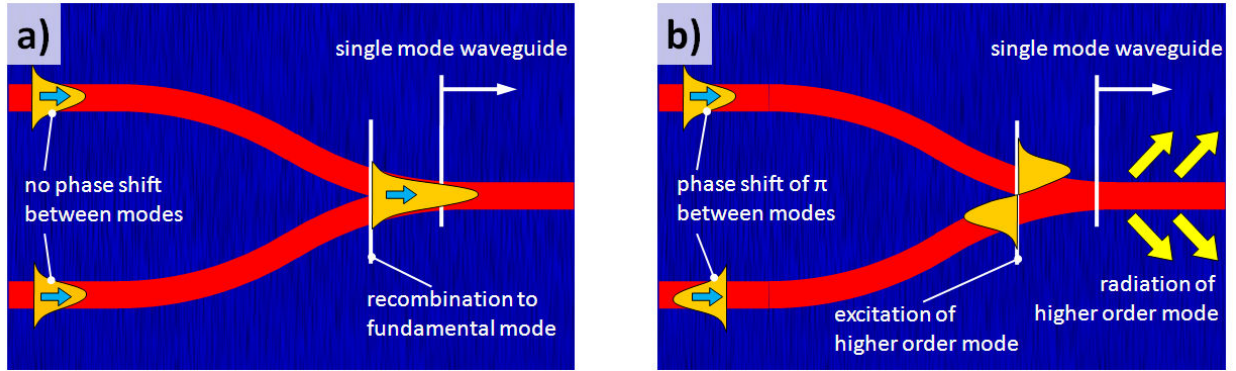


**Figure 4.7:** Two examples of the behavior of light in a combining Y-branch. In **a)** two modes with no phase difference between them are injected into the Y-branch and recombine at the end, whereas in **b)** a phase difference of  $\pi$  between the two modes leads to excitation of higher order modes, which then radiate away.

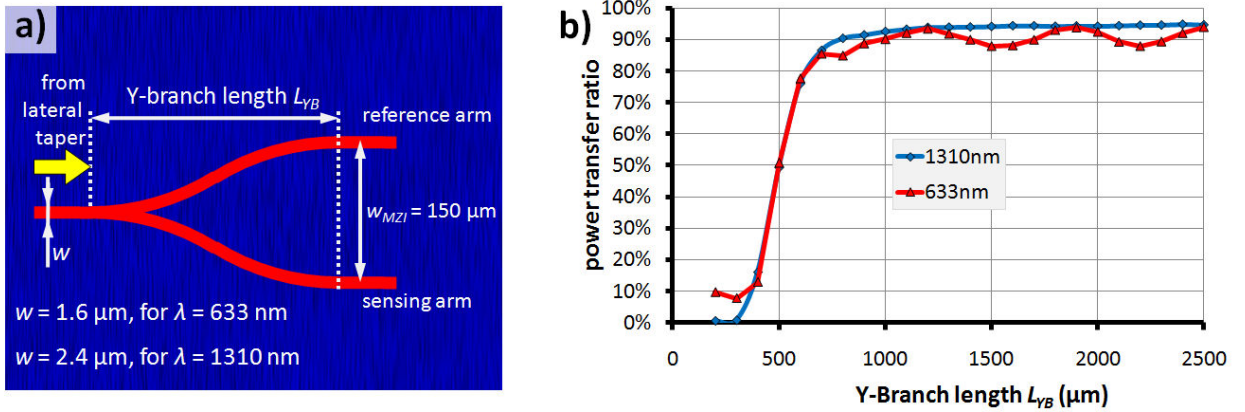


**Figure 4.8:** **a)** Shows the simulated Y-branch and **b)** the simulation results for Y-branches made from single mode waveguides as a function of the length of the Y-branch for  $\lambda = 1.31 \mu\text{m}$  and  $\lambda = 633 \text{ nm}$  obtained by 3D-BPM Simulation.

The Y-branches were designed using 3D BPM. They are composed of four identical arc waveguides with maximum radii allowed by the length of the Y-branch  $L_{LB}$  and the spacing  $w_{MZI}$  to minimize losses in the waveguide bends. The waveguide cross sections are adapted to the wavelength corresponding to the cross sections given in Fig. 4.5. The spacing between the two arms of the MZI was set to  $w_{MZI} = 150 \mu\text{m}$  for both wavelength to prevent crosstalk and allow for separation of the measurement and reference arm during the functionalization procedure.

Figure 4.8a) graphically summarizes the simulations parameters and Fig. 4.8b) plots the calculated power transfer ratio of the Y-branches as function of the Y-branch length  $L_{YB}$ , which is the main design parameter. On the basis of these results the length of the Y-branches are chosen as  $L_{YB} = 2500 \mu\text{m}$  and  $L_{YB} = 2000 \mu\text{m}$  for a wavelength of  $1310 \text{ nm}$  and  $633 \text{ nm}$ , respectively, to ensure efficient and reliable operation. The chosen Y-branch lengths result in bending radii of the waveguides of  $r_{YB} = 13.35 \text{ cm}$  for  $\lambda = 633 \text{ nm}$  and  $r_{YB} = 20.85 \text{ cm}$  for  $\lambda = 1310 \text{ nm}$  respectively.

### 4.2.3 Lateral tapers

#### Theory

In straight waveguides, all waveguide modes propagate independently. If the waveguide cross section changes as function of  $z$ , as is the case in taper structures, coupling between these modes occurs. Based on the coupled mode theory, the coupling coefficient  $C_{ab}$  between two waveguide modes with the mode numbers  $a$  and  $b$  can be defined as[165]

$$C_{ab}(z) = \frac{k_0}{4} \left[ \frac{\epsilon_0}{\mu_0} \right]^{1/2} \frac{1}{\beta_a(z) - \beta_b(z)} \int \vec{E}_a^*(x, y, z) \cdot \vec{E}_b(x, y, z) \frac{\partial n(x, y, z)^2}{\partial z} dx dy \quad (4.9)$$

where  $\beta_a(z)$  and  $\beta_b(z)$  are the propagation constants of the interacting waveguide modes with the mode fields  $\vec{E}_a(x, y, z)$  and  $\vec{E}_b(x, y, z)$ . The geometry of the taper structure is given by the 3D refractive index profile  $n(x, y, z)$ . The coupling coefficient  $C_{ab}$  gives the degree of coupling between the  $a$ -th and the  $b$ -th waveguide mode as function of  $z$ . To calculate the total amount of energy that is coupled from one mode to another,  $C_{ab}$  has to be integrated along the length of the taper  $L_T$ [46]:

$$\kappa_{ab} = \left| \int_0^{L_T} C_{ab}(z) e^{i\overline{\delta\beta}z} dz \right|^2 \quad (4.10)$$

In this equation,  $\overline{\delta\beta}$  is the average accumulated difference in propagation constants. The total power loss of the fundamental mode during propagation through the taper is given by  $\sum_{b=1}^{\infty} \kappa_{0b}$ . In regions where the coefficients  $C_{ab}$  are small, the waveguide cross section can be varied quickly without introducing too much mode coupling, while in regions where the coupling coefficients are large, only gradual changes of the waveguide cross sections can prevent strong mode coupling. For rib and wire waveguides, mode coupling between even and odd modes is very low due to the fact that even modes have a symmetric and odd modes an anti-symmetric mode profile, thus the integral  $\int \vec{E}_a^*(x, y, z) \cdot \vec{E}_b(x, y, z) dx dy$  gives zero. Adiabatic tapers are defined as tapers that vary the waveguide cross section so slowly that mode coupling can be neglected. For lateral tapers, as presented in the next section, it can be said that in general that mode coupling becomes the stronger, the wider the taper becomes. Due to the fact that the propagation constants of lateral higher order modes are very similar in wide waveguides,  $\frac{1}{\beta_a(z) - \beta_b(z)}$  becomes very large. Therefore, adiabatic tapering is not possible if the width of a lateral taper exceeds a certain value, which is in agreement with the simulation results presented below. This theory, as shown here, is not suitable to analytically describe the behavior of tapers or to give design rules. Nevertheless, this very short introduction to mode coupling in taper structures is presented to give insight into the basic mechanisms of how tapers work and to allow the interpretation of the simulation results later on.

#### Simulation results

Simulations were performed using 2D-BPM (see section 4.2.2) for lateral tapers of different lengths. These linear tapers are used to reduce the width of the waveguides after the gratings to the width of the single mode waveguides. Tapers for a wavelength of 1.31  $\mu\text{m}$  and 633 nm were simulated and the waveguide core layer thickness, the etch depth of the waveguides as well as the width of the single mode waveguides were adapted to the wavelength corresponding to the cross sections presented in

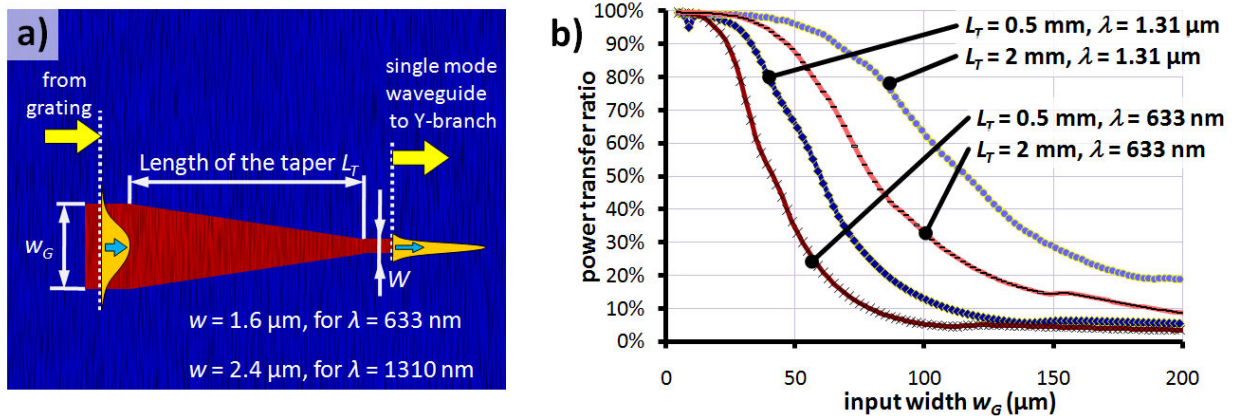


**Figure 4.9:** a) Taper structure and b), corresponding power transfer ratio as function of the input width  $w_G$  of tapers for different length, calculated using 2D-BPM for wavelength of 633 nm and 1310 nm.

Fig. 4.5. The results of these simulations are presented in Fig. 4.9b) for several taper lengths  $L$  as function of the input width of the taper. As expected, the power transfer ratio, defined as the ratio between the power of the fundamental mode at the beginning of the taper and the remaining power in the single mode waveguide, of tapers decreases with the input width. For small input widths, the tapers show adiabatic behavior and nearly all of the energy remains in the fundamental mode, the size of which is slowly decreased as the light propagates through the taper. If the taper input width exceeds a certain value, a considerable amount of optical power is coupled to higher order modes, which are gradually radiated away as the taper becomes narrower. Surprisingly, this cannot be overcome by increasing the length of the taper. Even when comparing tapers with the same slope, for example a taper with  $L = 0.5 \text{ mm}$  and  $w_G = 50 \mu\text{m}$  compared to a taper with  $L = 2 \text{ mm}$  and  $w_G = 200 \mu\text{m}$ , the longer taper with the larger input width shows a much weaker performance. However, this counter-intuitive behavior of tapers can be explained in the context of the theory presented above. For very wide waveguides, the propagation constants of the waveguide modes are very close. This induces strong coupling between these modes, which explains why this nonlinear relationship cannot be overcome by increasing the length or by adjusting the shape of the taper[46]. The simulation results for the tapers indicate that for 2 mm long lateral tapers the input width should not exceed  $50 \mu\text{m}$ . Since the input width of the taper defines the diameter of the incident beam on the grating, a grating width of  $30 \mu\text{m}$  is chosen in order to guarantee efficient lateral tapering into single mode waveguides.

This interesting behavior of lateral tapers was further investigated for several material systems, ranging from high index contrast SOI to low index contrast polymer waveguide systems as well as for two different waveguide structures. The first waveguide structure is a single mode rib waveguide, where the thicknesses of the waveguides are optimized for surface sensing for each material system, similar to the waveguides presented in section 4.2.1. The second waveguide type is a single mode wire waveguide with typical dimensions for the particular material system. The length of the tapers is fixed at 1 mm for these simulations. Unlike the simulations above, the substrate and the cladding in these simulations were assumed to be made of silicon dioxide with a refractive index of 1.46. The geometric parameters of all the simulated waveguide cross sections are summarized in Table 4.1. Within these simulations, the wavelength was set to  $1.55 \mu\text{m}$ . One might expect that due to the stronger lateral confinement, especially in material systems with a high refractive index difference, tapers with large input widths show better performance than in systems with a small index difference. However, the simulations as presented in Fig. 4.10 show a different picture. First of all, the most important conclusion of these

**Table 4.1:** Summary of the parameters refractive index of the waveguide core layer  $n_{wg}$ , waveguide thickness  $H$ , etch depth  $e$ , and width  $w$  of single mode rib- and wire-type waveguides used in the taper simulations shown in Fig. 4.10.

waveguide type	$n_{wg}$	$H$	$w$	$e$
silicon (Si) rib-waveguide	3.48	60 nm	1 $\mu\text{m}$	15 nm
silicon nitride (SiN) rib-waveguide	2.0	185 nm	1.8 $\mu\text{m}$	55 nm
SU-8 rib-waveguide	1.58	530 nm	2.5 $\mu\text{m}$	250 nm
polymer A rib-waveguide	1.50	1150 nm	4 $\mu\text{m}$	500 nm
polymer B rib-waveguide	1.48	1800 nm	6 $\mu\text{m}$	900 nm
silicon (Si) wire-waveguide	3.48	400 nm	400 nm	
silicon nitride (SiN) wire-waveguide	2.0	600 nm	600 nm	
SU-8 wire-waveguide	1.58	1.6 $\mu\text{m}$	1.6 $\mu\text{m}$	
polymer A wire-waveguide	1.50	2.5 $\mu\text{m}$	2.5 $\mu\text{m}$	
polymer B wire-waveguide	1.48	4 $\mu\text{m}$	4 $\mu\text{m}$	

simulations is that irrespective of the material system and the waveguide geometry, the taper efficiency drops significantly for input widths larger than about 50  $\mu\text{m}$ . All the tapers showed more or less the same performance. Another interesting aspect is the fact that in these simulations the tapers in the high index difference material systems (Si and SiN) showed the worst performance. It can be interpreted that the high optical input width, defined as  $w_G \cdot n_{wg}$ , for high refractive index has a stronger influence on the taper efficiency than the better lateral confinement.

The results of this investigation further reinforce the statement that efficient lateral tapering into single mode waveguides is basically independent of the type of the waveguide, the specific waveguide cross section and the materials used. As a rule of thumb, it can be said that efficient lateral tapering into single mode waveguides is not possible for input width larger than about 50  $\mu\text{m}$ .

#### 4.2.4 Grating couplers

##### Theory for grating output couplers

This section provides the basic definitions and relations that are necessary for the interpretation of the simulation results given in this section. It introduces the optimum spot size of a grating as an intuitive parameter that allows for a fast estimation of the optimum coupling configuration of a grating. The coupling strength  $\alpha$  of a grating defines the amount of optical power that is radiated away from the

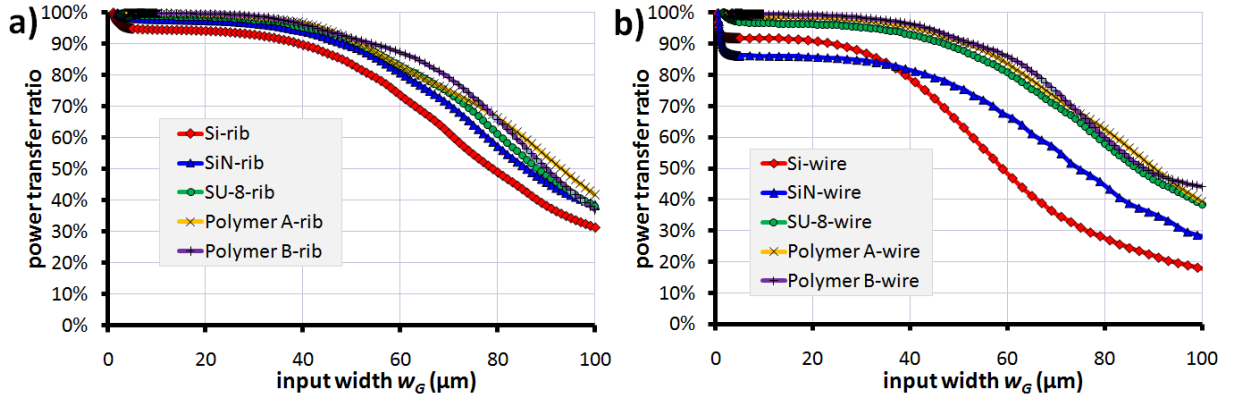


**Figure 4.10:** Simulation results for 1 mm long linear lateral tapers made from **a)** rib-type waveguides and **b)** wire-type waveguides in several material systems as function of the input width of the taper ( $\lambda = 1.55 \mu\text{m}$ ). The geometrical parameters of the waveguides are summarized in Table 4.1.

guided mode per unit length[166]. The coupling strength is linked to the imaginary part of the effective index  $\kappa$  of the waveguide mode in the grating region via  $\alpha = 2\pi\kappa/\lambda_0$ . The field distribution  $A(x, y, z)$  of the major field component of a waveguide mode propagating in a slab waveguide in positive  $z$ -direction can be defined as

$$A(x, y, z) = A_0 \tilde{A}(y) e^{i(\omega t - kz)} \quad (4.11)$$

where  $\tilde{A}(y)$  is the vertical mode profile,  $A_0$  a scalar that scales the amplitude, and  $k$  the norm of the wave vector. The wave vector points in  $z$ -direction and its norm is defined as  $k = 2\pi n_{eff}/\lambda_0$ , where  $\lambda_0$  is the free space wavelength and  $n_{eff}$  the effective index of the guided mode. The optical power  $P$  guided in this mode remains constant as long as the mode propagates in the slab waveguide. When entering an output grating, as illustrated in Fig. 4.11, a certain part of the energy of the guided mode is diffracted per unit length into several diffraction orders. If all incorporated materials are loss less, this can be expressed as a differential equation[167] for the power of the guided mode

$$\frac{dP(z)}{dz} = - \sum_m 2\alpha_m^c P(z) - \sum_m 2\alpha_m^s P(z) \quad z = [0, \infty] \quad (4.12)$$

or the amplitude of the guided mode

$$\frac{dA(z)}{dz} = - \sum_m \alpha_m^c A(z) - \sum_m \alpha_m^s A(z) \quad z = [0, \infty] \quad (4.13)$$

In these equations,  $\alpha_m^c$  and  $\alpha_m^s$  indicate the amount of energy that is diffracted into the  $m$ -th diffraction order into the cladding and the substrate, respectively. With the coupling strength  $\alpha$  of the grating defined as  $\alpha = \sum_m \alpha_m^c + \sum_m \alpha_m^s$ , these equations can be written as

$$\frac{dP(z)}{dz} = -2\alpha P(z) \quad \text{and} \quad \frac{dA(z)}{dz} = -\alpha A(z) \quad z = [0, \infty] \quad (4.14)$$



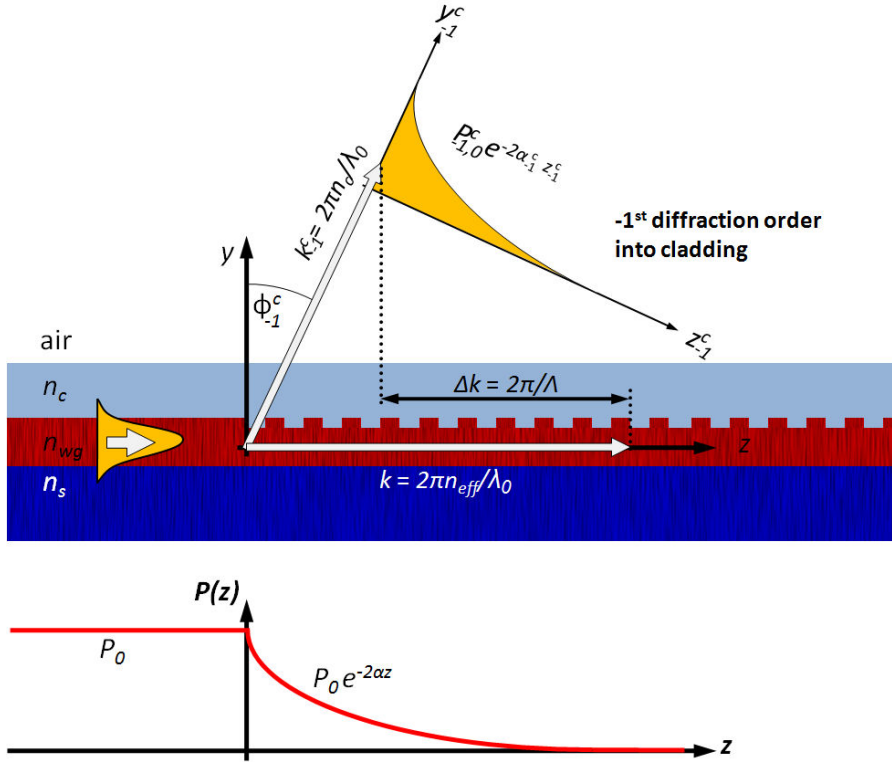


**Figure 4.11:** A grating output coupler that diffracts light into the -1st diffraction order; the graph below plots the optical power guided in the waveguide along  $z$ -direction.

The solution to these simple differential equations in the region  $z = [0, \infty]$  for the boundary conditions  $P(z = 0) = P_0$  and  $A(z = 0) = A_0$  is well known to be the exponentially decaying function. Therefore, the amplitude  $A$  and the power  $P$  of the guided mode decrease exponentially in  $z$ -direction in the following way[13, 168]:

$$A(z) = A_0 e^{-\alpha z} \quad z = [0, \infty] \quad (4.15)$$

$$P(z) = P_0 e^{-2\alpha z} \quad z = [0, \infty] \quad (4.16)$$

The light of the guided mode is diffracted into several diffraction orders. These diffraction orders share the same exponentially decaying profile along  $z$ -direction as the guided waveguide mode in the grating region[168]. The wave vectors of the diffraction orders are linked with the wave vector of the guided mode via the well-known grating equation (e.g. [65, 66, 169, 170])

$$k_{m,z}^{s/c} = k + m\Delta k \quad (4.17)$$

where  $k_{m,z}^{s/c}$  is the  $z$ -component of the wave vector of the  $m$ -th diffraction order. The grating vector is defined as  $\Delta k = 2\pi/\Lambda$ , where  $\Lambda$  is the period of the grating. The superscript denotes whether the diffraction order radiates into the cladding ( $c$ ) or into the substrate ( $s$ ). The length of the wave vectors  $k^{s/c} = 2\pi n_{s/c}/\lambda_0$  depends on the refractive index of the material the diffracted light is propagating

in. After calculating  $k_{m,z}^{s/c}$ , the out-coupling angle of the diffraction orders can be determined using  $\sin \phi_m^{s/c} = k_{m,z}^{s/c}/k^{s/c}$ . The number of diffraction orders depends on the grating period and on the refractive indices of the substrate and the cladding. If the grating is long enough to diffract all energy from the guided mode into the diffraction orders, the total power that is carried by each diffraction order  $P_{m,tot}^{s/c}$  is defined as

$$P_{m,tot}^{s/c} = P_0 \frac{\alpha_m^{s/c}}{\alpha} \quad (4.18)$$

Hence,  $\int_0^\infty e^{-2\alpha z} dz = 1/2\alpha$ ,  $P_{m,0}^{s/c}$  can be calculated the following way:

$$P_{m,tot}^{s/c} = P_0 \frac{\alpha_m}{\alpha} = P_{m,0}^{s/c} \int_0^\infty e^{-2\alpha z} dz = \frac{P_{m,0}^{s/c}}{2\alpha} \quad (4.19)$$

From this equation and from  $P_{m,0}^{s/c} = (A_{m,0}^{s/c})^2$  it follows that

$$P_{m,0}^{s/c} = 2\alpha_m^{s/c} P_0 \quad \text{and} \quad A_{m,0}^{s/c}(z) = \sqrt{2\alpha_m^{s/c}} A_0 \quad (4.20)$$

For shorter gratings analogous considerations can be done by replacing  $P_0$  with the amount of diffracted power in the short grating.

If the materials used are not loss less, absorption can be accounted for by introducing an additional term in equation (4.12):

$$\frac{dP(z)}{dz} = - \sum_m 2\alpha_m^c P(z) - \sum_m 2\alpha_m^s P(z) - 2\alpha_{abs} P(z) \quad z = [0, \infty] \quad (4.21)$$

$$\frac{dA(z)}{dz} = - \sum_m \alpha_m^c A(z) - \sum_m \alpha_m^s A(z) - \alpha_{abs} A(z) \quad z = [0, \infty] \quad (4.22)$$

All equations remain valid if  $\alpha$  is now defined as  $\alpha = \sum_m \alpha_m^c + \sum_m \alpha_m^s + \alpha_{abs}$ . It is to bear in mind that if absorption takes place, the total amount of diffracted power is not equal to the incident power from the guided mode, because the part  $P_{abs} = P_0 \frac{\alpha_{abs}}{\alpha}$  is lost in absorption.

In the case of coupling light out of a waveguide, the amplitude profile of the radiated beams is often of no relevance because large photodiodes directly attached on top of the grating can be used to collect all the light radiated away from the grating in the direction of the photodiode. The grating simply has to be made long enough ( $2\alpha z \gg 1$ ) so that all power can radiate away from the waveguide.

Most types of gratings, including simple binary grating couplers, diffract the guided light at approximately equal amounts into the substrate and the cladding. Therefore, if the grating is sufficiently long, an out-coupling efficiency of about 50% can be achieved. If a perfect mirror is applied to one side of the grating, the light radiating away in the opposite direction is reflected and the out-coupling efficiency can theoretically be increased to 100%.

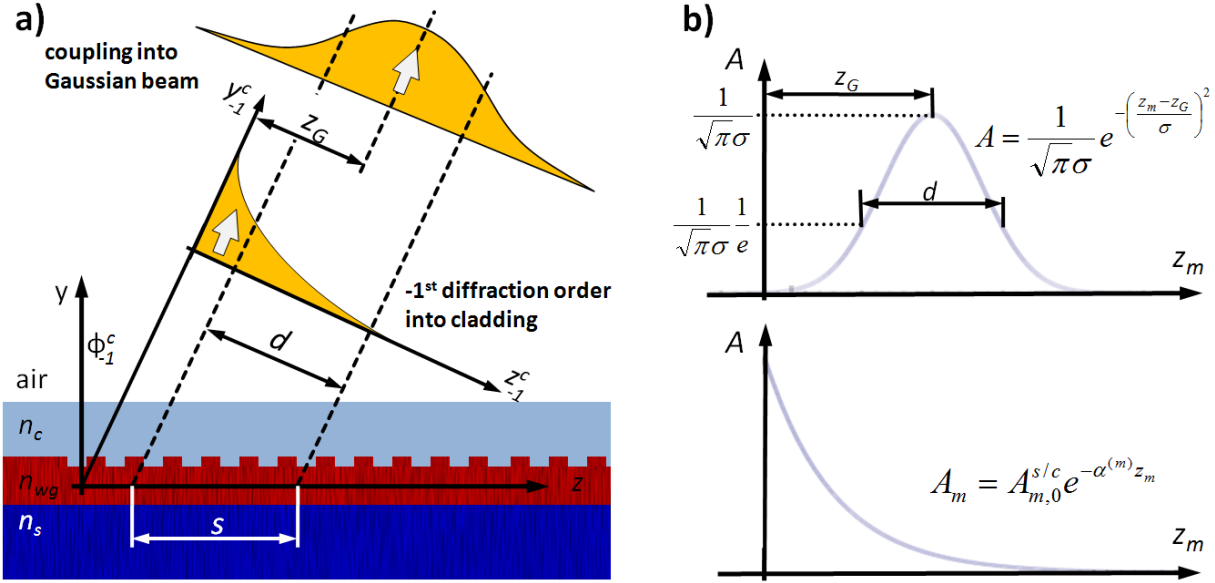


**Figure 4.12:** **a)** Situation for the output grating coupler when coupling the -1st diffraction order in direction of the cladding into a Gaussian beam. The offset  $z_G$ , the beam diameter  $d$  and the spot size  $s$  of the Gaussian beam are shown. The spot size of the beam on the grating is  $s = d / \cos \phi_{-1}^c$ . **b)** Definitions of a Gaussian beam and of the amplitude profile of the light diffracted into the  $i$ -th order.

However, if the diffracted light should be coupled into an optical fiber by means of a focusing element, only the light from one specific diffraction order can be coupled into the optical fiber. An overlap integral between the exponentially shaped amplitude profile of the diffracted light and the Gaussian beam shape, necessary for the coupling into an optical fiber defines the conversion efficiency. This overlap integral is given by[171]

$$\eta = \left[ \frac{4\beta_1\beta_2}{(\beta_1 + \beta_2)^2} \right] \frac{[\int A_1(x, z)A_2^*(x, z)dx dz]^2}{\int A_1(x, z)A_1^*(x, z)dx dz \int A_2(x, z)A_2^*(x, z)dx dz} \quad (4.23)$$

where  $A_1(x, z)$  and  $A_2(x, z)$  are the amplitude profiles and  $\beta_1$  and  $\beta_2$  are the propagation constants of the two overlapping modes. This overlap integral has to be carried out in a rotated coordinate system  $[x_m^{s/c}, y_m^{s/c}, z_m^{s/c}]$ , as depicted in Fig. 4.12a) that is aligned to the propagation direction of the diffraction order. The parameters  $\alpha$  and  $P_{m,0}^{s/c}$ , which determine the amplitude profile of the diffracted light, have to be adapted to the rotated coordinate system of the diffraction order, so that

$$\alpha^{(m)} = \frac{\alpha}{\cos \phi_m} \quad \text{and} \quad P_{m,0}^{(m),s/c} = \frac{P_{m,0}^{s/c}}{\cos \phi_m} \quad (4.24)$$

The superscript  $(m)$  denotes a variable in a coordinate system aligned to the  $m$ -th diffraction order. The law of energy conservation has to be fulfilled during this transformation.

$$P_{m,tot}^{(m),s/c} = P_{m,0}^{(m),s/c} \int_0^\infty e^{-2\alpha^{(m)}z_m} dz_m = \frac{P_{m,0}^{(m),s/c}}{2\alpha^{(m)}} = \frac{P_{m,0}^{s/c} \cos \phi_m}{2\alpha} = \frac{P_{m,0}^{s/c}}{2\alpha} = P_{m,tot}^{s/c} \quad (4.25)$$

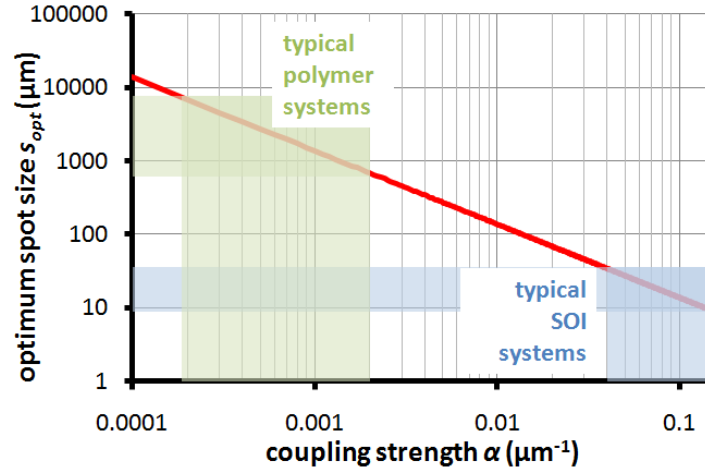


**Figure 4.13:** Relationship between coupling strength and optimum spot size; typical regions for SOI and for polymer waveguide systems are indicated.

In these equations,  $\phi_m$  is the angle of the diffraction order in the media where the coupling takes place. Even if the refractive indices of the substrate and the cladding are different, the coupling usually takes place in air, which is why  $\alpha_m$  does not depend on the diffraction order radiating into either the substrate or the cladding. The overlap integral between an amplitude profile of a Gaussian beam and an exponentially decreasing amplitude profile, as depicted in Fig. 4.12b), was numerically optimized and the following relations for optimum conversion were obtained[172]

$$\alpha_m d = 1.36756 \quad (4.26)$$

$$d/z_G = 1.46244 \quad (4.27)$$

The maximum conversion efficiency for these two types of amplitude profiles is nearly 80.1%[173] if equations (4.26) and (4.27) are satisfied. If it is assured that the optical fiber and optional optical elements are perfectly aligned to the propagation direction of the diffraction order, the out-coupling efficiency can be calculated as the percentage of optical power diffracted into the desired diffraction order times the conversion efficiency given by the overlap integral. In the case, where only two diffraction orders are present, one into the substrate and one into the cladding, and both are carrying approximately the same amount of power, the maximum achievable coupling efficiency is about 40% to Gaussian beams.

If optimum coupling conditions are maintained, the spot size  $s$  of the Gaussian beam on the grating, as shown in Fig. 4.12a), is defined by  $s = d / \cos \phi_m$ . Employing this definition and  $\alpha_m = \alpha / \cos \phi_m$ , equation (4.26) can be rewritten to give a relation between the optimum spot size  $s_{opt}$  of a Gaussian beam and the coupling strength  $\alpha$  of the grating independent on the angle and order of diffraction[174]

$$\alpha s_{opt} = 1.36756 \quad (4.28)$$

This very simple relationship between optimum spot size and coupling strength is plotted in Fig. 4.13 with some additional information about expected values for different material systems.

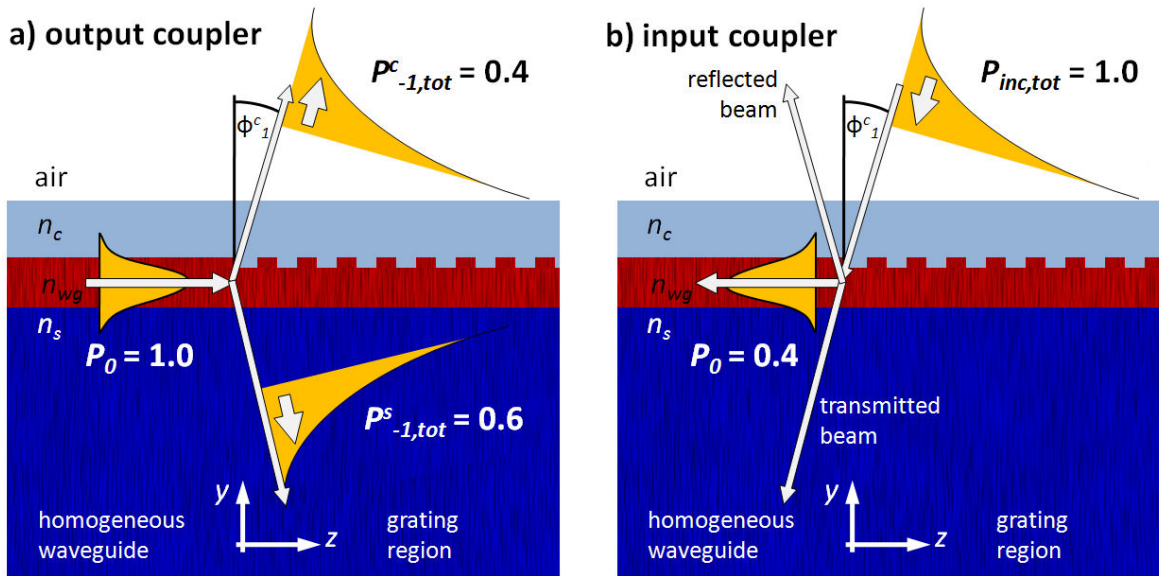


**Figure 4.14:** Simple example for the reciprocity theorem between output and input grating couplers. If the angle and the mode profile are preserved, the input coupler has the same efficiency as the corresponding output coupler. The reciprocity theorem makes no statement about the power in the transmitted and reflected beam in the case of the input coupler.

### Relation between input and output grating couplers

Input grating couplers and output grating couplers are linked by a reciprocity theorem[34, 169], which can be directly derived from Maxwell's equations. The reciprocity theorem states that if the exact mode profile and the angle of the beam is preserved, a grating coupler used for in-coupling has the same efficiency as the corresponding output coupler. An efficient output coupler is also an efficient input coupler for the same beam. Figure 4.14 shows a simple example for the application of the reciprocity theorem for grating couplers with one diffraction order into the cladding and the substrate. Therefore, all arguments that lead to equation (4.28) for output couplers are valid for input couplers as well. Thus, equation (4.28) is also valid for input couplers. It introduces the spot size of a grating as an important and intuitive parameter of a grating structure and allows for a fast and easy estimation of the optimum beam diameter.

### Simulation methods

Most simulations of grating couplers were carried out with the simulation tool Grinco, which was developed in the IT department of AIT. Grinco is an acronym for **g**rating **i**nput **c**oupler. This tool employs a rigorous Floquet-Bloch (FB) approach[175, 176, 177] to calculate the input coupling efficiency of waveguide grating couplers. In the current version, Grinco is restricted to 2D geometries.

The underlying theory of the FB approach, as summarized here, was published in 1999 in the paper by Norman Finger and Erich Gornik[175]. Norman Finger was the main developer of the simulation tool Grinco. The FB approach utilized in Grinco assumes an infinite long grating structure. The grating structure is described by a set of horizontal layers (see Fig. 4.15). Each layer  $j$  is either a uniform or a periodic layer. In principle, there is no limitation to the number of layers and also periodic and

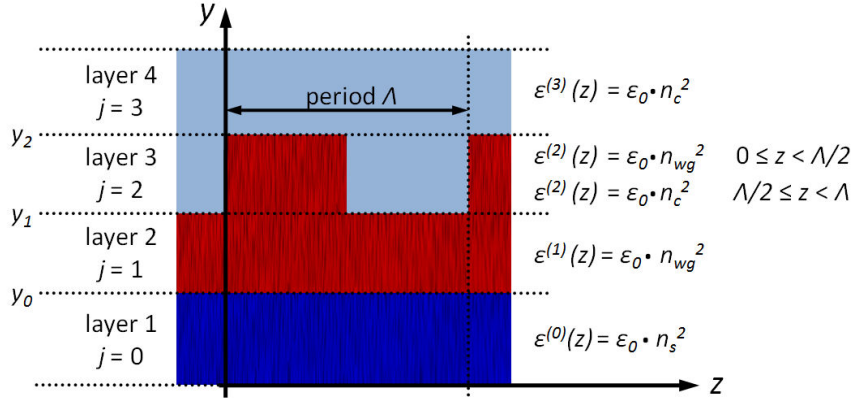


**Figure 4.15:** Schematic for the description of binary grating structures in the simulation tool Grinco. The grating is described as a set of horizontal layers. Within each layer, the dielectric permittivity depends on  $z$  only.

homogeneous layers can be arranged in any order. Due to the periodicity of the structure, the dielectric permittivity  $\epsilon^{(j)}(z)$  of the  $j$ -th layer can be expanded in a Fourier series of the grating vector  $\Delta k = 2\pi/\Lambda$ , where  $\Lambda$  is the period of the grating.

$$\epsilon^{(j)}(z) = \tilde{\epsilon}_0^{(j)} + \sum_{m=\pm 1, \pm 2, \dots} \tilde{\epsilon}_m^{(j)} e^{im\Delta kz} \quad (4.29)$$

For each layer, the dielectric permittivity has to be independent of  $y$ . For non-corrugated layers all  $\tilde{\epsilon}_m^{(j)}$  are zero except for  $\tilde{\epsilon}_0^{(j)}$ . Complicated grating structures such as slanted gratings or gratings with a saw tooth profile can be step-wise approximated by many thin layers. Floquet's theorem states that in periodic structures the electric field in every layer can be expressed as

$$E^{(j)}(y, z) = e^{i\beta_0 z} \sum_{m=0, \pm 1, \pm 2, \dots} E_m^{(j)}(y) e^{im\Delta kz} = \sum_{m=0, \pm 1, \pm 2, \dots} E_m^{(j)}(y) e^{i\beta_m z} \quad (4.30)$$

with  $\beta_m = \beta_0 + m\Delta k$ , where  $\beta_0$  is the complex propagation constant and a time dependence of  $e^{-i\omega t}$  for the electric field is implied. The 2D Helmholtz equation (see equation (4.2) in section 4.2.2)

$$\left[ \frac{\partial^2}{\partial y^2} + \frac{\partial^2}{\partial z^2} + k_0^2 \epsilon^{(j)}(z) \right] E(y, z) = 0 \quad (4.31)$$

has to be satisfied for each layer. Inserting equations (4.29) and (4.30) into equation (4.31) leads to an infinite set of coupled equations for the partial waves  $E_m^{(j)}(y)$  for each layer  $j$ .

$$\frac{d^2 E_m^{(j)}(y)}{dy^2} = \sum_{m=0, \pm 1, \pm 2, \dots} \left[ \delta_{mq} \beta_q^2 - k_0^2 \|\tilde{\epsilon}^{(j)}\|_{mq} \right] E_q^{(j)}(y) \quad (4.32)$$

In this equation,  $\delta_{qm}$  is the Kronecker-delta and  $\|\tilde{\epsilon}^{(j)}\|_{mq}$  is a matrix with

$$\|\tilde{\epsilon}^{(j)}\|_{mq} = \tilde{\epsilon}_{m-q}^{(j)} \quad (4.33)$$

The ansatz of complex exponential functions for the fields in each layer

$$E_m^{(j)}(y) = C_m^{(j)} e^{i\gamma^{(j)}y} \quad (4.34)$$

transforms the set of coupled equations into the eigenvalue problem

$$\sum_{q=-\infty}^{\infty} \left[ \delta_{mq} \beta_q^2 - k_0^2 \|\tilde{\epsilon}^{(j)}\|_{mq} \right] C_q^{(j)} = -[\gamma^{(j)}]^2 C_m^{(j)} \quad (4.35)$$

The eigenvalues  $[\gamma^{(j)}]^2$  and eigenvectors  $C_{ml}^{(j)}$  of this eigenvalue problem are related to the grating eigenfunctions

$$X_l^{(j)}(z) = \sum_m C_{ml}^{(j)} e^{i\beta_m z} \quad (4.36)$$

The electric field in every layer can be expanded in terms of these grating eigenfunctions in the following way:

$$E^{(j)}(y, z) = \sum_l \left[ A_l^{(j)} e^{i\gamma_l^{(j)}y} + B_l^{(j)} e^{-i\gamma_l^{(j)}y} \right] X_l^{(j)}(z) \quad (4.37)$$

where  $A_l^{(j)}$  and  $B_l^{(j)}$  are amplitude coefficients for waves propagating in the positive and negative  $y$ -direction. By using equation (4.36) and (4.30) the expression

$$E_m^{(j)}(y) = \sum_l C_{ml}^{(j)} \left[ A_l^{(j)} e^{i\gamma_l^{(j)}y} + B_l^{(j)} e^{-i\gamma_l^{(j)}y} \right] \quad (4.38)$$

is obtained for the partial waves of the electric field. For homogeneous layers, this expression can be further simplified due to the fact that only the zeroth Fourier component of the dielectric field  $\tilde{\epsilon}_0^{(j)}$  is unequal to zero. For numerical computations, the infinite set of partial waves is truncated to a finite set with  $m = -T, \dots, -1, 0, 1, \dots, T$ , where  $T$  is the truncation order. This gives a set of  $M = 2T + 1$  partial waves and the eigenvalue problem (4.35) is represented by a  $M \times M$  matrix and yields  $M$  eigenvalues and eigenvectors. The index  $l$ , labeling the grating eigenvalues, runs also from  $-T$  to  $T$ . It has to be noticed that  $A_l^{(0)}$  and  $B_l^{(S)}$ , where  $S$  is the number of layers, are known. These coefficients correspond to waves traveling towards the inside of the grating structure in the outer layers. They are usually set to zero, except when modeling an electromagnetic source with a field that is incident on the grating structure.

At the interfaces of the horizontal layers, the parallel field components  $E_x$  (represented here by  $E$ , because the major field of TE modes points in the  $x$  direction) and  $H_z$  as well as the tangential field component  $B_y$  have to be continuous. The even stricter criterion that for each partial wave  $E_m(x)$  and  $dE_m(x)/dy$  must be continuous ensures the continuity of the parallel and tangential field components. Matching the boundary conditions

$$E_m^{(j)}(y_j) = E_m^{(j+1)}(y_j) \quad (4.39)$$

$$\left. \frac{dE_m^{(j)}(y)}{dy} \right|_{y=y_j} = \left. \frac{dE_m^{(j+1)}(y)}{dy} \right|_{y=y_j} \quad (4.40)$$



gives a set of  $2SM$  equations for  $2SM$  unknown coefficients  $A_l^{(j)}$  and  $B_l^{(j)}$ . These boundary conditions can be written in the form of a matrix equation

$$\|F\|\vec{a} = 0 \quad (4.41)$$

with the coefficients arranged in a  $2SM$  sized vector

$$\vec{a} = (\vec{B}^{(0)}, \vec{A}^{(1)}, \vec{B}^{(1)}, \dots, \vec{A}^{(S-1)}, \vec{B}^{(S-1)}, \vec{A}^{(S)}) \quad (4.42)$$

where  $\vec{A}^{(j)}$  and  $\vec{B}^{(j)}$  are  $M$  sized vectors with  $\vec{A}^{(j)} = (A_{-T}^{(j)}, \dots, A_T^{(j)})$ . The complex propagation constant  $\beta_0$  is given by the solution of the equation

$$\det[\|F(\beta_0)\|] = 0 \quad (4.43)$$

Once  $\beta_0$  is found, the amplitude coefficients  $A_l^{(j)}$  and  $B_l^{(j)}$  as well as the electric fields  $E_m^{(j)}$  can be calculated. Finding one or more solutions to equation (4.43) is laborious numerical work and the performance of the simulation tool strongly depends on the implementation of the algorithm that searches solutions to this equation. Grinco calculates the fields of the partial waves for a given grating structures and allows for arbitrary incident fields. For the given incident field, the power in the guided mode in the grating region is calculated. The FB approach assumes an infinitely long grating structure. To calculate the input coupling efficiency of a grating coupler, Grinco calculates the power of the guided mode of the infinite grating structure as function of  $z$ . At the interface between the grating section and the unperturbed waveguide, partial waves of the FB modes describing the guided field in the grating region are matched to the modal field distribution of the adjacent unperturbed waveguide. The algorithm based on the FB approach calculates all fields in the grating region as if the grating structure is infinite. In real applications, all gratings are finite. The transition between the grating region and the waveguide region is modeled by a simple overlap integral neglecting all other possible effects that may occur at the end of the grating. For waveguide grating couplers, this model is sufficiently accurate to allow a precise calculation of the coupling efficiency.

The simulations performed with Grinco were extensively compared and benchmarked with finite difference time domain (FDTD) simulations. FDTD simulations are a standard simulation method for designing purposes of photonic structures. The FDTD method is a first order approximation of the Maxwell equations on a discrete grid. It's approximation of Maxwell's equations is both a blessing and a curse. The main advantage of FDTD is that the approximations do not restrict the generality of the simulation method, *i.e.* FDTD makes no assumptions about the underlying geometry. Therefore, it can be used for simulations of any kinds of photonic effects. On the other hand, FDTD simulations are very slow and require a lot of computer memory and computational power. The FDTD algorithm as outlined here and nowadays used is based on a paper by K.S. Yee[178] published in 1966. Within his paper, Yee introduced a numerically very stable and accurate computation scheme, which will be sketched here. The two rotational Maxwell equations are given by (see also equations (2.1) to (2.4) in chapter 2):

$$-\mu \frac{\partial \vec{H}}{\partial t} = \nabla \times \vec{E} \quad (4.44)$$

$$\epsilon \frac{\partial \vec{E}}{\partial t} = \nabla \times \vec{H} - \vec{j}_f \quad (4.45)$$

These two vector equations are abbreviated forms of six scalar equations. As examples the first lines of these two equations are

$$-\mu \frac{\partial H_x}{\partial t} = \frac{\partial E_z}{\partial y} - \frac{\partial E_y}{\partial z} \quad (4.46)$$

$$\epsilon \frac{\partial E_x}{\partial t} = \frac{\partial H_z}{\partial y} - \frac{\partial H_y}{\partial z} - J_{f,x} \quad (4.47)$$

The derivations in all six equations are now replaced by finite differences of the fields on neighboring grid points. Any grid point is characterized by three integers  $a, b, c$  that give the position of the grid point as  $(x, y, z) = (a \cdot \Delta x, b \cdot \Delta y, c \cdot \Delta z)$ . The parameters  $\Delta x, \Delta y, \Delta z$  are the spacings of the grid points in the  $x, y, z$  direction respectively, which are not necessarily equal. In his paper, Yee proposed to define the field components on different grid points within the unit cell of the grid (see Fig. 4.16) and at different time points, which allows for a more accurate modeling of the boundary conditions. By replacing the derivations with finite differences, equations (4.46) and (4.47) become

$$-\mu \frac{H_x^{n+1/2}(a, b + 1/2, c + 1/2) - H_x^{n-1/2}(a, b + 1/2, c + 1/2)}{\Delta t} = \quad (4.48)$$

$$\begin{aligned} &= \frac{E_z^n(a, b + 1, c + 1/2) - E_z^n(a, b, c + 1/2)}{\Delta y} - \\ &\quad - \frac{E_y^n(a, b + 1/2, c + 1) - E_y^n(a, b + 1/2, c)}{\Delta z} \\ \epsilon \frac{E_x^n(a + 1/2, b, c) - E_x^{n-1}(a + 1/2, b, c)}{\Delta t} &= \quad (4.49) \\ &= \frac{H_z^{n-1/2}(a + 1/2, b + 1/2, c) - H_z^{n-1/2}(a + 1/2, b - 1/2, c)}{\Delta y} - \\ &\quad - \frac{H_y^{n-1/2}(a + 1/2, b, c + 1/2) - H_y^{n-1/2}(a + 1/2, b, c - 1/2)}{\Delta z} - J_{f,x}^{n-1/2} \end{aligned}$$

The superscripts of the fields denote the time steps that the fields correspond to. Rearranging these two equations gives a very simple numerical scheme to calculate the fields of the next time step from the fields of the previous time step.

$$\begin{aligned} H_x^{n+1/2}(a, b + 1/2, c + 1/2) &= H_x^{n-1/2}(a, b + 1/2, c + 1/2) + \quad (4.50) \\ &+ \frac{\Delta t}{\mu \Delta z} [E_y^n(a, b + 1/2, c + 1) - E_y^n(a, b + 1/2, c)] - \\ &- \frac{\Delta t}{\mu \Delta y} [E_z^n(a, b + 1, c + 1/2) - E_z^n(a, b, c + 1/2)] \end{aligned}$$

$$\begin{aligned} E_x^n(i + 1/2, j, k) &= E_x^{n-1}(i + 1/2, j, k) + \quad (4.51) \\ &+ \frac{\Delta t}{\epsilon \Delta y} [H_z^{n-1/2}(a + 1/2, b + 1/2, c) - H_z^{n-1/2}(a + 1/2, b - 1/2, c)] - \\ &- \frac{\Delta t}{\epsilon \Delta z} [H_y^{n-1/2}(a + 1/2, b, c + 1/2) - H_y^{n-1/2}(a + 1/2, b, c - 1/2)] - \frac{\Delta t}{\epsilon} J_{f,x}^{n-1/2} \end{aligned}$$

Given the fields from the previous time step  $\vec{E}^{n-1}$  and  $\vec{H}^{n-1/2}$ , first  $\vec{E}^n$  and then  $\vec{H}^{n+1/2}$  can be calculated, which are the fields of the current time step. In most FDTD simulation packages, the simulations

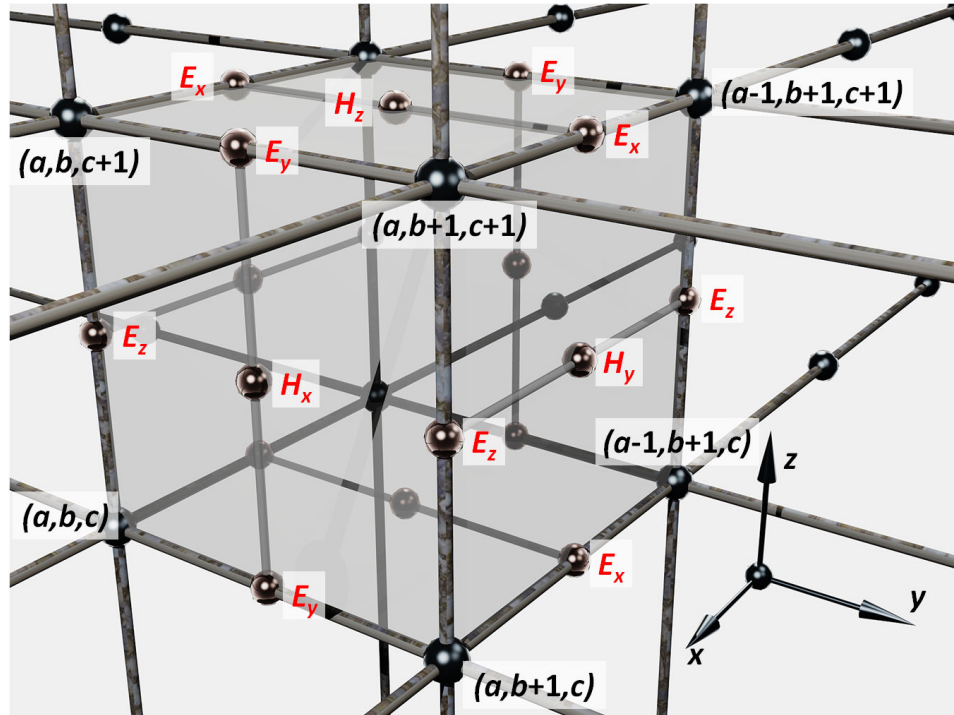


**Figure 4.16:** Position of the field components in a FDTD unit cell as proposed from Yee[178]. The  $\vec{E}$  field components are defined in the middle of the edges of the unit cell and the  $\vec{H}$  components are defined at the center of the faces.

start with all fields equal to zero at all points. In the next step, optical light sources are modeled by introducing, in most cases, a free current density  $j_f$  at several points of the grid, which leads to excitation of  $\vec{E}$  and  $\vec{H}$  fields that can propagate in the optical structure, defined by  $n(x, y, z)$ . The simulation software calculates the fields at all grid points for one time step after the other until the simulations reach their designated end. This numerical scheme reveals the main limitation of the FDTD method. All fields at all grid points of the current time step need to be stored in computer memory to make the calculation of the fields of the next time step possible. Moreover, in every time step, a calculation of all fields at all grid points is necessary. This is the reason why FDTD simulations usually take several hours up to many days, depending on the simulation domain, the simulation time and the resolution of the grid, even if powerful workstations or simulation clusters are provided. Due to the very simple computation scheme, FDTD is outstanding for parallelization on computer networks, because the simulation domain can simply be split into independent regions where only the boarder points need to be synchronized.

For 2D simulations simplified computations schemes exist but, nevertheless, they do not overcome the main limitation of FDTD simulations. To guarantee the stability of the computational algorithm it is necessary to satisfy a relation between the time increment  $\Delta t$  and the spacing of the grid points:

$$\sqrt{(\Delta x)^2 + (\Delta y)^2 + (\Delta z)^2} > c_{max} \Delta t \quad (4.52)$$

where  $c_{max}$  is the maximum light velocity in the simulation domain, and therefore, dependent on the refractive indices of the materials used. The FDTD simulations done during this work were performed using the freely available software package MEEP[179], developed by the MIT with subpixel smoothing for increased accuracy[157].

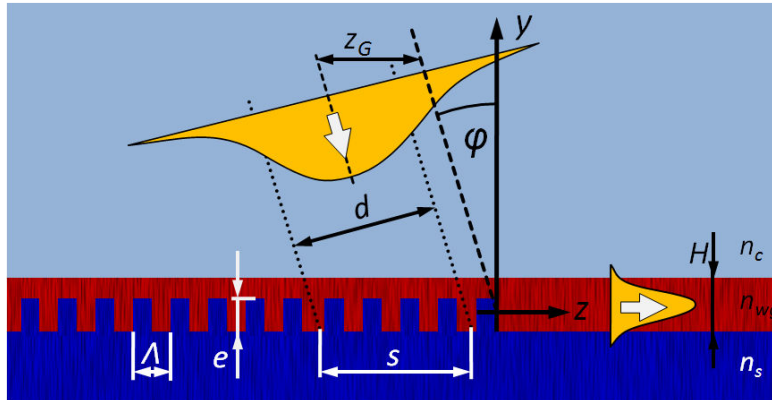


**Figure 4.17:** Input grating coupler structure as used in the simulations for the grating input coupler in section 4.2.4. A Gaussian beam with a diameter  $d$  (spot size  $s$  on the grating) is incident under the angle  $\varphi$  on a grating coupler with a period  $\Lambda$ . The thickness of the core layer  $H$ , the etch depth  $e$  and the offset of the Gaussian beam  $z_G$  is additionally shown.

The simulation tool Grinco is an extremely fast and powerful tool for designing grating couplers. Calculating the input coupling efficiency as function of the angle of incidence for a given grating structure is a matter of minutes. Doing the same with FDTD simulations tool takes many hours or days, even if the simulations are performed on powerful computer hardware. Grinco is limited to the simulation of pure periodic structures, *i.e.* any changes in the grating structures such as variations in the grating profile, the duty cycle or the etch depth are prohibited. On the other hand, the FDTD algorithm makes no assumptions to the underlying geometry and is able to realistically simulate all kinds of optical effects, even in 3D, if sufficient computational power and memory is provided and if material parameters are exactly known.

The simulations presented in the next sections are mostly performed with Grinco. Even for simple binary grating couplers, the three parameters, namely angle of incidence, position of the incident beam and etch depth of the grating need to be optimized for a given input beam. Such a design task is not possible with FDTD simulations within a feasible time frame. Therefore, all optimization of grating structures were done with Grinco and the results of Grinco were verified with FDTD simulations for specific coupling configurations. For all tested coupling configurations the results of Grinco agree very well with the results of the FDTD simulations. A comparison of results obtained from Grinco and from FDTD is given in Fig. 4.26 on page 78 on the example of a SU-8 grating coupler configuration.

### Simulation results

As was argued in section 4.2.3, the input width of lateral tapers, and therefore, the maximum beam diameter incident on the cladding is limited to about  $50\ \mu\text{m}$  to ensure efficient lateral tapering into single mode waveguides. In consequence, the beam diameter of the incident beam was chosen to be  $30\ \mu\text{m}$ . In a first attempt, input grating couplers in the chosen material system ( $n_s = 1.46$ ,  $n_{wg} = 1.65$ ,  $n_c = 1.52$ ) were simulated for a  $30\ \mu\text{m}$  wide Gaussian beam incident from the cladding, as depicted in Fig. 4.17. The thicknesses of the core layer were set to  $H = 160\ \text{nm}$  for  $\lambda = 633\ \text{nm}$  and  $H = 350\ \text{nm}$  for  $\lambda = 1.31\ \mu\text{m}$ , in accordance to the waveguide cross sections from section 4.2.1. The gratings are about  $200\ \mu\text{m}$  long to ensure that all optical power passes the grating and the periods of the gratings were set to  $\Lambda = 1.58\ \mu\text{m}$  for  $\lambda = 1.31\ \mu\text{m}$  and  $\Lambda = 766\ \text{nm}$  for  $\lambda = 633\ \text{nm}$ , giving an optimum angle

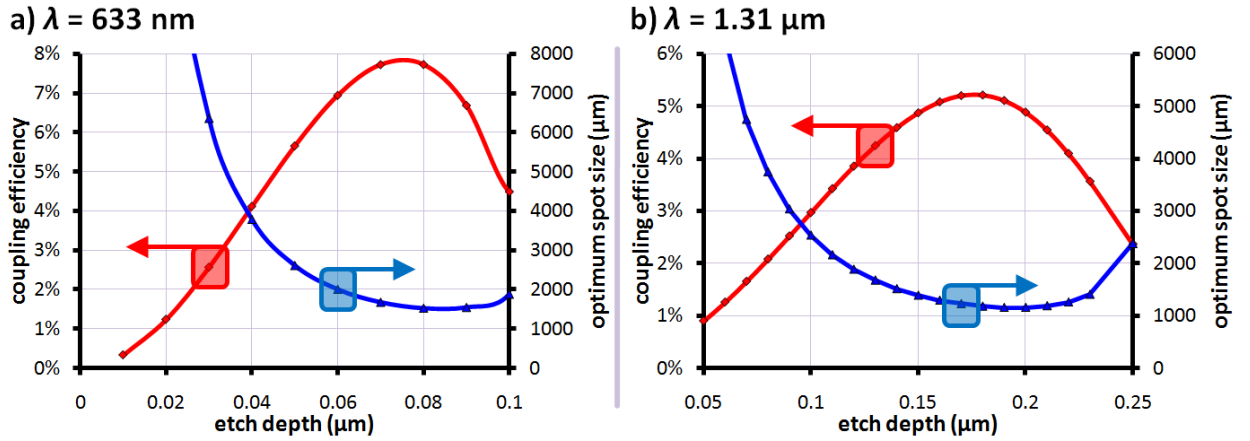


**Figure 4.18:** The input coupling efficiency and the optimum spot size of grating couplers as function of the etch depth  $e$  for **a)**  $\lambda = 633 \text{ nm}$  and **b)**  $\lambda = 1.31 \mu\text{m}$  ( $n_s = 1.46$ ,  $n_{wg} = 1.65$ ,  $n_c = 1.52$ ).

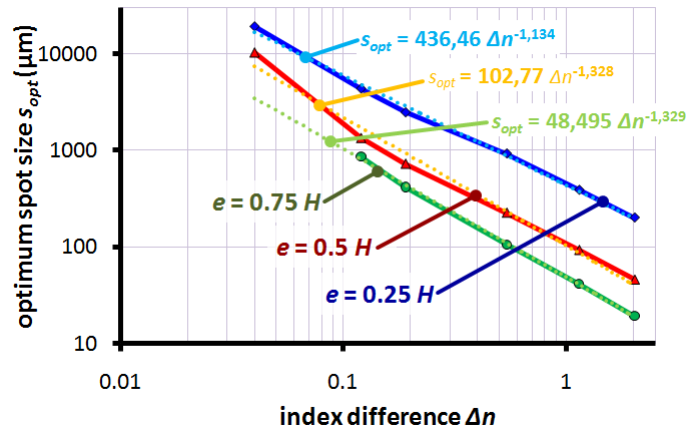


**Figure 4.19:** The optimum spot size of binary grating couplers as function of the index difference of the material system used. The three lines correspond to 25%, 50% and 75% etch depth from the total thickness  $H$  of the waveguide core layer. For each material system,  $H$  was optimized for surface sensing ( $\lambda = 1.55 \mu\text{m}$ ). Additional polynomial fits for these three lines are inserted. The parameters for these gratings used in the simulations are summarized in Table 4.2.

of incidence of about  $45^\circ$  in air, which allows for an easy alignment of the incident beams. Due to the choice of these large periods, a second diffraction order exists. However, the existence of a second diffraction order should have minor influence on the coupling efficiency since binary gratings show only very little second order coupling. The results of these simulations are presented in Fig. 4.18 as function of the etch depth  $e$  of the grating. For each point in these plots, the angle of incidence  $\varphi$  as well as the offset  $z_G$  of the Gaussian beam were optimized for maximum coupling efficiency. Nevertheless, the simulated grating couplers show only poor performance, which can be attributed to the large mismatch between the spot size of the used  $30 \mu\text{m}$  wide beam and the optimum spot sizes of the gratings, which is in the range of several millimeters, shown in Fig. 4.18. The maximum achievable coupling efficiencies are less than 8% for  $\lambda = 633 \text{ nm}$  and 5.5% for  $\lambda = 1.31 \mu\text{m}$ , which is far away from 40%, which is the theoretical maximum coupling efficiency from a Gaussian beam for a binary grating coupler.

**Table 4.2:** Parameters used in the simulations in section 4.2.5 and the results presented in Fig. 4.19: refractive index  $n_{wg}$ , thickness  $H$  of the waveguide core layer, and the grating period  $\Lambda$  of grating couplers.

core material	$n_{wg}$	$\Delta n$	$H$	$\Lambda$
silicon (Si)	3.48	2.02	60 nm	1.1 $\mu\text{m}$
silicon carbide (SiC)	2.6	1.14	100 nm	1.15 $\mu\text{m}$
silicon nitride (SiN)	2.0	0.56	185 nm	1.25 $\mu\text{m}$
polyimide (PI)	1.65	0.19	400 nm	1.35 $\mu\text{m}$
SU-8	1.58	0.12	530 nm	1.5 $\mu\text{m}$
polymer A	1.50	0.04	1150 nm	1.5 $\mu\text{m}$
polymer B	1.48	0.02	1800 nm	1.5 $\mu\text{m}$
polymer C	1.47	0.01	2700 nm	1.5 $\mu\text{m}$

To better understand the poor results for these grating couplers, a comprehensive study of grating couplers was performed. Grating couplers in different material systems were simulated for a wavelength of  $\lambda = 1.55 \mu\text{m}$ , which is a typical telecom wavelength. For a better comparability between the different material systems, a symmetrical waveguide system was assumed with the substrate and the cladding made from  $\text{SiO}_2$  ( $n = 1.46$ ). The thickness of the waveguide core layer was optimized for surface sensing in each material system, and the periods of these gratings were adapted to maintain an optimum angle of incidence of about  $20^\circ$  in air. All necessary parameters are summarized in Table 4.2. Gratings with the same etch depth  $e$ , measured in percent of the waveguide core layer thickness  $H$  were compared, namely 25%, 50%, and 75% of the waveguide core layer thickness. This data is plotted in Fig. 4.19, together with a polynomial fit for each line. These fits show good agreement with the simulated data and can be applied as fast tool to estimate the optimum coupling configuration for a given material system. These three fits are:

$$\begin{aligned}
 S_{opt} &= 436.46\Delta n^{-1.134} & \text{for } e = 0.25H \\
 S_{opt} &= 102.77\Delta n^{-1.328} & \text{for } e = 0.5H \\
 S_{opt} &= 48.495\Delta n^{-1.329} & \text{for } e = 0.75H
 \end{aligned} \tag{4.53}$$

According to these simulations, an optimum spot size suitable for a  $30 \mu\text{m}$  wide beam can be either reached by using silicon as waveguide core layer with an etch depth of about 50% of the core layer thickness or silicon carbide with an etch depth of 75%. Gratings in low index difference material systems have much larger optimum spot sizes. For gratings made from polyimide the optimum spot size ranges from 2.5 mm down to  $400 \mu\text{m}$ , depending on the etch depth. This is in good agreement with the simulation done at a wavelength of  $1.31 \mu\text{m}$  presented above. If the index difference is further reduced, the optimum spot size increases drastically. For the material system with the lowest index difference of  $\Delta n = 0.04$  studied in this comparison, the optimum spot size is in the range of centimeters.

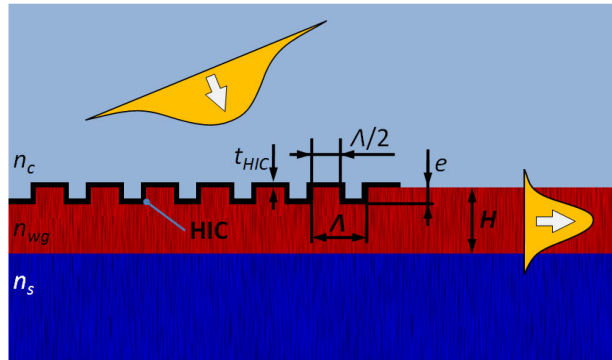


Figure 4.20: Input grating coupler with high index coating (HIC).

### 4.2.5 High index coating for grating couplers

#### Motivation

The simulations in the previous sections showed that efficient coupling into single mode waveguides by means of simple binary grating couplers and lateral tapers is not possible for low index difference material systems such as polymer material systems or inorganic material systems such as silicon oxynitride. For large beam diameters incident on the gratings, the gratings show good performance, but the lateral tapers are very inefficient, whereas for small beam diameters, the situation is reversed and grating couplers show a weak performance. To artificially increase the index difference in the grating region, grating couplers with a thin inorganic high index layer, a so called high index coating (HIC), were studied. This HIC is assumed to be applied as homogeneous layer on top of the grating that also covers the side walls of the grating structure in the same thickness (see Fig. 4.20). The HIC can be deposited employing conformal deposition techniques such as PECVD or sputtering. If necessary, the HIC outside of the grating region can be removed by etching or a lift-off process. Compared to the fabrication of the gratings with their small feature sizes, the lithography needed for the structuring of the HIC is easy, with feature sizes of several tens of microns.

This approach to increase the coupling strength of gratings has been previously mentioned for example in the context of weakly modulated diffused  $\text{Ti:LiNbO}_3$  waveguides[174, 180] or multimode polymer waveguides[166]. However, so far no systematic study about the effects of a HIC on grating structures has been performed. Here, a comprehensive numerical study on optimum beam diameters and coupling efficiencies of grating couplers with respect to grating modulation depth  $e$  and HIC thickness  $t_{HIC}$  is presented for different low index contrast material systems. Also deep etched structures and radiation effects at the interface of the waveguide without HIC and the grating with HIC are taken into account.

#### Simulation results and consequences

To explore the possibilities of HICs on grating couplers in material systems with low refractive index difference, the optimum spot sizes of such grating couplers were calculated. The calculation of the optimum spot size of a grating is easier and faster than the calculation and optimization of the coupling efficiency because only the complex refractive index of the guided mode in the grating region needs to be calculated and no optimization of the offset and the angle of the incident beam is necessary. The complex refractive index is an intrinsic property of the grating structure and does not depend on the



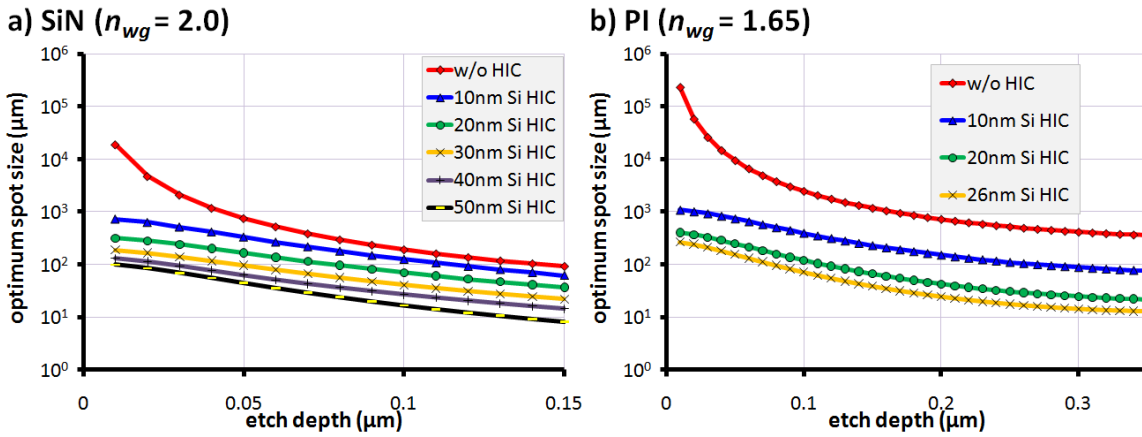


**Figure 4.21:** The optimum spot size calculated for **a)** silicon nitride (SiN) and **b)** polyimide (PI) as waveguide core layer material. For both material systems silicon ( $n = 3.48$ ) was used as HIC. ( $\lambda = 1.55 \mu\text{m}$ )

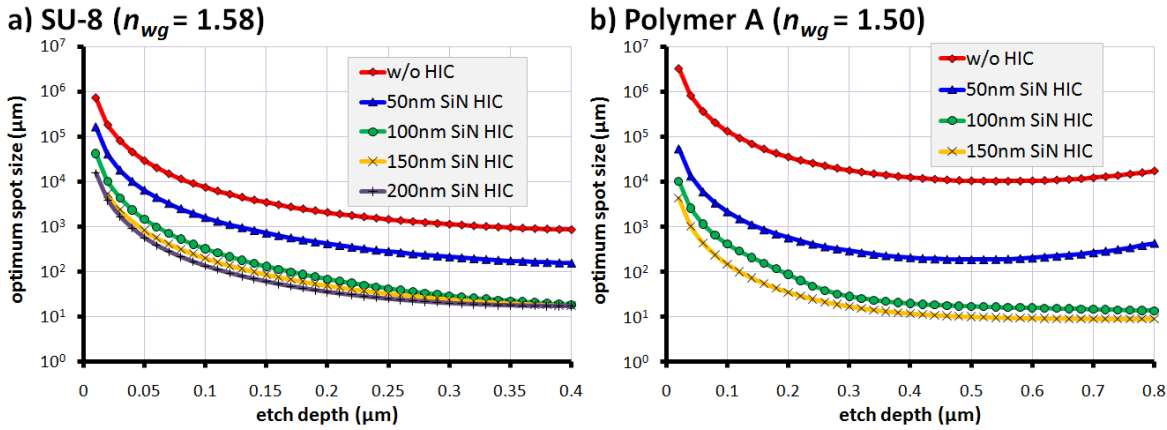


**Figure 4.22:** The optimum spot size calculated for **a)** SU-8 and **b)** polymer A as waveguide core layer material. For both material systems silicon nitride ( $n = 2.0$ ) was used as HIC. ( $\lambda = 1.55 \mu\text{m}$ )

incident beam. Simulations were performed for different waveguide material systems and for silicon nitride ( $n = 2.0$ ) and silicon ( $n = 3.48$ ) as HIC materials. As in section 4.2.4, the waveguide core layer thicknesses were optimized for surface sensing and the wavelength was  $\lambda = 1.55 \mu\text{m}$ . Again, silicon dioxide ( $n = 1.46$ ) was used as substrate and cladding. The simulation parameters thickness  $H$  and refractive index  $n_{wg}$  of the core layer as well as the period of the grating  $\Lambda$  as used in these calculations are summarized in Table 4.2.

Simulation results for the calculation on the optimum spot size are presented in Fig. 4.21, Fig. 4.22 and Fig. 4.23 for six different material systems. Figure 4.21 contains results for the material systems with the highest index difference, namely gratings made from silicon nitride ( $\Delta n = 0.54$ ) and polyimide ( $\Delta n = 0.19$ ), whereas 4.23 shows results for material systems with an extreme low index difference of only  $\Delta n = 0.02$  and  $\Delta n = 0.01$  to the silicon dioxide substrate and cladding. The last two material systems are SU-8 with an index difference of  $\Delta n = 0.12$  and polymer A with  $\Delta n = 0.04$ , given in Fig. 4.22. Silicon (Si) and silicon nitride (SiN) are used as HIC in these simulations. These two materials can be either sputtered or deposited with PECVD and are common materials in nearly every cleanroom environment.

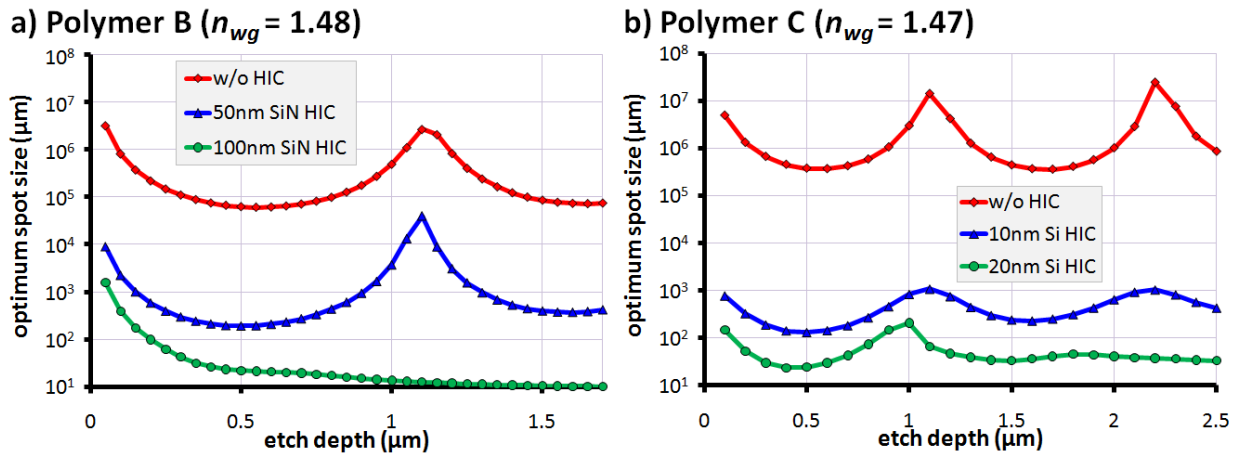


**Figure 4.23:** The optimum spot size calculated for **a)** polymer B and **b)** polymer C as waveguide core layer material. For **a)** silicon nitride ( $n = 2.0$ ) and for **b)** silicon ( $n = 3.48$ ) was used as HIC. ( $\lambda = 1.55 \mu\text{m}$ )

The simulations showed that for all material systems a strong reduction of the optimum spot size can be achieved by applying a HIC. For all material systems, an optimum spot size of nearly  $10 \mu\text{m}$  can be reached, provided that very large etch depths are used. Consequently, spot sizes as low as in SOI systems can be obtained with grating couplers in low index material systems with HIC. Obtaining very high etch depths compared to the waveguide core layer thicknesses is feasible in inorganic material systems where the grating is fabricated employing an etch step in most cases. For gratings in polymer material systems, where the polymer waveguide layer is applied by spin coating on patterned substrates, two issues have to be addressed, when using large etch depths. Firstly, the liquid polymer has to fill up the trenches completely in the spin coating step, which can be troublesome especially if high aspect ratios are necessary. The second point is that a grating structure with a large depth modulation influences the upper surface of the polymer and can cause ripples in the polymer surface. These ripples themselves can act as a grating structure and influence the coupling efficiency. However, at this stage, such fabrication related difficulties are not accounted for in this survey of the possibilities of HICs.

The lower the index contrast of the waveguide core layer to the surrounding layers, the higher the possible relative reduction of the optimum spot size. For SiN and PI gratings, a reduction of more than an order of magnitude is possible compared to gratings without HIC. In the case of the polymer B and polymer C waveguide systems, with a refractive index of  $n_{wg} = 1.48$  and  $n_{wg} = 1.47$  respectively, this relative reduction goes up to nearly four orders of magnitude. The peaks in the optimum spot size for these two material systems (see Fig. 4.23) can be observed also for other material systems with very low index differences, where the waveguides become thicker than the wavelength. These peaks are most likely caused by resonance effects occurring in the dielectric multi-layer system for specific etch depths.

It has to be mentioned that the necessary thickness of the HIC decreases as the index difference of the material system decreases. This can be readily observed when comparing the results for SU-8 and polymer A in Fig. 4.22 as well as the results for polymer B in Fig. 4.23a). The necessary thickness of the SiN HIC to reduce the spot size to about  $10 \mu\text{m}$  decreases from  $200 \text{ nm}$  for SU-8 to only  $100 \text{ nm}$  for the polymer B material system. This can be attributed to the fact that for lower refractive indices of the waveguide layer, the optical power becomes more easily confined in the HIC, thus enhancing the effect of the HIC. Simulations on Si and SiN HICs showed very similar performances in reducing

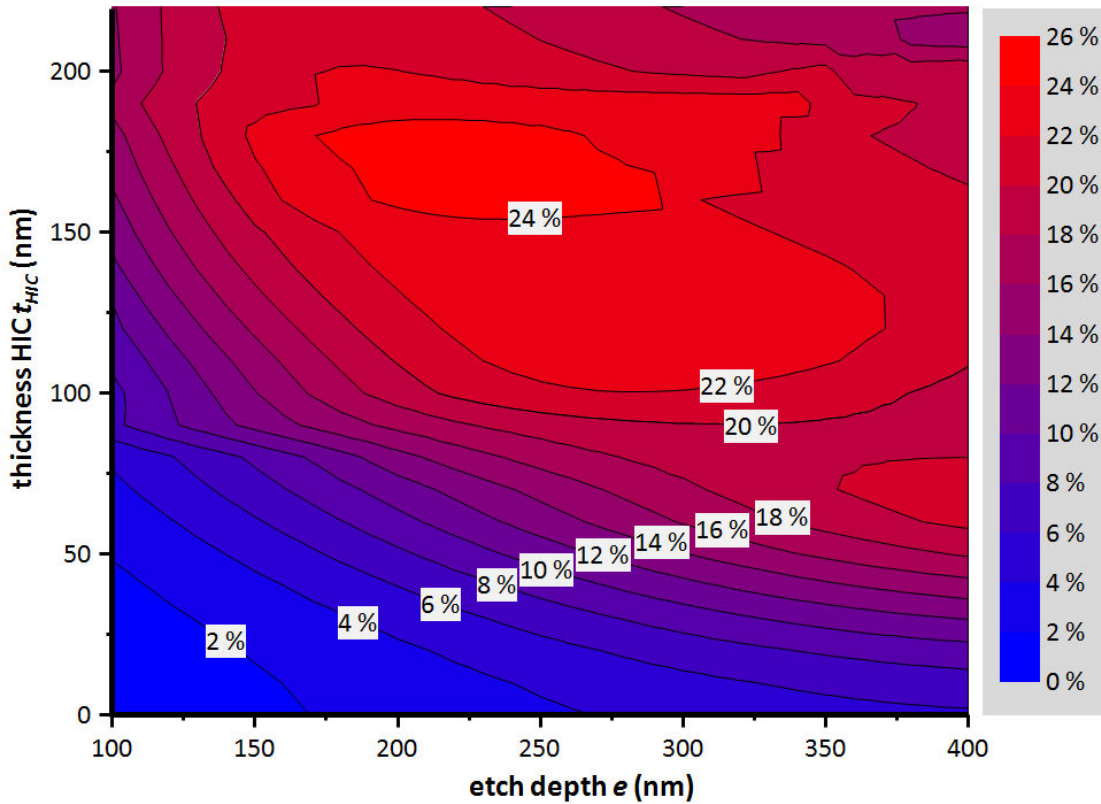


**Figure 4.24:** Input coupling efficiency for a 30  $\mu\text{m}$  wide Gaussian beam incident on a SU-8 waveguide grating as function of the etch depth  $e$  and the thickness of the SiN HIC  $t_{HIC}$ . For each plotted point, the angle of incidence and the position of the Gaussian beam were optimized for maximum in-coupling efficiency.

the optimum spot size. As expected, for Si HICs much smaller thicknesses are sufficient due to its very high refractive index. Figure 4.21b) shows simulation results of PI grating couplers with Si HICs of different thicknesses. A strong reduction of the spot size is already achieved at a HIC thickness of 20 nm. Therefore, a very precise control of the thickness of the deposited Si layer is required to obtain high coupling efficiency. This requirement is relaxed when using SiN as HIC, where a comparable effect is obtained with a HIC thickness of about 200 nm to 250 nm. Such thicknesses can be easily deposited using PECVD in a reliable and reproducible way.

To demonstrate the impact of HICs on the input coupling efficiencies of small gratings, the SU-8 waveguide system was chosen. SU-8 is a commercial photoresist with excellent spin coating properties that can be spin coated in thicknesses from several hundredth nanometers up to more than 100  $\mu\text{m}$ . Furthermore, it has very high temperature stability if adequately processed. This enables the deposition of high quality  $\text{SiO}_2$  as cladding employing PECVD, which allows for an exact experimental realization of the simulated structure in a later step. Table 4.2 and Fig. 4.20 provide details of the simulated structure. For uncoated gratings, the optimum spot size in this material system is in the range from 1 mm up to 10 mm, as shown in Fig. 4.22. In order to demonstrate the positive effect of the HIC, a TE-polarized Gaussian beam incident from the cladding with a diameter of 30  $\mu\text{m}$  was chosen. The surface grating at the waveguide core/cladding interface comprises hundred periods of  $\Lambda = 1.5 \mu\text{m}$ , *i.e.* the coupling condition is fulfilled for an angle of incidence of about 27 deg in air at  $\lambda = 1.55 \mu\text{m}$  for the uncoated gratings. Figure 4.24 shows a contour plot of the in-coupling efficiency for this grating

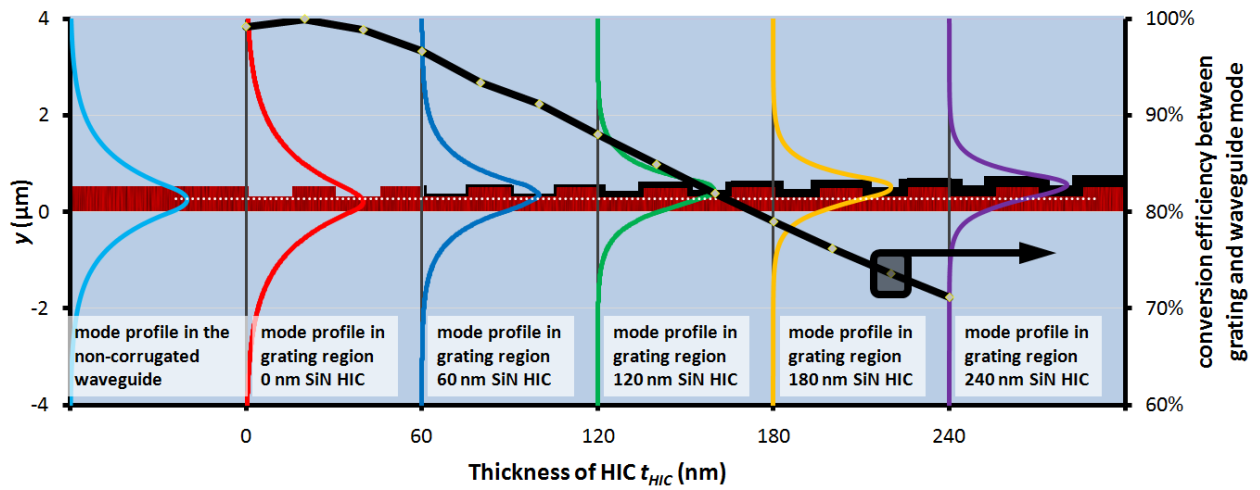


**Figure 4.25:** Simulated mode profiles in the grating region in a SU-8 material system with a 530 nm thick core layer and an etch depth of 210 nm. The left-most profile is the one of the fundamental mode in the non-corrugated waveguide and the other profiles show the profiles of the guided modes in the grating region for several thicknesses of the SiN HIC. The black curve overlaying the mode profiles gives the conversion efficiency between the waveguide mode in the homogeneous waveguide and the guided mode in the grating region, which is an important factor for the coupling efficiency of grating couplers. The corresponding grating structures are indicated in the background.

system as function of the etch depth  $e$  and the thickness of the HIC  $t_{HIC}$ . For each point in this graph, the angle of incidence  $\varphi$  as well as the longitudinal offset  $z_G$  of the Gaussian beam were optimized to obtain maximum in-coupling efficiency for each configuration. These simulations take into account radiation effects occurring at the transition of the guided mode from the grating structure to the non-corrugated waveguide due to the mismatch between the mode profiles of the guided modes inside and outside grating region. This effect increases with the thickness of the HIC, which leads to a stronger confinement of optical power within the HIC.

The simulations do not include reflection losses at the air/cladding interface, *i.e.* the simulated light source is located in the cladding material. As expected, the coupling efficiency of the uncoated gratings, represented by the lowest line in Fig. 4.24, is very low due to the large mismatch between the narrow beam used in the simulations and the optimum beam diameter. The efficiency of the uncoated gratings is always lower than 6%. A maximum input coupling efficiency of 25.1% was achieved for  $t_{HIC} = 180$  nm and  $e = 210$  nm, which corresponds to a relative increase of more than 6 dB. An important fact is that with increasing thickness of the HIC not only the efficiency increases, but also the optimum etch depth is shifted towards lower values, which simplifies the fabrication of the devices. The application of a HIC in this coupling configuration provides very relaxed fabrication tolerances. Every point within the range of *e.g.*  $140 \text{ nm} \leq t_{HIC} \leq 190 \text{ nm}$  and  $195 \text{ nm} \leq e \leq 300 \text{ nm}$  has a coupling efficiency higher than 22%.

The fact that the theoretical optimum coupling efficiency of 40% is not reached can be mainly attributed to two effects. First, radiation losses due to different mode profiles at the interface between the grating and the non-corrugated waveguide reduce the overall coupling efficiency. Figure 4.25 gives the mode profile of the fundamental mode in the non-corrugated waveguide at the left-most position as well as mode profiles of the guided mode in the grating region for several thickness of the HIC for the SU-8

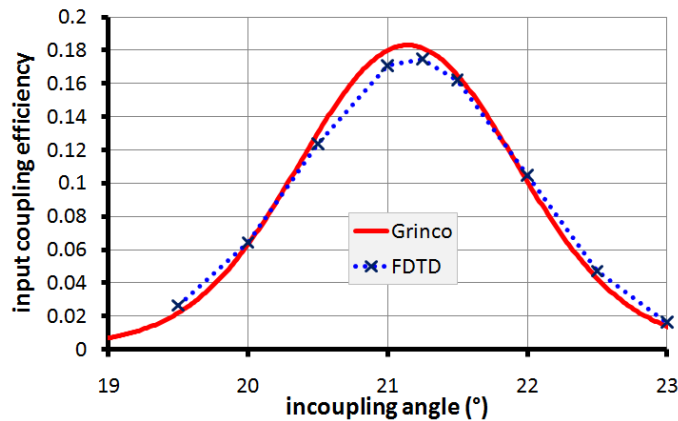


**Figure 4.26:** Comparison of simulation on the input coupling efficiency of a SU-8 grating coupler configuration ( $H = 530$  nm,  $e = 200$  nm,  $t_{HIC} = 100$  nm,  $z_G = 13$   $\mu$ m) obtained from Grinco and from FDTD, for a 30  $\mu$ m Gaussian beam.

grating system used for the simulations above. The etch depth is fixed at a value of 210 nm for the mode profiles in the grating region and the thickness of the HIC is varied from 0 nm up to 240 nm. The conversion efficiency between the waveguide mode and the modes in the grating regions was calculated using the overlap integral given in equation (2.47) on page 16 and is overlaid in Fig. 4.25. For the optimum coupling configuration with  $t_{HIC} = 180$  nm and  $e = 210$  nm the conversion efficiency at the waveguide/grating interface is about 79%, which reduces the maximum achievable coupling efficiency from 40% to 31.6%. Surprisingly, the maximum conversion efficiency was not found for the grating system without HIC, but for 20 nm SiN HIC. In the system without HIC, due to the etching of the core layer, additional low index material is introduced from the top into the waveguide region, thus leading to a small downward vertical shift of the peak amplitude. By applying a thin HIC, this effect is mostly compensated and so the maximum conversion efficiency can be found for a 20 nm SiN HIC. The thicker the HIC becomes, the more the guided mode is confined within the HIC. The guided modes become narrower and the peak amplitudes of the profiles are shifted towards the HIC, thus reducing the overlap integral with the fundamental waveguide mode.

The second effect that reduces the overall coupling efficiency is enhanced second order coupling. Due to the choice of the grating period, two diffraction orders are present both in the cladding and in the substrate. Binary gratings with a duty cycle of 0.5 have very low coupling coefficients for second order diffraction. The HIC breaks this symmetry and slightly increases second order coupling, which leads to a reduction of the in-coupling efficiency.

The results obtained from Grinco were benchmarked employing FDTD simulations. In Fig. 4.26, simulations from Grinco and FDTD are compared on the example of a SU-8 grating coupler with  $H = 530$  nm,  $e = 200$  nm,  $t_{HIC} = 100$  nm,  $z_G = 13$   $\mu$ m, for a 30  $\mu$ m wide beam. During the fabrication of grating couplers with HIC, the HIC is deposited on the already fabricated grating and then selectively removed outside the grating region. This necessitates an alignment step to align the remaining HIC with the grating structure. The sensitivity of the coupling efficiency to misalignment of the HIC with respect to the grating structure was investigated employing FDTD simulations. Figure 4.27) shows the field distributions of SU-8 gratings, with  $e = 200$  nm,  $t_{HIC} = 100$  nm for a 30  $\mu$ m wide Gaussian beam incident from the cladding, obtained from FDTD simulations. In case a), the HIC ends 20  $\mu$ m before the end of the grating region. The HIC ends exactly with the grating/waveguide interface in case b) and in case



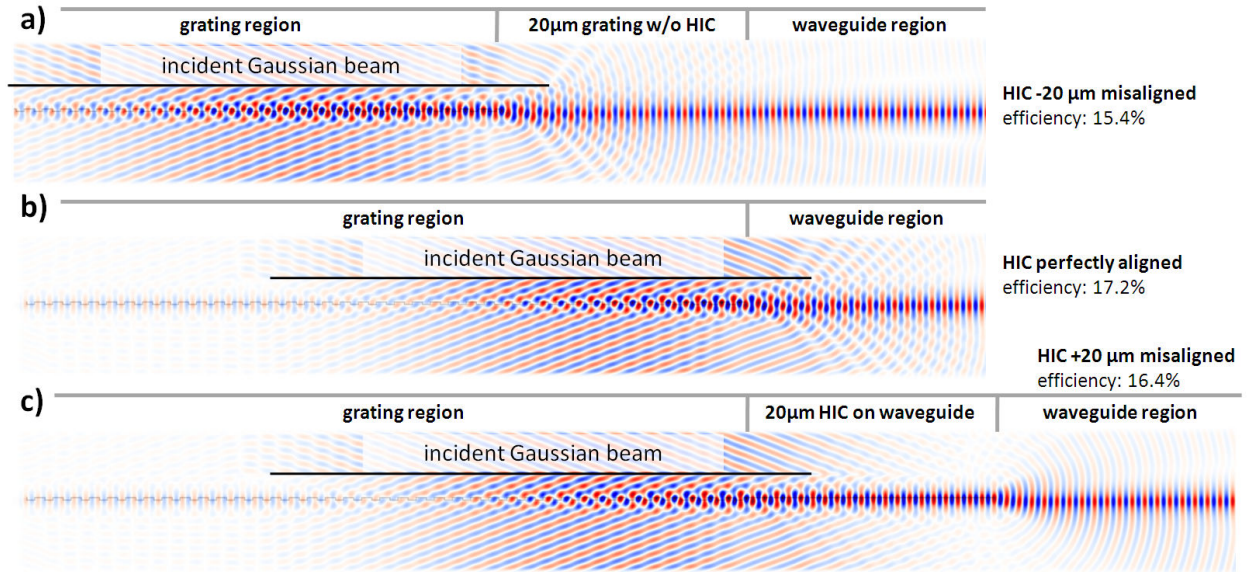


**Figure 4.27:** Field distributions of the major field component  $E_x$  of the TE mode for SU-8 grating couplers with SiN HIC ( $e = 200$  nm,  $t_{HIC} = 100$  nm) obtained from FDTD simulations. The refractive index profile of the waveguide grating coupler is indicated as a grey scale profile in the background. In **a)** the HIC ends  $20\ \mu\text{m}$  before the grating, in **b)** the HIC ends at the end of the grating, and in **c)** the HIC covers also  $20\ \mu\text{m}$  of the waveguide. The simulations showed nearly the same coupling efficiency for all these configurations, as shown in Fig. 4.28.

c), the HIC covers also  $20\ \mu\text{m}$  of the waveguide. The results of the FDTD simulations presented in Fig. 4.28 showed only minor influence of the alignment of the HIC with respect to the grating. If the HIC extends in the waveguide region, the slightly reduced coupling efficiency can be explained by the fact that the power in the guided mode in the grating region is at first transferred into a waveguide mode of the waveguide with HIC. The conversion efficiency of this transfer is given by an overlap integral (see equation (2.47)) between the mode profile in the grating region and in the waveguide region with HIC. Then, a second conversion takes place at the interface where the waveguide with HIC meets the waveguide without HIC. This double conversion leads to slightly higher radiation losses than in the case where the HIC covers the grating region only. In the case where the HIC ends before the grating, also only a slight reduction of the coupling efficiency was calculated, provided that the grating is still long enough to couple all available energy from the incident beam into the grating. Due to the low coupling strength of the grating without HIC, the guided mode in the grating region gains energy in the region with HIC, but travels nearly unaffected in the grating region without HIC. However, in this case, an adjustment of the position of the incident beam is necessary. If the position of the beam relative to the grating is not altered, the coupling efficiency drops significantly if the end of the HIC is located inside the grating region. In summary, it can be stated that the alignment of the HIC on the grating structure is not a critical parameter for a good performance of the grating coupler.

Similar simulations were carried out to show the effect of HICs on a waveguide grating system with very low index difference. Figure 4.29 shows the simulation results for input grating couplers made from polymer B with a refractive index of 1.48. For a  $30\ \mu\text{m}$  wide Gaussian beam the input coupling efficiency of the uncoated grating does not exceed 0.1%, which is caused by the huge mismatch between the optimum spot size of these uncoated gratings, which is larger than  $5\ \text{cm}$  and the used  $30\ \mu\text{m}$  wide

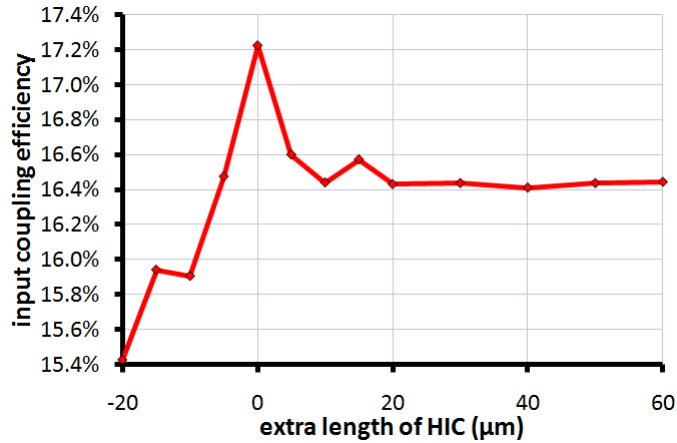


**Figure 4.28:** Input coupling efficiency for SU-8 grating couplers with a SiN HIC ( $e = 200$  nm,  $t_{HIC} = 100$  nm) for different end positions of the HIC obtained from FDTD simulations. The graph is plotted as function of extra length of the HIC with respect to the end of the grating region.

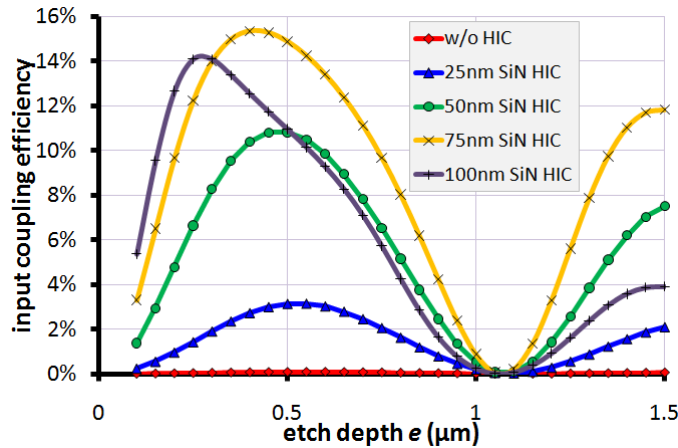


**Figure 4.29:** Input coupling efficiency for a  $30$  μm wide Gaussian beam ( $\lambda = 1.55$  μm) incident on grating couplers with a polymer B ( $n_{wg} = 1.48$ ) core layer as function of the etch depth and the HIC thickness.

beam. With a coupling efficiency of up to 15.35% the gratings with HIC showed a significantly improved performance. The very low coupling efficiencies at an etch depth around  $1.1$  μm can be explained by the large optimum spot sizes for this etch depth (see Fig. 4.23a) that are caused by interference effects in thick waveguides. This confirms the usefulness of the optimum spot size as a figure of merit for the design of efficient grating couplers. Such interference effect can be found in several material systems with very low index differences where the waveguides become very thick. Again, the maximum in-coupling efficiency in this material system is lower than the theoretical limit of 40%. Moreover, it is also lower than the maximum efficiency of the SU-8 gratings. The limiting factors for this reduced efficiency are the radiation losses at the interface of the grating region with HIC and the homogeneous waveguide without HIC. These radiation losses for this material system are higher than for SU-8. For the configuration with the maximum coupling efficiency ( $e = 400$  nm and  $t_{HIC} = 75$  nm) the coupling efficiency is reduced by a factor of 0.674.



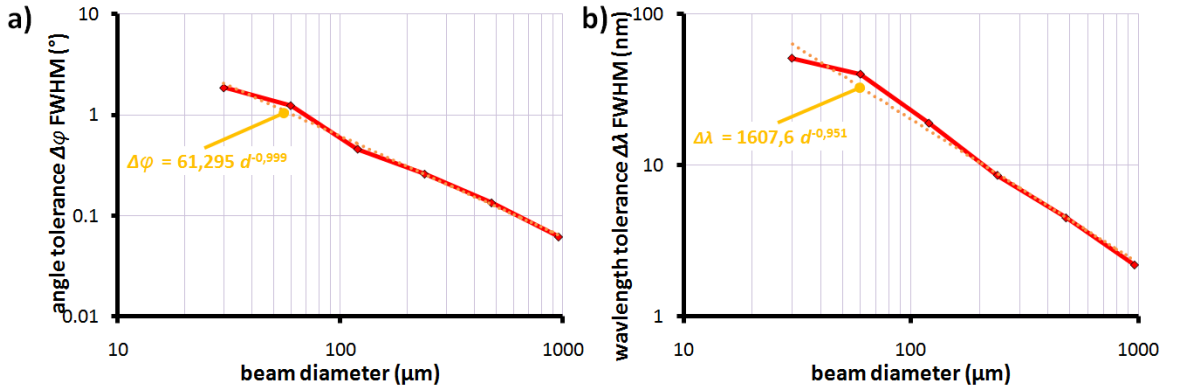


**Figure 4.30:** a) Angle and b) wavelength tolerances for SU-8 grating input couplers ( $t = 530$  nm,  $n_{wg} = 1.58$ ,  $\lambda = 1.55$  μm) as function of the incident beam diameter. For each beam diameter, the grating was optimized for efficient in-coupling (see Table 4.3) and the angle tolerance at fixed wavelength as well as the wavelength tolerance at a fixed angle were calculated.

**Table 4.3:** Parameters of the grating configurations used for the calculation of the angle and wavelength tolerances shown in Fig. 4.30

beam diameter $n_{wg}$	30 μm	60 μm	120 μm	240 μm	480 μm	960 μm
grating length	150 μm	300 μm	600 μm	1.2 mm	2.4 mm	4.8 mm
optimum etch depth $e$	210 nm	240 nm	170 nm	200 nm	230 nm	290 nm
optimum thickness of the HIC $t_{HIC}$	180 nm	90 nm	80 nm	70 nm	40 nm	0 nm

Summarizing the grating simulations, it can be stated that the application of a HIC strongly increases the in-coupling efficiency for small beam diameters even in material systems with very low index differences. The theoretical maximum in-coupling efficiency of about 40% cannot be reached due to increased second order coupling and radiation losses at the grating/waveguide interface. These negative effects become stronger for material systems with lower refractive index difference.

Further advantages of small gratings arise from the relaxed angle and wavelength tolerances. Simulations were performed for SU-8 input grating couplers in similar configurations as above, but for different beam diameters. For each beam diameter, the gratings were adapted for efficient in-coupling. Table 4.3 summarizes the parameters beam diameter  $d$ , etch depth  $e$ , thickness of the HIC  $t_{HIC}$  and the length of the grating as used in these simulations. Afterwards, the angle tolerance  $\Delta\varphi$  at a fixed wavelength of 1.55 μm as well as the wavelength tolerance  $\Delta\lambda$  for a fixed angle of incidence were calculated. Figure 4.30 shows the full width at half maximum (FWHM) of the in-coupling efficiency and corresponding fits as function of the beam diameter  $d$ . As expected, the angular tolerance  $\Delta\varphi$  as well as the wavelength tolerance  $\Delta\lambda$  increase if the beam diameter is reduced. The fits for these two parameters are:

$$\Delta\varphi = 61.295 d^{-0.999} \quad (4.54)$$

$$\Delta\lambda = 1607.6 d^{-0.951} \quad (4.55)$$

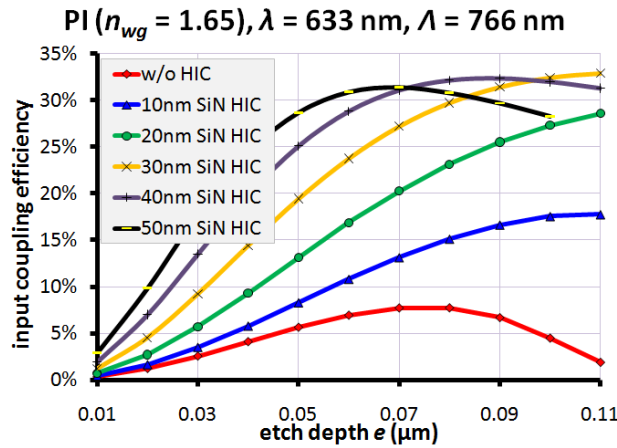


**Figure 4.31:** The input coupling efficiency for PI gratings with SiN HIC as function of the etch depth  $e$  for  $\lambda = 633$  nm. ( $\Lambda = 766$  nm,  $H = 160$  nm,  $n_s = 1.46$ ,  $n_{wg} = 1.65$ ,  $n_c = 1.52$ ).

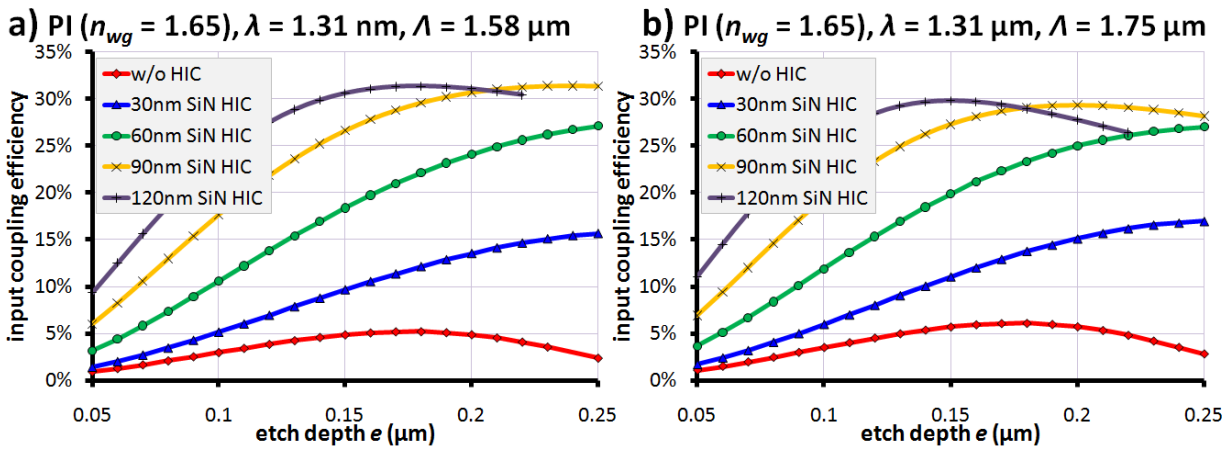


**Figure 4.32:** The input coupling efficiency for PI gratings with SiN HIC as function of the etch depth  $e$  for  $\lambda = 1.31$   $\mu\text{m}$ . In **a)** the grating period  $\Lambda = 1.58$   $\mu\text{m}$  gives an angle of optimum coupling of about  $45^\circ$  in air and in **b)**  $\Lambda = 1.75$   $\mu\text{m}$  results in an optimum coupling angle of about  $55^\circ$  in air. ( $H = 350$  nm,  $n_s = 1.46$ ,  $n_{wg} = 1.65$ ,  $n_c = 1.52$ )

The simulations showed good reciprocal behavior of the angle and the wavelength tolerance with respect to the beam diameter. For the smallest calculated beam diameter of 30  $\mu\text{m}$ , which corresponds to the SU-8 grating presented above in Fig. 4.24, the FWHM of the angular tolerance is larger than 2 degrees and FWHM of the wavelength tolerance exceeds 50 nm.

After this comprehensive study of gratings with HICs, the calculations on the grating couplers for the biosensor chip were continued. The results for the uncoated grating couplers, presented in Fig. 4.18 in section 4.2.4, were extended with simulations on grating couplers with SiN HIC. As depicted in Fig. 4.17, the grating is present at the substrate/core layer interface and a 30  $\mu\text{m}$  wide Gaussian beam is incident from the cladding. The simulation results for these gratings are plotted in Fig. 4.31 for  $\lambda = 633$  nm and in Fig. 4.32a) for  $\lambda = 1.31$   $\mu\text{m}$ . The coupling efficiency can be increased to more than 31% in both cases. In addition, grating couplers for a wavelength of  $\lambda = 1.31$   $\mu\text{m}$  with a grating period of  $\Lambda = 1.75$   $\mu\text{m}$  were simulated. The results are plotted in Fig. 4.32b). The larger period of these

gratings allows for an easier fabrication by means of conventional UV-lithography, and therefore, for an easier experimental verification of the simulated enhancement of the coupling efficiency. Due to the larger period of these gratings, the angle of optimum in-coupling is shifted from about  $45^\circ$  in air for  $\Lambda = 1.58 \mu\text{m}$  to about  $55^\circ$  in air for a period of  $\Lambda = 1.75 \mu\text{m}$ . The simulations of PI grating couplers verified that grating couplers made from materials with a refractive index similar to PI are excellently suited to be combined with a HIC. The coupling efficiency of such grating couplers can be strongly and easily increased by application of a HIC without sacrificing too much efficiency due to radiation losses and enhanced second order coupling.

#### 4.2.6 Summary of grating coupler simulations

Due to the comparatively small index difference in polymer waveguide systems, the coupling strength of grating couplers is very low, thus allowing efficient coupling only for very large (several hundred microns) gratings. The application of a thin high index coating (HIC) in the grating area increases the coupling strength of gratings in low index material systems and enables efficient coupling of narrow beams into single mode polymer waveguides. Since the HIC is only present in the comparatively small grating area, the optical quality of the HIC has only minor influence on the coupling efficiency. Therefore, low-temperature thin film deposition techniques such as sputtering, which are usually not used for optical waveguide fabrication because of low optical quality, can be employed for the HIC deposition. Silicon nitride (SiN) is a suitable HIC material because it is transparent in the visible and near infrared domain. By applying a HIC, the optimum etch depth can also be adjusted in a way that the grating has the same etch depth as the tapers and the waveguides. In addition, smaller gratings allow for larger angular and wavelength tolerances.

The lower the index difference of the material system, the less HIC is necessary to achieve a strong reduction in the optimum spot size. In nearly all material systems an optimum spot size of about  $10 \mu\text{m}$  can be reached, which corresponds to optimum spot sizes in SOI systems. The efficiency of small grating couplers in low index difference material systems can be significantly increased for small beam diameters by application of a HIC. In addition, the necessary etch depths of gratings for efficient coupling can be reduced by HICs. The theoretical maximum coupling efficiency of 40% for an input coupler cannot be reached due to radiation losses at the transition from the grating region to the homogeneous waveguide and enhanced second order coupling. The maximum achievable coupling efficiency depends on the refractive indices of the material system. The overall trend shows that the maximum achievable coupling efficiency decreases if the index difference decreases, because of higher radiation losses at the grating/waveguide interface. On the other hand, the relative increase in the coupling efficiencies between gratings with and without HIC is strongest in material systems with very low  $\Delta n$ . Grating couplers made from PI or materials with similar refractive indices show great potential in combination with HIC. The uncoated gratings have a very low coupling, which can be improved to more than 30% by the application of a HIC for a  $30 \mu\text{m}$  wide Gaussian beam.

#### 4.2.7 Further enhancement possibilities for grating couplers

The input grating couplers made from PI with HIC showed a theoretical performance of more than 30%, which is already a good value for a simple binary input grating coupler. To further increase the coupling efficiency, mainly four strategies can be applied.

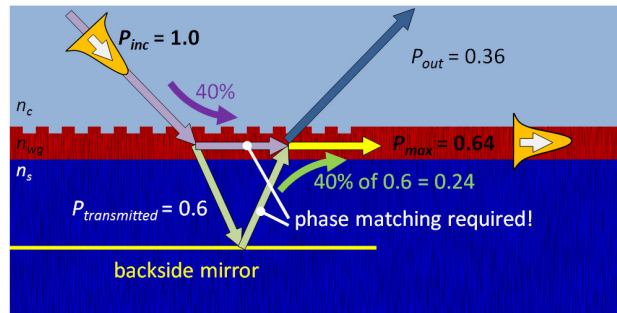


**Figure 4.33:** Principle of a backside mirror for a grating input coupler. The maximum coupling efficiency of an optimized grating coupler can be increased from 40% to 64%. Reflections at the grating interface can be neglected if the refractive index differences between the cladding and the waveguide core layer are small. For a successful increase of the coupling efficiency, phase matching between the in the first pass in-coupled light and the reflected beam is required.

The first strategy is reducing the period of the grating, so that only one diffraction order into the substrate and the cladding is present. This condition is satisfied only for very small angles of incidence, typically  $3^\circ$  to  $4^\circ$ . One also has to avoid the pitfall of a vertical incidence, which, due to symmetry reasons, couples light in both horizontal directions at the same efficiency, and therefore, reduces the coupling efficiency in the desired direction by half. The optimum in-coupling angle depends on several parameters such as the thickness and refractive index of the core layer as well as the thickness and refractive index of the HIC. Therefore, such coupling configurations leave only very little space for fabrication tolerances to avoid vertical incident.

A second technique can be the application of a kind of taper structure to smooth out the transition from the region with HIC to the region without HIC, to reduce radiation losses at this interface. Simulations of such a structure would require 3D-simulations either with a BPM or FDTD and have not been performed yet.

The third method to increase the efficiency of grating couplers can be the application of a backside metal[64, 72] or dielectric mirror[181] to force the light that is transmitted through the grating to a second pass. Theoretically, the coupling efficiency of an input grating coupler can be increased from 40% up to 64% (see Fig. 4.33). The distance between the grating and the mirror has to be chosen in such a way, that the reflected light interferes constructively with the incident light in the plane of the grating. The distance is dependent on the refractive index of the substrate, the angle of incidence and the effective index of the guided mode in the grating region. For the application of such a mirror at the biosensor chip, it would be possible to apply a mirror on top of the cladding and introduce the incident light through the substrate. However, this would require a very precise thickness control of the cladding layer.

Finally, a variation of the duty cycle or the etch depth of the grating in longitudinal direction can be introduced to optimize the overlap factor with the incident Gaussian beam[182], *e.g.* realized for grating couplers in SOI[181]. The duty cycle of a grating has strong influence on the coupling strength. This allows for an adjustment of the coupling strength along the grating for an optimized overlap with the incident beam. With this technique, the efficiency of a grating can be, in theory, increased from 40% up to 50%.

## 5 Experiments and results

This chapter contains the results of the experiments performed during this work. It first gives an overview on the fabrication of the MZI sensors employing silicon wafers with a SiO<sub>2</sub> layer on top as substrates that are patterned with a well established and reliable fabrication platform based on CMOS technology. Then, the optical elements necessary for the MZI are analyzed in detail, starting with the cross section of the spin coated polymer waveguides. In addition to this, grating couplers with HICs, which are a critical element for the realization of MZI sensors on injection molded substrates are investigated. Experimental results on the improvement of the coupling efficiency for small, low index contrast grating couplers by means of a high index coating are given and compared to the results from the simulations in the previous chapter.

Finally, biosensing with polymer waveguide based MZIs is demonstrated in the biotin-streptavidin system and the results are examined with respect to sensitivity and reproducibility. The biosensing experiments were first carried out on MZIs that were measured in end-face coupling configuration and then verified on MZI sensors with grating couplers for in- and out-coupling. The simulations in the previous chapter were given for wavelengths of 633 nm and 1310 nm. The experiments in this chapter were performed only at the telecommunication wavelength of 1310 nm. On the one hand, the shorter wavelength should provide increased sensor sensitivity in surface sensing experiments, but on the other hand, it shrinks down all optical structures. Especially the feature size of the grating couplers would drop below the limit of conventional UV-lithography if designed for a wavelength of 633 nm.

### 5.1 Sample fabrication

This section describes the fabrication of samples, on which the experiments were performed. The procedure is graphically summarized in Fig. 5.1. If the fabrication process of specific samples deviates from this default procedure, the changes are given in the corresponding section.

The samples were prepared on silicon wafers with a 5 μm thick thermal SiO<sub>2</sub> layer on top. After cleaving of the wafer into 3 cm x 3 cm pieces, the samples were cleaned with acetone in an ultrasonic bath for several minutes and then rinsed with isopropanol and blown dry in a nitrogen stream. In the next step, the primer hexamethyl-disiloxan (HMDS) and the positive-tone photoresist MIR 701 from MicroChemicals were applied employing spin coating. Spin coating of this photoresist at a rotation speed of 7500 rpm for 35 s gives a film thickness of about 475 nm. After a 60 s softbake at a temperature of 110°C on a hotplate, the photoresist film is ready for the UV-exposure step. The exposure was done using a manual mask aligner Karl Suss MJB3, equipped with a 350 W high pressure mercury lamp and UV 400 exposure optics. In this configuration, the mask aligner has an output of about 30 mW/cm<sup>2</sup> in the wavelength range from 350 nm to about 450 nm. The exposure was done in two steps. In the first step, the center of the sample was covered with a 2 cm x 2 cm chrome square on a quartz photomask. A 20 s exposure of the border area of the sample and a 25 s puddle development in MIF 726, also purchased from MicroChemicals, removes the inhomogeneous photoresist film at the edge of the samples

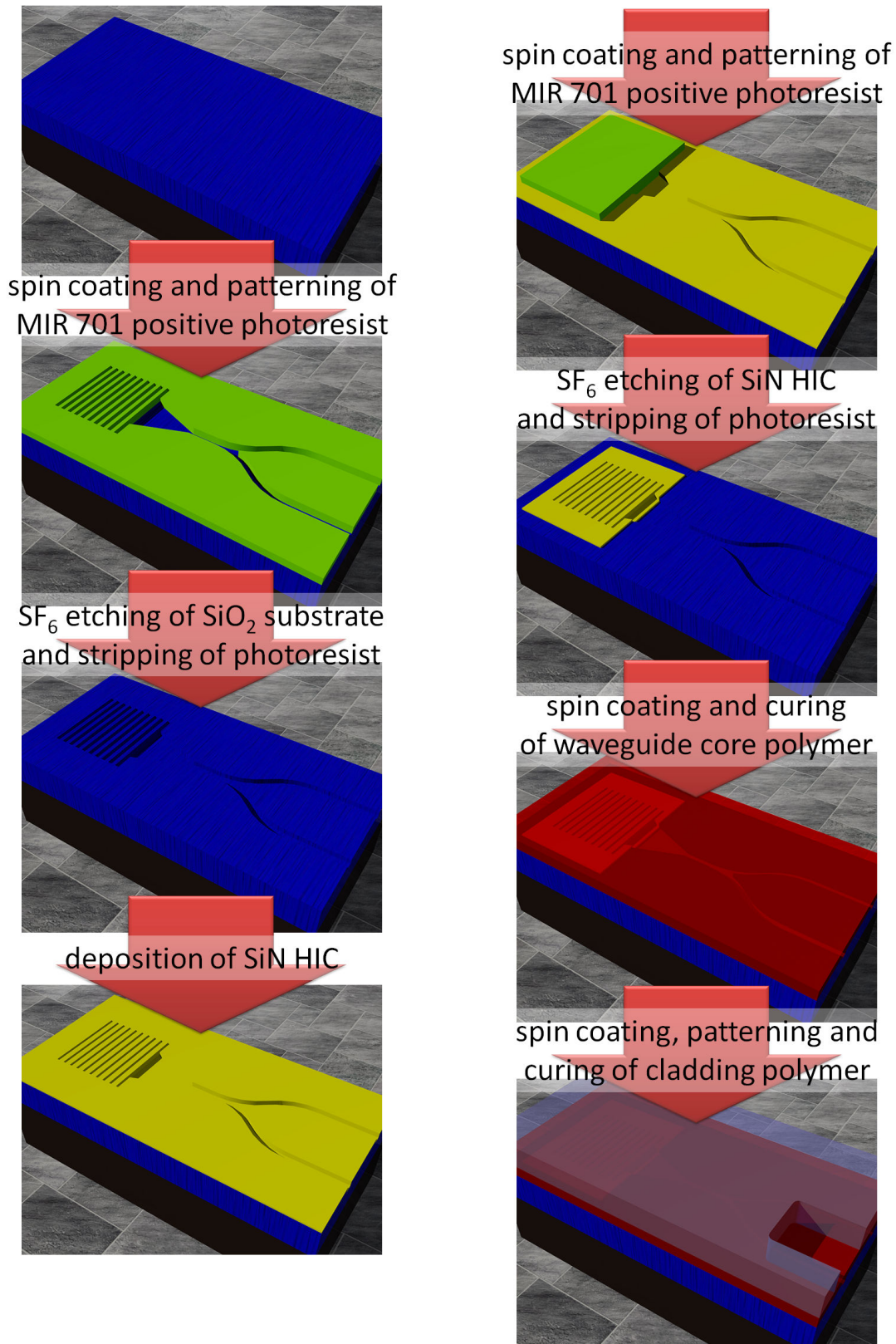


**Figure 5.1:** Summary of the default fabrication procedure.



**Table 5.1:** Process parameters for RIE of SiO<sub>2</sub> substrate and SiN HIC.

gas 1	gas 2	working pressure	plasma power	base pressure
20 sccm SF <sub>6</sub>	10 sccm Ar	50 mtorr	50 W	5 · 10 <sup>-5</sup> torr

**Table 5.2:** Process parameters of PECVD of SiN HIC.

gas 1	gas 2	working pressure	plasma power	temperature
180 sccm (98% N <sub>2</sub> / 2% SiH <sub>4</sub> )	20 sccm NH <sub>3</sub>	1 torr	10 W	350 °C

and leaves a very homogeneous 2 cm x 2 cm photoresist film in the middle of the sample, which allows for a more precise replication of small structures such as gratings and waveguides in the next exposure step. In this second exposure step, the grating and the waveguide structures were transferred into the photoresist film. The exposure time was set to 4.16 s and the photoresist film was developed for 17.5 s in MIF 726, giving the best results for the replication of the grating structures. The optical structures were transferred from the photoresist into the substrate employing reactive ion etching (RIE) on an Oxford Plasmalab 80 Plus. The process parameters of this RIE process are summarized in Table 5.1. In this mainly chemically driven etch process, SF<sub>6</sub> is used as etch gas for the SiO<sub>2</sub>. The etch rate of this process is about 20 nm/min, resulting in a process time of about 7.5 min for an etch depth of 150 nm. After the RIE, the remaining photoresist was stripped using acetone and an ultrasonic bath for several minutes. Then, the samples were rinsed with isopropanol and blown dry.

If the samples were intended to be used with grating couplers for in- and out-coupling, a silicon nitride (SiN) HIC was applied. The SiN HIC was deposited using plasma enhanced chemical vapor deposition (PECVD) and selectively removed outside the grating area employing a second RIE step. The deposition of the HIC was done on an Oxford Plasmalab 80 Plus with the parameters summarized in Table 5.2. The deposition rate of SiN using this process is about 9 nm/min. A deposition of 120 nm SiN HIC takes 13.3 min. After deposition of the HIC, a second lithography step is needed that covers the grating regions with photoresist and prevents the etching of the HIC beneath in the following RIE step. The photoresist was spin coated at a rotation speed of 4000 rpm for 35 s, followed by a soft bake of 60 s on a hotplate at 110 °C. Due to the very large feature sizes of the structures that have to be patterned in this lithography step, the exposure can be performed in a single step. The photoresist was exposed for 6.5 s on the same mask aligner as above and developed for 25 s in MIF 726.

Then, the HIC was removed using RIE with the same parameters as for the etching of the SiO<sub>2</sub> on the substrate (Table 5.1). Due to the very high etch rate of PECVD-deposited SiN of about 200 nm/min, typical etch times are below 1 min. The etch progress was monitored using a refractometer integrated in the Oxford Plasmalab. The etch process was aborted after a complete removal of the HIC with a safety margin of about 10 s, which results in a maximum over-etching into the SiO<sub>2</sub> below of less than 5 nm. After this etch step, the photoresist was stripped in a TePla 100-E oxygen plasma oven for 5 min at a power of 300 W, followed by an ultrasonic bath in acetone for several minutes and a rinse with isopropanol. The ash of the photoresist in the plasma oven before the acetone rinse was found to be necessary to avoid dirt of the samples during the strip of the photoresist.



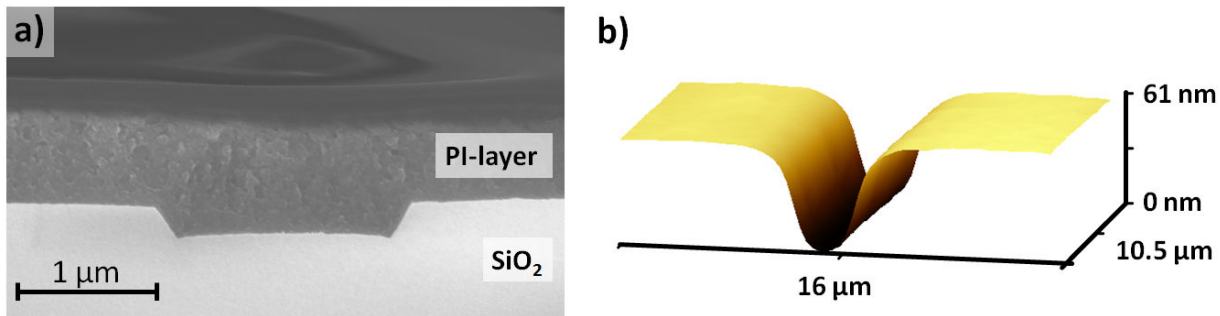


**Figure 5.2:** a) SEM micrograph of a 1.6  $\mu\text{m}$  wide inverted rib waveguide cross section obtained from a cleaved end facet of a sample. The rib waveguide has a 150 nm etch depth and a 450 nm thick PI core layer applied by spin coating. The side wall angle of the waveguide trench is about  $55^\circ$  b) AFM scan of the PI surface above a 1.6  $\mu\text{m}$  wide waveguide trench with an etch depth of 150 nm. The modulation depth of the PI surface is about one third of the etch depth of the waveguide trench in the  $\text{SiO}_2$  layer.

The remaining part of the fabrication procedure is the spin coating of the core layer and the cladding polymer. The core layer polymer PI2771 is designed to be spin coated in film thicknesses of several microns, which is much too thick for surface sensing applications. Therefore, the PI solution has to be diluted with n-methyl-2-pyrrolidone (NMP). The dilution factor and the rotation speed for the spin coating step depend on the desired film thickness. For a film thickness of 450 nm, the PI is diluted 1:0.8 with NMP with the rotation speed set to 4500 rpm, while for a film thickness of 160 nm the dilution factor is 1:1.5 with the rotation speed set to 5500 rpm. After a 1 min softbake at  $100^\circ\text{C}$ , a 30 s flood exposure to UV light at the Karl Suss MJB3 mask aligner was followed by a 1 h thermal cure step at a temperature of  $200^\circ\text{C}$ . After cool down of the samples, the surface of the PI layer was exposed to an oxygen plasma in the TePla plasma oven for about 30 s to increase the adhesion of the cladding polymer. The Ormoclad cladding polymer was applied by spin coating at a rotation speed of 1500 rpm and a 2 min softbake at  $120^\circ\text{C}$ . The measurement windows of the MZIs were transferred into the cladding during a 90 s UV-exposure at the mask aligner. After a 5 min post exposure bake at  $120^\circ\text{C}$ , the samples were developed in Ormodev for 40 s and then rinsed with isopropanol and blown dry in a nitrogen stream. The final step in the fabrication procedure was a 3 h hardbake of the cladding polymer on a hotplate at  $150^\circ\text{C}$ .

For the use of the samples in end face coupling configuration, the samples were cleaved to produce smooth and flat sample facets, which allowed a very close approximation of optical fibers, thus minimizing coupling losses between the fibers and the optical waveguides.

## 5.2 Analysis of waveguide cross section

The inverted rib waveguides are the basic elements in the MZI. Their single mode behavior is a prerequisite for the proper function of the MZI. In theory, the PI, which is spin coated as a liquid, should completely fill up the waveguide trench etched into the  $\text{SiO}_2$  substrate, and therefore, generate a perfect inverted rib waveguide structure with a flat surface. Measurements on samples revealed that this perfect waveguide structure cannot be reached. Figure 5.2a) gives a SEM micrograph of a waveguide cross section from a cleaved facet of a sample, while Fig. 5.2b) shows an AFM scan of the PI surface on a similar waveguide. The width of this specific waveguide is 1.6  $\mu\text{m}$  with an etch depth of 150 nm. The SEM micrograph reveals that the etch process of the  $\text{SiO}_2$  leads to a side wall angle of only  $55^\circ$ . The AFM scan gives the information that the surface of the PI layer has a 60 nm dip over the waveguide

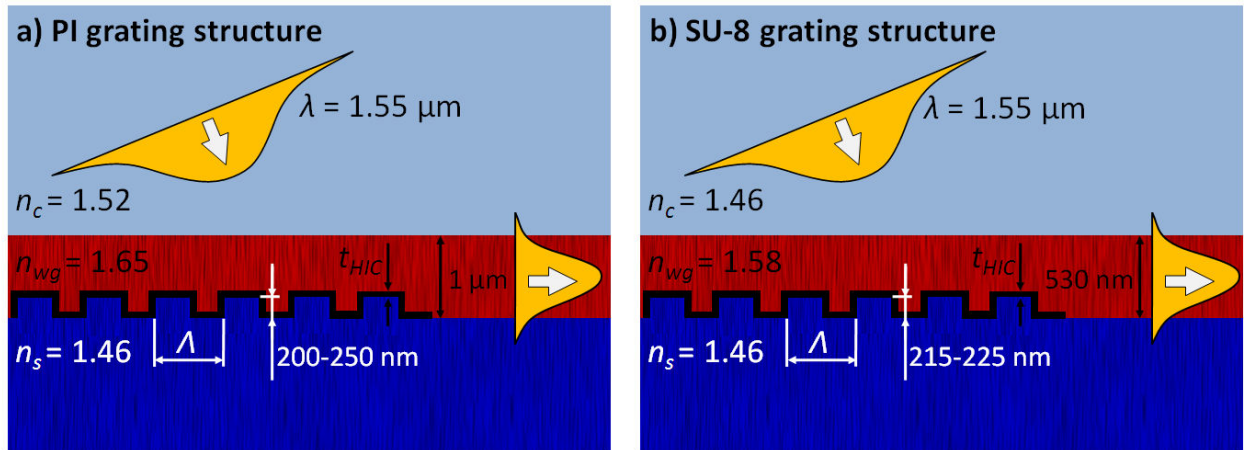


**Figure 5.3:** a) PI and b) SU-8 grating structures as fabricated as well as used for the simulations and measurements presented in section 5.3.

trench, which corresponds to roughly one third of the etch depth of the waveguide trench. In the experiments it was found that the shape and the depth of this dip cannot be significantly influenced by changing the dilution of the PI solution or the rotation speed in the spin coating step. Variations in the duration of the soft or hard back steps also showed to have no impact on the waveguide cross section. This behavior is in agreement with the explanation that the dip in the PI surface profile is caused by the evaporation of the solvent in the liquid PI solution. In the liquid state, the PI layer in the region of the waveguide trench is thicker, thus containing more organic solvent. In the soft bake step, the solvent evaporates, leading to shrinkage of the layer. In the region of the waveguide trench, this shrinkage is more pronounced due to the larger amount of solvent present, which then results in a dip in the surface of the solidified PI.

It has to be mentioned that the exact waveguide cross section is not critical to the function of the MZI, as long as the single mode behavior of the waveguide is maintained. The MZI measurements presented below indicate that there are no negative effects arising from this waveguide cross section.

### 5.3 Grating couplers with high index coating

The positive effect of HICs on grating couplers, predicted in the simulations in the previous chapter, was experimentally verified for PI and SU-8 waveguide gratings fabricated on silicon wafers. In order to facilitate the waveguide fabrication, grating structures slightly different to the one presented in section 4.2.5 were chosen. Whereas in the simulations of the SU-8 gratings, given in Fig. 4.24 of section 4.2.5, the gratings of the SU-8 waveguides were present at the core layer/cladding interface, the gratings are now present at the substrate/core layer interface. For the PI gratings, a waveguide core layer thickness of 1 μm was chosen. The fabricated grating structures, which are also used for the simulations in this section, are depicted in Fig. 5.3 for both material systems.

The default fabrication procedure given in section 5.1 was adapted for the fabrication of these samples because first measurements with grating couplers showed strong disturbance of the incident beam from reflected light at the Si/SiO<sub>2</sub> interface. To avoid these reflections, a 210 nm SiN anti-reflection layer was deposited on bare Si-wafers using PECVD with the parameters given in Table 5.2. Afterwards, a 3.4 μm

**Table 5.3:** Process parameters of PECVD of SiO<sub>2</sub> layer.

gas 1	gas 2	working pressure	plasma power	temperature
710 sccm (98% N <sub>2</sub> /2% SiH <sub>4</sub> )	425 sccm N <sub>2</sub> O	1 torr	10 W	300 °C

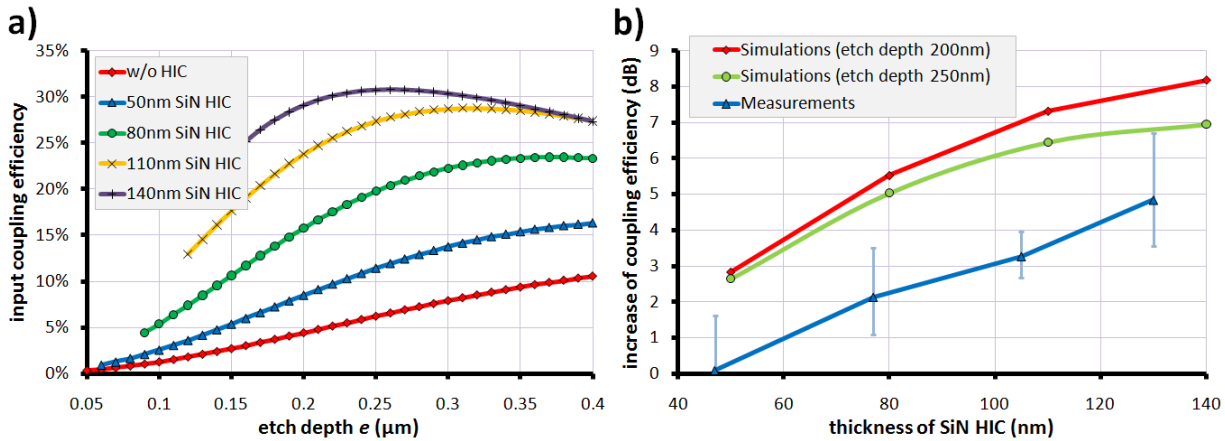


**Figure 5.4:** a) Simulation results on the input coupling efficiency for the measured PI grating coupler system. b) Relative enhancements of the input coupling efficiency for PI grating couplers with SiN HIC of different thicknesses, compared to gratings without HIC. Calculated increase of the coupling efficiency from the simulations given in a) for etch depth of 200 nm and 250 nm as well as experimentally obtained values are shown.

thick SiO<sub>2</sub> layer was deposited, again employing PECVD. The parameters for the deposition of the SiO<sub>2</sub> are given in Table 5.3. With the so prepared Si-wafers, the samples were fabricated using the default fabrication procedure. The etch depth varied slightly over the samples due to variations in the RIE process and was measured to be between 200 nm and 250 nm for the PI gratings and between 215 nm and 225 nm for the SU-8 gratings. The 1  $\mu\text{m}$  thick PI layer was spin coated at a rotation speed of 3600 rpm with PI2771 diluted 1:0.5 in NMP, exposed to UV light and thermally cured. For the SU-8 gratings, the 530 nm thick core layer was spin coated using SU-8 2000.5 from Microchem Corp at a rotation speed of 2500 rpm. After the spin coating step, the SU-8 layer was hard baked at a temperature of 300 °C for 20 min. The cladding of the SU-8 gratings was made from SiO<sub>2</sub> that was deposited using PECVD (see Table 5.3). The PI gratings have a period of 1.75  $\mu\text{m}$  and the SU-8 gratings have a period of 1.5  $\mu\text{m}$ . The gratings were investigated with a 30  $\mu\text{m}$  wide Gaussian beam incident from the cladding at a wavelength of 1.55  $\mu\text{m}$ .

The incident light from a single mode fiber was focused on a 30  $\mu\text{m}$  large spot using a focusing element. The grating couplers coupled the incident light into 30  $\mu\text{m}$  wide waveguides. At the end of the samples, the in-coupled light is transferred into a multi mode fiber with a 50  $\mu\text{m}$  core by end face coupling.

For each HIC thickness, eleven gratings with and eleven gratings without HIC were measured and compared. In order to suppress all possible influences, neighboring gratings with and without HIC were compared on the same sample. An enhancement of the input coupling efficiency induced by the HIC could be confirmed for both material systems. Despite a strong increase of the coupling efficiency

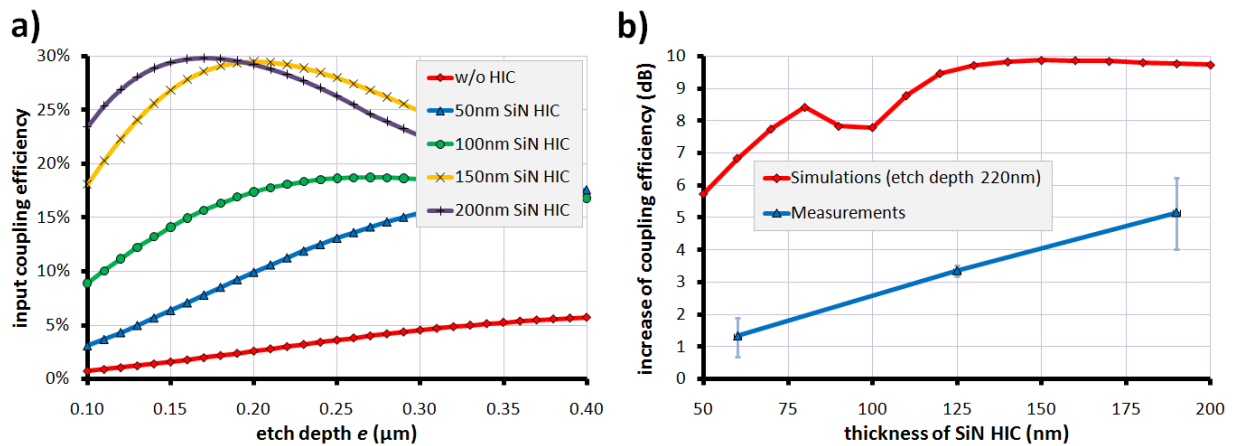


**Figure 5.5:** a) Simulation results on the input coupling efficiency for the measured SU-8 grating coupler system. b) Relative enhancements of the input coupling efficiency for SU-8 grating couplers with SiN HIC of different thicknesses, compared to gratings without HIC. Calculated increase of the coupling efficiency from the simulations given in a) for etch depth of 220 nm and experimentally obtained values are shown.

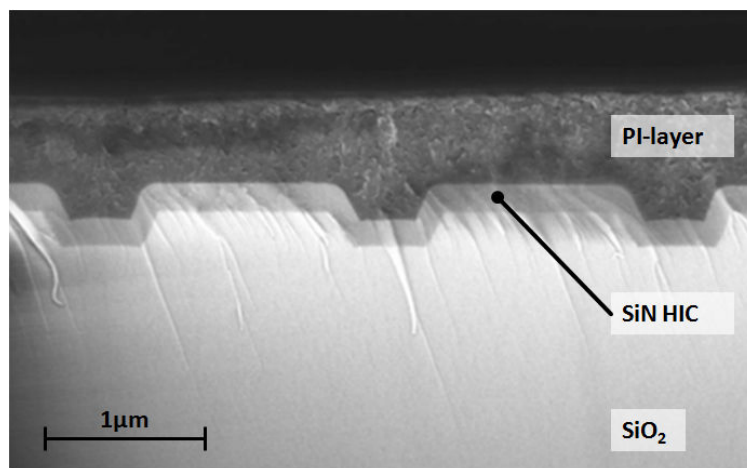


**Figure 5.6:** SEM micrograph of a grating coupler cross section taken from a cleaved facet on a reference sample.

through the HIC, the measured enhancement is not as high as predicted in the simulation. Figure 5.4 and Fig. 5.5 give the simulation results for the fabricated grating structures and compare the predicted coupling efficiency enhancements from the simulations and the measured enhancement for the PI and the SU-8 gratings, respectively. As possible reasons for the mismatch in the enhancement of the coupling efficiency between the simulations and experiments, imperfections of the fabricated grating structures such as variations of the duty cycle and the waveguide core layer thickness as well as non-vertical side walls and corrugations of the surface of the waveguide core layer due to imperfect planarization in the spin coating process were identified. A further reason for the differences between measurements and simulations may be an insufficient quality of the phase front of the 30  $\mu\text{m}$  spot on the grating.

To obtain additional information about the fabricated grating structure, atomic force microscope measurements of the grating and the core layer surface as well as SEM measurements of grating cross sections on reference samples were performed for the PI based gratings. In the SEM micrograph of

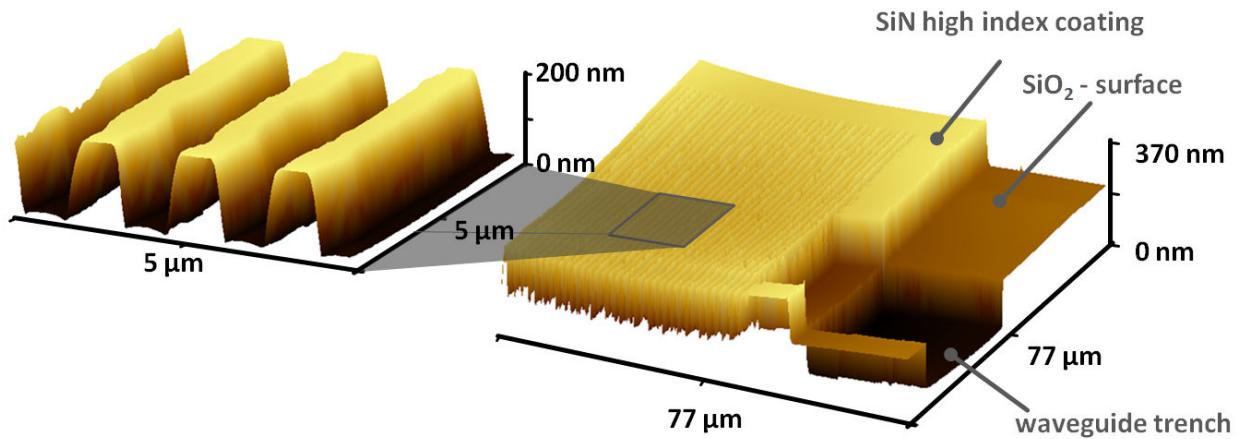


**Figure 5.7:** AFM scan of a grating coupler with HIC and the adjacent 30  $\mu\text{m}$  wide waveguide trench before spin coating of the polymer core layer. The inset shows a detailed scan of the grating region.

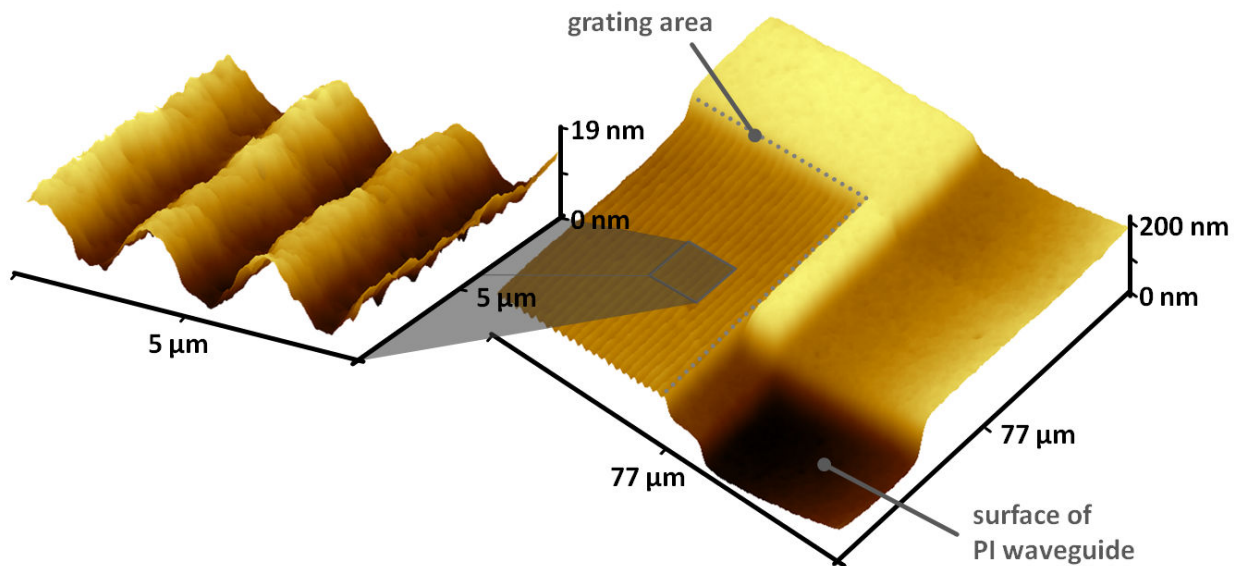


**Figure 5.8:** AFM scan of the PI surface over a grating coupler with HIC and the waveguide trench. The inset shows a detailed scan of the PI surface over the grating region. Both scans reveal the non-perfect planarization of the PI in the spin coating step.

the grating cross section, given in Fig. 5.6, certain deviations of the fabricated grating structure from the simulated model can be recognized, *i.e.* the angle of the grating side walls is only about  $55^\circ$  and variations of the duty cycle of the grating are obvious. The duty cycle of a grating is a critical parameter for the coupling efficiency. Simulations of grating couplers with different duty cycles confirmed that for the uncoated gratings a deviation from the optimum duty cycle by 0.2, which means a duty cycle of 0.3 or 0.7, reduces the absolute coupling efficiency by 2.2 dB. For the gratings with 140 nm SiN HIC, the same variation of the duty cycle leads to a 1 dB decrease of the coupling efficiency. Since the gratings were patterned by conventional UV lithography, the duty cycle may vary from grating to grating and, thus, influence the experimental results.



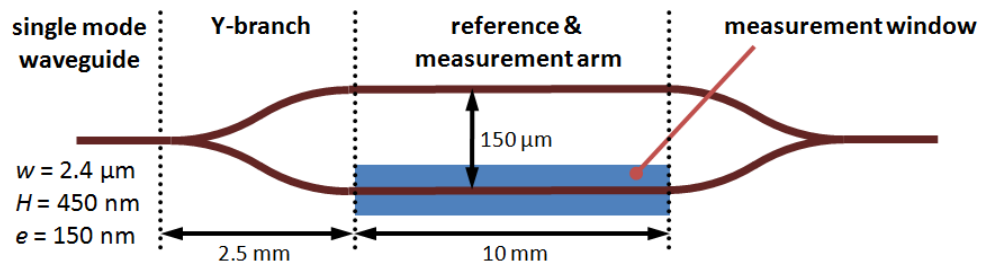


**Figure 5.9:** Waveguide layout of the MZI sensor in end face coupling configuration.

As a second factor, effects of waveguide core layer thickness variations on the enhancement of the input coupling efficiency were numerically investigated. It was found that variations of the core layer thickness have only little influence on the absolute coupling efficiency of a single grating, but can degrade the relative enhancement of the input coupling efficiency between a grating with and without HIC. According to simulations, deviations of  $\pm 100$  nm of the PI core layer thickness on a grating with an etch depth of 250 nm lead to changes of the enhancement of the input coupling efficiency between a grating with 140 nm HIC and an uncoated grating of about 1 dB.

To estimate the effect of the sidewall angle on the coupling efficiency, the Fourier-components, which determine the coupling behavior of the grating, of a perfect rectangular grating cross section and a grating cross section with a sidewall angle of  $55^\circ$  were compared. The Fourier-components for both cross sections are nearly the same, indicating that variations of the sidewall angle have no impact on the coupling efficiency of the grating structure. The SEM picture also shows that the HIC on the sidewalls is as thick as on the horizontal interfaces, which corresponds to the simulation model. AFM measurements of the grating coupler region are given in Fig. 5.7 for the etched  $\text{SiO}_2$  surface with HIC and in Fig. 5.8 for the PI surface on a similar grating after the spin coating step. The AFM scan in Fig. 5.8 revealed that the  $1 \mu\text{m}$  thick PI layer has a corrugated surface with a modulation depth of about 20 nm. The simulation model was adopted to account for this surface topology and the calculations revealed that a modulation of less than 100 nm has only minimal impact on the coupling efficiency.

## 5.4 First measurements with end face coupled MZIs

The aim of the measurements in this section was to quickly prove the proper function of the MZIs as well as to test the stability of the sensor signal, the measurement setup, and the fluidic system without incorporating grating couplers for in- and out-coupling and the surface modification, which is necessary for biosensing experiments.

### Setup description and fluidics system

The samples for the measurements in this section were fabricated using the default fabrication procedure, presented in section 5.1, with a core layer thickness of about 450 nm, but without HIC. The layout of the MZI sensors is depicted in Fig. 5.9. The measurement setup for this kind of measurements is described in Fig. 5.10 and Fig. 5.11. The light from a tunable laser source (TLS,  $\lambda = 1280$  nm to 1360 nm) is transported to the sample by means of a polarization maintaining fiber (PM-fiber). The PM-fiber is cleaved to minimize coupling losses to the sample.

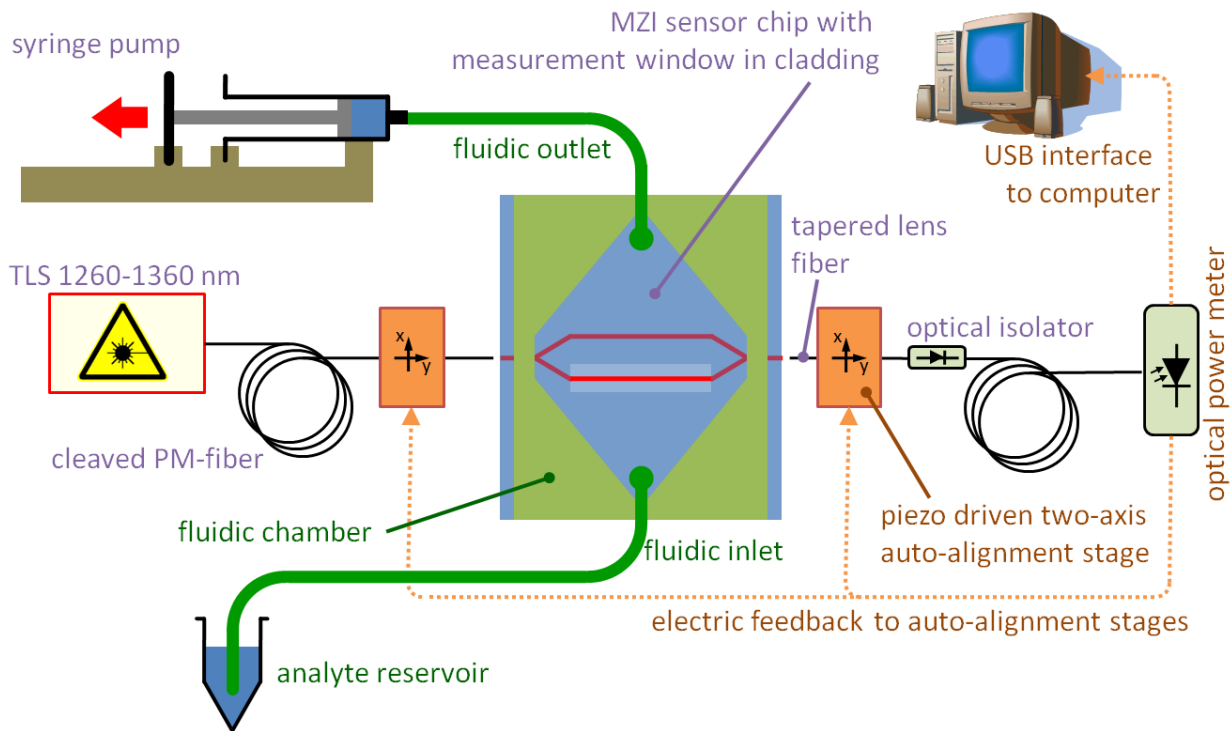


**Figure 5.10:** Depiction of the measurement setup for homogeneous measurements with end face coupling.

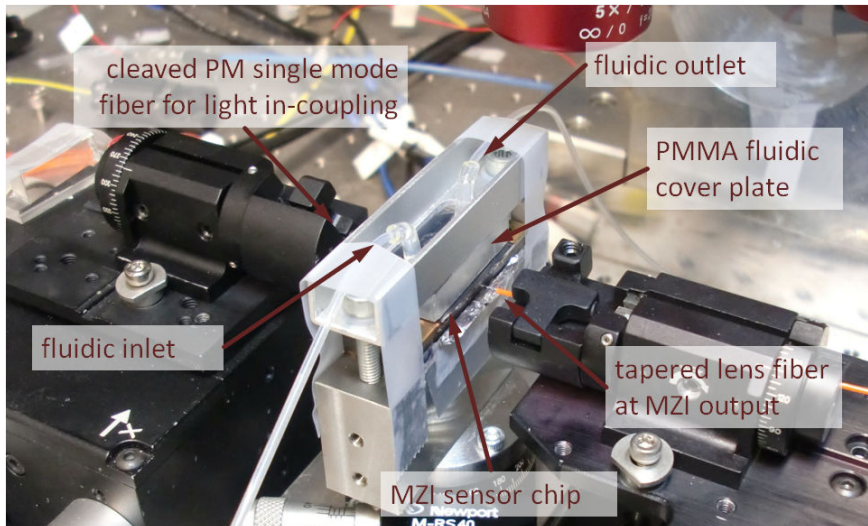


**Figure 5.11:** Measurement setup with mounted MZI sensor chip and fluidic system.

At the end of the sample, the out-coming light is collected by a tapered lens fiber. The alignment of the fibers with respect to the waveguides is assisted by piezo-driven two-axis auto-alignment stages that optimize the position of the fibers at the in- and output for optimum transmission. An optical isolator is inserted between the tapered lens fiber and the optical power meter to improve the signal-to-noise ratio.



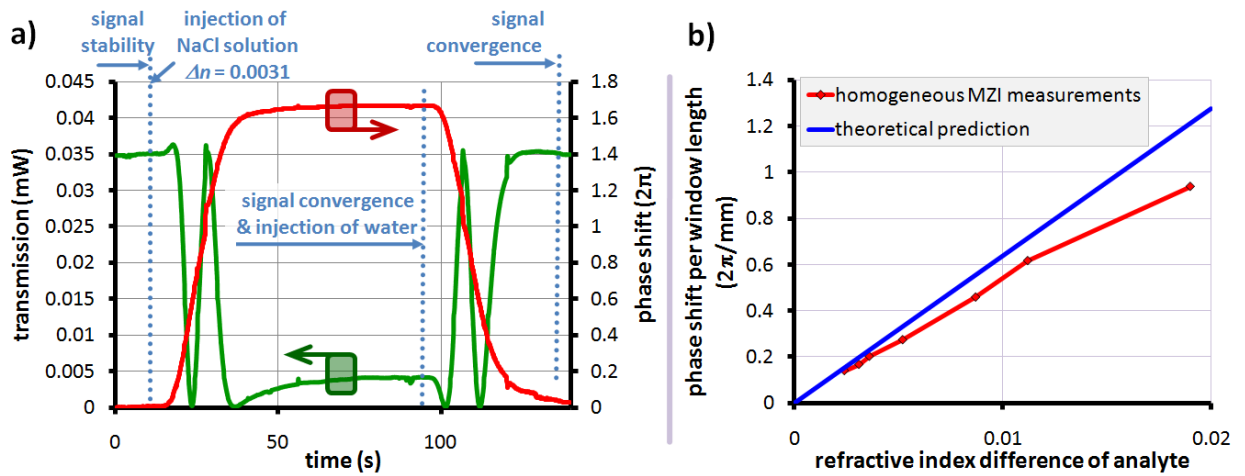


**Figure 5.12:** **a)** Transmission and calculated phase shift of a MZI sensor during a homogeneous measurement. Water that is rinsed over the sensor is exchanged with a NaCl solution ( $\Delta n = 0.0031$ ). This leads to a phase shift of more than  $3\pi$  in the measurement arm. Then, the NaCl solution is exchanged back with water and the sensor goes to its initial state. **b)** Experimentally measured phase shifts of MZI sensors as function of the refractive index difference between water and the NaCl solutions as well as the theoretically predicted values for a slab waveguide with  $H = 450$  nm.

The fluidic system comprises a flow chamber made from PDMS, a PMMA cover plate, a syringe pump, several tubes and an analyte reservoir. The hand-made PDMS flow chamber is placed on the sample and defines a fluidic channel over the measurement window with a height of about  $300\ \mu\text{m}$  and a width of about  $1.2\ \text{mm}$ . The PMMA cover plate, which also provides the fluidic connections, is pressed on the PDMS layer and seals the fluidic channel from the top. After these preparations, the analyte reservoir and the syringe pump can be connected.

### Homogeneous measurements

Homogeneous measurements with MZIs were performed by rinsing water alternating with NaCl solution over the sensor by means of the PDMS flow chamber. Figure 5.12a) shows the transmission curve ( $\lambda = 1.31\ \mu\text{m}$ ) of a measurement with a MZI comprising a  $10\ \text{mm}$  long measurement window. At the beginning, water is rinsed over the sensor and the transmission of the sensor is stable. Then, the water is exchanged with a NaCl solution ( $\Delta n = 0.0031$ ). The higher refractive index of the NaCl solution changes the propagation constant of the waveguide mode in the measurement window and leads to a phase shift with respect to the waveguide mode in the reference arm. This phase shift is transformed to a modulation of the transmitted power by the MZI. The extinction ratio of the MZI, defined as the ration between the maximum and the minimum transmission of the MZI sensor, is larger than  $20\text{dB}$  for this measurement. The accumulated phase shift during this measurement is calculated by reversing the sinusoidal characteristic of the MZI, which is given in equation (3.8) on page 32. If the NaCl solution is again exchanged against water, the phase shift is reversed and the sensor goes back to its initial state. The refractive indices of the NaCl solutions were determined with a refractometer at a wavelength of  $633\ \text{nm}$ . These measurements were performed with different concentrations of NaCl in water. Figure 5.12b) shows the measured and the theoretically predicted phase shift of the sensors as function of the refractive index difference between water and the NaCl solutions. The sensors showed very linear response to the change of the refractive index of the solution. The experimentally obtained phase shifts

are slightly lower than the predicted phase shifts. This can be mainly attributed to deviations of the core layer thickness from the design value of 450 nm and variations of the refractive index of the core layer from that assumed in the calculations. Both quantities have strong influence on the sensitivity of homogeneous measurements. As a summary, three important criteria for successful measurements with a MZI sensor are:

1. Stability of sensor signal as long as the refractive index of the sample fluid that is rinsed over the sensor remains constant.
2. Linearity of the phase shift with respect to index difference between the sample fluids that are rinsed over the sensor.
3. Reversibility of the sensor signal. From the physical point of view, the refractive index of the sample fluid should be the only variable factor during a measurement. For each sample fluid, the sensor has a defined state. The sensor must reach this state independent on the condition before the specific sample fluid is rinsed over the sensor.

## 5.5 MZI online measurements of biotin-streptavidin binding

For the demonstration of the biosensing abilities of the sensors, measurements of the biotin-streptavidin binding process were chosen because of its well-known characteristics (e.g. [183, 184]) and the wide range of published results that can be used for comparison. The interaction between biotin and streptavidin is commonly used to validate the sensitivity of biosensors[28, 29] because of the high mass of the protein streptavidin (60 kDa) that serves as analyte and the strong affinity between biotin and streptavidin (binding constant  $K_a \approx 10^{14}$ ).

Moreover, surface bound streptavidin provides free binding sites for biotin and can be utilized for immobilization of biotinylated ligands such as biotin-tagged DNA strands. Thus, the biotin-streptavidin biorecognition system can serve as flexible platform for more advanced biosensing experiments[30].

### 5.5.1 Modification of the polyimide (PI) surface

A surface modification protocol for the binding of biotin on the PI surface was developed and optimized for maximum streptavidin binding capacity on the PI surface, while not thinning or attacking the PI core layer. In addition, the distance of the molecular binding sites for the target molecules to the polyimide surface was minimized in order to expose the target molecules to the maximum intensity of the evanescent tail of the guided mode, and therefore, achieving maximum sensitivity. Details on the optimization of the developed surface modification protocol have been published in [185].

For cleaning and activation of the surface in the optimized protocol, the polyimide samples were treated with oxygen plasma for one minute at room temperature, 40 W power and 1 mbar in the plasma system Femto (generator: 2.45 GHz) from Diener, Stuttgart, Germany. The effects of atomic oxygen[186], oxygen plasma exposure[187] and oxygen reactive ion etching[188] on polyimide surfaces are well described. Judging from these reports, it can be expected that short oxygen plasma exposure does not destroy the thin film of polyimide, but leads to surface peroxides[188] and hydroxyl (-OH) groups[189] after dipping the activated surface into water. These reactive groups can serve as binding sites in the first

functionalization step with 3-mercaptopropyl trimethoxysilane (MPTMS), which carries reactive thiol (-SH) groups and subsequently may react specifically with the maleimide moiety in the maleimide-PEG<sub>2</sub>-biotin. For the silanization of the oxygen activated polyimide surface, the samples were dipped into MPTMS solution (acetate buffer 0.07 M, 25%v methanol, 2.8%v TritonX-100 and 3%v 3-mercaptopropyl trimethoxy silane) for one hour at room temperature. Finally, the samples were dipped for two hours into M-PEG<sub>2</sub>-Biotin solution (5  $\mu$ M Maleimide-PEG<sub>2</sub>-Biotin solved in ultrapure water with 10%v isopropanol and 10%v phosphate buffer) at room temperature. The resulting biotinylated polyimide surface is used to immobilize streptavidin.

For the measurement of the total streptavidin binding capacity, fluorescence-labeled streptavidin was bound to the biotinylated PI surface. Thus, 1  $\mu$ M Chromeon 642-streptavidin in 150 mM PBS buffer was spotted by means of a pipette on ten different biotinylated samples. After a reaction time of 1 h and cleaning, the samples were analyzed by fluorescence scans. The fluorescence intensity was measured at 633 nm excitation wavelength and 692 nm emission filter with a fluorescence scanner. For quantification, a calibration set was prepared on untreated polyimide samples. Different concentrations (10-200 fmol/mm<sup>2</sup>) of Chromeon 642-streptavidin were spotted on untreated polyimide samples and the spots were dried at room temperature in the dark to create a solid standard array. With the resulting calibration curve a concentration of  $144 \pm 20$  fmol/mm<sup>2</sup> was determined for ten biotinylated samples.

This result for the surface coverage with streptavidin is better than what can be expected in theory on a perfectly planar surface. The streptavidin ligand has a size of  $4.5 \times 4.5 \times 5.8$  nm<sup>3</sup>[190] and occupies a binding area of 26 nm<sup>2</sup>. By optimal (100%) packing density, the concentration of the streptavidin on the planar surface would be estimated as 64 fmol/mm<sup>2</sup>. The published closest coverage of streptavidin on planar surfaces are about 66% (42 fmol/mm<sup>2</sup>) for two dimensional crystals[190, 191] and 40% (26 fmol/mm<sup>2</sup>)[28] on a silicon surface with a streptavidin monolayer. Higher concentrations of streptavidin, *e.g.* 37,000 fmol/mm<sup>2</sup> have been achieved employing a three-dimensional binding matrix[192]. The result of  $144 \pm 20$  fmol/mm<sup>2</sup> evidences a more than two dimensional binding behavior of streptavidin on the polyimide surface.

In order to gain additional information on the reasons of the high binding capacity of the PI surface, the surface structure and roughness were monitored by atomic force microscopy (AFM). Polyimide samples were analyzed by AFM in tapping mode before treatment, after MPTMS modification and biotin functionalization, as well as after streptavidin immobilization (see Fig. 5.13). The untreated polyimide film showed a smooth surface with a mean roughness,  $R_a = 0.379$  nm. After the MPTMS functionalization, the surface roughness increased to a  $R_a = 0.56$  nm and nanoporous structures with a maximal depth of 10 nm and a diameter of up to 50 nm have been found. The surface properties of the biotin functionalized sample were similar with  $R_a = 0.57$  nm.

After the immobilization of Chromeon 642-streptavidin, the surface shows in comparison less nanoporous structures and the maximal depth was about 3 nm. These results prove that the proposed polyimide film functionalization method does not cause a significant change of the surface roughness, which is beneficial for keeping the propagation losses in the waveguide low. Nevertheless, it seems that the nanoporous structure of the functionalized surface is responsible for the high streptavidin binding capacity by providing an enlarged binding area with a high number of possible binding sites.

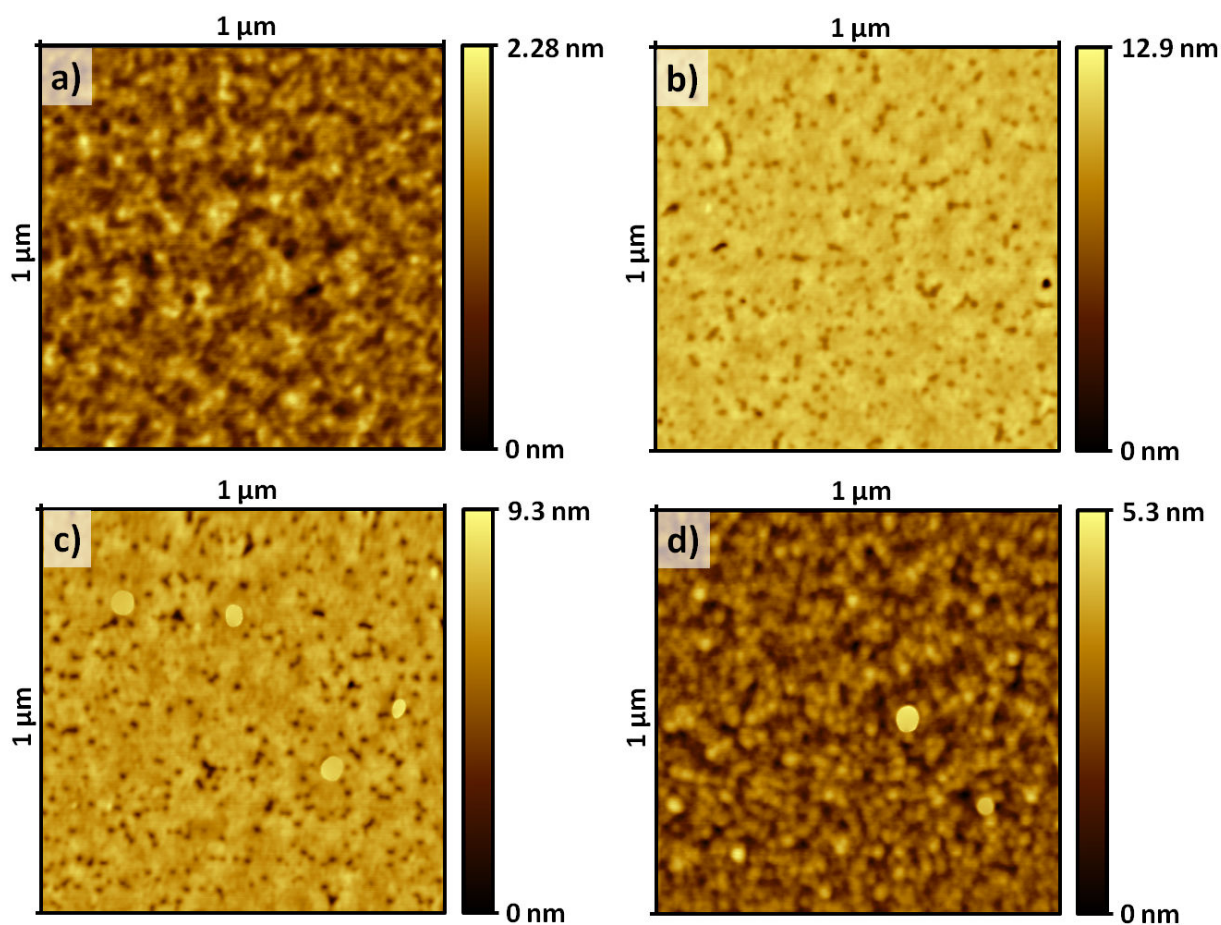


**Figure 5.13:** AFM scans of the PI surface before and after the surface modification steps; **a)** before treatment, **b)** after MPTMS modification, **c)** after biotin functionalization and **d)** after streptavidin immobilization.

### 5.5.2 Reproducibility of binding experiments and blocking of the modified PI surface

In the first online measurement of biotin-streptavidin binding on the sensor surface, the sensor was first rinsed with 150 mM phosphate buffered saline (PBS) solution (pH 7.2) at a flow rate of 20  $\mu\text{l}/\text{min}$ , which corresponds to an average flow speed of about 2.5 cm/min. This allowed verifying of the stability of the sensor signal. At the beginning of the measurement, the wavelength of the tunable laser light source was adjusted to a point where the MZI showed maximum transmission. Although this point does not show maximum sensitivity for small changes of the effective index of the propagating mode, it simplifies the calculation of the phase shift out of the sensor transmission. Then, a concentration of 10  $\mu\text{g}/\text{ml}$  Chromeon 642-streptavidin dissolved in PBS at a flow rate of 20  $\mu\text{l}/\text{min}$  was introduced to the 10 mm long measurement window of the sensor and the change in the transmission of the MZI sensor as function of time was recorded. Figure 5.14 plots the transmitted power of the MZI sensor during this measurement. From this data, the accumulated phase shift during this measurement was calculated by reversing the sinusoidal characteristic of the MZI (Eq. (3.8) on page 32). The calculated phase shift for this measurement is given in the same diagram as the transmitted power in Fig. 5.14. For this measurement, the insertion loss from the laser source to the photo detector is better than 16 dB. The ratio between maximum and minimum transmitted power of the MZI is 14 dB.

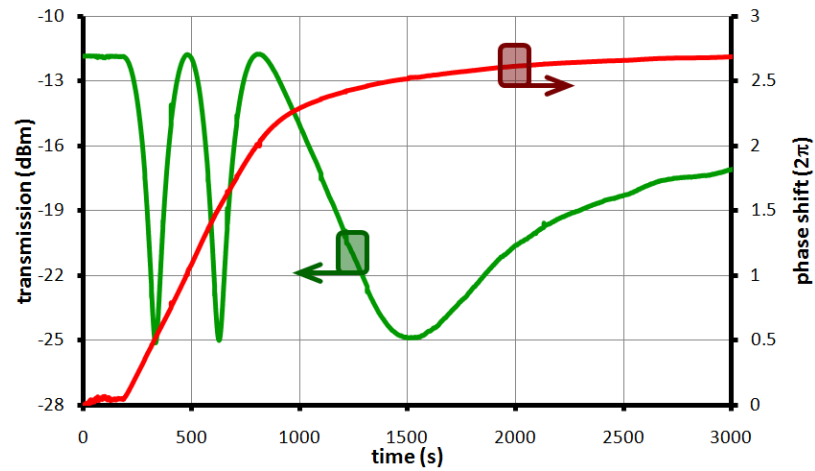


**Figure 5.14:** Transmitted power and calculated phase shift of a MZI sensor (10 mm long measurement window) with a non-blocked surface during the detection of 10  $\mu\text{g/ml}$  streptavidin dissolved in PBS solution. The ratio between the maximum and the minimum transmission of the MZI sensor is 14 dB, with an insertion loss of about 16 dB. ( $\lambda = 1.31 \mu\text{m}$ )

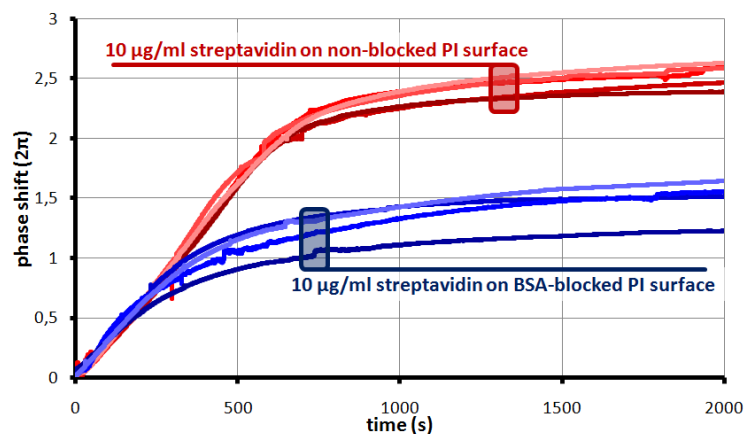


**Figure 5.15:** Phase shifts obtained from MZI measurements of biotin-streptavidin binding (10  $\mu\text{g/ml}$  concentration of streptavidin in PBS solution) on BSA-blocked (blue lines) and non-blocked (red lines) PI surfaces. The BSA-blocking of the PI surface reduces the maximum streptavidin binding capacity by about 40%, but suppresses non-specific binding. The standard deviation at  $t = 2000 \text{ s}$  of these measurements is 4% for the non-blocked surfaces and 12% for the BSA-blocked surfaces.

Repeated measurements of the same streptavidin concentration on different samples were performed to estimate the standard deviation of the phase shift. These measurements are given as red curves in Fig. 5.15. All samples showed very similar behavior. The slope of the phase shift is de facto identical for all curves. At the time of 2000 s the calculated phase shift of these measurements varies between  $2.39 \cdot 2\pi$  and  $2.63 \cdot 2\pi$ . The calculated standard deviation for this set of curves is around 4%.

Experiments verified that no significant amount of streptavidin binds to an untreated PI surface, which was tested by rinsing PBS solution alternating with 10  $\mu\text{g/ml}$  streptavidin in PBS solution over an untreated sensor. In such measurements, the sensors showed a perfectly reversible characteristic. Nev-

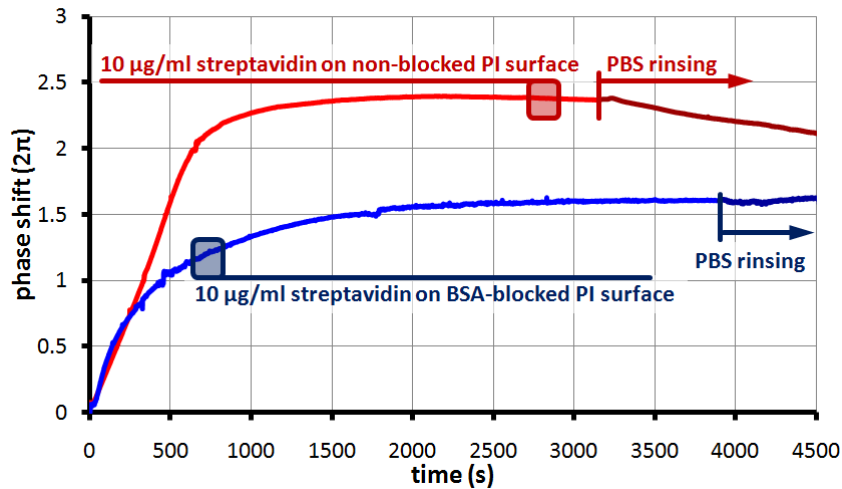


**Figure 5.16:** Comparison of results on streptavidin binding and rinsing with PBS solution on BSA-blocked and non-blocked sensors. On the BSA-blocked sensor the phase shift remains stable during PBS rinsing, while on the non-blocked surface weakly bound streptavidin is washed away, thus reducing the phase shift.

ertheless, it was found that the modified surface not only attracts streptavidin molecules on the desired biotin binding sites, but there is also a certain amount of non-specific binding. This became evident when samples were prepared by exposing the surface to oxygen plasma and MPTMS solution, but without dipping into M-PEG<sub>2</sub>-Biotin solution. If then pure PBS buffer and PBS buffer with streptavidin is rinsed over the sensor, the sensor showed a non-reversible response, which indicates streptavidin binding, even without biotin present at the sensor surface. In additional experiments it was verified that unspecific binding of streptavidin on the PI surface can be blocked employing bovine serum albumin (BSA). For this purpose, the sensor surface was exposed to oxygen plasma and MPTMS solution, but instead of dipping the samples into M-PEG<sub>2</sub>-Biotin solution, the samples were dipped into phosphate buffered saline (PBS) buffer solution with 100 µg/ml BSA for 30 min. After blocking of the MPTMS functionalized surface with BSA, PBS buffer with and without streptavidin was rinsed over the sensor surface. The small observed response was caused by the slightly different bulk refractive index of the PBS solution with streptavidin and could be fully reversed by rinsing the sensor again with pure PBS, which proves that the BSA blocking procedure successfully prevents non-specific binding of streptavidin on the sensor surface.

After these experiments, online measurements of streptavidin binding on BSA-blocked sensors with a concentration of 10 µg/ml were done in the same way as on the non-blocked surfaces. The results for the measurements with the BSA-blocked surfaces are given as blue lines in Fig. 5.14. Comparing the results of the sensors with and without BSA-blocked surfaces revealed that the total binding capacity of streptavidin, and therefore, the maximum achievable phase shift during a measurement is reduced by about 40% when using a BSA-blocked surface. From these results, it can be concluded that without BSA blocking, 40% of the sensor response is induced by non-specific binding for high concentrations of streptavidin on the PI surface.

The samples with and without BSA-blocking show a different behavior when rinsing pure PBS solution over the sensor surface after the streptavidin binding process. In contrast to BSA-blocked samples, where rinsing with PBS after the streptavidin binding process does not result in a reduction of the phase shift, rinsing with PBS solution after the measurement on non-blocked samples reduces the phase shift



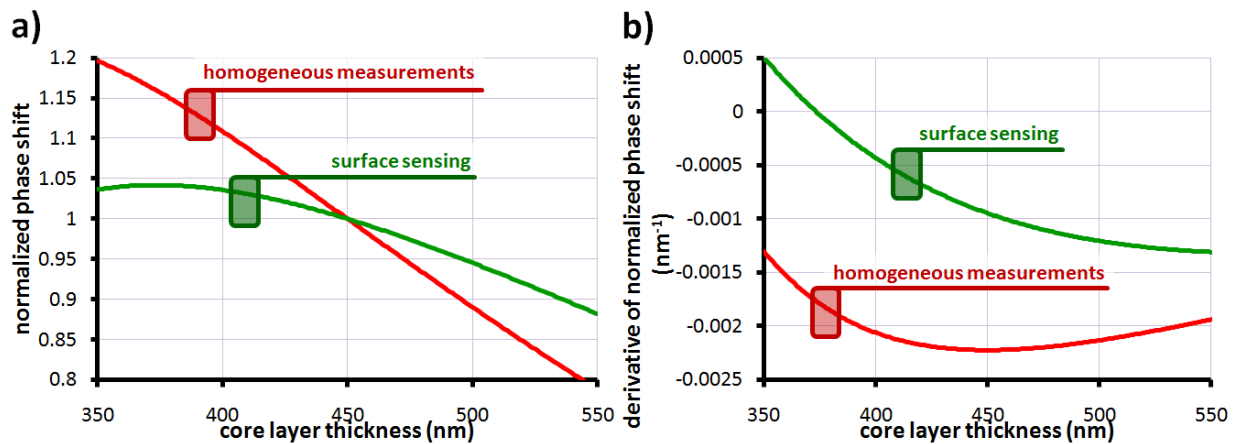


**Figure 5.17:** a) Calculated sensitivity for surface sensing and homogeneous sensing experiments as function of the waveguide core layer thickness, normalized to the sensitivities at the design thickness of 450 nm. b) Derivations of the curves given in a). For small variations of the core layer thickness, the ratio between the derivative of the homogeneous sensitivity and the derivative of the surface sensitivity gives the ratio between the variations of the phase shift in homogeneous and surface sensing experiments.

by about 10% because weakly bound streptavidin is washed away. The corresponding measurements can be compared in Fig. 5.16. On the other hand, these results not only indicate that on the BSA-blocked sensors all streptavidin on the sensor surface has strongly bound to its biotin counterpart, but also that the BSA molecules have stable bindings to the sensor surface and cannot be washed away in a fluidic stream.

As reasons for the variations in the repeated measurements of 10  $\mu\text{g/ml}$  streptavidin, which are given in Fig. 5.15, one can identify two possible classes of sources: deviations in the physical sensor geometry from one sample to another and variations in the surface modification procedure. From the physical point of view, the sensitivity of the sensors in surface sensing applications as well as for homogeneous measurements is defined by the layout of the sensor, the refractive indices of the materials and the cross section of the waveguides. The layout of the sensor, including the arrangement of the waveguides, but also the length and the position of the measurement window is defined by a lithography step, and should, therefore, be reproducible to a high degree. The refractive indices of the  $\text{SiO}_2$  substrate should not be subject to change. The waveguide core polymer PI and the cladding material Ormoclad are commercial products with defined properties of high stability. It can, therefore, be assumed that if processed in a reproducible way, the refractive indices of these materials are constant on all samples.

The waveguide cross section includes the width and etch depth of the waveguide trenches and the thickness of the waveguide core layer. The waveguide width is defined in the lithography step in a reproducible way. In addition, it has only a minor influence to the sensitivity parameters, which are mainly determined by the vertical light distribution in the waveguide. The vertical light distribution mostly depends on the waveguide core layer thickness, which is again dependent on the spin coating process of PI, but as argued in section 5.2, to a smaller degree also on the etch depth of the waveguide trench. The etch depth is a physical parameter that can be measured easily and it was found that it can be assumed that the etch depth does not vary more than  $\pm 10\%$ . The exact thickness of the PI after the spin coating process depends on several parameters, such as the ambient temperature and humidity or the exact amount of organic solvent in the PI precursor.



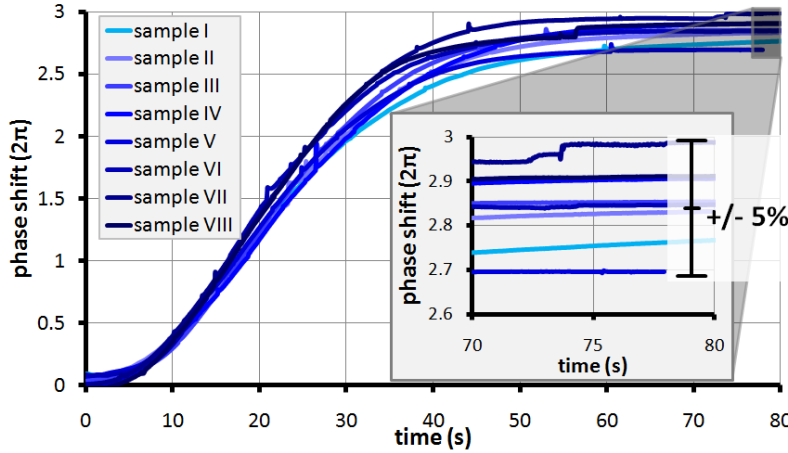


**Figure 5.18:** Phase shifts of homogeneous measurements ( $\text{H}_2\text{O}$  exchanged against PBS solution,  $\Delta n = 0.0052$ ) on samples also used for streptavidin binding experiments. From the variation in the homogeneous measurements ( $\pm 5\%$ ) it can be calculated that these samples should not vary more than  $\pm 2\%$  in surface sensing experiments.

Importantly, under the assumption that the thickness of the waveguide core layer is the only relevant parameter varying, it can be stated that there is a relationship between variations in homogeneous measurements and in surface sensing scenarios. As a result, if for a set of samples data exists for homogeneous measurements, the expected variations in surface sensing experiments can be calculated from the known variations in the homogeneous measurements. Figure 5.17a) plots the calculated sensitivity for surface sensing and homogeneous sensing experiments as function of the waveguide core layer thickness, normalized to the sensitivities at the design thickness of 450 nm. From this data, it can be concluded that if a specific sensor has a core layer thickness of 500 nm, instead of the design value of 450 nm, its homogeneous sensitivity drops by about 12% and its surface sensitivity drops by about 5.5%. The converse argument is that if a sample shows 12% less sensitivity for homogeneous sensing than a sample with 450 nm core layer thickness, this sample has a core layer thickness of 500 nm and its sensitivity in surface sensing applications is reduced by 5.5%.

For small deviations of the core layer thickness from the design value, it can be assumed that the relation between the sensitivity and the thickness is linear and the derivative of the sensitivities (presented in Fig. 5.17b)) gives the slope of the sensitivity parameter as function of the core layer thickness. Therefore, the ratio between the derivative of the homogeneous sensitivity and the derivative of the surface sensitivity gives the ratio between the variations of the phase shift in homogeneous and surface sensing experiments.

For the design thickness of 450 nm, the derivation of the homogeneous sensitivity is  $-0.0022 \text{ nm}^{-1}$ , while the derivative of the surface sensitivity is  $-0.0009 \text{ nm}^{-1}$ . The ratio between these values

$$-0.0009 \text{ nm}^{-1} / -0.0022 \text{ nm}^{-1} = 0.409 \quad (5.1)$$

gives the ratio between variations in homogeneous measurements and surface sensing applications. For each sample used for streptavidin binding experiments, a homogeneous measurement was performed by rinsing first pure  $\text{H}_2\text{O}$  and then PBS solution over the samples ( $\Delta n = 0.0052$ ). Figure 5.18 shows examples of these homogeneous measurements. From this data, it can be concluded that these

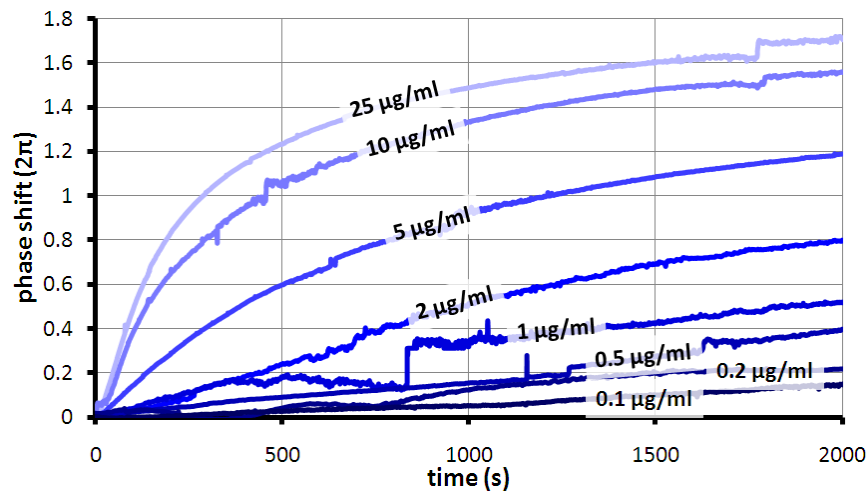


**Figure 5.19:** Measured phase shifts as function of time for different streptavidin concentrations in PBS solution on BSA-blocked PI surfaces ( $\lambda = 1.31 \mu\text{m}$ ). The steps in the measurement curves (e.g. curve for  $25 \mu\text{g/ml}$  at a time of 1750 s or curve for  $1 \mu\text{g/ml}$  at a time of 850 s) are caused by the correction of a misalignment of the input or output fiber. The setup suffers from a slow mechanical drift, which is corrected intentionally by activating the fiber auto alignment system. The automatic switching of the optical power meter between different measurement ranges can also result in dips or peaks in the measurement curves, e.g. in the curve for  $10 \mu\text{g/ml}$  at a time of 330 s or curve for  $0.5 \mu\text{g/ml}$  at a time of 1150 s.

samples that have been produced in different batches in different weeks in the cleanroom, differ in homogeneous measurements by about  $\pm 5\%$ . With the calculated ratio of 0.409 it can be expected that the same samples vary about  $\pm 0.409 \cdot 5\% = 2.05\%$  in surface sensing scenarios. From this result, it can be concluded that the main part of the deviations in the streptavidin binding experiments is caused by variations in the biology/chemical part of the sensor.

### 5.5.3 Concentration dependent measurements

To get information about the dynamic range of the sensors, measurements were performed for different concentrations of streptavidin in PBS solution ranging from  $25 \mu\text{g/ml}$  down to  $0.1 \mu\text{g/ml}$ . Figure 5.19 and Fig. 5.20 summarize these measurements, for BSA-blocked and non-blocked surfaces respectively. As expected, the higher the streptavidin concentration, the larger the induced phase shift in the interferometer. The steps in the measurement curves (e.g. curve for  $25 \mu\text{g/ml}$  at a time of 1750 s or curve for  $1 \mu\text{g/ml}$  at a time of 850 s in Fig. 5.19) are caused by the correction of a misalignment of the input or output fiber. The setup suffers from a slow mechanical drift, which is corrected intentionally by activating the fiber auto alignment system. The automatic switching of the optical power meter between different measurement ranges can also result in dips or peaks in the measurement curves, e.g. in the curve for  $10 \mu\text{g/ml}$  at a time of 330 s or curve for  $0.5 \mu\text{g/ml}$  at a time of 1150 s in Fig. 5.19.

Figure 5.21 plots the measured phase shift as a function of the streptavidin concentration for fixed times of 200 s, 500 s, and 1000 s. For the lowest concentration of  $0.1 \mu\text{g/ml}$  streptavidin on the BSA-blocked sensors, the phase shift is  $0.007 \cdot 2\pi$  at  $t = 200 \text{ s}$ ,  $0.028 \cdot 2\pi$  at  $t = 500 \text{ s}$  and  $0.0549 \cdot 2\pi$  at  $t = 1000 \text{ s}$ . In order to facilitate measurements of low concentrations with small resulting phase shifts, it is beneficial to start close to a point of minimum transmission by adjusting the wavelength of the laser

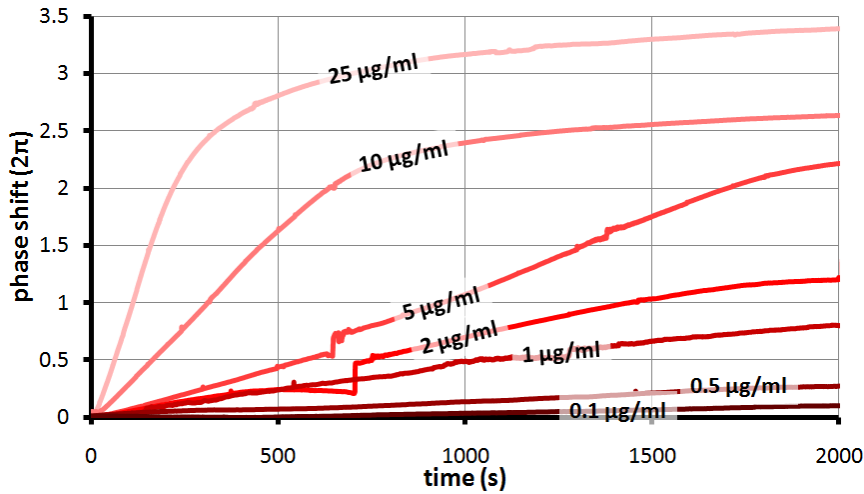


**Figure 5.20:** Measured phase shifts as function of time for different streptavidin concentrations in PBS solution on non-blocked PI surfaces ( $\lambda = 1.31 \mu\text{m}$ ).

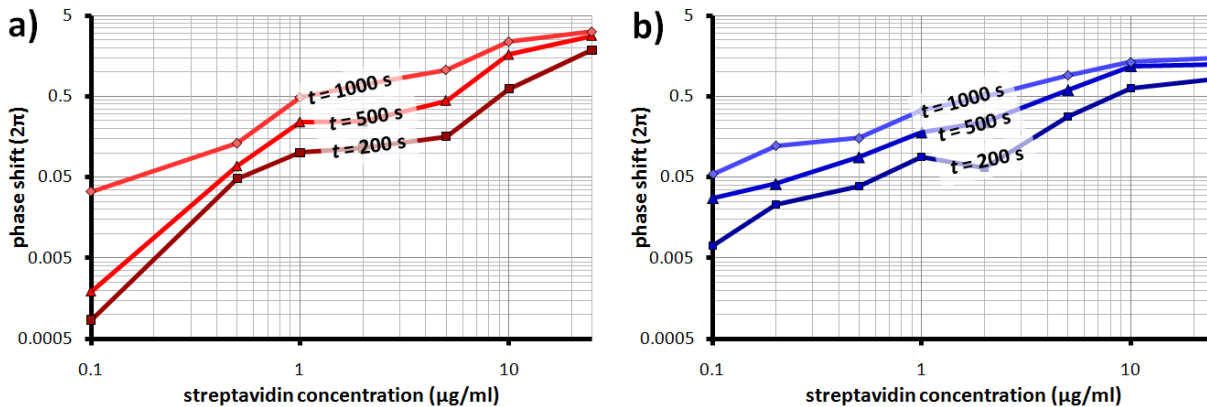


**Figure 5.21:** Phase shift as function of the streptavidin concentration measured at 200 s, 500 s and 1000 s, for **a)** non-blocked and **b)** BSA-blocked sensors.

source. If the transmitted power is measured on a linear scale, the most sensitive point of the MZI for small changes of the effective mode index is the so called quadrature point, where the MZI transmit half of the maximum power. When measuring on a logarithmic scale, the points of maximum sensitivity are shifted towards the transmission minimum. The higher the extinction ratio, the higher is the maximum sensitivity and the closer are the points of maximum sensitivity to the transmission minimum. Keeping that in mind and assuming a ratio of 15 dB between the minimum and maximum transmission of the MZI, the given phase shifts translate to a change in the transmission by nearly 1dB for  $t = 500 \text{ s}$  and nearly 3 dB for 1000 s, which can be resolved easily.

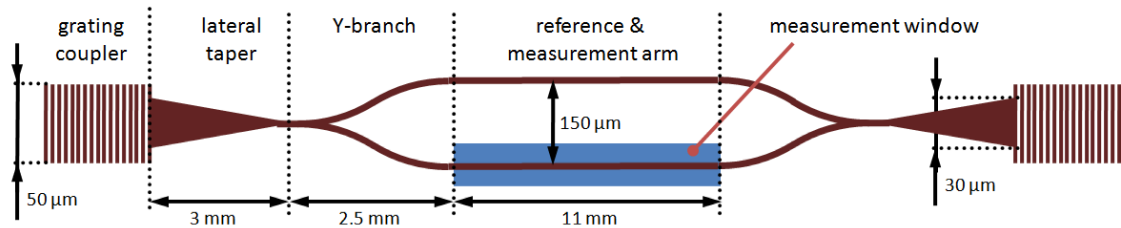


Figure 5.22: Waveguide layout of the MZI sensor with grating couplers.

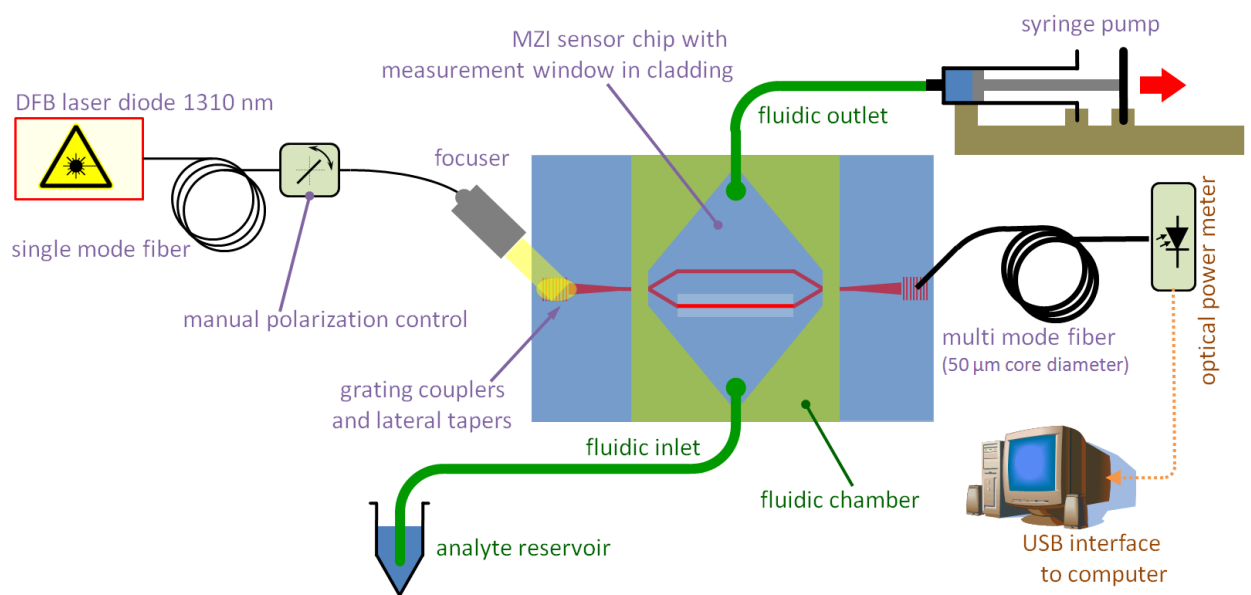
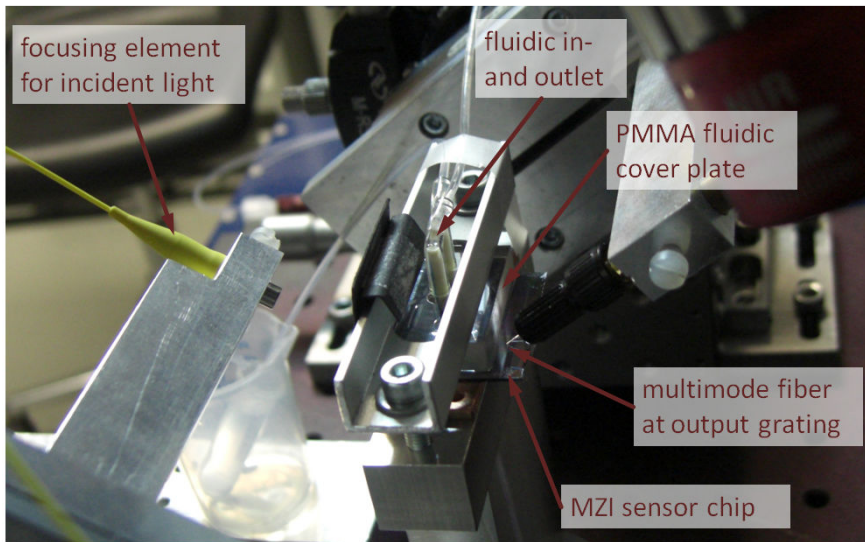


Figure 5.23: Schematic of the measurement setup for samples with grating couplers.

## 5.6 Verification on MZIs with grating couplers

The results presented in the previous section have been obtained from samples that were measured in end face coupling configuration. The fabrication of such samples is faster and less critical compared to samples with grating couplers, because the deposition of the HIC can be omitted and no sub- $\mu\text{m}$  structures have to be patterned. On injection molded substrates, an end face coupling configuration cannot be applied due to the fact that no high quality sample end facet can be provided by cleaving of the samples like on a silicon wafer. Therefore, grating couplers are needed to couple light into and out of waveguides on injection molded substrates.

In order to demonstrate the sensor concept with grating couplers as coupling elements and to verify some of the results from the previous section with this new layout, several experiments, carried out on samples in end face coupling configuration, have been repeated on samples with grating couplers. The layout of the new sensor samples (given in Fig. 5.22) is transferable on injection molded substrates without any changes.



**Figure 5.24:** Picture of the measurement setup for samples with grating couplers.

### Device and setup

The MZIs on these samples are sandwiched between two lateral tapers that increase the waveguide width to  $30\ \mu\text{m}$  and lead to  $50\ \mu\text{m}$  wide gratings with a period of  $1.75\ \mu\text{m}$ . At a wavelength of  $1310\ \text{nm}$  the optimum angle for in- and out-coupling is around  $52^\circ$  for this grating coupler period. The MZI design itself is identical to that used on the samples in end face configuration, except that the measurement window is one millimeter longer, and therefore, has a length of eleven millimeters. The samples have been fabricated according to the default fabrication procedure given in section 5.1 with a core layer thickness of about  $500\ \text{nm}$ .

The setup for these measurements is depicted in Fig. 5.23, while a picture of the setup is given in Fig. 5.24. The light from a distributed feedback laser diode with a center wavelength of  $1310\ \text{nm}$  is transported employing a single mode fiber to a manual polarization controller and subsequently to a focusing element that focuses the light to a  $30\ \mu\text{m}$  spot on the input grating coupler. At the end of the sample, the out-coming light from the output grating coupler is collected by a cleaved multi-mode fiber with a core diameter of  $50\ \mu\text{m}$ . The alignment of the focusing element and the multi mode fiber with respect to the grating couplers is done by manual five-axis alignment stages. These stages allow the adjustment of the focus point of the focusing element and the tip of the multimode fiber in all three dimensions as well as the adjustment of the coupling angle and the focus distance without losing the focal point. The light collected from the multimode fiber is then guided to a photodetector. The fluidic system was applied in the same way as on the samples in end face coupling configuration.

### Experiments

On the sensors with grating couplers, measurements of  $10\ \mu\text{g/ml}$  streptavidin binding on BSA-blocked surfaces were repeated. The calculated phase shifts of these measurements are given as green lines in Fig. 5.25, in addition to the results of the corresponding measurements in end face coupling configuration (blue lines). Comparing these two sets of curves, it becomes obvious that the induced phase shift on the MZIs in grating coupler configuration is about 35% higher than the results from the MZIs

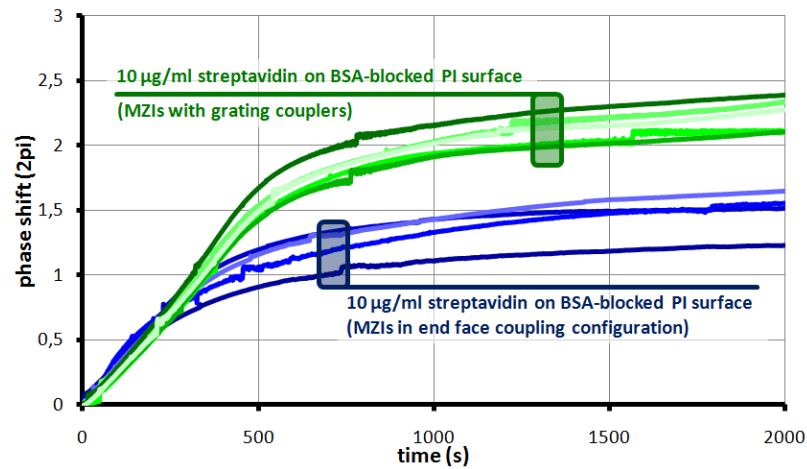


**Figure 5.25:** Phase shifts of biotin-streptavidin binding experiments ( $10 \mu\text{g/ml}$  concentration of streptavidin in PBS solution) obtained from MZIs in end face coupling configuration (blue lines) and with grating couplers (green lines) on BSA-blocked PI surfaces. The standard deviation of the measurements with grating couplers is 5.5% ( $t = 2000 \text{ s}$ ).

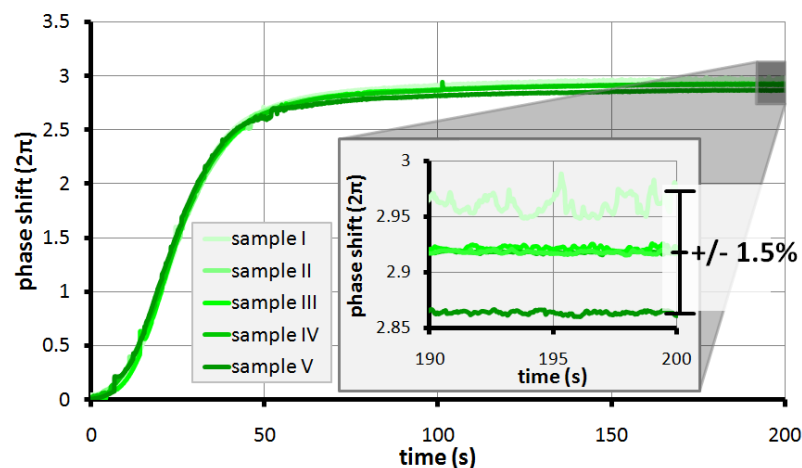


**Figure 5.26:** Phase shifts of homogeneous measurements ( $\text{H}_2\text{O}$  exchanged against PBS solution,  $\Delta n = 0.0052$ ) on MZIs with grating couplers also used for streptavidin binding experiments. From the variation in the homogeneous measurements ( $\pm 1.5\%$ ) it can be calculated that these samples should not vary more than  $\pm 0.61\%$  in surface sensing experiments.

with end face coupling. This higher signal can be partly explained by the fact that the measurement window is 10% longer than on the MZIs measured by end face coupling. The remaining 25% percent difference can be most likely attributed to variations of the surface modification. Another reason might be the modified fluidic chamber. While the end face coupled MZIs were placed in the middle of the  $3 \text{ cm} \times 3 \text{ cm}$  silicon chip, the MZIs with grating couplers were placed near the border of the silicon chip, necessitating another PDMS flow chamber with a different layout of the fluidic channels. This may have lead to different flow conditions on the sensor surface raising the streptavidin binding, and therefore, the sensor signal.

The homogeneous measurements performed on these samples (see Fig. 5.26) show only little deviations between different samples. The samples were processed in the same batch in the cleanroom, and therefore, have variations of only  $\pm 1.5\%$  in their homogeneous sensitivity. According to the calculations in the previous section, this value can be translated to an expected variation of  $\pm 1.5 * 0.409 = 0.61\%$  for surface sensing applications.



## 6 Summary and conclusion

The focus of this work was the demonstration of a planar integrated single mode polymer waveguide based sensor that employs the highly sensitive Mach-Zehnder interferometer (MZI) principle for the detection of binding events of biomolecules on the sensor surface. The design of the sensor was kept fully compatible with cost-efficient mass production technologies for polymers, such as injection molding and spin coating. This work is to be seen as one step towards the realization of all-polymer sensor chips, where the low index polymer substrate carrying all necessary optical structures for the sensor is fabricated by injection molding, while the high index core layer and the low index cladding layer are applied by spin coating. This approach takes full advantage of the powerful technology platform that is available for polymer processing and makes the proposed device attractive as disposable sensor for applications where ultra-high sensitivity is not required and fabrication costs are a driving factor.

The necessary theoretical background for the design of the sensor was given and followed by an overview and comparison of currently used optical sensor concepts and commercially available products utilizing photonic sensor concepts for the detection of biomolecules. Polyimide (PI,  $n = 1.65$ ) was selected as waveguide core material andOrmoclad ( $n = 1.52$ ) was selected for the UV-patternable cladding. Then, the optical elements for the MZI sensor were rigorously simulated and the polymer waveguide based sensor was designed using the novel approach of utilizing thin film polymer waveguides for biosensing applications. Particular attention was paid to the simulations of grating couplers in waveguide material systems with comparatively low index contrast, which are a critical element for the realization of the all-polymer sensor on the injection molded substrates. The fact that a thin inorganic high index coating (HIC) on top of small grating couplers, used to couple light into narrow single mode waveguides by means of lateral tapers, significantly increases the coupling efficiency was predicted with simulations and experimentally verified. In the simulations, the input coupling efficiency of PI based grating couplers of about 5%, was increased to more than 30% by the application of a silicon nitride (SiN) HIC. In the experiments, an increase of the coupling efficiency by about 5dB due the application of a HIC was verified. Insights gained from these simulations and experiments are not only valid for PI waveguide grating couplers, but also for all similar low-index contrast material systems.

A surface modification protocol for the binding of biotin on the PI surface was developed for maximum streptavidin binding capacity, while not attacking the thin PI core layer. With fluorescent labeled Chromeon 642-streptavidin, a maximum population density of  $144 \text{ fmol/mm}^2$  was measured on the PI surface. This result for the surface coverage with streptavidin is better than what can be expected in theory on a perfectly planar surface and evidences a more than two-dimensional binding behavior of streptavidin on the PI surface, which can, at least partly, be explained by the nano-porous structure of the PI surface.

Finally, the MZI biosensor on an inorganic substrate, with a layout ready to be transferred to an injection molded substrate without any changes, was demonstrated in the biotin-streptavidin system, which is commonly used to benchmark the performance of optical biosensors. Results of online measurements of streptavidin binding for concentrations ranging from  $25 \text{ }\mu\text{g/ml}$  down to  $0.1 \text{ }\mu\text{g/ml} = 1.66 \text{ nMol}$  were shown and a high factor of reproducibility of the binding experiments was confirmed. Highly sensitive

devices have been demonstrated for the detection of the protein streptavidin. Examples are sub-nM detection of streptavidin with ring resonators in the most sensitive SiO<sub>2</sub>/SiN material system at a wavelength of 633 nm by Ksendzov et al.[96] or the detection of 60 fM streptavidin with a SOI ring resonator array by Iqbal et al.[30]. Due to the comparatively low refractive index contrast, the demonstrated polymer based sensor cannot compete with these demonstrations in terms of sensitivity. Nevertheless, it has to be mentioned that depending on the instrumental effort, the achievable sensitivity even of SOI based sensing devices can be significantly lower than that of the above cited systems. For instance, the smallest measured streptavidin concentrations reported in recent publications employing SOI ring resonators are in the range of 0.1 µg/ml[28] and 1 µg/ml[193], which is, despite the comparatively low theoretical surface sensitivity and the large wavelength of 1310 nm, similar to the results in this work, where the focus was laid on the development of a sensor device that can be mass-produced at minimal costs and effort.

The theoretical sensitivity of the sensor can be improved by a factor of four by changing the wavelength to 633 nm and adopting the waveguide cross sections and the grating couplers to this wavelength. Nevertheless, the fabrication of smaller structures is beyond the possibilities of conventional UV-lithography. This limitation ceases to apply after the transfer of the sensor concept on the injection molded substrate. For injection molding, only one master stamp carrying the optical structures has to be fabricated, which can be done using e-beam lithography.

Fabricated samples with PI waveguides showed an excellent long-term stability, which is an important factor in the context of the development of a commercial product. It could be proven that the devices do not significantly change their transmission or their sensitivity within two years, if stored in a clean and dark place.

## 7 Outlook

Parallel to the realization and demonstration of the polymer waveguide based biosensor on inorganic substrates, which is the main topic of this work, also an injection molding process for the polymethylpentene (PMP) polymer substrates was developed in collaboration with the company Hubertus Goller plastic engineering[194]. This outlook gives a short overview on the progress of the development of the injection molding technology for the sensor substrates made from the material chosen in section 4.1. In addition, preliminary results of DNA measurements with the PI waveguide based sensor on inorganic substrates are presented. These first results obtained for very high DNA concentrations serve as a proof of principle and provide an estimation of the maximum phase shifts that can be induced in the polymer MZI. The determination of the dynamic range of the sensor and the limit of detection remains an issue for ongoing research.

### 7.1 Injection molding results

Injection molding (see Fig. 7.1) requires an injection mold with a cavity containing the structures to be replicated. An injection mold was designed and fabricated that is able to take different circular mold inserts (2" diameter) as carriers of these structures. The design of the mold allows the adjustment to the specific thickness of the mold inserts. Therefore, the use of different mold inserts such as Si wafers, metal plates, glass plates or nickel stamps is possible. In the injection mold, the mold inserts are pressed from the backside against a ring with a diameter of 43 mm, which is also the diameter of the resulting injection molded substrates. In the presented experiments, nanopatterned 2" silicon wafers serve as exchangeable mold inserts and are directly employed for the injection molding process. The use of directly patterned Si wafers as mold inserts ensures optimum feature quality. Moreover, this approach provides maximum flexibility in design, especially for prototyping purposes and small series production, while keeping effort and costs low. The Si wafers can be fabricated by either optical or electron beam lithography and subsequent etching.

#### Injection molding of nanostructures

In recent years, progress in the replication of nanostructures employing injection molding processes has been reported and structures with sub-100 nm features were successfully replicated. For example, pillars with sub-100 nm features in polystyrene (PS) and polycarbonate (PC)[195] or holes with a diameter of 50 nm in PC[196] or nanofeatures of protein complexes in the 10-nm range in polyethylene (PE), polypropylene (PP), cyclic olefins copolymers (COC), polymethylmethacrylate (PMMA) and biodegradable polymers[197] have been demonstrated. In most cases, advanced versions of injection molding processes based on compact disk (CD) fabrication have been employed for the replication of nanostructures. A large amount of experience has been gained using typical standard technical polymers such as PC, PS or PMMA. The Ni-based master stamps for these replication processes are fabricated

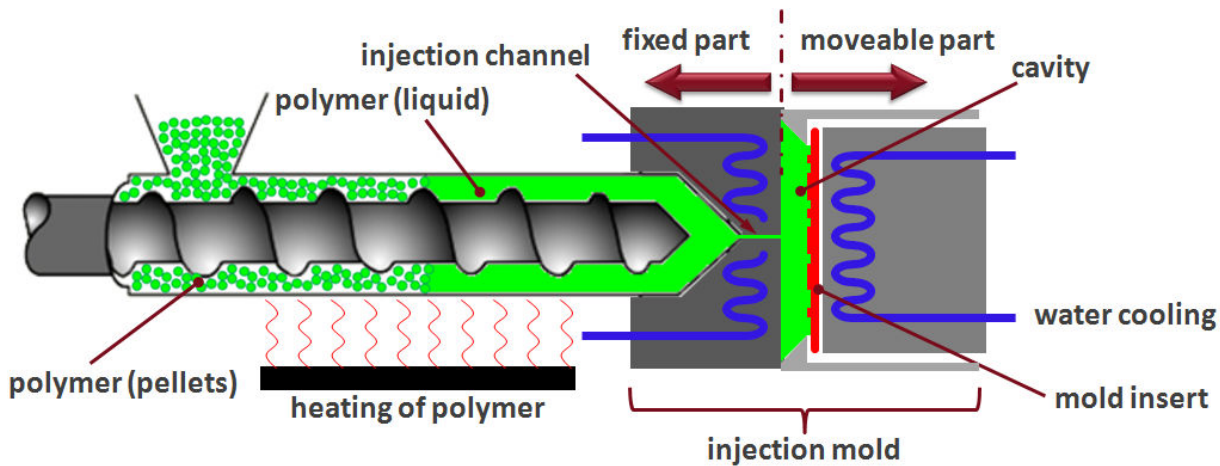


**Figure 7.1:** Schematic of the injection molding process with exchangeable mold inserts.

by a comparatively expensive electroplating process, which additionally bears the risk of introducing defects into the pattern during the process. The omission of the electroplating process step, which is required in case of the conventional injection molding procedure, simplifies the whole process. In addition, the electroplating process can degrade the quality of structures with very small feature sizes. Due to the excellent release properties of PMP, no additional surface treatment of these wafers was necessary after the etching process.

In order to evaluate the quality of the PMP injection molding process and its limits with respect to feature size, various test structures were replicated, which have been etched into 2" Si wafers with different sizes and depths. The mold inserts for the replication of nanopatterns were fabricated by 100 kV electron beam lithography, metal lift-off and dry etching. For the injection molding process, standard parameters according to the PMP datasheet were used and no pre-evacuation of the mold was applied.

Figure 7.2 shows atomic force microscopy (AFM) measurements of various nanostructures with feature sizes between 300 nm and 100 nm. Figure 7.2a) shows the replication of a checker board pattern with an edge length of 300 nm, Fig. 7.2b) a replication of cross bars with 100 nm feature size, Fig. 7.2c) lines and spaces with 200 nm period, and Fig. 7.2d) replications of meander structures with 150 nm feature size. The mold insert used for this replication has a modulation depth of about 150 nm. Most replicated structures on the replicated PMP disks have nearly the same modulation depth as the mold insert. Only the modulation depth of the lines and spaces is considerably smaller than that of the original structures.

Figure 7.3 directly compares the smallest nanostructures on the mold insert and the injection molded PMP substrates. The feature size of these nanostructures is about 50 nm. Figures 7.3a) to 7.3c) show SEM pictures of meander structures, cross bars structures and pillars on the 2" Si mold insert after fifty injection molding processes, while Fig. 7.3d) to 7.3f) show their replicated counterparts on the PMP substrates. A 2 nm gold layer was sputtered on the Si mold insert as well as on the investigated PMP substrate before the SEM measurements. This very thin layer did not form a homogeneous layer on the Si wafer, which is responsible for the island-like surface structure that is obvious in Fig. 7.3a) to 7.3c). The modulation depth of the mold insert for this replication is about 65 nm. AFM measurements were performed for replicated nanostructures from this mold insert and it was found, that the modulation depth for these structures is about 55 nm, which is only 10 nm less than the modulation depth of the

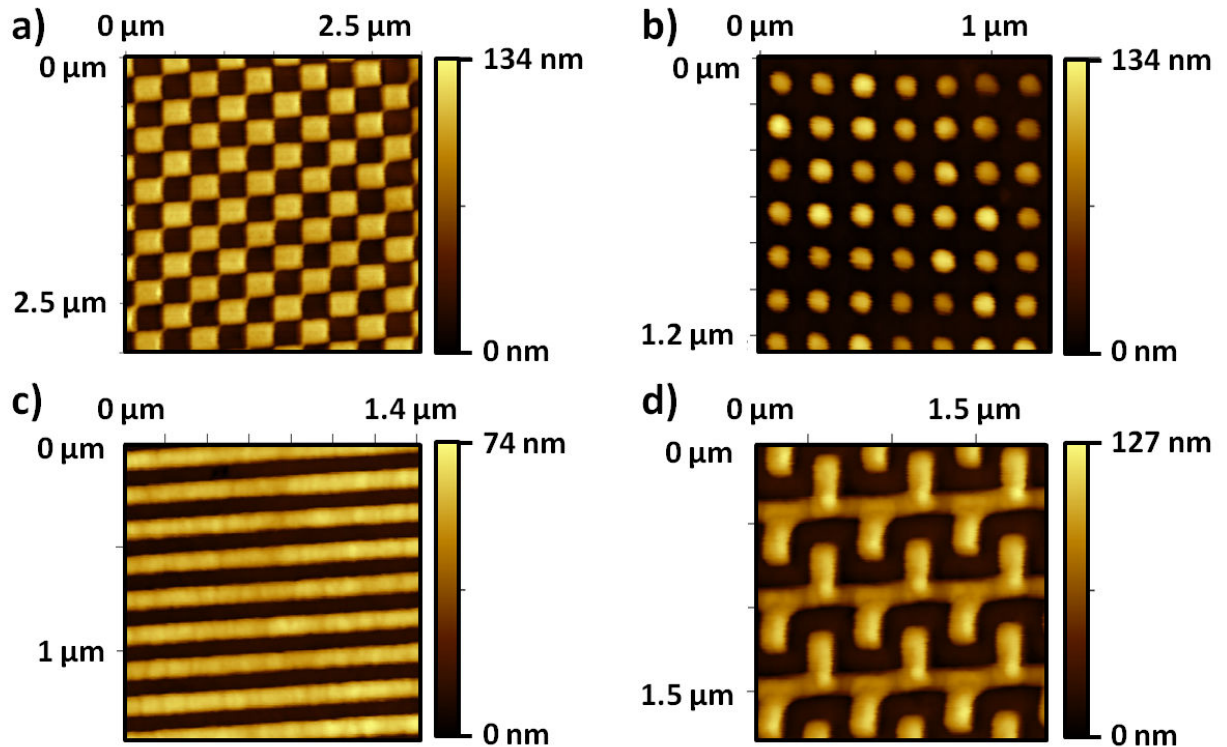


**Figure 7.2:** AFM measurements of nanostructures replicated into PMP; **a)** checker board structure with a feature size of 300 nm; **b)** replicated crossbars pattern with 100 nm feature size; **c)** lines and spaces with 100 nm feature size; **d)** replicated meander structure with 150 nm feature size; The modulation depth of the structures on the silicon mold insert is about 150 nm. Most replicated structures nearly reach the full modulation depth of the mold insert. Only the lines and spaces show a smaller modulation depth.

mold insert. Therefore, the aspect ratio for these nanostructures is larger than 1. In summary, the AFM measurements and the SEM pictures confirmed that all nanostructures were well replicated. All replicates structures have a flat top surface and most structures nearly reach the full modulation depth of the mold insert.

### Injection molding of optical structures and waveguides

For optical and photonic applications, the requirements in terms of feature sizes are often more relaxed than for the replication of nanostructures as presented above. On the other hand, the surface quality in terms of roughness and the contour accuracy of the replication can be vitally important for many optical applications. The ability of the injection molding process to replicate nanostructures with very small feature sizes indicates that larger structures can be replicated in a high quality with respect to surface roughness and contour accuracy, provided that the mold insert shows a sufficient quality. In the design of the MZI, the grating couplers are the most challenging structures in term of feature size. For polymer waveguide grating couplers, the period is typically in the range of 1-2  $\mu\text{m}$  for near infrared light and several hundreds of nanometers for visible light. In Fig. 7.4, AFM measurements for replicated grating couplers are presented. Figure 7.4a) gives an overview scan of a 50  $\mu\text{m}$  wide grating coupler with a period of 1.58  $\mu\text{m}$ , which can be used to couple light with a wavelength of 1.31  $\mu\text{m}$  at an angle of

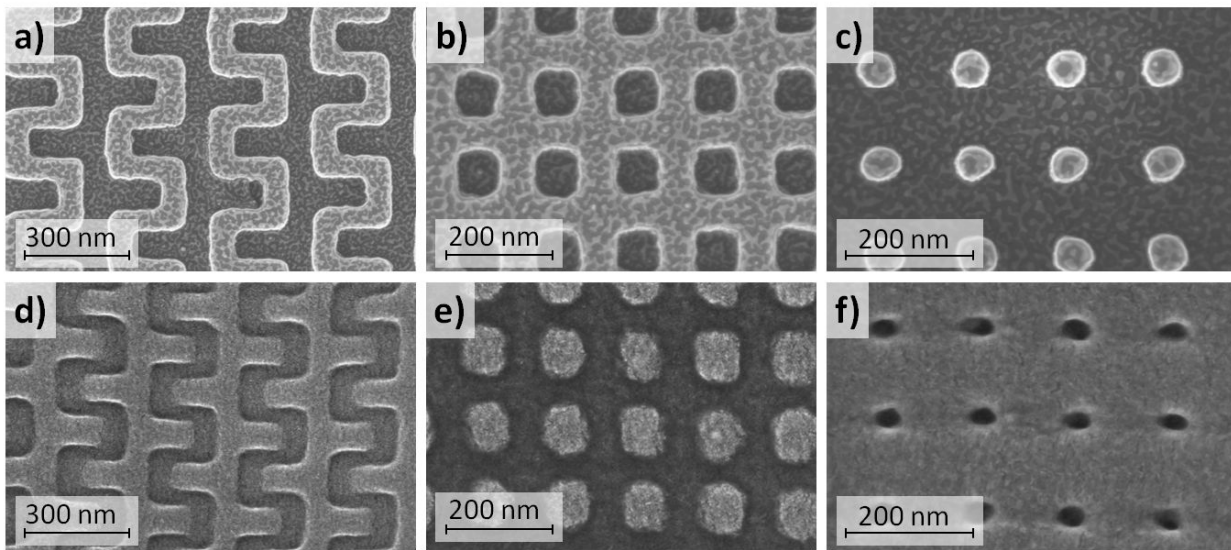


**Figure 7.3:** The pictures a), b) and c) show SEM micrographs of nanostructures with about 50 nm feature size on the silicon mold insert after fifty injection molding processes (bright areas are heightened and dark areas are deepened) and d), e) and f) show corresponding SEM images of the injection molded PMP substrates. To minimize the influence on the nanostructures for SEM characterization, a 2 nm thin gold layer was sputtered on the mold insert and the PMP substrate. This layer was too thin to form a homogeneous layer on the Si wafer and is responsible for the island-like surface structures that are visible in pictures a)-c).

incidence of about  $45^\circ$  into single mode polymer waveguides. This measurement shows a defect-free replicated grating coupler with well defined grating lines. In Fig. 7.4b) a detailed AFM scan of a grating coupler with a period of 500 nm is given. The investigated grating coupler is precisely replicated from the silicon mold insert. It has flat horizontal surfaces with very little surface roughness. The duty cycle and the modulation depth of the grating are the same as on the mold insert.

For first wave guiding experiments, samples were prepared based on injection molded PMP substrates. On these substrates, the commercial photoresist mr-UVL 6000 from micro resist technology was spin coated as waveguide core layer with a thickness of about 500 nm. The light of a fiber-coupled HeNe laser ( $\lambda = 633$  nm) was then collimated to a beam diameter of 500  $\mu\text{m}$  and coupled into a 500  $\mu\text{m}$  wide inverted rib waveguide by means of a grating coupler. The picture in Fig. 7.5 shows the measurement setup with the mounted sample and the incident light beam that is coupled into the waveguide core layer and propagates in the waveguide on the injection molded substrate.

The demonstration of the all-polymer MZI sensor was so far prevented from high propagation losses in single mode waveguides on the injection molded substrates. For the fabrication of waveguides, a high replication quality along the whole length of the waveguide is necessary, because already a small number of localized defects can lead to a significantly increased loss in the waveguide. Figure 7.6 gives an AFM scan of a 5  $\mu\text{m}$  wide waveguide trench and reveals two important imperfections of the replicated structure. First, the trench profile is not perfectly symmetric. This can be most likely attributed to shear forces that occur in the cooling of the sample in the injection molding process due to the high shrinkage of the PMP. The second imperfection is the insufficient replication quality of the edges of the waveguide trench. It was found that this is caused by residuals of PMP that stick on the Si stamp in the corners of the rib to be replicated. In contrast to many other materials tested, PMP has only a comparatively small tendency to leave residuals on the Si surface. Nevertheless, it seems that this non-perfect replication

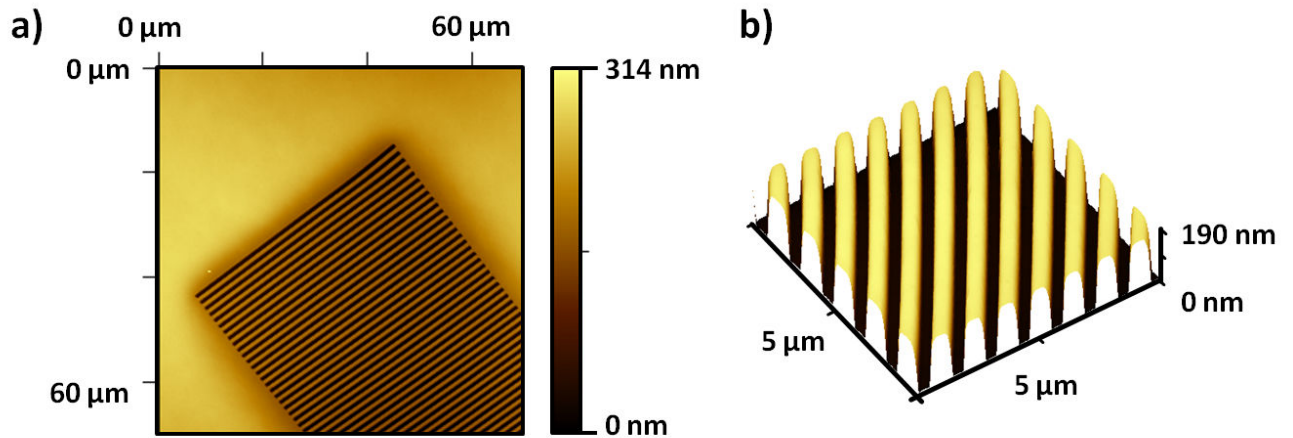


**Figure 7.4:** a) AFM scan of a 50  $\mu\text{m}$  wide waveguide grating coupler with a period of 1.58  $\mu\text{m}$ . b) Detailed analysis of the inner region of a grating coupler with a period of 500 nm. The AFM measurement reveals that the replicated grating coupler has flat surfaces of very high quality and fully reaches the modulation depth of the mold insert that was used for this replication.

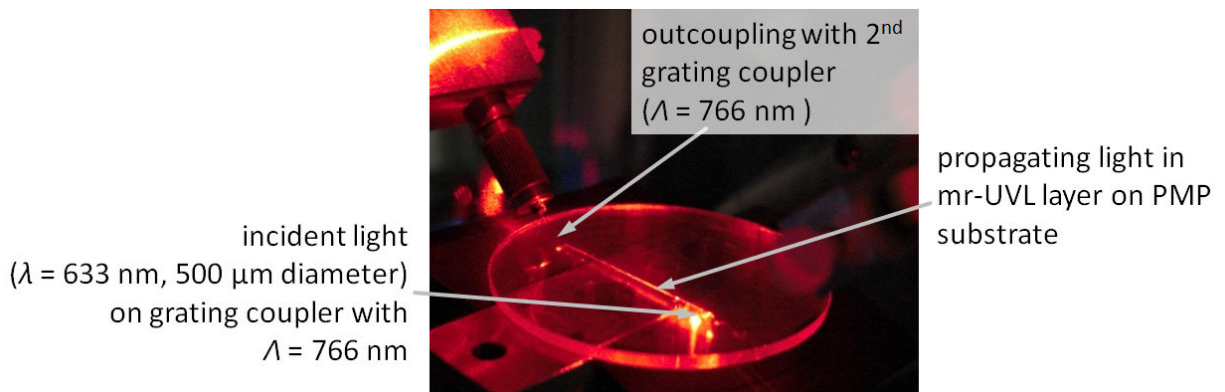


**Figure 7.5:** Injection molded PMP substrate with a 500 nm thick spin coated core layer made from mr-UVL 6000. The incident light ( $\lambda = 633 \text{ nm}$ , 500  $\mu\text{m}$  diameter Gaussian beam) is coupled by means of a grating coupler ( $\Lambda = 766 \text{ nm}$ ) into a 500  $\mu\text{m}$  wide inverted rib waveguide. At the end of the waveguide, the guided light is out-coupled by another grating coupler.

of the waveguide trenches introduces a high amount of scattering to the propagating waveguide mode and is responsible for the large losses in single mode waveguides. One option to prevent residuals on the Si surface in the future and to improve the replication is the use of anti-stiction layers on the Si surfaces. Such layers are often made from fluorinated self assembled monolayers and are a common technology in micro-electro-mechanical systems (MEMS).



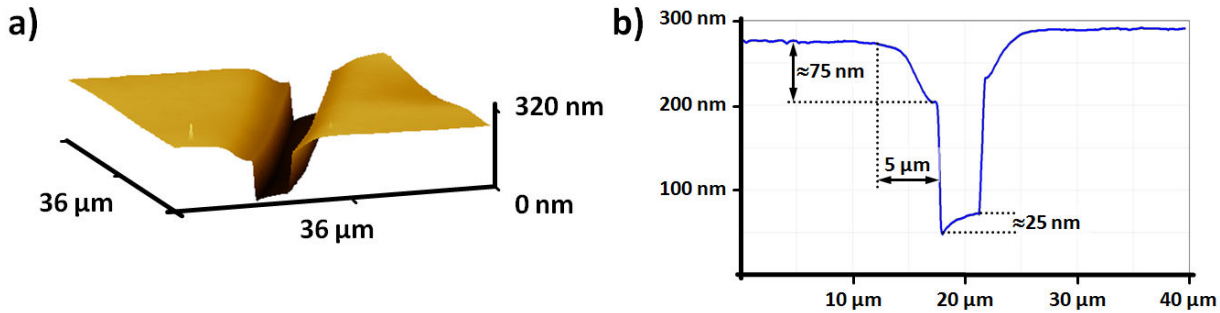


**Figure 7.6:** Analysis of a waveguide trench on an injection molded substrate. **a)** 3D illustration of an AFM scan of the PMP surface and **b)** extracted trench profile from this AFM scan, revealing imperfections in the replication, such as a non-flat bottom or defects at the edges of the profile.

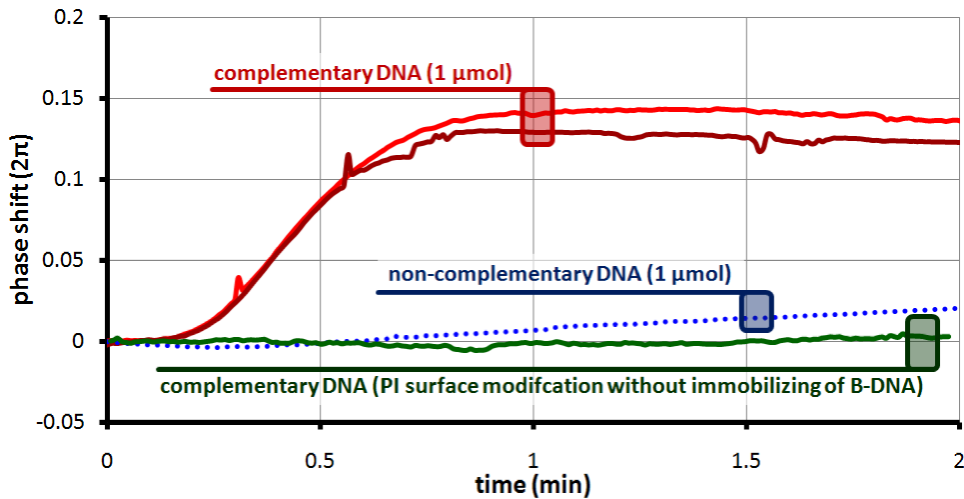


**Figure 7.7:** Phase shifts of DNA measurements of 1  $\mu\text{Mol}$  complementary DNA (red lines) and 1  $\mu\text{Mol}$  non-complementary DNA (blue, dotted line). The green line shows the measurement of 1  $\mu\text{Mol}$  complementary DNA on a sample, where the last step in the surface modification protocol was omitted, which was the modification of the surface with biotin-tagged DNA. This measurement proves that no significant amount of DNA binds non-specifically to the PI surface.

## 7.2 Online measurements of DNA binding

In addition to the detection of proteins, such as streptavidin, the detection of the binding characteristics of DNA strands is the second important field of medical applications, where optical sensors are assumed to be of great benefit due to their online measurement capabilities. DNA strands usually have a smaller mass than streptavidin, and therefore, induce a smaller sensor response.

The samples for the DNA binding experiments were processed in the cleanroom as given in section 5.1, but without HIC. Then, the samples were silanized and biotinylated as for the streptavidin measurements (surface modification protocol given in section 5.5.1). On the biotinylated PI surface, 100  $\mu\text{g/ml}$  streptavidin in PBS solution was rinsed over the surface to bind a maximum amount of streptavidin on the surface. The surface was then rinsed with ultrapure water for 30 minutes to remove any unbound

**Table 7.1:** Sequences of used DNA strands.

abbreviation	DNA sequence and notes
B-DNA	<b>sequence:</b> TCG CCA TTC GTT GAC TAC TTC TTA T biotin-tagged DNA, can bind to streptavidin
C-DNA	<b>sequence:</b> ATA AGA AGT AGT CAA CGA ATG GCG A complementary DNA sequence to B-DNA, can to B-DNA, labeled with Cy3 fluorescent dye
N-DNA	<b>sequence:</b> TTT GAG ACG GAG TCT CGT T non-complementary DNA sequence to B-DNA, cannot bind to B-DNA, labeled with Cy5 fluorescent dye

streptavidin. Finally, biotin-tagged DNA (B-DNA) was introduced to the sensor surface for 10 minutes at a concentration of 1  $\mu\text{Mol/l}$  in PBS solution. The biotin side of the B-DNA strand binds to the surface bound streptavidin and provides binding sites for complementary DNA strands. The exact DNA sequences of the DNA strands used is given in Table 7.1. The samples were measured in end face coupling configuration.

To prove the sensor capability for online detection of DNA binding events on the sensor surface, DNA strands with a complementary sequence (C-DNA, see Table 7.1) dissolved in PBS solution were rinsed over the sensor. The calculated phase shift of the MZI measurements are given as red lines in Fig. 7.7. Due to the high concentration of 1  $\mu\text{Mol}$  and the fast diffusion of the small DNA molecules in the PBS solution, the sensor showed a fast response and reached its saturation already after about one minute. As expected, the acquired phase shift in these measurements is considerably smaller than in streptavidin binding experiments. Nevertheless, a clear identification of the DNA binding process is possible, also supported from the quick sensor response, which minimizes negative effects such as sensor drift. To test for non-specific binding, C-DNA was rinsed over a sensor, functionalized with a surface modification protocol that omitted the last step, which is the immobilization of B-DNA on the sensor surface. The measurement (dark green line in Fig. 7.7) revealed that no significant amount of DNA binds non-specifically to the sensor surface. The selectivity of the binding process was investigated by introducing 1  $\mu\text{Mol}$  non-complementary DNA (N-DNA, see Table 7.1) to the sensor surface. The sensor showed only a very small response to this N-DNA. The measurement curve is presented as blue, dotted line in Fig. 7.7.

In summary, it can be said that the PI waveguides based MZI sensor shows a small, but well defined response in measurements of DNA strands. The DNA binding on the sensor surface was found to be specific and selective. These promising first results put emphasis on the fact that biotin-streptavidin system is a suitable platform for the development of advanced biosensing applications.



## Bibliography

- [1] K. Tiefenthaler and W. Lukosz, "Sensitivity of grating couplers as integrated-optical chemical sensors", *Journal of the optical society of america*, **6** (2), 209-220 (1989).
- [2] F. Brosinger, H. Freimuth, M. Lacher, W. Ehrfeld, E. Gedig, A. Katerkamp, F. Spener and K. Cammann, "A label-free affinity sensor with compensation of unspecific protein interaction by a highly sensitive integrated optical Mach-Zehnder interferometer on silicon", *Sensors and Actuators B*, **44**, 350-355 (1997).
- [3] L.U. Kempen and R.E. Knuz, "Replicated Mach-Zehnder interferometers with focusing grating couplers for sensing applications", *Sensors and Actuators B*, **38-39**, 295-299 (1997).
- [4] K. De Vos, I. Bartolozzi, E. Schacht, P. Bienstman and R. Baets, "Silicon-on-Insulator microring resonator for sensitive and label-free biosensing", *Optics Express*, **15** (12), 7610-7615 (2007).
- [5] J.B. Wright, I. Brener, K.R. Westlake, D.W. Branch, M.J. Shaw, G.A. Vawter, "A platform for multiplexed sensing of biomolecules using high-Q microring resonator arrays with differential readout and integrated microfluidics", *Proceedings of SPIE*, **7605**, 76050C-1 (2010).
- [6] X. Fan, I.M. White, S.I. Shopova, H. Zhu, J.D. Suter and Y. Sun, "Sensitive optical biosensors for unlabeled targets: A review", *analytica chimica acta*, **620**, 8-26 (2008).
- [7] H. Mukundan, A.S. Anderson, W.K. Grace, K.M. Grace, N. Hartman, J.S. Martinez and B.I. Swanson, "Waveguide-Based Biosensors for Pathogen Detection", *Sensors*, **9** (7), 5783-5809 (2009).
- [8] R. Bruck and R. Hainberger, "Efficiency enhancement of grating couplers for single-mode polymer waveguides through high index coatings", *Proceedings of the ECIO*, ThP07 (2008).
- [9] R.G. Heideman, G.J. Veldhuis, E.W.H. Jager and P.V. Lambeck, "Fabrication and packaging of integrated chemo-optical sensors", *Sensors and Actuators B*, **35**, 234 (1996).
- [10] R.G. Heideman, R.P.H. Kooyman and J. Greve, "Performance of a highly sensitive optical waveguide Mach-Zehnder interferometer sensor", *Sensors and Actuators B*, **10**, 209-217 (1993).
- [11] F. Prieto, B. Sepulveda, A. Calle, A. Llobera, C. Dominguez, A. Abad, A. Montoya, and L.M. Lechuga, "An integrated optical interferometric nanodevice based on silicon technology for biosensor applications", *Nanotechnology*, **14**, 907-912 (2003).
- [12] K.K. Tung, W.H. Wong and E.Y.B. Pun, "Polymeric optical waveguides using direct ultraviolet photolithography process", *Applied Physics A*, **80**, 621-625 (2005).
- [13] R. Waldhäusl, B. Schnabel, P. Danneberg, E.-B. Kley, A. Bräuer and W. Karthe, "Efficient coupling into polymer waveguides by gratings", *Applied Optics*, **36** (36), 9383-9390 (1997).
- [14] W.B. Guo, C.S. Ma, D.M. Zhang, K.X. Chen, Y. Zhao, Z.C. Cui and S.Y. Liu, "Parameter optimization and structural design of polymer arrayed waveguide grating multiplexer", *Optics Communications*, **201** (1-3), 45-53 (2002).
- [15] E.Y.B. Pun, "Photonic Integrated Polymer Waveguide Amplifiers", *ICTON*, Tu.B2.3 (2005).
- [16] E.F. Schipper, A.M. Brugman, C. Dominguez, L.M. Lechuga, R.P.H. Kooyman and J. Greve, "The realization of an integrated Mach-Zehnder waveguide immunosensor in silicon technology", *Sensors and Actuators B*, **40** (2-3), 147-153 (1997).
- [17] B. Sepulveda, J. Sanchez del Rio, M. Moreno, F. J. Blanco, K. Mayora, C. Dominguez and L. M. Lechuga, "Optical biosensor microsystems based on the integration of highly sensitive Mach-Zehnder interferometer devices", *Journal of Optics A: Pure and Applied Optics*, **8**, 561-566 (2006).

- [18] K. Zinoviev, L. G. Carrascosa, J. Sanchez del Rio, B. Sepulveda, C. Dominguez and L. M. Lechuga, "Silicon photonic biosensors for lab-on-a-chip applications", *Advances in Optical Technologies*, 383927 (2008).
- [19] A. Densmore, D.X. Xu, S. Janz, P. Waldron, T. Mischki, G. Lopinski, A. Del age, J. Lapointe, P. Cheben, B. Lamontagne and J. H. Schmid, "Spiral-path high-sensitivity silicon photonic wire molecular sensor with temperature-independent response", *Optics Letters*, **33** (6), 596-598 (2008).
- [20] B.Y. Shew, Y.C. Cheng and Y.H. Tsai, "Monolithic SU-8 micro-interferometer for biochemical detections", *Sensors and Actuators A*, **141** (2), 299-306 (2008).
- [21] D. Esinenco, S. D. Psoma, M. Kusko, A. Schneider and R. Muller, "SU-8 micro-biosensor based on Mach-Zehnder interferometer", *Reviews on Advanced Materials Science*, **10**, 295-299 (2005).
- [22] R. Muller, P.Obreja, M. Kusko, D. Esinenco, C. Tibeica, G. Conache, L. Buia, D. Apostol, V. Damian, M. Mateescu, M. Diaconu and L. Moldovan, "SU 8 Used as Optical Waveguide in Integrated Optical Microsensor for Biological Applications", *Proc. of SPIE*, **5972**, 5972-35 (2005).
- [23] M. Nordstr om, D.A. Zauner, A. Boisen and J. Hubner, "Single-Mode Waveguides With SU-8 Polymer Core and Cladding for MOEMS Applications", *IEEE Journal of Lightwave Technology*, **25** (5), 1284-1289 (2007).
- [24] G. T. Paloczi, Y. Huang, A. Yariv, J. Luo and A.K.Y. Jen, "Replica-molded electro-optic polymer Mach-Zehnder modulator", *Appl. Phys. Lett.*, **85**, 1662-1664 (2004).
- [25] A. Densmore, D.X. Xu, P. Waldron, S. Janz, P. Cheben, J. Lapointe, A. Delage, B. Lamontagne, J.H. Schmid and E. Post, "A Silicon-on-Insulator Photonic Wire Based Evanescent Field Sensor", *IEEE Photonics Technology Letters*, **18** (23), 2520-2522 (2006).
- [26] M.A. Webster, R.M. Pafchek, A. Mitchell and A. Koch, "Width Dependence of Inherent TM-Mode Lateral Leakage Loss in Silicon-On-Insulator Ridge Waveguides", *IEEE Photonics Technology Letters*, **19** (6), 429-431 (2007).
- [27] P. Muellner, N. Finger and R. Hainberger, "Lateral leakage in symmetric SOI rib-type slot waveguides", *Optics Express*, **16** (1), 287-294 (2008).
- [28] D.X. Xu, A. Densmore and A. Delage, "Folded cavity SOI microring sensors for high sensitivity and real time measurement of biomolecular binding", *Optical Express*, **16** (19), 15137-15148 (2008).
- [29] S. Busse, V. Scheumann, B. Menges and S. Mittler, "Sensitivity studies for specific binding reactions using the biotin/streptavidin system by evanescent optical methods", *Biosensors and Bioelectronics*, **17**, 704-710 (2002).
- [30] M. Iqbal, M. Gleeson, B. Spaugh, F. Tybor, W. Gunn, M. Hochberg, T. Baehr-Jones, R. Bailey, and L. Gunn, "Label-Free Biosensor Arrays Based on Silicon Ring Resonators and High-Speed Optical Scanning Instrumentation", *IEEE Journal of Selected Topics in Quantum Electronics*, **16** (3), 654-661 (2010).
- [31] G. T. Reed, *Silicon photonics*, John Wiley & Sons Ltd., Sussex, England (2008).
- [32] G. Lifante, *Integrated Photonics*, John Wiley & Sons Ltd., Sussex, England (2003).
- [33] K. Okamoto, *Fundamentals of Optical Waveguides*, Academic Press, San Diego, USA (2000).
- [34] H. Nishihara, M. Haruna and T. Suhara, *Optical Integrated Circuits*, McGraw-Hill Book Company, New York, USA (1985).
- [35] C. R. Pollock and M. Lipson, *Integrated Photonics*, Kluwer Academic Publishers, Dordrecht, Netherlands (2003).
- [36] E.A.J. Marcatili, "Slab-coupled waveguides", *Bell System Technical Journal*, **53**, 645-674 (1974).
- [37] Comsol, *Femlab 3.1.0.163*, April 2005, FEMLAB GmbH, Berliner Str. 4, 37073 Goettingen, Germany.
- [38] J. Jin, *The Finite Element Method in Electromagnetics*, John Wiley and Sons, New York, USA, second edition (2002).
- [39] K. Petermann, "Properties of optical rib-waveguides with large cross-section", *Archiv f ur Elektronik und  bertragungstechnik*, **30** (3), 139-140 (1976).

- [40] R.A. Soref, J. Schmidtchen and K. Petermann, "Large single-mode rib waveguides in GeSi-Si and Si-on-SiO<sub>2</sub>", *IEEE Journal of Quantum Electronics*, **27** (8), 1971-1974 (1991).
- [41] V. Ramaswamy, "Strip loaded film waveguide", *Bell System Technical Journal*, **53** (4), 697-705 (1974).
- [42] S. P. Pogossian, L. Vescan and A. Vonsovici, "The single-mode condition for semiconductor rib waveguides with large cross section", *IEEE Journal of Lightwave Technology*, **16** (10), 1851-1853 (1998).
- [43] P. Müllner and R. Hainberger, "Single-mode criterion for rib waveguides with small cross sections", *Proceedings of the SPIE*, **6115**, 436-443 (2006).
- [44] Y. Shani, C.H. Henry, R.C. Kistler, K.J. Orlowsky and D.A. Ackerman, "Efficient coupling of a semiconductor laser to an optical fibre by means of a tapered waveguide in silicon", *Applied Physics Letters*, **55** (23), 2389-2391 (1989).
- [45] S.R. Park and B.H. O, "Novel Design Concept of Waveguide Mode Adapter for Low-Loss Mode Conversion", *IEEE Photonics Technology Letters*, **13** (7), 675-677 (2001).
- [46] T. Bakke, C.T. Sullivan and S.D. Mukherjee, "Polymeric optical spot-size transformer with vertical and lateral tapers", *Journal of Lightwave Technology*, **20** (7), 1188-1197 (2002).
- [47] A. Domval, R. Oron and M. Oron, "Low Loss Optical Interconnects to Silicon Waveguides", *Proceedings of SPIE*, **6123**, 61231E-1 (2006).
- [48] I. Moerman, P.P. Van Daele and P.M. Demeester, "A Review on Fabrication Technologies for the Monolithic Integration of Tapers with III-V Semiconductor Devices", *IEEE Journal of Selected Topics in Quantum Electronics*, **3** (6), 1308-1320 (1997).
- [49] K.K. Lee, D.R. Lim, D. Pan, C. Hoepfner, W.Y. Oh, K. Wada, L. Kimerling, K.P. Yap and M.T. Doan, "Mode transformer for miniaturized optical circuits", *Optics Letters*, **30** (5), 489-500 (2005).
- [50] V.R. Almeida, R.R. Panepucci and M. Lipson, "Nanotaper for compact mode conversion", *Optics Letters*, **28** (15), 1302-1304 (2003).
- [51] G. Roalkens, P. Dumon, W. Bogaerts, D. Van Thourhout and R. Beats, "Efficient Silicon-on-Insulator Fiber Coupler Fabricated Using 248-nm-Deep UV Lithography", *IEEE Photonics Technology Letters*, **17** (12), 2613-2615 (2005).
- [52] J. Jansson, "Prism coupling selectivity in anisotropic uniaxial waveguide", *Applied Optics*, **20** (2), 374-380 (1981).
- [53] W.A. Pasmooij, P.A. Mandersloot and M.K. Smit, "Prism-Coupling of Light into Narrow Planar Optical Waveguides", *IEEE Journal of Lightwave Technology*, **7** (1), 175-180 (1989).
- [54] P.K. Tien and R. Ulrich, "Theory of Prism-Film Coupler and Thin-Film Light Guides", *Journal of the optical society of America*, **60** (10), 1325-1337 (1969).
- [55] M.H. Shih, W.J. Kim, W. Kuang, J.R. Cao, H. Yukawa, S.J. Choi, J.D. O'Brien, P.D. Dapkus and W.K. Marshall, "Two-dimensional photonic crystal Mach-Zehnder interferometers", *Appl. Phys. Lett.*, **84**, 460-462 (2004).
- [56] A. Adibi, R.K. Lee, Y. Xu, A. Yariv and A. Scherer, "Design of photonic crystal optical waveguides with single mode propagation in the photonic bandgap", *Electronics Letters*, **36** (16), 1376-1378 (2000).
- [57] N. Skivesen, A. Tetu, M. Kristensen, J. Kjems, L.H. Frandsen and P.I. Borel, "Photonic-crystal waveguide biosensor", *Optics Express*, **15** (6), 3169-3176 (2007).
- [58] V. Toccafondo, J. Garcia-Ruperez, M. Jose Banuls, A. Griol, J. Garcia-Castello, S. Peransi-Llopis and A. Maquieira, "DNA Detection Using a Photonic Crystal Waveguide Sensor", *Optical Sensors, OSA Technical Digest*, SWB3 (2010).
- [59] D. Tailleart, H. Chong, P.I. Borel, L.H. Frandsen, R.M. De La Rue and R. Beats, "A Compact Two-Dimensional Grating Coupler Used as a Polarization Splitter", *IEEE Photonics Technology Letters*, **15** (9), 1249-1251 (2003).
- [60] W. Bogaerts, D. Tailleart, P. Dumon, D. Van Thourhout and R. Beats, "A polarization-diversity wavelength duplexer circuit in silicon-on-insulator photonic wires", *Optics Express*, **15** (4), 1567-1578 (2007).

- [61] J. Canning, "Fiber Gratings and Devices for Sensors and Lasers", *Lasers and Photonics Reviews*, **2** (4), 275-289, Wiley, USA (2008).
- [62] K.O. Hill, Y. Fujii, D.C. Johnson and B.S. Kawasaki, "Photosensitivity in optical fiber waveguides: application to reflection fiber fabrication", *Applied Physics Letters*, **32**, 647 (1978).
- [63] P. Ferraro and G. De Natale, "On the possible use of optical fiber Bragg gratings as strain sensors for geodynamical monitoring". *Optics and Lasers in Engineering*, **37**, 115-130 (2002).
- [64] S. Ura, T. Fujii, T. Suhara and H. Nishihara, "Efficiency-enhanced third-order grating coupler", *Applied Optics*, **38** (14), 3003-3007 (1999).
- [65] T. Touam and S. I. Najafi, "Symmetric profile beams from waveguides with asymmetric grating couplers", *Applied Optics*, **36** (12), 2554-2558 (1997).
- [66] A. Kocabas, F. Ay, A. Dana and A. Aydinli, "An elastomeric grating coupler", *Journal of Optics A: Pure and Applied Optics*, **8**, 85-87 (2006).
- [67] T. Mossberg, C. Greiner and D. Iazikov, "Impact of high-resolution photolithography on integrated photonics", *Microlithography world*, **14** (3), 28 (2005).
- [68] M. Hagberg, N. Eriksson and A. Larsson, "High efficiency surface emitting lasers using blazed grating outcouplers", *Applied physics letters*, **67** (25), 3685 (1995).
- [69] K. Kincade, "OPTOELECTRONIC APPLICATIONS: NANOPHOTONICS - Silicon photonics sets the stage for optical datacom", *Laser focus world*, **44** (3), (2008).
- [70] Luxtera, 2320 Camino Vida Roble Carlsbad, CA 92011, [www.luxtera.com](http://www.luxtera.com).
- [71] G. Voirin, D. Gehringer, O.M. Parriaux and B. Usievich, "Si<sub>3</sub>N<sub>4</sub>/SiO<sub>2</sub>/Si waveguide grating for fluorescent biosensors", *Proceedings of SPIE*, 1009-116 (1999).
- [72] R. Orobtcouk, A. Layadi, H. Gualous, D. Pascal, A. Koster and S. Laval, "High-efficiency light coupling in a submicrometric silicon-on-insulator waveguide", *Applied Optics*, **39** (31), 5773-5777 (2000).
- [73] T.W. Ang, G.T. Reed, A. Vonsovici, A.G.R. Evans, P.R. Routely and M.R. Josey, "Highly efficient unibond silicon-on-insulator blazed grating coupler", *Applied Physics Letters*, **77** (25), 4214-4216 (2000).
- [74] D. Heitmann and C. Ortiz, "Calculation and Experimental Verification of Two-Dimensional Focusing Grating Couplers", *IEEE Journal of Quantum Electronics*, **17** (7), 1257-1263 (1981).
- [75] Y. Sohn, Y. Park, D. Suh, H. Ryn and M.C. Pael, "Focusing Grating Coupler for Blue Laser light", *IEEE Photonics Technology Letters*, **16** (1), 162-164 (2004).
- [76] S. Kristjansson, N. Eriksson, P. Modh and A. Larsson, "Surface-Emitting Tapered Unstable Resonator Laser with Integrated Focusing Grating Coupler", *IEEE Photonics Technology Letters*, **12** (10), 1319-1321 (2000).
- [77] K. Kintaka, Y. Imaoka, J. Ohmori, S. Ura, R. Satoh and N. Nishihara, "A guided-Mode-Selective Focusing Grating Coupler", *IEEE Photonics Technology Letters*, **16** (2), 512-514 (2004).
- [78] F. Van Laere, T. Claes, J. Schrauwen, S. Scheerlinck, W. Bogaerts, D. Taillaert, L. O'Faolain, D. Van Thourhout and R. Baets, "Compact Focusing Grating Couplers for Silicon-on-Insulator Integrated Circuits", *IEEE Photonics Technology Letters*, **19** (23), 1919-1921 (2007).
- [79] O. Parriaux and G.J. Veldhuis, "Normalized Analysis for the sensitivity optimization of integrated optical evanescent-wave sensors", *IEEE Journal of Lightwave Technology*, **16** (4), 573-582 (1998).
- [80] A. Aulasevich, R.F. Roskamp, U. Jonas, B. Menges, J. Dostalek and W. Knoll, "Optical Waveguide Spectroscopy for the Investigation of Protein-Functionalized Hydrogel Films", *Macromolecular Rapid Communications*, **30** (9-10), 1022-1336 (2009).
- [81] K. De Vos, J. Giroones, S. Popelka, E. Schacht, R. Beats and P. Bienstmann, "SOI optical microring resonator with poly(ethylen glycol) polymer brush for label-free biosensor applications", *Biosensors and Bioelectronics*, **24** (8), 2528-2533 (2009).
- [82] O. Prucker, C.A. Naumann, J. Rhe, W. Knoll and C.W. Frank, "Photochemical attachment of polymer films to solid surfaces via monolayers of benzophenone derivatives", *Journal of American Chemical Society*, **121**, 8766-8770 (1999).



- [83] P.W. Beines, I. Klosterkamp, B. Menges, U. Jonas and W. Knoll, "Responsive thin hydrogel layers from photo-cross-linkable poly(N-isopropylacrylamide) Terpolymers", *Langmuir*, **23** (4), 2231-2238 (2007).
- [84] A. Ymeti, J. Greve, P.V. Lambeck, T. Wink, S.W.F.M. van Hövell, T.A.M. Beumer, R.R. Wijn, R.G. Heideman, V. Subramaniam and J.S. Kanger, "Fast, Ultrasensitive Virus Detection Using a Young Interferometer Sensor", *Nano Letters*, **7** (2), 394-397 (2007).
- [85] A. Brandenburg and R. Henninger, "Integrated optical Young interferometer", *Applied Optics*, **33** (25), 5941-5947 (1994).
- [86] Z.M. Qi, S. Zhao, F. Chen and S. Xia, "Integrated Young interferometer sensor with a channel-planar composite waveguide sensing arm", *Optics Letters*, **34**, 2213-2215 (2009).
- [87] R. Narayanaswamy and O. S. Wolfbeis, *Optical Sensors*, Springer-Verlag, Berlin, Germany, (2004).
- [88] nGimat Co., 5315 Peachtree Blvd, Atlanta, GA 30341, [www.ngimat.com/electronics/sensors.html](http://www.ngimat.com/electronics/sensors.html).
- [89] Farfield Group Ltd, Electra Way CW1 6GU, Cheshire, United Kingdom, [www.farfield-group.com](http://www.farfield-group.com).
- [90] R.G. Heideman and P.V. Lambeck, "Remote opto-chemical sensing with extreme sensitivity: design, fabrication and performance of a pigtailed integrated optical phase-modulated Mach-Zehnder interferometer system", *Sensors and Actuators B*, **61**, 100-127 (1999).
- [91] D.G. Garton, S.L. Kwiatkowski, G.F. Lipscomb and R.S. Lytel, "20 GHz electro-optic polymer Mach-Zehnder modulator", *Applied Physics Letters*, **58** (16), 1730-1732 (1991).
- [92] C.T. Zheng, C.S. Ma, X. Yan, X.Y. Wang and D.M. Zhang, "Design and analysis of a polymer Mach-Zehnder interferometer electro-optic switch over a wide spectrum of 110 nm", *Optical Engineering*, **48** (5), 054601 (2009).
- [93] R.A. Mayer, K.H. Jung, W.D. Lee, D.L. Kwong and J.C. Campbell, "Thin-film thermo-optic Ge<sub>x</sub>Si<sub>1-x</sub> Mach-Zehnder interferometer", *Optics Letters*, **17**, 1812-1814 (1992).
- [94] R.L. Espinola, M.C. Tsai, J.T. Yardley and R.M. Osgood, "Fast and low-power thermo-optic switch on thin silicon-on-insulator", *IEEE Photonics Technology Letters*, **15** (10), 1366 - 1368 (2003).
- [95] B.J. Luff, J.S. Wilinson, J. Piehler, U. Hollenbach, J. Ingenhoff and N. Fabricius, "Integrated optical Mach-Zehnder Biosensor", *IEEE Journal of Lightwave technology*, **16** (4), 583-592 (1998).
- [96] A. Ksendzov and Y. Lin, "Integrated optics ring-resonator sensors for protein detection", *Optics Letters*, **30** (24), 3344-3346 (2005).
- [97] X. Fan, I.M. White, H. Zhu, J.D. Suter and H. Oveys, "Overview of novel integrated optical ring resonator bio/chemical sensors", *Proceedings of SPIE*, **6452**, 64520M (2007).
- [98] J. Niehusmann, A. Vörckel, P.H. Bolivar, T. Wahlbrink, W. Henschel and H. Kurz, "Ultra-high-quality-factor silicon-on-insulator microring resonator" *Optics Letters*, **29**, 2861-2863 (2004).
- [99] C.-Y. Chao, W. Fung and L.J. Guo, "Polymer Microring Resonators for Biochemical Sensing Applications", *IEEE Journal of selected topics in quantum electronics*, **12** (2), 134-142 (2006).
- [100] J.C. Brazas and L. Li, "Analysis of input-grating couplers having finite length", *Applied Optics*, **34**, 3786-3792 (1995).
- [101] J. Vörös, J.J. Ramsden, G. Csucs, I. Szendrő, S.M. De Paul, M. Textor and N.D. Spencer, "Optical grating coupler biosensor", *Biomaterials*, **23**, 3699-3710 (2002).
- [102] MicroVacuum Ltd, Kerékgyártó u. 10, Budapest, H-1147, [www.owls-sensors.com](http://www.owls-sensors.com).
- [103] Dynetix AG Schulstrasse 1 CH-7302 Landquart [www.dynetix.ch](http://www.dynetix.ch).
- [104] M. Wiki and R. E. Kunz, "Wavelength-interrogated optical sensor for biochemical applications", *Optics Letters*, **25** (7), 463-465 (2000).
- [105] Corning Incorporated, One Riverfront Plaza, Corning, NY 14831 USA [www.corning.com/lifesciences/us\\_canada/en/whats\\_new/epic\\_system.aspx](http://www.corning.com/lifesciences/us_canada/en/whats_new/epic_system.aspx).
- [106] B.T. Cunnigham, P. Li, B. Lin and J. Pepper, "Colorimetric Resonant Reflection as a Direct Biochemical Assay Technique", *Sensors and Actuators B*, **81**, 316-328 (2002).

- [107] SRU Biosystems, Inc. 14-A Gill Street Woburn, MA 01801 [www.srubiosystems.com](http://www.srubiosystems.com).
- [108] T. Nikolajsen and K. Leosson, "Surface plasmon polariton based modulators and switches operating at telecom wavelength", *Applied physics letters*, **85** (24), 5833-5835 (2004).
- [109] T.-J. Wang, C.-W. Tu and H.-L. Chen, "Surface plasmon resonance waveguide biosensor by bipolarization wavelength interrogation", *IEEE Photonics technology letters*, **16** (7), 1715-1717 (2004).
- [110] T.-J. Wang, C.-W. Tu and F.-K. Liu, "Integrated-optic surface plasmon resonance biosensor using gold nanoparticles by bipolarization detection", *IEEE Journal of selected topics in quantum electronics*, **11** (2), 493-499 (2005).
- [111] W.-C. Kuo, C. Chou and H.-T. Wu, "Optical heterodyne surface-plasmon resonance biosensor", *Optics Letters*, **28** (15), 1329-1331 (2003).
- [112] K. Matsubara, S. Kawata and S. Minami, "Optical chemical sensor based on surface plasmon measurement", *Applied optics*, **27**, 1160-1163 (1998).
- [113] J. Dostalek, A. Kasry and W. Knoll, "Long range surface plasmons for observation of biomolecular binding events at metallic surfaces", *Plasmonics*, **2**, 97-106 (2007).
- [114] R. Slavík and J. Homola, "Ultrahigh resolution long range surface plasmon-based sensor", *Sensors and Actuators B*, **132** (1), 10-12 (2007).
- [115] A. Kasry and W. Knoll, "Long range surface plasmons fluorescence spectroscopy", *Applied Physics Letters*, **89**, 101106 (2006).
- [116] GE Healthcare Europe GmbH, Munzinger Strasse 5, 79111 Freiburg, Germany, [www.biocore.com](http://www.biocore.com).
- [117] Bio-Rad Laboratories, Clinical Diagnostics Group, 4000 Alfred Nobel Drive, Hercules, CA 94547, [www.bio-rad.com](http://www.bio-rad.com).
- [118] Graffinity Pharmaceuticals GmbH, Im Neuenheimer Feld 518, 69120 Heidelberg, Germany, [www.graffinity.com/index.php](http://www.graffinity.com/index.php).
- [119] FUJIFILM Corporation, Akasaka 9-chome, Minato-ku, Tokyo 107-0052, Japan, [www.fujifilm.com/products/life\\_science\\_systems/other\\_product/ap3000/ap3000.html](http://www.fujifilm.com/products/life_science_systems/other_product/ap3000/ap3000.html).
- [120] ICx Technologies, 2100 Crystal Drive, Suite 650, Arlington, VA 22202, [www.discoverensiq.com/products/sensiq](http://www.discoverensiq.com/products/sensiq).
- [121] Reichert Inc., 3362 Walden Ave., Depew, NY 14043, [reichertspr.com/products.html](http://reichertspr.com/products.html).
- [122] N.J. Tao, S. Boussaad, W.L. Huang, R.A. Arechabaleta and J.D. Agnese, "High resolution surface plasmon resonance spectroscopy", *Review of Scientific Instruments*, **70** (12), 4656-4660 (1999).
- [123] R. Slavik, J. Homola and J.C. Ctyroky, "Single-mode optical fiber surface plasmon resonance sensor", *Sensors and Actuators B*, **54**, 74-79 (1999).
- [124] D. Monzón-Hernández and J. Villatoro, "High-resolution refractive index sensing by means of a multiple-peak surface plasmon resonance optical fiber sensor", *Sensors and Actuators B*, **115**, 227-231 (2006).
- [125] A. Suzuki, J. Kondoh, Y. Matsui, S. Shiokawa and K. Suzuki, "Development of novel optical waveguide surface plasmon resonance (SPR) sensor with dual light emitting diodes", *Sensors and Actuators B*, **106**, 383-387 (2006).
- [126] F.C. Chien, C.Y. Lin, J.N. Yih, K.L. Lee, C.W. Chang, P.K. Wei, C.C. Sun and S.J. Chen, "Coupled waveguide-surface plasmon resonance biosensor with subwavelength grating", *Biosensors and Bioelectronics*, **22**, 2737-2742 (2006).
- [127] J. Dostalek, J. Homola and M. Miler, "Rich information format surface plasmon resonance biosensor based on array of diffraction gratings", *Sensors and Actuators B*, **107**, 154-161 (2005).
- [128] G.G. Nenninger, P. Tobiska, J. Homola and S.S. Yee, "Long-range surface plasmons for high-resolution surface plasmon resonance sensors", *Sensors and Actuators B*, **74**, 145-151 (2001).
- [129] A. Ymeti, J.S. Kanger, J. Greve, P.V. Lambeck, R. Wijn and R.G. Heideman, "Realization of a multichannel integrated Young interferometer chemical sensor", *Applied Optics*, **42**, 5649-5660 (2003).

- [130] A. Yalçın, K.C. Papat, J.C. Aldridge, T.A. Desai, J. Hryniewicz, N. Chbouki, B.E. Little, O. King, V. Van, S. Chu, D. Gill, M. Anthes-Washburn, M. Selim Unlu and B.B. Goldberg, "Optical sensing of biomolecules using microring resonators", *IEEE Journal of Selected Topics in Quantum Electronics*, **12**, 148-155 (2006).
- [131] C.-Y. Chao, W. Fung and L.J. Guo, "Polymer microring resonators for biochemical sensing applications", *IEEE Journal of Selected Topics in Quantum Electronics*, **12**, 134-142 (2006).
- [132] A. Yalcin, K.C. Papat, J.C. Aldridge, T.A. Desai, J. Hryniewicz, N. Chbouki, B.E. Little, O. King, V. Van, S. Chu, D. Gill, M. Anthes-Washburn and M.S. Unlu, "Optical sensing of biomolecules using microring resonators", *IEEE Journal of Selected Topics in Quantum Electronics*, **12** (1), 148-155 (2006).
- [133] K. De Vos, I. Bartolozzi, E. Schacht, P. Bienstman and R. Baets, "Silicon-on-Insulator microring resonator for sensitive and label-free biosensing", *Optics Express*, **15** (12), 7610-7615 (2009).
- [134] C.A. Barrios, K.B. Gylfason, B. Sánchez, A. Griol, H. Sohlström, M. Holgado and R. Casquel, "Slot-waveguide biochemical sensor", *Optics Letters*, **32** (21), 3080-3082 (2007).
- [135] V.M.N. Passaro, F. Dell'Olio, B. Casamassima and F. De Leonardis, "Guided-Wave Optical Biosensors", *Sensors*, **7**, 508-536 (2007).
- [136] R.C. Bailey, A.L. Washburn, A.J. Qavi, M. Iqbal, M. Gleeson, F. Tybor and L.C. Gunn, "A Robust Silicon Photonic Platform for Multiparameter Biological Analysis", *Proceedings of SPIE*, **7220**, 7220-22 (2009).
- [137] N. Darwish, D. Caballero, M. Moreno, A. Errachid, J. Samitier, "Multi-analytic grating coupler biosensor for differential binding analysis", *Sensors and Actuators B*, **144** (2), 413-417 (2010).
- [138] J. Dostalek and J. Homola, "Surface plasmon resonance sensor based on an array of diffraction gratings for highly parallelized observation of biomolecular interactions", *Sensors and Actuators B*, **129**, 303-310 (2009).
- [139] E.D. Palik, *Handbook of optical constants of solids*, Academic Press, Boston (1991).
- [140] N. Daldosso, M. Melchiorri, F. Riboli, M. Girardini, G. Pucker, M. Crivellari, P. Bellutti, A. Lui and L. Pavesi, "Comparison among various Si<sub>3</sub>N<sub>4</sub> waveguide geometries grown within a CMOS fabrication pilot line", *IEEE Journal of Lightwave Technology*, **22** (7), 1734-1740 (2004).
- [141] W. Stutius and W. Streifer, "Silicon nitride films on silicon for optical waveguides", *Applied Optics*, **16** (12), 3218-3222 (1977).
- [142] G. Pandraud, H.T.M. Pham, P.J. French and P.M. Sarro, "Polarization-insensitive PECVD SiC waveguides for sensor platform", *Optical Materials*, **28**, 380-384 (2006).
- [143] G. Pandraud, H.T.M. Pham, P.M. Sarro and P.J. French, "PECVD SiC Rib Waveguides Loss and Passive Devices", *European Conference on integrated Optics*, **12**, 262-265 (2005).
- [144] A. Vonsovici, G.T. Reed and A.G.R. Evans, "beta-SiC-on insulator waveguide structures for modulators and sensor systems", *Material Science in Semiconductor Processing*, **3**, 367-374 (2000).
- [145] T. Flaim, Y. Wang, R. Mercado, "High Refractive Index Polymer Coatings for Optoelectronics Applications", *Proceedings of the SPIE*, **5250**, 423-434 (2004).
- [146] P. Obreja, M. Kusko, D. Cristea, M. Purica and F. Comanescu, "Doped polymers with controllable refractive index - preparation, processing and applications", *Proceedings of the Symposium on Photonics Technologies*, 392-395 (2006).
- [147] [www.texloc.com/closet/cl\\_refractiveindex.html](http://www.texloc.com/closet/cl_refractiveindex.html).
- [148] A.S. Holland, A. Mitchel, V.S. Balkunje, M.W. Austin, M.K. Raghunathan, "Fabrication of Raised and Inverted SU8 Polymer Waveguides", *Proceedings of SPIE*, **5644**, 353-366 (2005).
- [149] H. Ma, A.K.-Y. Jen and L.R. Dalton, "Polymer-based optical waveguides: materials, processing and devices", *Advanced Materials*, **14** (9), 1339-1356 (2002).
- [150] R. Yoshimura, M. Hikita, S. Tomaru and S. Imamura, "Low-loss polymeric optical waveguides fabricated with deuterated polyfluoromethacrylate", *IEEE Journal of Lightwave Technology*, **16** (6), 1030-1037 (1998).
- [151] K. Tamaki, H. Takase, Y. Eriyama and T. Ukachi, "Recent progress on polymer waveguide materials", *Journal of Photopolymer Science and Technology*, **16** (5), 639-648 (2003).

- [152] Mitsui Chemicals America, Inc, 800 Westchester Ave., Rye Brook, NY 10573, [www.mitsuichemicals.com](http://www.mitsuichemicals.com).
- [153] Zeon Europe GmbH, Niederkasseler Lohweg 177, 40547 Düsseldorf, Germany, [www.zeonex.com](http://www.zeonex.com).
- [154] HD MicroSystems GmbH, Hugenottenallee 173-175, 63263 Neu-Isenburg, Germany, [hdmicrosystems.com](http://hdmicrosystems.com).
- [155] BASF AG, 67056 Ludwigshafen, Germany, [www.basf.com/group/corporate/de/](http://www.basf.com/group/corporate/de/).
- [156] micro resist technology GmbH, Köpenicker Str. 325, 12555 Berlin, Germany, [www.microresist.de](http://www.microresist.de).
- [157] A. Farjadpour, D. Roundy, A. Rodriguez, M. Ibanescu, P. Bermel, J.D. Joannopoulos, S.G. Johnson and G. Burr, "Improving accuracy by subpixel smoothing in FDTD", *Optics Letters*, **31** (20), 2972-2974 (2006).
- [158] R. Scarmozzino, A. Gopinath, R. Pregla and S. Helfert, "Numerical techniques for modeling guided-wave photonic devices", *IEEE Journal of selected topics in quantum electronics*, **6**(1), 150-162 (2000).
- [159] R. Scarmozzino and R.M. Isgood Jr., "Comparison of finite-difference and Fourier-transform solution of the parabolic wave equation with emphasis on integrated-optics applications", *Journal of the optical Society of America A*, **8** (5), 724-731 (1991).
- [160] G.R. Hadley, "Transparent boundary conditions for beam propagation", *Optics Letters*, **16** (9), 624-626 (1991).
- [161] W.P. Huang and C.L. Xu, "Simulation of three-dimensional optical waveguides by a full-vector beam propagation method", *IEEE Journal of quantum electronics*, **29** (10), 2639-2649 (1993).
- [162] C.L. Xu, W.P. Huang, J. Chrostowski and S.K. Chaudhuri "A full vectorial beam propagation method for anisotropic waveguides", *IEEE Journal of lightwave technology*, **12** (11), 1926-1931 (1994).
- [163] G.R. Hadley, "Wide-angle beam propagation using Pade approximant operators", *Optics Letters*, **17** (20), 1426-1428 (1992).
- [164] H. Rao, R. Scarmozzino and R.M. Osgood Jr., "A Bidirectional Beam Propagation Method for Multiple Dielectric Interfaces", *IEEE Photonics technology letters*, **11** (7), 830-832, (1999).
- [165] A.W. Snyder and J.D. Love, *Optical waveguide theory*, Springer, USA (1983).
- [166] N. Destouches, D. Blanc, J. Franc, S. Tonchev, N. Hendrickx, P. Van Daele and O. Parriaux, "Efficient and tolerant resonant grating coupler for multimode optical interconnections", *Optics Express*, **25**, 1687-1696 (2007).
- [167] K.A. Bates, L. Li, R.L. Roncone and J.J. Burke, "Gaussian beams from variable groove depth grating couplers in planar waveguides", *Applied Optics*, **32** (12), 2112-2116 (1993).
- [168] S. Miyanaga and T. Asakura, "Intensity profile of outgoing beam from uniform and linearly tapered grating couplers", *Applied Optics*, **20** (4), 688-695 (1981).
- [169] T. Tamir, *Integrated Optics*, Springer-Verlag New York, (1982).
- [170] K. Ogawa, W.S.C. Chang, B.L. Sopori and F.J. Rosenbaum, "A theoretical analysis of etched grating couplers for integrated optics", *IEEE Journal of quantum electronics*, **9** (1), 29-42 (1973).
- [171] C. Pollok, M. Lipson, *Integrated Photonics*, Norwell: Kluwer Academic Publishers, ch. 11, 273 (2003).
- [172] O. Parriaux, V.A. Sychugov and A. Tishchenko, "Coupling gratings as waveguide functional elements", *Pure Applied Optics*, **5**, 435-469 (1996).
- [173] T. Tamir and S.T. Peng, "Analysis and Design of Grating couplers", *Applied Physics*, **14**, 235-254 (1977).
- [174] O. Parriaux, V.A. Sychugovz and A.V. Tishchenko, "Coupling gratings as waveguide functional elements", *Pure Applied Optics*, **5**, 453-469 (1996).
- [175] N. Finger and E. Gornik, "Analysis of metallized-grating coupled twin-waveguide structures", *IEEE Journal of Quantum Electronics*, **35** (5), 832-843 (1999).
- [176] R. J. Noll and S. H. Macomber, "Analysis of grating surface emitting lasers", *IEEE Journal of Quantum Electronics*, **26**, 456 (1990).

- [177] G. Hadjicostas, J. K. Butler, G. A. Evans, N. W. Carlson and R. Amantea, "A numerical investigation of wave interactions in dielectric waveguides with periodic surface corrugations", *IEEE Journal of Quantum Electronics*, **26**, 893 (1990).
- [178] K.S. Yee, "Numerical solution of initial boundary value problems involving Maxwell's equations in isotropic media", *IEEE Transactions on Antennas and Propagation*, **14** (9), 302-307 (1966).
- [179] Meep - MIT Electromagnetic Equation Propagation, <http://ab-initio.mit.edu/wiki/index.php/Meep>.
- [180] A.A. Spikhal'skii, "Effective use of diffraction gratings in optical devices based on diffused waveguides", *Soviet Journal of Quantum Electronics*, **15**, 1018-1020 (1985).
- [181] D. Taillaert, P. Bienstmann and R. Baets, "Compact efficient broadband grating coupler for silicon-on-insulator waveguides", *Optics Letters*, **29** (23), 2749-2751 (2004).
- [182] B. Schmid, A. Petrov and M. Eich, "Optimized grating coupler with fully etched slots", *Optics Express*, **17** (3), 11066-11076 (2009).
- [183] N.M. Green, "Avidin", *Advances in Protein Chemistry*, **29**, 85-133 (1975).
- [184] M. Weisser, G. Tovar, S. Mittler-Neher, W. Knoll, F. Brosinger, H. Freimuth, M. Lacher and W. Ehrfeld, "Specific bio-recognition reactions observed with an integrated Mach-Zehnder interferometer", *Biosensors and Bioelectronics*, **14**, 405-411 (1999).
- [185] E. Melnik, R. Bruck, R. Hainberger and M. Lämmerhofer, "Multi-step surface functionalization via biotinylation and streptavidin immobilization for polyimide based evanescent wave photonic biosensors", *Analytical & Bioanalytical Chemistry*, to be published(2010).
- [186] Z. Wei, L. Weiping, L. Huicong and Z. Liqun, "Erosion of a Polyimide Material Exposed to Simulated Atomic Oxygen Environment", *Chinese Journal of Aeronautics*, **23**, 268-273 (2010).
- [187] B. Zhu, H. Iwata, I. Hirata and Y. Ikada, "Hydrophilic modification of a polyimide film surface", *Journal of Adhesion Science and Technology*, **14** (3), 351-361 (2000).
- [188] R. Flitsch and Y. Shih, "A study of modified polyimide surfaces as related to adhesion", *The Journal of Vacuum Science and Technology*, **8** (3), 2379-2381 (1990).
- [189] Y. Nakamura, Y. Suzuki, Y. Watanabe, "Effect of oxygen plasma etching on adhesion between polyimide films and metal", *Thin Solid Films*, **290-291**, 367-369 (1996).
- [190] J. Spinke, M. Liley and F.J. Schmitt, "Molecular recognition at self-assembled monolayers: Optimization of surface functionalization", *Journal of Chemical Physics*, **99** (9), 7012-7019 (1993).
- [191] S.A. Darst, M. Ahlers and P.H. Meller, "Two-dimensional crystals of streptavidin on biotinylated lipid layers and their interactions with biotinylated macromolecules", *Biophysical Journal*, **59**, 387-396 (1991).
- [192] F. Pippig and A. Holländer, "Hydrogel nanofilms for biomedical applications: Synthesis via polycondensation reactions", *Macromolecular Bioscience*, **10**, 1093-1105 (2010).
- [193] P. Bienstmann, K. De Vos, T. Claes, P. Debackere, R. Baets, J. Girones and E. Schacht, "Biosensors in Silicon on Insulator", *Proceedings of SPIE*, **7220**, 72200O (2009).
- [194] Hubertus Goller Ges.m.b.H., Donaustraße 110, A-3400 Klosterneuburg, Austria, [www.goller.com](http://www.goller.com).
- [195] D. Macintyre and S. Thoms, "The fabrication of high resolution features by mould injection", *Microelectronic Engineering*, **41/42**, 211-214 (1998).
- [196] H. Schiff, C. David, M. Gabriel, J. Gobrecht, L.J. Heyderman, W. Kaiser, S. Köppel and L. Scandella, "Nanoreplication in polymers using hot embossing and injection molding", *Microelectronic Engineering*, **53**, 171-174 (2000).
- [197] N. Gadegaard, S. Mosler and N.B. Larsen, "Biomimetic Polymer Nanostructures by Injection Molding", *Macromolecular Materials and Engineering*, **288**, 76-83 (2003).

# Appendix

## Abstract in english

The selective detection of biomolecules, such as proteins or DNA strands, is of vitally importance for medical diagnosis. Optical biosensors are believed to be a promising way to overcome the limitations of expensive and time-consuming state-of-the-art diagnostic tests by offering label free analyte detection employing selective molecular binding processes, fast sensor response, real time measurements of the analyte binding processes and a high level of integration. Because of hygienic standards and to prevent cross contaminations, sensors including the fluidic systems have to be designed as single use systems for most medical applications. Therefore, fabrication costs are another critical parameter that has to be taken into account for the development of new sensor systems.

In this thesis, the development of a fully integrated Mach-Zehnder interferometer biosensor, based on high index contrast polymer waveguides is reported. An additional advantage of the highly sensitive Mach-Zehnder interferometer concept is the simple read out system, which can be composed of a single mode laser diode with a fixed wavelength and a photodiode. The optical sensor design, based on grating waveguide couplers for light in- and out-coupling as well as single mode polymer waveguides, is fully compatible with cost-efficient mass production technologies for polymers such as injection molding and spin coating, which makes the sensor an attractive alternative to inorganic optical sensors. Polyimide ( $n = 1.65$ ) was selected as waveguide core material and Ormoclad ( $n = 1.52$ ) was selected for the UV-patternable cladding. The sensor elements are rigorously simulated and optimized applying the parameters from the selected materials. For an improved efficiency of small grating couplers in material systems with comparatively low index contrasts, the novel approach of a high index coating on top of grating couplers was applied. Simulations revealed a nearly 8 dB increase in the maximum coupling efficiency into narrow single mode waveguides by means of grating couplers due to the high index coating. The positive effect of the high index coating was then experimentally verified.

Biosensing capabilities of the sensors were demonstrated in the biotin-streptavidin system. For the binding experiments, the surface of the polyimide waveguide core layer was functionalized with 3-mercaptopropyl trimethoxy silane and maleimide tagged biotin. An optimized surface modification protocol was developed for maximum streptavidin binding capacity, while not attacking the thin polymer core layer. With fluorescent labeled Chromeon 642-streptavidin, a maximum population density of  $144 \text{ fmol/mm}^2$  was measured on the polyimide surface. This result for the surface coverage with streptavidin is better than what can be expected in theory on a perfectly planar surface and evidences a more than two-dimensional binding behavior of streptavidin on the PI surface, which can at least be partly explained by the nano-porous structure of the PI surface.

Finally, the polymer waveguide based biosensor was applied for label-free online measurements of biotin-streptavidin binding processes on the sensor surface at a wavelength of 1310 nm. Despite the large wavelength and the comparatively low surface sensitivity of the sensor system due to the low index contrast in polymer material systems compared to inorganic material systems, streptavidin concentrations down to  $0.1 \text{ }\mu\text{g/ml}$  were resolved.

## Abstract in german

Die selektive Detektion von Biomolekülen, wie z.B. Proteinen oder Teilen von DNA, ist von essentieller Bedeutung für die medizinische Diagnostik. Optische Biosensoren werden aktuell als vielversprechende Kandidaten gehandelt, um die Beschränkungen teurer und zeitaufwändiger state-of-the-art diagnostischer Tests zu überwinden indem sie markerfreie Messung des Analyten durch selektive molekulare Anbindungsprozesse, schnelle Sensorreaktion, die Fähigkeit zur Echtzeitmessung der Bindereaktion des Analyten sowie geringen Platzbedarf und ein hohes Maß an Integration bieten. Aufgrund hygienischer Anforderungen und um Kontaminationen zwischen Sensoren zu vermeiden, müssen Sensoren und fluidische Systeme für die meisten medizinischen Anwendungen als Einweggeräte ausgelegt werden. Daher sind Fabrikationskosten ein wichtiger Faktor, der in der Entwicklung neuer Sensorsysteme berücksichtigt werden muss.

In dieser Arbeit wird die Entwicklung eines vollständig integrierten Mach-Zehnder Interferometer Biosensors, basierend auf Hochindexkontrast Polymerwellenleitern, dargelegt. Ein weiterer Vorteil des Mach-Zehnder Interferometer ist das unkomplizierte Auslesesystem, welches aus einer Laserdiode mit einer fixen Wellenlänge und einer Photodiode aufgebaut werden kann. Das Design des optischen Sensors, basierend auf optischen Beugungsgittern für die Kopplung von Licht in und aus dem Sensor sowie monomodigen Polymerwellenleitern, ist vollständig kompatibel mit weit verfügbaren und kosteneffizienten Technologien zur Massenproduktion von Polymer-basierten Bauteilen, wie Spritzgießen und Aufschleudern, was diesen Sensor zu einer interessanten Alternative zu anorganischen Sensorkonzepten macht. Polyimid ( $n = 1.65$ ) wurde für die Wellenleiterschicht und Ormoclad ( $n = 1.52$ ) für die Deckschicht ausgewählt. Die Elemente des Sensors wurden unter Anwendung der Parameter der selektierten Materialien vollständig simuliert und optimiert. Um die Koppeffizienz kleiner Gitterkoppler in Materialsystemen mit niedrigem Indexkontrast zu erhöhen, wurde der neuartige Zugang einer Hochindex Beschichtung von Gitterkopplern angewandt. In den Simulationen zeigte sich eine Steigerung der maximalen Koppeffizienz mittels Gitterkopplern in schmale, monomodige Wellenleiter durch die Aufbringung dieser Hochindex Beschichtung um nahezu 8 dB. Der positive Effekt der Hochindex Beschichtung wurde anschließend experimentell verifiziert.

Die Fähigkeiten der Sensoren für biologische Messungen wurden im Biotin-Streptavidin System gezeigt. Für die Bindung von Streptavidin auf der Sensoroberfläche während dieser Experimente wurde die Sensoroberfläche mit 3-mercaptopropyl trimethoxy Silan und Maleimid-markiertem Biotin funktionalisiert. Eine optimierte Oberflächenmodifizierung wurde entwickelt, welche die Polyimid-Oberfläche nicht angreift oder dünnt. Mit fluoreszenzmarkiertem Streptavidin wurde eine maximale Besetzungsdichte von  $144 \text{ fmol/mm}^2$  gemessen. Diese Besetzungsdichte ist höher als man auf einer perfekt planen Ebene bei dichter Packung erwarten kann, womit ein mehr als zweidimensionales Bindungsverhalten von Streptavidin auf dem Polyimid bewiesen wird, was zumindest teilweise durch die nanoporöse Struktur des Polyimids erklärt werden kann.

Zuletzt wurde der auf Polymerwellenleitern basierte Sensor für die markerfreie Echtzeitmessung der Bindungsprozesse von Biotin-Streptavidin bei einer Wellenlänge von 1310 nm eingesetzt. Trotz der großen Wellenlänge und des geringen verfügbaren Brechungsindexkontrastes in Polymer-Materialsystemen, verglichen mit anorganischen Materialsystemen, konnten Streptavidin Konzentrationen ab  $0.1 \mu\text{g/ml}$  erfolgreich detektiert werden.



## List of publications and presentations

R. Bruck, E. Melnik, P. Muellner and R. Hainberger, "Integrated polymer-based Mach-Zehnder interferometer label-free streptavidin biosensor compatible with injection molding", *Biosensors and Bioelectronics*, submitted (2010).

E. Melnik, R. Bruck, R. Hainberger and M. Lämmerhofer, "Multi-step surface functionalization via biotinylation and streptavidin immobilization for polyimide based evanescent wave photonic biosensors", *Analytical and Bioanalytical Chemistry*, submitted (2010).

R. Bruck, R. Hainberger, R. Heer, N. Kataeva, A. Köck, M. Krapf-Günther, K. Kaiblinger, F. Pipelka and B. Bilenberg, "Direct replication of nanostructures from silicon wafers in polymethylpentene by injection molding", Oral presentation at SPIE Opto + Photonics in San Diego and *Proceedings of SPIE*, **7788**, 77880A (2010).

P. Muellner, R. Bruck, R. Hainberger, M. Karl, M. Baus and T. Wahlbrink, "Silicon nanophotonic components for an integrated refractometric sensor array", *Procedia Engineering* (2010).

S. Schrittwieser, J. Schotter, T. Maier, R. Bruck, P. Muellner, N. Kataeva, K. Soulantika, F. Ludwig, A. Huetten and H. Brueckl, "Homogeneous biosensor based on optical detection of the rotational dynamics of anisotropic nanoparticles", *Procedia Engineering* (2010).

R. Bruck and R. Hainberger, "Efficient coupling of narrow beams into polyimide waveguides by means of grating couplers with high-index coating", *Applied Optics*, **49** (10), 1972-1978 (2010).

R. Hainberger, P. Muellner and R. Bruck, "SOI photonic wire Bragg gratings for interferometric sensor arrays", *Proceedings of the ECIO* (2010).

R. Hainberger, R. Bruck and P. Muellner, "Silicon photonic wire Bragg reflectors for wavelength-multiplexed interferometric sensor arrays", *Proceedings of the Nanophotonics conference* (2010).

R. Hainberger, R. Bruck, N. Kataeva, R. Heer, A. Köck, P. Czepl, K. Kaiblinger, F. Pipelka and B. Bilenberg, "Nanopatterned polymethylpentene substrates fabricated by injection molding for biophotonic applications", *Microelectronics Engineering*, **87**, 821-823 (2010).

R. Hainberger, R. Bruck, N. Kataeva, R. Heer, A. Köck, P. Czepl, K. Kaiblinger, F. Pipelka and B. Bilenberg, "Injection molding of nanopatterned polymethylpentene substrates for bio-optical applications", Poster presentation at MNC and *Proceedings of International Microprocesses and Nanotechnology Conference* (2009).

R. Hainberger, R. Bruck, P. Muellner, K. Roppert, W. Boxleitner, C. Pacher and N. Finger, "Design of silicon and polymer photonic waveguide structures for sensing applications", *Proceedings of Photonics North* (2009).

R. Bruck, "Optical biosensors based on polymer waveguide technology", Oral presentation at Nano and Photonics (2009).

R. Bruck and R. Hainberger, "Efficient small grating couplers for low-index difference waveguide systems", Oral presentation at Photonics West and *Proceedings of the SPIE*, **7218**, 7218-9 (2009)

R. Bruck and R. Hainberger, "Polymer waveguide based biosensor", Oral presentation at Photonics Prague and *Proceedings of the SPIE*, **7138**, 71380N (2008)

P. Muellner, R. Bruck, K. Roppert and Rainer Hainberger, "Label-free DNA sensing with an integrated optical Mach-Zehnder interferometer based on SOI technology", *Mikroelektroniktagung* (2008).

R. Bruck and R. Hainberger, "Efficiency enhancement of grating couplers for single mode polymer waveguides through high index coatings", Poster presentation at ECIO and *Proceedings of the ECIO*, **ThP07** (2008).

## Curriculum vitae

Name: Roman Bruck

---

Address: Flachg. 43/9, 1150 Vienna, Austria

---

Birth: 3.8.1979 in Vienna

### Education:

---

Elementary school: Eduard-Suess-Gasse, 1150 Vienna 1986-1990

---

Secondary school: Gymnasium auf der Schmelz 1990-1994

---

**Secondary college for engineering,**  
special training focus: automation

Passed with distinction 1994-1999

---

National service: 4<sup>th</sup> Gardekompanie, Maria-Theresien caserne 1999-2000

---

University: **Master of science in physics at the university of Vienna,** 2000-2005  
focus on computational physics

Passed with distinction

Title of Diploma Thesis: *Monte Carlo simulations on hydrogen isotopes filter based on carbon nanotubes*

---

**PhD thesis in physics at the university of vienna and the Austrian Institute of Technology,** department Nano Systems 2006-2010

Title of PhD thesis: *High index difference polymer waveguide Mach-Zehnder interferometer biosensor, compatible with injection molding and spin-coating*

Publications during PhD-thesis: 4 peer-reviewed journal papers, 10 publications in conference proceedings, 7 presentations on international conferences

---